MAGNETICALLY SEPARABLE NANOCOMPOSITES WITH ENHANCED PHOTOCATALYTIC ACTIVITIES FOR SOME SELECTED DYES AND PESTICIDES DEGRADATIONS

A THESIS SUBMITTED IN PARTIAL FULFILLMENT OF THE REQUIREMENTS FOR THE DEGREE OF DOCTOR OF PHILOSOPHY

BROJENDRO SINGH SHAGOLSEM

MZU REGISTRATION NUMBER: 2001043

Ph.D. REGISTRATION NUMBER: MZU/Ph.D./1527 of 05.11.2020

DEPARTMENT OF CHEMISTRY

SCHOOL OF PHYSICAL SCIENCES

MAY, 2024

MAGNETICALLY SEPARABLE NANOCOMPOSITES WITH ENHANCED PHOTOCATALYTIC ACTIVITIES FOR SOME SELECTED DYES AND PESTICIDES DEGRADATIONS

BY

BROJENDRO SINGH SHAGOLSEM

Department of Chemistry

Under the supervision of

Prof. N. MOHONDAS SINGH

Submitted

In partial fulfillment of the requirement of the Degree of Doctor of Philosophy in Chemistry of Mizoram University, Aizawl.

MIZORAM UNIVERSITY

DEPARTMENT OF CHEMISTRY

MIZORAM: AIZAWL – 796004

Prof. N. Mohondas Singh, HoD

THESIS CERTIFICATE

This is to certify that the thesis entitled **"*Magnetically Separable Nanocomposites with Enhanced Photocatalytic Activities for Some Selected Dyes and Pesticides Degradations*"** submitted to Mizoram University, Aizawl for the award of the degree of Doctor of Philosophy by ***Mr. Brojendro Singh Shagolsem*** **(Regd. No.: MZU/Ph.D./1527 of 05.11.2020)**, research scholar in the Department of Chemistry, is the record of original research work carried out under my supervision. He has been duly registered and the thesis presented is worthy of being considered for the award of the degree. This work has not been submitted elsewhere for any degree in any other Universities.

Date: (Prof. N. MOHONDAS SINGH)
Place: Supervisor

Phone: (0389) 2330860/2330832 Fax: (0389) 2330860 nmdas08@rediffmail.com

Declaration of the Candidate

Mizoram University

May, 2024

I, Brojendro Singh Shagolsem, hereby declare that the subject matter of this thesis is the record of work done by me, that the contents of this thesis did not form basis of the award of any previous degree to me or to do the best of my knowledge to anybody else, and that the thesis has not been submitted by me for any research degree in any other University/ Institute.

This is being submitted to the Mizoram University for the degree of Doctor of Philosophy in Chemistry.

(BROJENDRO SINGH SHAGOLSEM)
Candidate

(Prof. N. MOHONDAS SINGH)
Head

(Prof. N. MOHONDAS SINGH)
Supervisor

ACKNOWLEDGEMENT

First and foremost, I would like to express all my profound sense of gratitude to my honored supervisor Prof. Nongmaithem Mohondas Singh, Professor, Department of Chemistry, School of Physical Science, Mizoram University, Aizawl for his constant inspiration at every stage of my research work. His serious involvement, thoughtfulness and patience helped me to complete my work in time. It was an invaluable experience to work under him and also gained a tremendous knowledge through his supervision. His guidance will remain unforgettable throughout my journey.

My sincere thanks also go to Prof. Suman Rai, Dean of School of Physical Science, Prof. N. Mohondas Singh, Head, Department of Chemistry and other faculty members Prof. Diwakar Tiwari, Prof. Muthukumaram R, Dr. Zodinpuia Pachuau, Dr. R. Lalrempuia, Dr. A. Bimolini Devi, Dr. Joydeep Das, Dr. Manjeet Singh, Dr. G. Rajendra Kumar, Department of Chemistry, Mizoram University, for their kind support and continue to motivate during the course of my research work.

I also would like to thank Mr. John Vanlalhruaia, Technical Assistant, Department of Chemistry, MZU and other non-teaching staffs for their help and co-operation during my research work.

I would like to express my sincere thanks to Dr. Rakesh Singh Moirangthem, Associate Professor, Department of Physics, Manipur University and Dr. Naorem Premjit Singh, Assistant Professor, A.R.S.D College, Delhi for their persistent support, guidance and invaluable helps throughout my research journey.

I am very thankful to my fellow labmates Dr. Ramananda Singh Naorem, Mr. Herojit Singh Nongmaithem Ms. Lallianmawii, Ms. Niveda Leishangthem, Mr. PC Chuaudingpuia, Ms. Fidelia Lalrindiki, and all the Research Scholars in the Department of Chemistry, Mizoram University, for their co-operations and helps.

I am very thankful to my parents, Manglem Singh Shagolsem and Memma Devi Wahengbam, my wife Wahengbam Inaocha Devi and my brothers and sisters for their endless love, support, care etc. during my academic career.

Lastly, I would like to thank Almighty God, without his grace, none of this would be possible.

Date: (BROJENDRO SINGH SHAGOLSEM)

Place:

TABLE OF CONTENTS

LISTS OF TABLES

List of tables (Continued) **Page no.**

LISTS OF FIGURES

Lists of Figures (Continued) **Page no.**

Lists of Figures (Continued) **Page no.**

Lists of Figures (Continued) **Page no.**

Lists of Figures (Continued) **Page no.**

ABBREVIATIONS

2,4 DCP	2,4-Dichlorophenol
BET	Brunauer–Emmett–Teller
CB	Conduction Band
cm	Centimetre
EDAX	Energy Dispersive X-Ray Analysis
eV	Electron Volt
FESEM	Field Emission Scanning Electron Microscope
FTIR	Fourier Transform Infrared Spectroscopy
FWHM	Full Width at Half Maximum HP Hexagonal Phase
HRTEM	High Resolution Transmission Electron Microscope
JCPDS	Joint Committee on Powder Diffraction Standards
KeV	Kilo volts
LED	Light Emitting Diode
MB	Methylene Blue
mg	Milligram
min	Minute
mL	Millilitre
MNPs	Magnetic nanoparticles
NPs	Nanoparticles
PL	Photoluminescence
ppm	Parts per million
RhB	Rhodamine B
rpm	Round per minute
SAED	Selected Area Electron Diffraction
SEM	Scanning Electron Microscope
TCAA	Trichloroacetic acid
TEM	Transmission Electron Microscope
TOC	Total organic carbon
UV	Ultraviolet
VB	Valance band
XRD	X-Ray Diffraction

CHAPTER 1

INTRODUCTION

1.1 Background

A photocatalyst needs sunlight to accelerate a chemical process, which is critical as the economy and industry rapidly expand, necessitating the resolution of pollution issues. Organic pollutants, which are water-soluble, easily enter water systems, causing severe illnesses. Nanomaterials offer unique solutions to mitigate pollution due to their expansive surface area [Nethravathia *et al*., (2015)]. Solar energy is increasingly vital for long-term pollution control, particularly in industrial applications like eliminating hazardous textile dyes [Mei *et al*., (2018)]. This method transforms organic chemicals into inorganic compounds, removing textile manufacturing dyes from wastewater [Ho *et al*., (2018); Hasnat *et al*., (2005)]. Methylene blue (MB), rhodamine B (RhB), 2,4-dichlorophenol (2,4-DCP), and trichloroacetic acid (TCAA) must be degraded for environmental remediation. Photocatalysts, adsorbents, and sophisticated oxidation methods employing TiO_2, ZnO, and Graphene Oxide have been used to degrade these contaminants. Strong oxidative power, chemical stability, and non-toxicity make TiO_2 and ZnO popular photocatalysts with wide band gap energy. In UV light, they produced ROS that destroy organic contaminants. Since they are non-toxic and reusable, both degrade MB, RhB, and other organic dyes with minimum environmental impact. It needs adjustments or doping to work well in visible light. GO's rare electrical characteristics and high surface area make it ideal for photocatalysis. It can be used alone or with TiO_2. GO-based composites improve visible light pollutant degradation. Though low-impact, GO production and disposal must be controlled to avoid environmental damage. Titanium dioxide (TiO_2), Zinc Oxide (ZnO), and Graphene Oxide (GO) nanoparticles exposed to UV light generate reactive oxygen species (ROS) that degrade organic pollutants like dyes and pesticides. Using visible light-activated materials such doped TiO_2, ZnO, or GO. The high surface area and porosity of activated carbon and biochar allow contaminants to adsorb onto their surfaces.

Another material is biochar, it is a carbon-rich material made from biomass

pyrolysis, and activated carbon has a high surface area and porosity, making it an efficient adsorbent for dyes and pesticides. These are effective at removing impurities, it can get saturated and need regeneration or replacement which may release secondary pollutants. Biochar made from agricultural waste is eco-friendly, hence reduces greenhouse gasses by sequestering carbon. It generated hydroxyl radicals (•OH) from hydrogen peroxide (H_2O_2) and iron ions (Fe^{2+}). Advanced Oxidation Processes (AOPs) use Fenton and Photo-Fenton Reactions and Ozonation. Using iron ions (Fe^{2+}), the Fenton reaction generates hydroxyl radicals (•OH) from hydrogen peroxide (H_2O_2). Photo-Fenton employed light to boost the reaction while the powerful oxidant Ozone (O_3) degrades organic contaminants under UV light. These mechanisms efficiently degrade many contaminants but iron sludge disposal and management can be environmentally harmful. Similarly, ozonation also works but must be controlled to avoid bromate and ozone consumption demands a lot of energy.

Electrochemical methods also degrade dyes and pesticides by generating H_2O_2 in situ via electrochemical reduction of oxygen and Fenton reaction, and electrocoagulation uses electric current to dissolve sacrificial anodes (usually iron or aluminum) to create coagulants that adsorb and remove pollutants. Chemical methods degraded pollutants using oxidizing agents like hydrogen peroxide, potassium permanganate, or sodium hypochlorite, while sonochemical degradation used high-frequency ultrasound to create cavitation bubbles and extreme local conditions that generated ROS.

Researchers commonly used two approaches to develop efficient photocatalysts responsive to visible light and solar energy. It is important to note that one highly effective method for enhancing the efficiency of photocatalysts such as g-C_3N_4 is through the chemical modification of these materials. This modification leads to a significant improvement in the separation of charge carriers within the band gap, according to Mohammed's (2020) research. Alternately, hybrid or heterogeneous molecules that contain components that are responsive to visible light were incorporated [Mohammed (2023); Chin *et al*., (2016); Wang *et al*., (2018); Chin *et al*., (2016)]. An area of research that is expanding tremendously is hybrid and

heterogeneous photocatalysis based on solid semiconductors. [Mohammed Ismael, Ying Wu (2019); Mohammed (2022)]. Getting catalysts down to the nanoscale level improves their optical properties. Smaller particles are better at binding excitation and giving off light. Therefore, altering electron-hole pairing in excited states depends on semiconductor size. Broad bandgap photocatalysts must become cost-effective, considering only 5% of solar energy is in the UV light spectrum. SnO_2's low photocatalytic efficiency can be addressed by integrating it with a semiconductor with a broad and small range of band gap energy [Mohammed *et al*., (2022)]. Heterojunction semiconductors enhance visible light photocatalysts by segregating electrons and holes. The use of g-C_3N_4 in solar light collectors and energy converters is effective due to its suitable bandgap and unique properties [Zhou *et al*., (2013)]. Doping the photocatalytic system with g-C_3N_4 can improve its performance, reducing the band gap's energy and increasing charge collection and transfer [Mohammed Ismael, Ying Wu (2019); Che *et al*., (2023)]. Graphitic carbon nitride, or g-C_3N_4, is a polymeric semiconductor material considered metal-free and active when exposed to visible light. This property makes it a potential catalyst for converting solar energy. The practicality of choosing it is due to its capacity to absorb visible light, scalability, and stability [Zhang *et al*., (2012); Zhou *et al*., (2013); Pan *et al*., (2012); Wang *et al*., (2012)]. Modifying or doping g-C_3N_4 is straightforward due to its organic nature, allowing tuning of its electronic bandgap structure. Iron oxide compounds, known for their magnetic properties, can be part of a three-component photocatalyst easily recoverable with an external magnet. Fe_3O_4 is an iron oxide compound that stands out because of its strong photocatalytic and magnetic properties. It is used in many different areas [Li *et al*., (2011); Yang *et al*., (2009); Jing *et al*., (2011); Xu *et al*., (2012); Chen *et al*., (2008); Xie *et al*., (2008); Ren *et al*., (2011)]. In order to improve photocatalytic activity, scientists have looked into using different compounds and materials, such as TiO_2, ZnO, WO_4, and others. Approximately 5% of solar energy is in the UV light spectrum, making wide band gap photocatalysts less cost-effective. Combining SnO_2 with a semiconductor with a narrow bandgap and broadband energy range can address its photocatalytic limitations. This method claims that heterojunction semiconductors can create an electric field inside them. This effectively separates electrons and holes, allowing the photocatalyst to work better in visible light.

The synthesis of Fe_3O_4 using plant extracts as reducing, oxidising, and capping agents is outlined, and various analytical techniques are proposed to study the obtained products. The Tauc plot approach will be used to determine the band gap energy using fluorescence and absorbance spectrum measurements.

We likely chose to investigate the photocatalysis of dyes and pesticides using various SnO_2 materials under LED light irradiation for several reasons such as this are known to exhibit enhanced photocatalytic properties due to synergistic effects and can lead to improved efficiency in degrading organic pollutants. LED light irradiation is preferred for photocatalytic applications due to its energy efficiency and targeted wavelength emission, which can optimize the photocatalytic process while minimizing energy consumption and environmental impact. Fe_3O_4-based composites are chosen for their magnetic properties, which can facilitate separation of the catalyst from the treated water after photocatalysis. Additionally, the stability and recyclability of these materials are crucial for practical applications. Investigating various composite materials (such as those doped or co-doped with different elements) fills a research gap in understanding how specific modifications affect photocatalytic performance. This can lead to innovations in developing more efficient and versatile photocatalysts for water treatment applications.

1.2 Metal oxides

The physical and chemical properties of nano-sized materials are better than those of atomic or bulk materials because of the effects at the mesoscopic level, the quantum level, the surface, and on tiny objects. These characteristics include exceptionally high magnetic susceptibility, Curie temperature, and coercivity [Kim *et al.*, (2003); Raj *et al.*, (2002); Beydoun *et al.*, (2000); McMichael *et al.*, (1992)]. These features are not only present in Fe_3O_4 MNPs but are also biocompatible and non-toxic. This means they can be used in many biomedical ways, including dynamic sealing [Shen *et al.*, (1992)], biosensors, contrast agents in magnetic resonance imaging, localizers in therapeutic hyperthermia, and magnetic targeted drug delivery systems [Jordan *et al.*, (1999); Cao *et al.*, (2004); Li *et al.*, (2005)]. In order to be effective in tissue fluid, Fe_3O_4 MNPs require a material that exhibits a narrow size distribution,

exceptional dispersion, and a robust magnetic response. However, they aggregate in fluids due to magnetic interactions and high surface energies. Researchers have used various synthetic polymers, such as polyamides, chitosan (CS), poly (acrylic acid), polyglycidyl methacrylate, and poly (ethylene glycol), as coating agents to alter the surfaces of iron oxide particles [Tao *et al.*, (2008)]. Despite polymeric coatings' ability to decrease aggregation, the larger particles they produce have fewer magnetic characteristics, are less evenly distributed throughout tissues, are less cleared of metabolic waste, and are less able to penetrate interstitial spaces. Because of this, it is essential to find good ways to change the surface of Fe_3O_4 MNPs to have a controlled size distribution and spread well in both water and non-water solutions.

1.2.1 Fe_3O_4

Iron (II, III) oxide, or Fe_3O_4, commonly known as magnetite, possesses unique properties as a dark powder, often mislabelled as ferromagnetic. It has both permanent magnetism and ferrimagnetic properties. Fe_3O_4 finds widespread application as a pigment, particularly in the production of photocatalyst, owing to its adjustable particle size and form, making it more suitable for synthesis than extraction from natural deposits. The Haber process, water-gas shift reaction, and magnetic resonance imaging (MRI) are among the processes utilising Fe_3O_4.

1.2.2 SnO_2

Tin (IV) oxide, or SnO_2, is an inorganic compound known as stannic oxide, with cassiterite being its mineral form. It is colourless, diamagnetic, and amphoteric, crystallising in its rutile structure. SnO_2 is employed in gas detection, such as in carbon monoxide detectors, and research explores doping with various chemicals for applications like high-voltage varistors etc.

1.3 g-C_3N_4

Graphitic carbon nitride (g-C_3N_4), a formula similar to C_3N_4, is helpful for many reactions because it can speed up reactions and act like a semiconductor. Despite limitations such as low electrical conductivity and a small specific surface area, adding carbon nanomaterials, such as carbon nanotubes, showed promise in addressing these

deficiencies and enhancing the material's performance. Water electrolyzers and proton exchange membrane fuel cells are examples of applications.

1.4 Transition element

Transition metals are chemical elements found in the periodic table's d-block; this element category is also referred to as a transition element. It is a chemical element between groups 3 and 12, except group 3 on occasion. Because they are metals, they have high electrical and thermal conductivity and a luxurious and reflective character. In the majority of the groups, except groups 11 and 12, both the melting and boiling points are high, in addition to extremely high levels of hardness. They can assume multiple oxidation states because they are able to create coordination complexes by affixing themselves to a wide range of different ligands and by taking on the colour of a wide variety of pigments. Compounds or elements that contain them, a wide variety of substances, including coordination complexes and oxides, are widely used as catalysts, and they also contribute to the production of alloys that yield favourable properties. Unpaired d electrons cause a significant number of compounds, including the majority of them, to exhibit potent paramagnetic activity. Transition metals, such as nickel, iron, and cobalt, and inner transition metals, like gadolinium, only contain ferromagnetic elements at temperatures close to room temperature. The (n-1)d orbitals of transition metals play a significant role in shaping their features. These qualities include magnetic properties, the ability to form colourful compounds, and variety in oxidation states.

In contrast to the valence s and p orbitals (ns and np, respectively), which undergo only slight alterations across a transition series, these orbitals contribute only a small amount to the characteristics in question. Transition metals keep their valence shells' electrical configuration within a transition series. This means that the times when the d orbitals change element properties are more evenly spaced across the plane. The partially filled d shell is responsible for the similarities that exist among transition elements, even though there are distinctions that are specific to each group. When d-electrons are present, this property causes a lot of paramagnetic compounds to form. These compounds then give rise to substances with colours that come from d-d

electrical transitions that happen during compound synthesis in many different oxidation states. The slight energy difference between these states enables these transitions. Because the majority of transition metals can bind to a wide variety of ligands, it is also possible to create a wide variety of complexes involving transition metals.

1.5 Literature Reviews

Dye and other organic pollutants present a significant threat to human health and well-being, and their existence in the environment poses a significant risk to human health. Insecticides and dyes used in the textile industry for plant preservation contaminate water, contributing to environmental destruction and endangering the lives of living beings. The presence of these pollutants, found in concentrations ranging from micrograms to nanograms per litre, is a cause for concern due to their potential accumulation. The degradation and eradication of these contaminants at such levels constitute a significant challenge that needs to be addressed. It is becoming more recognised that solar energy can facilitate pollution degradation over a prolonged period, which has led to its emergence as a significant factor in supporting the breakdown of pollutants. In the realm of semiconductor materials that possess photocatalytic characteristics, SnO_2 has attracted a considerable amount of research. According to Xinping *et al.,* (2008), the fact that it is non-toxic, can oxidise substances effectively, is stable, and is resistant to corrosion when exposed to light or chemicals makes it a desirable material.

On the other hand, the broadband gap of SnO_2 restricts its application to UV light, accounting for only five per cent of the available sunlight. Researchers investigated a nanocomposite heterojunction containing TiO_2 or SnO_2 to overcome this constraint. Kamat *et al.,* (2014) described in detail how the movement of charge carriers between compounds leads to the separation of electrons and holes when they come into contact with each other, using light as a catalyst. It is because of the relative band locations that this separation takes place, which ultimately leads to electron transfer to the conduction band of SnO_2. However, difficulties continue to exist, particularly when TiO_2 completely envelops SnO_2, making it more difficult for

photoexcited electrons to combine with molecules of other reactants. Researchers have attempted to improve photocatalysis efficiency by developing catalysts capable of absorbing visible light. In order to change band gaps or make electron-hole separation bigger, one of the most important methods is to change UV-active photocatalysts like TiO_2. Tang *et al.*, (2014) explored hybrid molecules, which contain chemicals activated by visible light, as an additional strategy. The size of materials, mainly when they are in the form of nanoparticles, has a substantial impact on their optical properties. Examples of these features include bandgap, excitation, and emission characteristics. Iron oxide compounds, especially Fe_3O_4, had vigorous photocatalytic activity and magnetic properties, which made it possible to use a big magnet to recover the material. A wide range of uses for Fe_3O_4 include the delivery of drugs, the storage of lithium, the treatment of wastewater, magnetic resonance imaging, and the separation of proteins. Increasing the photocatalytic activity of various compounds, such as TiO_2, ZnO, WO_4, SnO_2 and others, has been the focus of a significant research and development effort. Incorporating plant extracts into the synthesis of nanomaterials as reducing or capping agents has garnered attention because it is both cost-effective and environmentally friendly. Under the influence of visible light, Fe_3O_4, SnO_2, and Fe_3O_4/SnO_2 have demonstrated their ability to degrade dyes, each through their unique process. The heterojunction of $Fe_3O_4/SnO_2/g\text{-}C_3N_4$, which can be retrieved with an external magnet, offers a practical solution for separation and recycling challenges. It is essential to coat Fe_3O_4 with either organic or inorganic compounds in order to achieve stability, dispersion, and prevent aggregation. Scientists have made ternary nanocomposites, like $Fe_3O_4/SnO_2/g\text{-}C_3N_4$, which improve the material's ability to absorb all kinds of light, from ultraviolet to visible. This also makes the material better at reacting with light. Due to its magnetic properties, Fe_3O_4 makes it easy to get the nanocomposite photocatalyst back using an outside magnet. This has the potential to further improve cost-effectiveness by reusing catalysts.

1.5.1 Structure of SnO_2

Tin (IV) oxide, which is transparent and colourless, symbolizes that in the 4+ oxidation state, several compounds of tin are present [Batzill and Diebold, (2005); He

and Zhou, (2013)]. Other names for tin (IV) oxide include stannic oxide, cassiterite, and stannous oxide. This inorganic substance exhibits a remarkable degree of transparency to light, and it can effectively reflect light in the infrared range. Furthermore, it possesses remarkable thermal and chemical stability, as demonstrated by Bouras *et al.*, (2014) researchers. Researchers have explored the potential applications of SnO_2 in various fields, including sensors, catalysts, optoelectronic devices, infrared mirrors, and transparent films [Anandan and Rajendran, (2015)]. These features have sparked an investigation into these applications due to their powerful oxidizing capabilities; oxide is a handy tool for cleaning water and surfaces contaminated with pollutants.

According to Yu *et al.,* (2015), SnO_2 shares a crystal structure with rutile phase. It is an octahedral polar crystal with dimensions of a = b = 0.398 nm and c = 0.402 nm, which are characterized by these dimensions. According to Entradas *et al.,* (2014), the (6, 3) coordination structure is created by three tin (IV) ions encased in an oxygen-containing environment, bordering each oxygen ion in a single unit cell. The presence of nine oxygen ions characterizes this structure. It was found that SnO_2 could react with light, and SnO_2 became a possible alternative because it is susceptible to light, does not change with temperature, is cheap, and is not toxic [Rakibuddin and Ananthakrishnan, (2016)]. According to Abe *et al.,* (2006), the octahedral network influences the mobility of the e^-h^+ pair, which is crucial for increased photocatalytic activity. It is common for semiconductors to display a lower energy band that is abundant in electrons (the conduction band, or CB) and an upper energy band that is devoid of electrons (the valence band, or VB). Two critical parameters, the band gap and the Fermi level, control the semiconductor characteristics of any material. The energy disparity between the conduction and valence bands is called the band gap, while the Fermi level depicts electrons' putative energy level. According to Kim *et al.,* (2012), semiconductors' metallic oxide lattice structure contains impurities that have a significant impact on their electrical properties. In n-type and p-type semiconductors, respectively, doping causes a change in the Fermi level, which, in turn, has an effect on the bandgap spacing.

When exposed to visual electromagnetic radiation [Mete *et al.,* (2009); Sun *et*

al., (2016)], catalysts generate excited electrons with lower energy requirements, exhibiting photocatalytic activity and the catalysts demonstrate such activity when exposed to light. The inherent characteristics of SnO_2 increase its electrical conductivity [Zhang *et al.*, (2014)], thereby reducing the band gap width and improving its semiconductor characteristics. There is a significant energy gap in SnO_2 (3.6 eV), the same as photoactivation in the UV range. This makes it a promising photocatalyst for breaking down organic pollutants [Ahmed *et al.*, (2011)]. SnO_2 plays a significant role in breaking down organic pollutants. ZnO and SiO_2 are other suitable photocatalysts for this purpose. Modification of metal oxides can decrease their band gap energies, enabling activation by electromagnetic radiation with lower energies. This is because, within the visible region of the electromagnetic spectrum, it has meagre electrical resistance, excellent electrical conductivity, and significant optical transparency. These characteristics are responsible for the characteristics above. SnO_2 is a material that has proven to be useful in a variety of applications [Mistry *et al.*, (2016)]. Metal oxides, such as tin oxide (SnO_2), can be used as sensing materials and catalysts for the degradation of organic contaminants due to their significant affinity for carbon monoxide and hydrogen. According to Azam *et al.*, (2010), SnO_2 photo-anodes offer several benefits in dye-synthesized solar cells and other semiconductor materials. These benefits include enhanced charge separation size distributions, faster charge transport, and strong recombination resistances.

1.5.2 SnO_2 that has not been doped is utilized in the process of photocatalytic destruction of organic contaminants

While most applications commonly use doped SnO_2 for the photodegradation of organic contaminants, undoped material has proven to be an efficient photocatalyst in certain instances. Because pure SnO_2 has a naturally large band gap, visible light is unable to generate enough energy to initiate the synthesis of e^- and h^+ pairs. Despite its effectiveness, the procedure requires UV radiation to activate the metal oxide. The results of recent research have brought to light a number of instances in which undoped SnO_2 nanoparticles have remarkable photodegradation capabilities. For example, researchers used SnO_2 nanocrystals generated from tin salts chelated with amino acids to degrade rhodamine B. The study showed that after 150 min of radiation exposure,

they nearly eliminated the amount of rhodamine B. Additionally, exposing nanocrystalline SnO_2 particles, derived from tin oxalate and filtered through an eggshell membrane, to UV light for an hour significantly reduced the presence of rhodamine B by 95%. Haritha *et al*., (2016) and Diallo *et al*., (2016) found that undoped SnO_2 nanoparticles can also undergo oxidative degradation for various dyes. These dyes include methylene blue, eosin Y, congo red, and violet 4 dyes.

1.5.3 Improving SnO_2 photodegradation efficiency

Even though SnO_2 semiconductors have the potential to act as photocatalysts, their rapid recombination rate and high activation energy of photogenerated electron holes (h^+ in VB) and electrons (e^- in CB), which are both significant factors, make it difficult to use them in practical applications [Yang *et al*., (2010)]. Utilising the reduction in recombination of e^-h^+ couples can enhance photocatalytic activity and facilitate industrial applications. When more semiconductors are included in the metal oxide, one of the options available is to change the electron gap energy of the metal oxide. The doped material should have better photocatalytic activity because it has less activation energy and a faster e^-h^+ pair recombination rate [Tojo *et al*., (2008); Kovács *et al*., (2015)]. As a result of these two factors, the material should be able to demonstrate improved photocatalytic activity. Cristante *et al*., (2007) reported that the production method significantly influences the photocatalytic capabilities of the active ingredient-doped material. Changing external factors can significantly alter the overall success of the photocatalytic process [Cheng *et al*., (2010); Anju *et al*., (2012)], necessitating precise calibration of the photon source's light intensity or wavelength, as well as the reaction mixture's temperature, to achieve the desired results. In the following section, we will look at various ways to improve the metal oxide's characteristics in order to guarantee increased catalytic activity.

1.5.4 A method for selectively doping SnO_2 to enhance photodegradation efficiency

1.5.4.1 Combinations of SnO_2 and other semiconductors

According to Srinivasan and Bandyopadhyaya, (2016), doping SnO_2 with semiconductors having either a short or large band gap greatly enhances the metal

oxide's photocatalytic activity. Xiong and Balkus, (2007) have frequently utilized SnO_2 in combination with TiO_2 semiconductors. With the help of doped SnO_2, Vinodgopal and Kamat were able to photodegrade Acid Orange 7. Vinodgopal and Kamat, (1995) determined that the optimal SnO_2/TiO_2 ratio for the degradation process is 2:1. A study by Hou *et al*., (2007) found that SnO_2/TiO_2 nanotubes with different amounts of SnO_2 increased the metal oxide's catalytic activity by making more surface area available for methylene blue absorption. Using this nanotube suspension containing 5% SnO_2 produced the highest photocatalytic activity. Tu *et al*., (2009) found similar results for the contaminant methylene blue. Also, a comparable SnO_2/TiO_2 composite material efficiently decomposed rhodamine B [Abdel-Messih *et al.*, (2013)].

1.5.4.2 SnO_2 doped with transition metals

According to research by Kim *et al*., in 2005, adding metal ions to semiconductors is a good way to increase the photocatalytic activity of visible light so that organic molecules can be broken down by oxidation. Researchers have extensively studied the electrical properties of SnO_2 and investigated several transition metals, such as gold, silver, cobalt, iron, and manganese, for their potential to influence these properties. Utilising these metals can yield the following results like Self-doped SnO_{2-x} nanocrystals doped with Sn^{2+} work as strong photocatalysts that can break down organic pollutants when they are exposed to light. Using self-doped SnO_{2-x} and exposed to visible light, degraded methyl orange [Xu *et al*., (2011)]. Exchanging Sn^{2+} ions for Sn^{4+} ions in the rutile structure forms oxygen vacancies, lowering the band gap energies and facilitating photocatalyst activation when exposed to visible light [Fan *et al*., (2013)]. Guang and colleagues found that the firing temperature significantly influences the photocatalytic activity of SnO_2 nanocrystals doped with different amounts of Ag. As the temperature increased, the photocatalytic properties of the nanocrystals decreased, according to the researchers.

Modest amounts of transition metal ions, such as cerium (Ce^{3+}) or manganese (Mn^{2+}), increase the number of oxygen vacancies in semiconductors [Anandan and Rajendran, (2015)]. As a result, the semiconductors' electrical characteristics and

luminescence activity are enhanced [Gu *et al*., (2004)]. Adding gold to SnO_2 significantly enhances its photocatalytic activity i.e., Mulvaney and his colleagues showed that gold-coated SnO_2 particles function as efficient catalysts. This is because the dopant has the ability to attract electrons, resulting in a more efficient charge distribution. When Wu *et al*., (2013) and You *et al*., (2013) used gold-doped SnO_2 to break down organic dyes, it had more surface area, better visible light absorption, and more photocatalytic activity. There are changes in particle size and surface area when metalloids or transition metals are added to SnO_2 nanocomposites. This leads to lower band gap energies in the nanoscale region. In this case, nanoparticles of SnO_2 doped with cobalt showed higher photocatalytic activity, while also showing a significant decrease in grain size. Entradas *et al*., (2014) elucidated the ability of cobalt-doped SnO_2 nanocomposites to degrade 4-hydroxybenzoic acid upon exposure to ultraviolet light. According to Huang *et al*., (2012), using Zn-doped SnO_2 nanorods to break down acid fuchsin worked better than using pure nanoparticles.

1.5.4.3 Rare earth metals that have been doped into SnO_2

Semiconductors made of TiO_2 or SnO_2 with rare earth elements added greatly improved their photocatalytic capabilities. The metal oxide that has been doped demonstrates catalytic activity across the whole electromagnetic range, including the visible range [Reszczyńska *et al*., (2015)]. One possible explanation for the higher catalytic capabilities is that the BET technique revealed that doped SnO_2 displayed an increase in surface area while simultaneously exhibiting a decrease in particle size. Furthermore, preventing the recombination of electron-hole pairs leads to an improvement in charge separation and a rise in the formation of reactive species on the surface of the photocatalyst [Reszczyńska *et al*., (2015)]. The creation of matrix defects decreases the effective energy of the optical band gap due to doping and increases the semiconductor's photocatalytic capabilities, which in turn enhances the effects indicated above [Hays *et al*., (2005)]. Their photocatalytic activity in decomposing organic pollutants is just one of their many uses; semiconductors doped with rare earth elements have found other practical uses.

Piguet *et al*., (1993) noted that rare earth metals' strong luminous qualities have led to their application in laser generation as well as in fluorescent displays and lamps. The acid/base characteristics of semiconductors are also strongly correlated with their catalytic properties [Carreño *et al*., (2004)]. The acidic oxide SnO_2 has an isoelectronic point (iep) that ranges from 4 to 7, Y_2O_3 has an iep of about 11 while La_2O_3's iep is in the 10–12 range. When ethanol gas was detected using SnO_2 doped with La_2O_3, the significance of the dopant's acid/base characteristics became clear. The change from RO_x to R_2O_{x+1} (for example, from CeO_2 to Ce_2O_3) can occur under both reducing and oxidising circumstances because of the redox pair (Ce^{3+}/Ce^{4+}), which is why cerium doping has garnered so much interest. Furthermore, the formation of oxygen vacancies, which are highly mobile and easily formed, enhances the photocatalytic capabilities [Li *et al*., (2005)].

Moreover, according to Liu *et al*., (2008), $e^- h^+$ couples can be formed when incompletely occupied 4f orbitals are combined with vacant 5d orbitals. Singh *et al*., (2014) characterized the enhanced photocatalytic degradation of several dyes in SnO_2 doped with samarium by a smaller band gap and a larger surface area of the nanoparticles. Degradation experiments on organic contaminants were conducted using $Ti/Sb/SnO_2$ electrodes with a variety of rare earth metals doped into them. The addition of gadolinium and europium as dopants for SnO_2 led to an increase in the activity of the photocatalyst, which was another benefit of this method. The study was strange because it found that cerium had a small but noticeable effect on the activity of the catalyst [Cui *et al*., 2012]. Al-Hamdi and colleagues showed that lanthanum-doped SnO_2 broke down phenol very well when it was exposed to light. Two hours of UV-light irradiation were enough to oxidatively remove nearly 95% of the phenol in the water sample. Compared to an unadulterated SnO_2 sample, the doped material demonstrated much higher efficiency [Al-Hamdi *et al*., (2014)]. Al-Hamdi *et al*., (2015) observed similar outcomes with gadolinium-doped SnO_2. Lanthanum-doped SnO_2 also exhibited greater photocatalytic phenol degradation. Sunlight exposure almost completely removed the contaminant from the sample in less than two and a half hours [Al-Hamdi *et al*., (2016)].

1.5.4.4 Conditions influencing the photodegradation of organic contaminants in aqueous SnO_2 solutions

In order to determine the total efficiency of the process, it is essential to have a solid understanding of the quantity of catalysts necessary for a large-scale application. As a result, numerous organizations have discussed their thoughts on the ideal SnO_2-based photocatalyst concentration for organic pollutant breakdown. As the catalyst concentration increases, the photocatalytic degradation rate rises, but once the catalyst reaches its optimal loading, it begins to fall [Ibhadon and Fitzpatrick, (2013)]. Since the catalyst's active surface area in suspension increases, the first rise in photocatalytic activity makes perfect sense. Wei *et al.*, (2009) found that turbidity and light transmission in the suspension decrease when catalyst concentration increases. According to Paradeshi and Patil, (2008), the catalyst particles exhibit limited photocatalytic activity at the surface, whose value falls as the amount of catalyst loading increases. Optimizing the reaction conditions with a 65 mg doped SnO_2 catalyst in a 50 mL solution confirmed this overall pattern in the photocatalytic degradation of phenol. As previously mentioned, increased catalyst loading led to decreased catalytic oxidation activity. We have noted a similar association for additional photocatalytically active nanoparticles. The optimal activity of TiO_2 declines as the catalyst loading increased and then leading to significantly decreased light penetration. Kashif and Ouyang, (2009) reported a steady decline in the phenol degradation rate once the catalyst concentration exceeded the optimal level.

1.6 Contaminant concentration

According to Khataee and Zarei, (2011), the photodegradation efficiency typically declines as the concentration of contaminants increases. Due to their light absorption, organic dyes reduce the amount of radiation that can activate the catalyst nanoparticles. Several factors contribute to this, such as a reduction in the reaction rate, which slows down the disintegration of pollutant molecules until the catalyst surface's active sites return. The reaction pace slows until active sites are again available on the catalyst's surface, and fewer pollutants are broken down. In our investigations, we examined a variety of initial concentrations for the photocatalytic degradation of

phenol, from 5 to 50 ppm. According to the results, phenol degraded quickly at 10 ppm. Al-Hamdi *et al.,* (2016) found that once the beginning concentration was greater than 15 ppm, the deterioration rate went through a gradual slowing period.

1.7 pH effect

The pH of the polluted solution affects the efficiency of the photocatalytic degradation of aromatic dyes. A critical factor in determining the oxidation potential is pH, which must be carefully considered. Because many organic pollutants have acidic functional groups, it regulates the pollutant's charge and the photocatalyst's surface charge. Performing the reaction within the photocatalyst's allowable stability range is paramount. According to numerous studies, organic contaminants degrade more quickly in environments with lower pH ranges. Researchers in this field have often noted that slightly acidic conditions enhance the breakdown of phenol [Anju *et al.,* (2012)]. The pollutant is more attracted to the photocatalyst surface, and breakdown rates are guaranteed to be boosted at a slightly acidic pH range [Ahmed *et al.,* (2011)]. However, the reaction rate decelerates dramatically when the reaction mixture's pH falls below a certain threshold. Maintaining a constant pH in the reaction mixture, slightly higher than the organic acid's pKa value but lower than the nanocomposite's surface charge (pHzpc), can speed up the photodegradation rate of chlorophenoxyacetic acid. According to Abdullah *et al.,* (2013), this method guarantees that the deprotonated acid interacts with the photocatalyst favourably, leading to faster reactions. Each organic dye has a different pKa value, and the point of zero charge differs for each photocatalyst. Because pH is essential, the reaction must be carefully controlled, and the settings must be optimised [Trellu *et al.,* (2016)].

1.8 Surface effect

According to Sarkar *et al.,* (2016), the catalyst's crystallinity is a key factor in the overall efficiency. Because they can absorb more reactants, heterogeneous catalysts with large surface areas usually work better. Doping with SnO_2 changes and disrupts the metal oxide's crystal structure, reducing crystal size and increasing active surface area. So, SnO_2 doping serves a twofold purpose: it changes the semiconductor's electrical characteristics by reducing the band gap, and it increases the catalyst-

pollutant contact area all at once [Alanko *et al.*, (2012)]. This effect was visible in our group's experiments using SnO_2 samples doped with various metals at different concentrations. The photocatalyst's surface area rose, enhancing catalytic activity in every case. There was a consistent rise up to a different threshold for every pollutant (based on things like ion size and charge).

1.9 Objectives of study

We utilise the co-precipitation and hydrothermal method to fabricate a hybrid heterojunction nanocomposite. The optimal components for this nanocomposite would consist of g-C_3N_4, melamine, and tin oxide (SnO_2). This procedure will be carefully considered and our primary focus will be on nanoparticle development and research. The production of these nanoparticles will include utilising plant extracts derived from several plants, such as the stink bean (*Parkia speciosa*), jackfruit (*Atocarpus heterophyllus*), and lemon (*Citrus x lemon*). Sreeja *et al.* (2021) have reported that carbohydrates are the primary chemical constituents of both the stink bean (*Parkia speciosa*) and the jackfruit (*Atocarpus heterophyllus* L). Moreover, these substances encompass a wide array of constituents, including vitamin C, phenolic compounds, flavonoids, riboflavin, thiamine, beta-carotene, fatty acids, iron, and volatile oils, among numerous others. The flavonoids, phenolic content, and other components present in the plant extract facilitate the oxidation and reduction reactions that create nanoparticles. When visible light hits them, the g-C_3N_4 semiconductor with a small bandgap and the SnO_2 semiconductor with a broad bandgap join to make a p-n heterojunction. This could create a lot of electron-hole pairs. Visible light effectively separates the electron-hole pairs generated by photons, leading to a substantially increased level of active photocatalyst.

The composite, synthesised with the aid of Fe_3O_4, demonstrates magnetically active characteristics. Another advantage is that applying an external magnet will improve the retrieval of the nanocomposite photocatalyst. Magnetic separation offers more benefits than centrifuge or filter paper filtration methods. The latter process would not alter the photocatalyst's shape, size, or structure, which could potentially affect the former's photocatalytic activity. Reusing the catalyst could improve the

photocatalyst's efficiency in terms of cost. Using the green synthesis method, the objective is to generate oxides and their heterojunctions, or nanocomposite products. These plants are easily accessible in the north-east area of India and have therapeutic characteristics. Advanced analytical techniques and procedures, such as X-ray diffraction (XRD) and X-ray photoelectron spectroscopy (XPS), were used to examine the oxides and their heterojunction nanocomposites. These procedures yield essential data regarding the distinctive properties of the oxides, encompassing their structure, dimensions, and other attributes. A more in-depth look at the catalysts' magnetic properties was done using techniques like scanning electron microscopy (SEM), transmission electron microscopy (TEM), energy dispersive X-ray spectroscopy (EDX), Fourier transform infrared spectroscopy (FT-IR), Ultraviolet-visible and photoluminescence spectroscopy, and Vibrational sample magnetometer (VSM).

CHAPTER 2
METHODOLOGY

2.1 MATERIALS AND APPARATUS

Easily accessible plants in any Mizoram market were utilised to make the plant extract, including stink bean (*Parkia speciosa*), lemon (*Citrus x lemon*), and jackfruit (*Atocarpus heterophyllus* L). The following chemicals were sourced from India: Merck (ferric nitrate, ammonium ferrous sulphate, and tin dichloride pentahydrate), HiMedia (melamine), Alfa aesar (praseodymium chloride, and yttrium acetate). Sd fine, India supplied the sodium hydroxide (NaOH), Sigma Aldrich, India the rhodamine B and methylene blue, and SRL, India, the 2,4-DCP and TCAA and $AgNO_3$ reagents, all of which are of analytical quality.

All of the studies were carried out using ion-free distilled water. In order to eliminate ions from the water, we employed the Millipore distillation system (Direct-Q3). An electronic balance (Mettler Toledo, model:ME104E) was used to measure the weight of each compound. The pH measurement was done using a pH-meter (Microprocessor pH Meter LT-50). A standard pH4.0, 7.0, and 12.0 buffer solution was used to calibrate the pH meter.

2.1.1 X-Ray diffraction (XRD)

The synthesised photocatalysts undergo XRD pattern analysis to determine their crystal structures and phase purity by analysis of XRD patterns. We determined the XRD patterns of the nanocomposite using an XRD machine (XRD-Rigaku, Smartlab, IIT, Dhanbad) to determine the nanocomposite's XRD patterns. Before insertion into the machine, the desiccated nanocomposite is placed either on a glass slide or in a sample container; then, the material is introduced into the machine.

In addition, the software in the machine was used to establish the operational 2θ ranges (0–80º) at 0.05º/minute (2θ) scan rate for the analysis of all nanocomposites synthesis in this study, and all measurements were conducted at room temperature.

2.1.2 UV-visible Spectroscopy

UV-visible spectroscopy is a potent analytical method used extensively in chemistry to examine how matter interacts with ultraviolet (UV) and visible light. This approach is used in many different areas of chemistry and yields valuable information about the electronic structure of molecules.

In chemistry, UV-visible spectroscopy is used in the following important ways: Quantitative examination of chemical substances is frequently performed using UV-visible spectroscopy (Evolution 220, Thermo Scientific). Using existing calibration curves, the concentration of a material in a sample can be ascertained by measuring the absorbance of light at particular wavelengths. Because of this, UV-visible spectroscopy is a crucial technique in industries including biochemistry, pharmaceuticals, and environmental monitoring. Chemical reactions can be observed in real-time using UV-visible spectroscopy.

By tracking variations in absorbance throughout the reaction, researchers can learn more about a reaction's kinetics, locate intermediates, and improve reaction conditions. This will be very helpful for studies on catalysis and organic synthesis. Environmental chemistry uses UV-visible spectroscopy to measure the concentration of various compounds in environmental samples, identify pollutants, and monitor water quality. The basic principle behind this method is the Beer-Lambert Law, which states that the absorbance (A) of a solution is directly proportional to the concentration (c) of the absorbing species and the path length (l) of the sample:

$$A = \varepsilon . C . l$$

Where A is the absorbance, ε is the molar absorptivity (also known as the extinction coefficient) of the absorbing species at a specific wavelength, l is the path length of the sample (typically measured in centimeters), C is the concentration of the absorbing species in solution (usually in molarity, M). The molar absorptivity (ε) is a constant for a given substance at a particular wavelength and is usually determined

experimentally. It depends on the chemical structure of the molecule and the wavelength of light being absorbed.

2.1.3 FT-IR Spectrophotometer

Fourier transform infrared spectroscopy (FT-IR) technique with the ATR method can be used to determine the vibrational spectra of a material. We can readily study the FT-IR spectra to determine whether the sample contains water molecules adsorbed throughout the manufacturing process. A conventional approach involves utilising a small amount of the powdered material to analyse FT-IR spectra, typically within the wavelength range of 400 to 4000 cm^{-1}. In order to record the FT-IR spectra of all of the manufactured nanocomposites, a FT-IR spectrometer manufactured by Shimadzu (Iraffinity-1s) utilised the ATR technique.

2.1.4 Scanning Electron Microscope (SEM) and (EDAX)

The synthesised photocatalysts were examined using scanning electron microscopy (SEM) and energy-dispersive X-ray spectroscopy (EDAX) with a FE-SEM-Zeiss Supra 55 instrument to ascertain their morphology and elemental composition. We applied the nanocomposite to carbon-coated tape and used a blower to expel it forcefully in order to streamline the process of obtaining measurements. After being inserted into the sample chamber of the scanning electron microscopy (SEM) machine, a high voltage is used to scan the tape. We recorded the image obtained from the scanning electron microscope (SEM). Further, we scanned a specific area of the scanning electron microscope (SEM) image to measure the EDAX bands. Subsequently, we presented the components inside that particular area as a visual representation resembling a spectrum and documented it for future reference.

2.1.5 Transmission Electron Microscope (TEM)

The size, shape, and crystallinity of the sample can be assessed by evaluating the TEM pictures, HRTEM patterns, and SAED patterns produced from the transmission electron microscopy (JEM-100CX II instrument) at IIT Dhanbad. Operating voltage of TEM analysis was at the range of 200-300 KeV. In order to capture the offered images, it was essential to dissolve the powder sample into a solvent and distribute it.

For example, methanol has undergone ultrasonic agitation for thirty minutes. After dispersing the particles, we extracted a small quantity and placed it on the surface of a carbon-covered copper grid. Subsequently, we allow the item to be desiccated in the immediate vicinity before inserting it into the apparatus to capture the required photographs.

2.1.6 X-ray photoelectron spectroscopy

X-ray photoelectron spectroscopy (XPS) is crucial in offering comprehensive insights into materials' composition, chemical state, and electronic structure. Further, X-ray photoelectron spectroscopy (XPS) is crucial in chemistry because it can analyse the surface of materials, making it highly valuable. It provides information on the elemental composition and chemical states of atoms within the sample's uppermost nanometers. Understanding surface reactions, catalysis, and the behaviour of thin coatings is crucial. It can differentiate between various chemical states of components in a sample. Precise information is essential for determining oxidation states, coordination environments, and chemical bonding, which provide a valuable understanding of the reactivity and stability of materials. It enables the measurement and evaluation of the precise amounts of elements present. We can estimate the concentration of each element on the surface by quantifying the intensity of photoelectron peaks. Precise composition management is crucial in sectors like materials research, as it has significant value. It is efficient in detecting and measuring surface pollutants. This is especially crucial in areas like electronics and manufacturing, where even small levels of contaminants can substantially affect the quality of materials. Catalysis research commonly uses it to examine the active sites and changes in the chemical states of catalysts during reactions. In this present investigation, XPS-PHI (5000 Versa Probe III) at IIT Dhanbad was used to determine the prepared nanocomposite's chemical composition and binding states. This information is essential for enhancing catalytic processes and developing catalysts with higher efficiency. It offers vital insights into the electrical configuration of materials, particularly the energies required to bind electrons.

2.1.7 Photoluminescence Spectrophotometer

We used a photoluminescence spectrophotometer (F-7000, Hitachi) to determine the excitation and emission of the as-prepared nanocomposite. Photoluminescence spectroscopy often determines the wavelengths of excitation and emission of a sample. During this particular spectroscopy, it was necessary to determine an excitation wavelength (the wavelength that exhibited the highest absorption) in order to determine an emission wavelength and vice versa. In most instances, the photoluminescence spectra demonstrate the presence of second-order spectra as well; when the proper filters are not used, it is possible to eliminate them with an appropriate filter.

2.1.8 BET (Brunauer-Emmett-Teller)

The BET (Brunauer-Emmett-Teller) method is a crucial approach in surface chemistry and materials science. Materials primarily use it to determine their specific surface area and porosity. The significance of BET in chemistry is apparent in a variety of applications. Here are several essential elements that emphasize its importance: The fundamental objective of the BET method is to quantify the specific surface area of materials with pores. It is essential to comprehend the magnitude of the material's surface area, which is accessible for interactions, adsorption, and chemical reactions. The specific surface area is essential in catalyst design, adsorption study, and material development with pores. People commonly use it to evaluate the adsorption properties of materials such as zeolites, activated carbons, and metal-organic frameworks. Comprehending the surface area and pore structure assists in forecasting and enhancing the adsorption capacity for gases, liquids, or solutes. BET analysis is useful for determining the size and distribution of pores in materials with a porous structure, such as nanoporous solids and membranes. This knowledge is vital for gas separation, water purification, and drug delivery systems. The Brunauer-Emmett-Teller (BET) method is highly valuable in physisorption investigations, namely for the adsorption of gas molecules onto a solid surface without any accompanying chemical reactions. This is relevant for examining the interaction between gases and materials and predicting gas storage capabilities. Environmental chemistry uses BET to analyze soil and sediment samples. Comprehending the precise surface area of these materials is

essential for evaluating their ability to absorb and trap impurities and pollutants. Industries that manufacture materials with specified surface area requirements, such as catalysts or adsorbents, utilize the BET method for quality control. This method guarantees uniformity in the production process and the intended functionality of the end product. The Brunauer-Emmett-Teller (BET) (NOVA 1000E) at Tezpur University analyzes and describes the surface properties of nanoparticles in this study of ternary nanocomposites.

2.1.9 Total Organic Carbon (TOC)

TOC analysis is an essential chemistry approach for evaluating environmental, pharmaceutical, and water quality assessments. The underlying mechanism of Total Organic Carbon (TOC) analysis entails quantifying the aggregate quantity of carbon contained in organic components within a given sample. Various techniques are employed to ascertain the total organic carbon (TOC) content. However, the fundamental concept revolves around the oxidation of organic carbon into carbon dioxide (CO_2) and subsequently quantifying the resulting CO_2. It is commonly used to assess the quality of water, soils, sediments, and other environmental samples. The CO_2 produced from the oxidation of organic carbon is measured using a detector, typically a non-dispersive infrared (NDIR) detector. The amount of CO_2 is directly proportional to the TOC content in the sample and it is calculated based on the amount of CO_2 detected. This is often done using calibration standards with known concentrations of organic carbon to ensure accuracy and precision. Determining total organic carbon (TOC) yields essential data regarding the amount of organic matter in a given sample. This information is particularly significant in a range of applications, including evaluating the effects of human activities on natural ecosystems in environmental studies. It aids in monitoring organic contaminants, comprehending the biodegradability of organic substances, and assessing the efficacy of remediation.

2.1.10 Vibrating Sample Magnetometry (VSM)

Vibrating Sample Magnetometry (VSM) is a commonly employed experimental method that measures the magnetic properties of different materials. VSM is an important tool in chemistry because it lets scientists study the magnetic properties of different materials, such as ferromagnetic, antiferromagnetic, and paramagnetic

compounds. This resource provides extensive information on magnetic properties, including magnetic moment, coercivity, and susceptibility. Materials science employs the VSM to examine and enhance the magnetic characteristics of materials. When developing magnetic materials used in data storage, sensors, and medicinal applications utilising magnetic nanoparticles, it is essential to evaluate this aspect carefully. The VSM (model 7400 series, at IIT Guwahati) is used to study the magnetic nanoparticles in photocatalysis. By utilising an external magnetic field, magnetic catalysts may be easily separated from reaction mixtures, allowing for their repeated usage and improving the overall efficiency of catalytic processes.

2.1.11 Liquid Chromatography-Mass Spectrometry (LCMS)

LC-MS, or Liquid Chromatography-Mass Spectrometry, is a highly effective analytical method employed for the purpose of separating, identifying, and quantifying the various constituents present in a combination. The working premise of this system integrates two primary methodologies: liquid chromatography and mass spectrometry. In LC-MS, the liquid chromatograph's effluent is directly fed into the mass spectrometer. The individual components that have been separated by the LC column enter the mass spectrometer sequentially.

Mass spectra are obtained in a continuous manner as the components separate, giving information on the identity and amount of the chemicals in the sample. The substances can be identified by comparing the acquired mass spectra with databases or reference spectra. Moreover, the magnitude of the ions in the mass spectra can be utilised to measure the quantity of each component existing in the sample.

The mass spectra acquired from LC-MS analysis are further processed and examined using dedicated software. This software facilitates the identification of chemicals in a sample by analyzing their mass-to-charge ratios and fragmentation patterns. Quantitative analysis can be conducted by comparing the intensities of specific ions to those of internal or external standards.

Citrus x lemon, *Parkia speciosa,* and *Artocarpus heterophyllus* L leaves were gathered from Mizoram. The leaves underwent thorough shade-drying, followed by crushing into small fragments, and were thereafter stored in separate containers for future utilization.

2.2 Methods

2.2.1 Plant extraction

The Soxhlet extraction method is a conventional technique used to extract compounds from plant materials using a solvent. It allows for continuous extraction and can be particularly beneficial for extracting compounds from plants. In order to extract the desired components from the plant, a thorough dehydration process was carried out on the plant components. Subsequently, the dehydrated plant components were meticulously ground to obtain particles of an appropriate size for the extraction procedure. The measured amount of dehydrated plant material was used to determine the effectiveness of the extraction process and achieve the specified chemical concentration. The solvent used depends on the quantity of plant material and the desired concentration of extracted compounds. The Soxhlet extractor was assembled by placing the plant material into the thimble, or cellulose extraction thimble, which was then inserted into the Soxhlet extractor. Next, the Soxhlet extractor was connected to a round-bottom flask placed beneath it and a condenser positioned above it. The round-bottom flask was filled with 200 mL of ethyl acetate. Next, the solvent in the round bottom flask was heated to a temperature of 80ºC or until it reached its boiling point. The temperature was then maintained steadily using a heating mantle with temperature control.

As the solvent evaporates, it rises through the Soxhlet extractor and extracts compounds from the plant material. The concentrated solvent is returned to the round-bottom flask, therefore completing the extraction process. The continuous extraction method optimises the extraction efficiency to its total capacity. The Soxhlet device is operated for 3 days to extract compounds from the plant material thoroughly. After extraction, remove the Soxhlet apparatus from the heat source and let it cool down to the surrounding temperature. Obtain the round-bottom flask containing the extract from the Soxhlet apparatus and transfer the extract to a sterilised round-bottom flask. In order to concentrate the extract, a rotary evaporator was used to evaporate the solvent while applying low pressure and mild heating. This stage involves the removal of the ethyl acetate solvent, which leads to preserving the extracted compounds. To

retain the integrity of the concentrated extract, store it in an appropriate container, such as a vial or amber bottle, at a temperature of -40ºC until it is ready for further analysis or usage.

2.2.2 Preparation of Fe_3O_4 magnetic Nanoparticles by using plant extract

Synthesized Fe_3O_4 magnetic nanoparticles using a slightly modified version of the process described by Soto et al. [Soto-Robles *et al.*, (2019)]. This was accomplished by mixing 7.80 g of ferric nitrate and 4.40 g of ammonium ferrous chloride in a 2:1 solution with 20 mL of deionized water. A 5 M sodium hydroxide solution was rapidly added to the previously described solution, or additional sodium hydroxide solution was added to reach a pH of 9 while violently stirring. 2 mL of plant extract (*Parkia speciosa*) was used as capping or reducing or oxidizing agent to decrease the aggregation of Fe_3O_4. Later on, the mixture was autoclaved under atmospheric pressure for 12 hours at 120°C. We gradually cooled the autoclave to room temperature after sealing it. We removed the precipitate with a magnet and cleaned it several times with a 1:1 mixture of ethanol and water until the pH reached 7.0. After that, they were dried for 12 hours at 60°C in a hot air oven to produce more binary or ternary nanocomposites.

2.2.3 Preparation of SnO_2

The initial steps in synthesising SnO_2 involved mixing $SnCl_2.5H_2O$ with a 4M NaOH solution. In a beaker, 2g of $SnCl_2$ and 20 mL of water were mixed, and then, after that, they were set on a magnetic stirrer set to 60°C. We heated and stirred the $SnCl_2$ beaker while slowly adding NaOH until the pH level reached 8. The precipitate formed immediately after NaOH was added. A 2 mL plant extract (*Parkia speciosa*) was then used as a capping agent to reduce the nanocomposite's excessive adherence. Autoclaving, which entails subjecting the solution to a temperature of 110°C for 10 hours while maintaining high pressure, is followed by vigorous stirring on a magnetic stirrer for another 2-3 hours. After the autoclave cooled to ambient temperature, we spun the solid substance at 5500 rpm and repeatedly washed it with water and ethanol until the pH reached 7.0. The subsequent step was to dry the SnO_2 in a hot air oven at 60°C for 12 hours. After that, they were dried for 12 hours at 60°C in a hot air oven to

produce more binary or ternary nanocomposites which can be utilized in environmental applications such as water purification and air treatment by degrading organic pollutants and harmful gases under UV or LED light irradiation.

2.2.4 Preparation of g-C_3N_4

30 g of melamine were placed in an alumina crucible, which was covered with a lid, and calcined in a muffle furnace at 500ºC for 2 hours. We obtained the g-C_3N_4 powder through a neat crusting process. We might then use it to make a binary or ternary photocatalyst.

2.2.5 Preparation of Fe_3O_4/SnO_2 nanocomposite

The Fe_3O_4 magnetic nanoparticles were dispersed by sonicating 2g of the as-prepared material with 20 mL of deionized water in a beaker for one hour. In order to create a binary nanocomposite of Fe_3O_4 and SnO_2 at a ratio of 1:3, the chemical $SnCl_2.5H_2O$ (6g) was added. The mixture was rapidly agitated after adding a 5 mL portion of a 5M sodium hydroxide solution, or more volumes were added until the pH reached 9. The nanocomposite aggregation was then minimised by using a 2 mL quantity of plant extract (*Parkia speciosa*) as a capping agent. Later on, the mixture was autoclaved under atmospheric pressure for 12 hours at 120°C. We used a magnet to draw out the residue after bringing the autoclave to room temperature and washed it with a 1:1 ethanol/water solution until the pH reached 7.0. 12 hours drying process was performed on the Fe_3O_4/SnO_2 (FS) combination in a hot air oven set at 60°C to create ternary nanocomposites.

2.2.6 Preparation of Fe_3O_4/g-C_3N_4 nanocomposite

2g of Fe_3O_4 magnetic nanoparticles were sonicated in a beaker for an hour in 20 mL of deionized water, to which 6g of g-C_3N_4 was added to get a 1:3 wt/wt Fe_3O_4/g-C_3N_4 (FG) binary nanocomposite. After rapidly spinning, we added 5 M sodium hydroxide to reach pH ~9; then, we added 2 mL of plant extract (*Parkia speciosa*) to reduce nanocomposite agglomeration by acting as a capping agent. Autoclaving the solution at 120°C for 12 hours at atmospheric pressure was done. After the autoclave, we slowly and gently brought the solution down to room temperature. The precipitate

was retrieved using an external magnet and rinsed with a solution of ethanol and water in a 1:1 proportion until the pH level equalled 7.0. In order to increase the production of ternary nanocomposites, after being heated to 60°C for 12 hours, the material was air-dried in an oven with hot air.

2.2.7 Preparation of $Fe_3O_4/SnO_2/g\text{-}C_3N_4$

20 mL of de-ionized water was added to a beaker containing 2g of Fe_3O_4/SnO_2 magnetic nanoparticles, and then the mixture was sonicated for an hour. In order to create this ternary nanocomposite $Fe_3O_4/SnO_2/g\text{-}C_3N_4$, 2g of $g\text{-}C_3N_4$, which is melamine that has been calcinated at 500°C and 2 mL of plant extract (*Parkia speciosa*) was added and stirred for three hours at 70ºC. Afterwards, the solution was autoclaved under atmospheric pressure for 12 hours at 120°C. After gradually cooling the autoclave to room temperature, we extracted the magnetic precipitate. We then repeatedly washed the precipitate with a 1:1 mixture of ethanol and water until its pH reached 7.0. Following a 12 hour drying procedure in a hot air oven set at 60°C, the $Fe_3O_4/SnO_2/g\text{-}C_3N_4$ composite having a 1:1 ratio of Fe_3O_4/SnO_2 and $g\text{-}C_3N_4$ was obtained, named FSG1, was further dehydrated using acetone. In this manner, we have synthesized several nanocomposites, FSG2 and FSG3, consisting of $Fe_3O_4/SnO_2/g\text{-}C_3N_4$, with different amounts of $g\text{-}C_3N_4$ (specifically, 4g and 6g) and a fixed amount of 2g of Fe_3O_4/SnO_2 respectively. The primary objective of this composite was to induce dye degradation.

2.2.8 Preparation of Fe_3O_4/Ag-doped $g\text{-}C_3N_4$

In a beaker filled with 20 mL of deionized water, 2 g of Fe_3O_4 magnetic nanoparticles were sonicated for an hour; following this, 6 g of $g\text{-}C_3N_4$ (calcinated melamine) was combined and sonicated for a further 2 hours. Subsequently, the aforementioned beaker was moved onto a magnetic stirrer, and 0.16g (or 1 wt.% of $g\text{-}C_3N_4$) of silver nitrate was added. We then let it stir at room temperature for an additional hour. Following a quick spin, we added 5M sodium hydroxide to bring the pH down to about 9. Next, we added 2 mL of plant extract (*Atocarpus heterophyllus* L), which served as a capping agent to lessen the agglomeration of the nanocomposite. The autoclave was set at 120°C with air pressure for 12 hours to sterilise the solution.

After autoclaving, the temperature was lowered to room temperature. In order to clean it, we used a 1:1 mixture of ethanol and water until the pH hit 7.0, after which we used an external magnet to remove the precipitate. In order to facilitate the design of ternary nanocomposites, the material was heated to 60°C for 12 hours and then air-dried in an oven using hot air. We have designated the final dried Fe_3O_4/Ag (1 wt.%)-doped g-C_3N_4 as FAG1. In this manner, we have synthesised several Fe_3O_4/Ag-doped g-C_3N_4 nanocomposites, designated FAG2, FAG3, FAG4, and FAG5, with varying weights of silver nitrate (i.e., 3, 5, 7, and 9 wt.%) relative to the weight of g-C_3N_4 respectively.

2.2.9 Preparation of Fe_3O_4/Ag-doped SnO_2

In a beaker, 20 mL of de-ionised water was used to sonicate 4 mg of Fe_3O_4 magnetic nanoparticles for one hour, adding 12 mg of SnO_2. The mixture was then mixed with a magnetic stirrer at 70°C for 2 hours after adding a precisely calculated amount of $AgNO_3$ (12 mg). We heated and stirred the solution again, then added drops of sodium hydroxide until the pH reached 8. We then applied a coating agent consisting of 2 mL of *Parkia speciosa* plant extract to prevent excessive clumping of the nanocomposite. Magnets were used to remove the precipitate after the solution had cooled to room temperature after being autoclaved at 110°C for 10 hours. We used a solution of ethanol and water (1:1) for several washes until the pH reached 7.0. Fe_3O_4/Ag_x: Sn_yO_2 (x:y = 1:1), named FAS1, which has been dried for 10 hours in a 60°C hot air oven, was then further dehydrated with acetone. Then, various Fe_3O_4/Ag_x: Sn_yO_2 nanocomposites were created with a different weight ratio of Ag (36, and 4 mg) relative to the weight of Fe_3O_4/SnO_2 and these nanocomposites were named FAS2, and FAS3, respectively. We stored the precipitates of FAS1, FAS2, and FAS3 with extreme care to conduct thorough research into their characteristics and potential uses.

2.2.10 Preparation of Fe_3O_4/Pr^{3+}: SnO_2 nanocomposite with plant extract (jackfruit leaves).

The standard starting materials used were Fe_3O_4 and $SnCl_2$, together with $PrCl_3$ and 4 M NaOH. A mixture of Fe_3O_4 (2mg), $SnCl_2.5H_2O$ (6mg), i.e., in the ratio of 1:3 (wt./wt.), and 20 ml of water was combined in a beaker. A precisely measured amount of $PrCl_3$ (0.068mg) was incorporated into this blend, and then, at 70°C, the combined

ingredients were mixed for 2 hours using a magnetic stirrer. We heated and stirred the mixtures, adding sodium hydroxide drops until the pH reached 8. Following this, a 2 mL quantity of plant extract (*Artocarpus heterophyllus* L) was utilised as a coating agent to prevent excessive agglomeration of the nanocomposite. Subsequently, the solution underwent autoclaving at 110°C for 10 hours, and after that, the autoclave was lowered to room temperature gradually, and a magnet was used to extract the precipitate. It was washed many times with a mixture of ethanol and water in a 1:1 ratio until the pH reached 7.0. After a 10 hour drying process in a hot air oven at a temperature of 60°C, the Fe_3O_4/(1 at.%)Pr^{3+}:SnO_2, named FPS1, was further dehydrated using acetone. In this manner, we have synthesised several Fe_3O_4/Pr^{3+}-doped SnO_2 nanocomposites, designated FPS2, FPS3, FPS4, and FPS5, with varying atomic percentages of praseodymium (i.e., 3, 5, 7, and 9 at.%) relative to the weight of Fe_3O_4/SnO_2 respectively. We preserved the FPS1, FPS2, FPS3, FPS4, and FPS5 precipitates with great care to conduct meticulous analysis and investigation of their properties and potential uses.

2.2.11 Preparation of Pr^{3+},Y^{3+} co-doped tin dioxide with ferrous ferric oxide (Fe_3O_4/Pr^{3+},Y^{3+}: SnO_2) (FPYS with different at.%)

The Fe_3O_4/Pr^{3+},Y^{3+}:SnO_2 samples were synthesised using the hydrothermal technique, in which $SnCl_2$ (6mg), $Y(NO_3)_3$ (0.112mg), Pr $(CH_3CO_2)_3$ (0.129mg), and prepared Fe_3O_4 (2mg) were dissolved in 20 mL of distilled water in a beaker. The mixture was subjected to magnetic stirring for 3 hours at a temperature of 70°C. Subsequently, the acidity level of the combination was assessed, and to neutralise the acidic solution, 4 M NaOH was gradually added until the pH approached 8. Upon adding and stirring the 2 mL of plant extract (*Parkia speciosa*) extract as a coating agent to prevent excessive agglomeration of the nanocomposite for a further 4 hours, we saw the formation of black-coloured precipitation. Next, the solution was autoclaved at 110°C for 10 hours. After gradually cooling the autoclave to room temperature, we separated the resulting precipitate using an external magnet and washed it several times with a solution containing equal proportions of water and ethanol until the pH level reached 7.0. Following a 10 hour drying period in a hot air oven set at 60°C, the material named FPYS1 (consisting of Fe_3O_4/(1

at.%)Pr^{3+},Y^{3+}:SnO_2 was further dehydrated using acetone. In this manner, we have synthesised several Fe_3O_4/Pr^{3+},Y^{3+}-codoped SnO_2 nanocomposites, designated FPYS2, FPYS3, FPYS4, and FPYS5, with varying atomic percentages of praseodymium and Yttrium ions (i.e., 3, 5, 7, and 9 at.%) relative to the weight of Fe_3O_4/SnO_2 respectively. We preserved the FPYS1, FPYS2, FPYS3, FPYS4, and FPYS5 precipitates with great care to conduct meticulous analysis and investigation of their properties and potential uses.

2.2.12 Characterization

The nanoparticles underwent UV-visible spectrocopy, FT-IR, XRD, FESEM, HRTEM, XPS, PL, EPR, BET, TOC, VSM and other analyses after their hydrothermal production. The measurement of XRD verified the phase purity of the nanocomposite.

2.2.13 Photocatalytic studies

The irradiation solution's absorption intensity was assessed to examine the photocatalytic efficiency of the prepared ternary nanocomposite. For this, rhodamine B (RhB), methylene blue (MB), 2,4-dichlorophenol (2,4-DCP), and trichloroacetic acid (TCAA) were used as model pollutants. We sonicated the nanocomposite in an 8 ppm pollutant solution for 30 min in the dark to complete the adsorption-desorption process. The suspension was then irradiated by an LED light at 15 cm above the solution for 30 min, which was kept on a magnetic stirrer. The nanocomposite's dyes or pesticides degradation efficiency was calculated from the starting and finishing concentrations, and absorption intensity was recorded by a thermoscientific UV-visible spectrophotometer.

2.2.14 pH effect

The pH level can significantly impact the process of photodegradation reactions, particularly in water-based environments. The pH can impact the rate and mechanism of photodegradation processes through various means. Various chemicals can exist in different ionisation states based on the pH of the solution and can exhibit varied levels of vulnerability to photodegradation. For example, acidic or basic conditions can either facilitate or impede the creation of reactive intermediates that drive photodegradation. pH-dependent parameters, such as the presence of reactive species, the stability of

intermediates, and the effectiveness of light absorption, affect the rate of photodegradation reactions. Under some circumstances, particular pH conditions can either accelerate or impede the photodegradation rates and influence the stability of both the substrate and the photoproducts. For example, alterations in pH can result in the creation of either more stable or less stable intermediates, which can impact the overall effectiveness of photodegradation. Further, it influences the formation of reactive species, like free radicals or excited states, often involved in photodegradation processes. Changes in pH can alter the pathways leading to the production of these reactive species, thereby influencing the entire degradation process. This investigation used HCl or NaOH to create various pH solutions or ranges from 5 to 10.

2.2.15 Dosage studies

The dosage effect of a photocatalyst pertains to the impact of the quantity or concentration of the photocatalyst on the efficiency and outcome of a photocatalytic reaction. The photocatalytic process is generally maximised by finding the best concentration or dosage of photocatalyst. When dosages are lower than the ideal level, the reaction may occur slower because only a limited number of active sites are available for catalysis. On the other hand, when using greater dosages, an excessive amount of photocatalyst might cause the particles to clump together or form a protective layer, decreasing the amount of surface area accessible for the reaction. The dose of the photocatalyst can impact the reaction kinetics by influencing aspects such as the pace at which reactants are adsorbed onto the surface of the catalyst, the rate at which charge carriers are generated and migrate, and the rate at which surface reactions occur. The quantity of photocatalysts can affect mass transport phenomena, such as reactants and products moving to and from the catalyst's surface. Elevated concentrations of photocatalysts can result in heightened mass transport restrictions, especially if the catalyst particles coalesce or if the reaction takes place in a restricted area, which influences the light absorption characteristics of the reaction mixture. The presence of photocatalyst particles at elevated concentrations may scatter or absorb light, thereby reducing the penetration distance of light into the solution. Thus, the amount of photocatalyst required for a photocatalytic reaction directly impacts the

procedure's cost. Hence, optimising the dose to attain the desired reaction rate and product yield is crucial while simultaneously minimising the expense associated with catalyst usage. Furthermore, practical factors like the catalyst's availability, stability, and ease of separation may influence the selection of the most suitable dosage.

2.2.16 Magnetic separation

Magnetically active photocatalysts possess magnetic features that enable their effortless separation from reaction mixtures by applying an external magnetic field, facilitating their collection and reuse. The photocatalyst is permitted to facilitate the intended reaction when exposed to light until the reaction is fully completed or the necessary conversion level is attained. This may entail procedures such as the breakdown of pollutants, the production of hydrogen, or the creation of organic compounds. After the photocatalytic reaction is finished, administer an external magnetic field to the mixture of the reactions. Including magnetic nanoparticles in the photocatalyst enables it to be easily and efficiently separated from the solution by responding to a magnetic field. This can be accomplished by using either a magnet or a magnetic separator. This step is crucial for preserving the effectiveness and specificity of the photocatalyst for subsequent reactions. In order to eliminate any remaining solvent and moisture, it is necessary to subject the washed photocatalyst to a vacuum or an optimal temperature for drying. Thorough drying is crucial to avoid the clumping or breakdown of the photocatalyst when it is stored or used again.

CHAPTER 3
RESULTS AND DISCUSSIONS

3.1 Effect of g-C_3N_4 on SnO_2 in Fe_3O_4/SnO_2/g-C_3N_4 ternary nanocomposite for degradation of dyes and pesticides.

Designing photocatalysts that degrade organic contaminants like dyes and pesticides is important for environmental cleanup. The synergistic effects of its elements make ternary nanocomposites promising photocatalytic materials. The ternary nanocomposite Fe_3O_4/SnO_2/g-C_3N_4 contains magnetite, tin oxide, and graphitic carbon nitride. Due to its broad band gap energy of SnO_2, alone is inefficient under visible light. When mixed with other materials, it transports electrons and slows electron-hole pair recombination. g-C_3N_4 is a polymer made of carbon and nitrogen atoms which has unique 2D layered structure makes it thermally and chemically stable. As a photocatalyst and support material in composites, g-C_3N_4 improves photocatalytic component dispersion and stability and it has high electron mobility and stability characterize it. Due to its magnetic characteristics, Fe_3O_4 makes photocatalyst recovery and recycling easier. It makes the composite magnetic, allowing an external magnetic field to separate the photocatalyst from the reaction mixture.

The nanocomposite Fe_3O_4/SnO_2/g-C_3N_4 (FSG2) (with a ratio of Fe_3O_4/SnO_2 and g-C_3N_4=1:2) exhibited excellent photodegradation of RhB dye (Sigma Aldrich) dye in an aqueous solution, as depicted in Fig. 3.1.1.

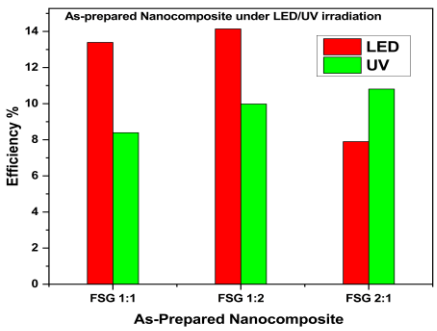

Fig. 3.1.1 Degradation efficiency of as-prepared catalyst by exposing to UV and LED light.

Based on these studies, we discovered that a ternary nanocomposite with 1:2 of Fe_3O_4/SnO_2 and g-C_3N_4 exhibited remarkable efficiency in the degradation of RhB when exposed to LED light. Our focus is on characterizing and exploring the applications of Fe_3O_4/SnO_2/g-C_3N_4 (FSG2), which has 1:2 ratio of Fe_3O_4/SnO_2 and g-C_3N_4.

3.1.1 Powder XRD analysis

XRD is based on the constructive interference of monochromatic X-rays scattered by a crystalline sample. When X-rays interact with a crystal, they are diffracted at specific angles depending on the spacing between the crystal planes. Nanocomposites made of Fe_3O_4, SnO_2, and g-C_3N_4 were compared to single components of Fe_3O_4 and SnO_2 in their diffraction patterns. The diffraction pattern of the cubic inverse spinel Fe_3O_4 was determined to be in agreement with JCPDS No. 82-1533, and the points at which the peaks occurred were 30.077°, 35.426°, 37.057°, 43.054°, and 62.57°, respectively. These angles correspond to the miller indices (220), (311), (222), (400), and (440). The lattice parameters were all equal to 8.395 Å, and the cell volume was 591.717 cubic units. In contrast, the tetragonal rutile crystal phase of SnO_2 (JCPDS No. 41-1445) have a cell volume of 71.163. The *hkl* planes of (110), (101), (111), and (310) corresponded to the diffraction peaks at $2\theta = 26.611°$, 33.893°, 38.969°, 51.781°, and 65.939°, respectively. This nanocomposite displayed three sets of diffraction patterns, each signifying a crystal structure: cubic for Fe_3O_4, tetragonal for SnO_2, and hexagonal for g-C_3N_4. The X-ray diffraction (XRD) pattern confirmed the synthesis of Fe_3O_4/SnO_2/g-C_3N_4 nanocomposites, revealing the absence of impurity peaks corresponding to specific phases. The tetragonal structure of SnO_2 remains unchanged when Fe_3O_4 and g-C_3N_4 are added. By examining the diffraction peaks of Fe_3O_4 (311), SnO_2 (110), and g-C_3N_4 (101), the Debye-Scherrer formula was used to determine the crystallite size of ternary nanocomposites of Fe_3O_4/SnO_2/g-C_3N_4 while the lattice parameters and cell volume of these preaperd catalyst were calculated by using unit cell volume software. We examined the particle and composite structure, as well as the grain size, using powder X-ray diffraction (XRD). Fig. 3.1.2(a)-(e) presented the X-ray diffraction patterns of nanocomposites made of Fe_3O_4, SnO_2, Fe_3O_4/SnO_2, Fe_3O_4/g-C_3N_4, and Fe_3O_4/SnO_2/g-C_3N_4.

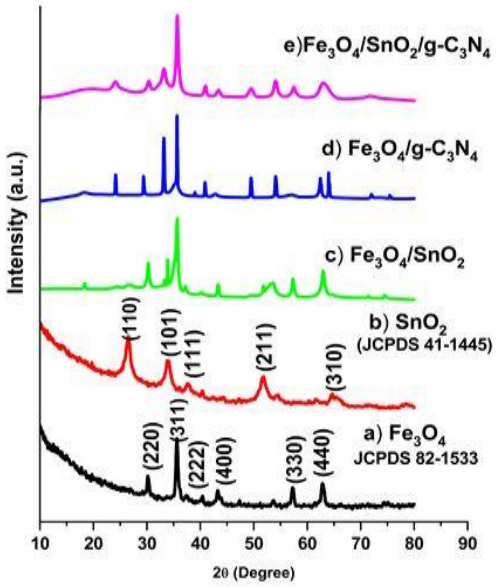

Fig. 3.1.2 Powder XRD pattern of (a) Fe_3O_4 (b) SnO_2 (c) Fe_3O_4/ SnO_2 (d) Fe_3O_4/g-C_3N_4 (e) Fe_3O_4/SnO_2/g-C_3N_4 (FSG2).

We estimated the sizes and morphologies of the crystal samples using the Scherrer equation and XRD data and given in Table 3.1.1.

$$D = \frac{K\lambda}{\beta \text{Cos}\,\theta} \qquad (3.1)$$

Where, the average size of crystallites, D, in nm. The component K (0.89) represents the grain form factor, X-ray wavelength (λ) in nm and θ is Bragg diffraction angle. which is measured in nm, also affects the average size of crystallites.

Table 3.1.1 presented the mean grain size, lattice characteristics, and volume of prepared Fe_3O_4, SnO_2, Fe_3O_4/ SnO_2, Fe_3O_4/g-C_3N_4, Fe_3O_4/SnO_2/g-C_3N_4 (FSG2) samples.

Sample	Crystallite Size (nm)	Lattice Parameters			Cell volume
		a (Å)	b (Å)	c (Å)	
Fe_3O_4	27.116	8.395	8.395	8.395	591.717
SnO_2	14.586	4.732	4.732	3.177	71.163
Fe_3O_4/SnO_2	31.921	8.438	8.438	8.438	600.805

	20.103	4.730	4.730	3.178	71.125
Fe_3O_4/g-C_3N_4	31.695 63.453	8.382 6.286	8.382 6.286	8.382 4.368	589.108 81.073
Fe_3O_4/SnO_2/g-C_3N_4 (FSG2)	33.268 25.171 63.478	8.408 4.754 6.281	8.408 4.754 6.281	8.408 3.198 4.369	594.440 72.294 80.961

3.1.2 FT-IR analysis

Fourier-transform infrared spectroscopy (FTIR) is a technique used to obtain an infrared spectrum of absorption or emission of a solid, liquid, or gas. It is widely used for identifying organic, polymeric, and, in some cases, inorganic materials by detecting their vibrational modes. Fe_3O_4, SnO_2, and Fe_3O_4/SnO_2/g-C_3N_4 (FSG2) nanocomposites are depicted in Fig. 3.1.3((a)-(d)) with their FT-IR spectra. The intensity of peaks might change due to the presence of multiple phases and broadening of peaks can suggest the formation of a more amorphous structure or indicate particle size effects.

In nanocomposites of Fe_3O_4, SnO_2, and Fe_3O_4/SnO_2, the stretching and bending vibrations of water molecules are responsible for the noticeable absorption band between 1620 and 1682 cm^{-1} and 3426 and 3375 cm^{-1}. Because of bending vibrations, a transmittance band at 1635 cm^{-1} is produced when asymmetrical water molecules are present. The carboxylate anion in the plant extract forms COO-Fe bonds when it reacts with the hydroxyl radical groups on Fe_3O_4. According to Yasser and Abdel-Monem (2016), absorption peaks at 1103 cm^{-1} and 1357 cm^{-1} are produced by this process.

The broad absorption peak seen between 400 and 600 cm^{-1} was caused by the metal-oxygen (M-O) stretching mode. Sn-O bond stretching vibrations at 432 and 524 cm^{-1} were seen in the Fe-O bending spectra of Fe_3O_4 nanoparticles.

The absorption peaks at 1219 and 1319 cm^{-1} for C-N stretching revealed the respiration pattern of S-triazine derivatives, particularly trigonal C-N or bridging C-NH-C units made from g-C_3N_4. The 432–524 cm^{-1} range also contains the metal oxide vibrations of Sn–O and Fe–O. At 1543 cm^{-1}, the absorption peak is stronger for the N-H bond in g-C_3N_4. In most cases, the nanomaterial's characteristics are unaffected by the addition of Fe_3O_4 and g-C_3N_4 to SnO_2.

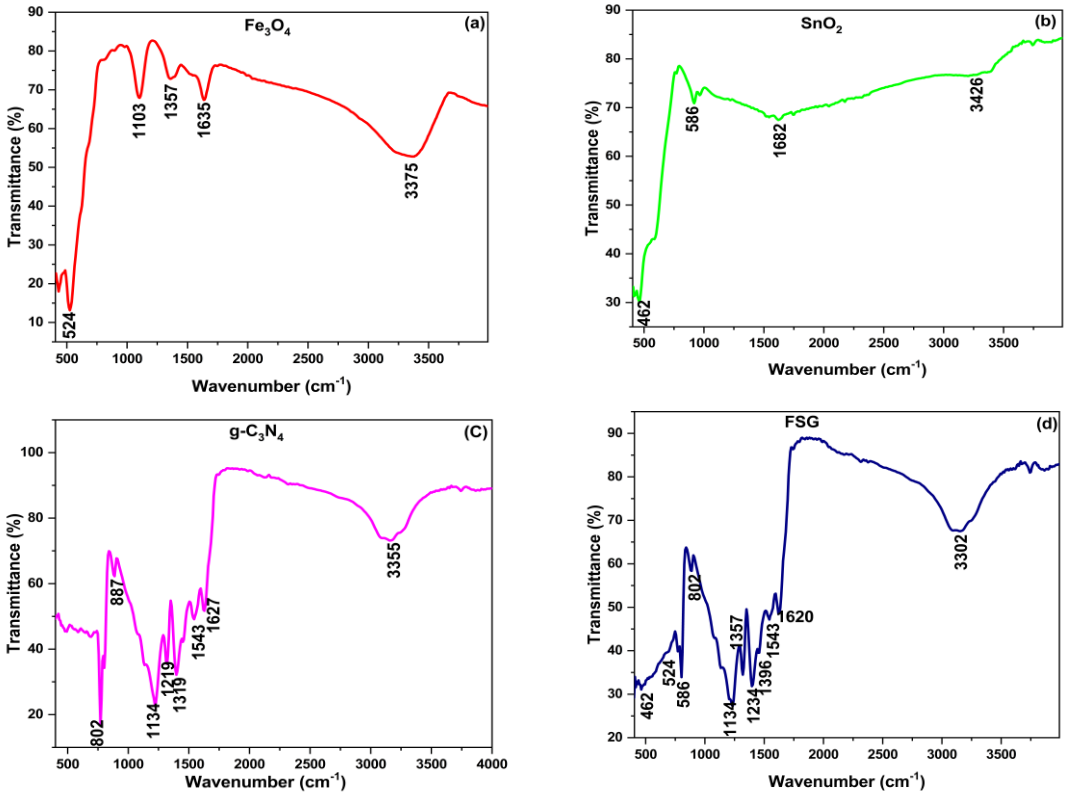

Fig. 3.1.3 FT-IR of a) Fe_3O_4 b) SnO_2 c) g-C_3N_4 d) Fe_3O_4/SnO_2/g-C_3N_4 (FSG2)

3.1.3 UV-Visible Spectroscopy

Confirmation of the necessary substance(s), preparation, and analysis of the band gap energies of the produced material or photocatalyst were carried out using the thermoscientific UV-visible spectrophotometer. As seen in Fig. 3.1.4 (a) and (c), the baseline was adjusted by utilizing double-distilled water within the 200 to 1000 nm wavelength range. Data from the UV-visible spectra were used to calculate the band-gap energies using the Tauc plot method [Abdel-Monem *et al*., (2017)].

$$(\alpha h\vartheta)^{1/n} = A(h\vartheta - E_g) \qquad (3.2)$$

The absorption coefficient is denoted by α, and Eg stands for a fixed energy value. Light frequency, measured in electron volts (eV), is denoted by the symbol hϑ. When we use prepared photocatalysts, the value of n remains 1/2, despite potential changes based on the photocatalyst's transition. If we plot the (αhϑ)^(1⁄n) against hϑ on a graph

and then extrapolate the linear regression, we can find, Eg. As shown in Fig. 3.1.4 (b) and (d), the band gap energy of the nanocomposite as it was made is 2.35 eV. The band gap energies of Fe_3O_4, SnO_2, and g-C_3N_4 are 1.726, 3.02, and 2.80 eV, respectively.

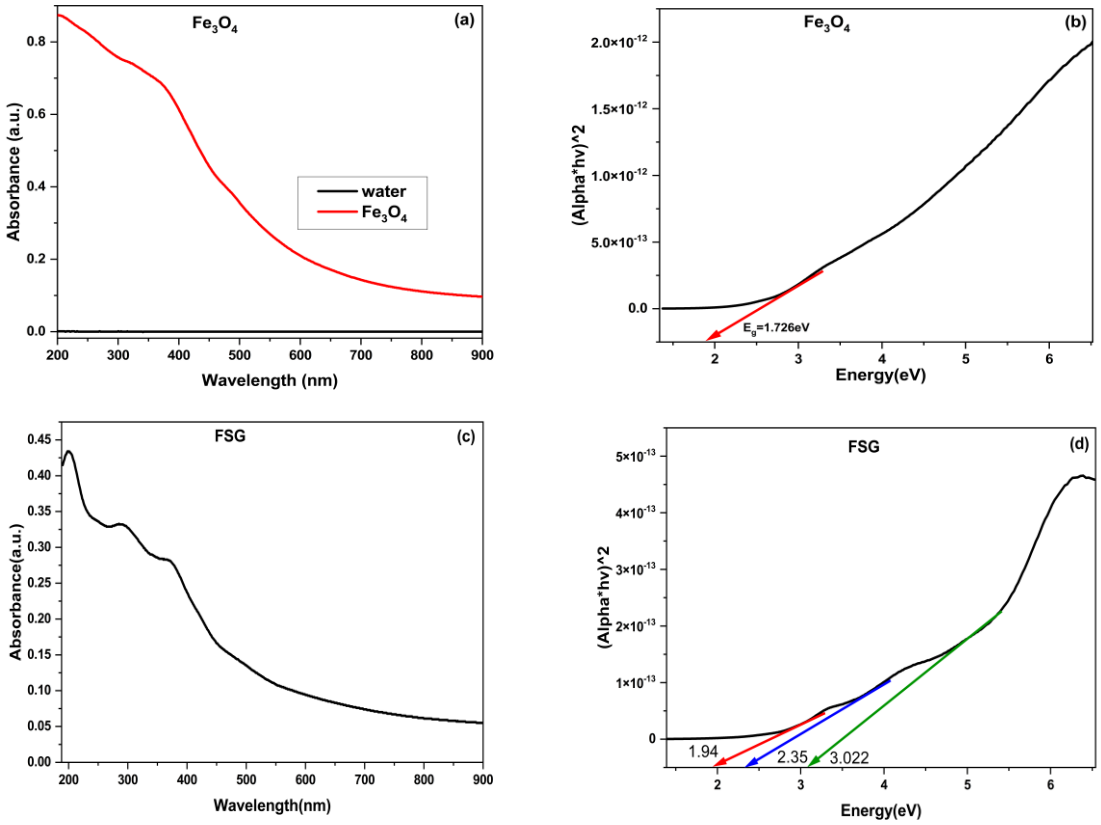

Fig. 3.1.4 (a) UV-visible spectroscopy spectrum of Fe_3O_4 (b) Band gap Energy calculation of Fe_3O_4 (c) UV-visible spectroscopy spectrum of $Fe_3O_4/SnO_2/g\text{-}C_3N_4$ (FSG2) (d) Band gap Energy calculation of $Fe_3O_4/SnO_2/g\text{-}C_3N_4$ (FSG2).

3.1.4 SEM analysis

We observed a condensed layer, possibly the porous structure of g-C_3N_4, on the surface of SnO_2 in the composite (Fig. 3.1.5(a)). We found the same thing as other studies that looked at g-C_3N_4 and SnO_2 together [Wang *et al.*, (2022)]. This nanocomposite showed particle clusters. Small, crystalline formations, sometimes rough or porous, appeared. Layered, flaky g-C_3N_4 is usual in which particles were evenly distributed across the g-C_3N_4 matrix, resulting in thin, flat sheets or plates, occasionally stacked. The average crystallite size was determined to be 30.49nm.

Effective composite formation requires uniform particle size distribution and efficient intermixing in the g-C_3N_4 matrix. Fig. 3.1.5(b) displayed the EDAX spectrum that verified the sample components.

The EDAX spectrum detected iron, tin, carbon, nitrogen, oxygen, and possibly other components produced from plant extracts. The EDAX of the Fe_3O_4/SnO_2/g-C_3N_4 (FSG2) nanocomposite showed that the carbon, nitrogen, oxygen, iron, and tin elements were all clearly visible. Elements C, N, O, and Fe had their emission maxima at 0.5, 0.6, 1, and 6.5 keV, respectively, whereas Sn has its emissions at 3.5 keV. Fig. 3.1.5(c) presented the estimated average size of the as-prepared nanocomposite, which is 30.49 nm.

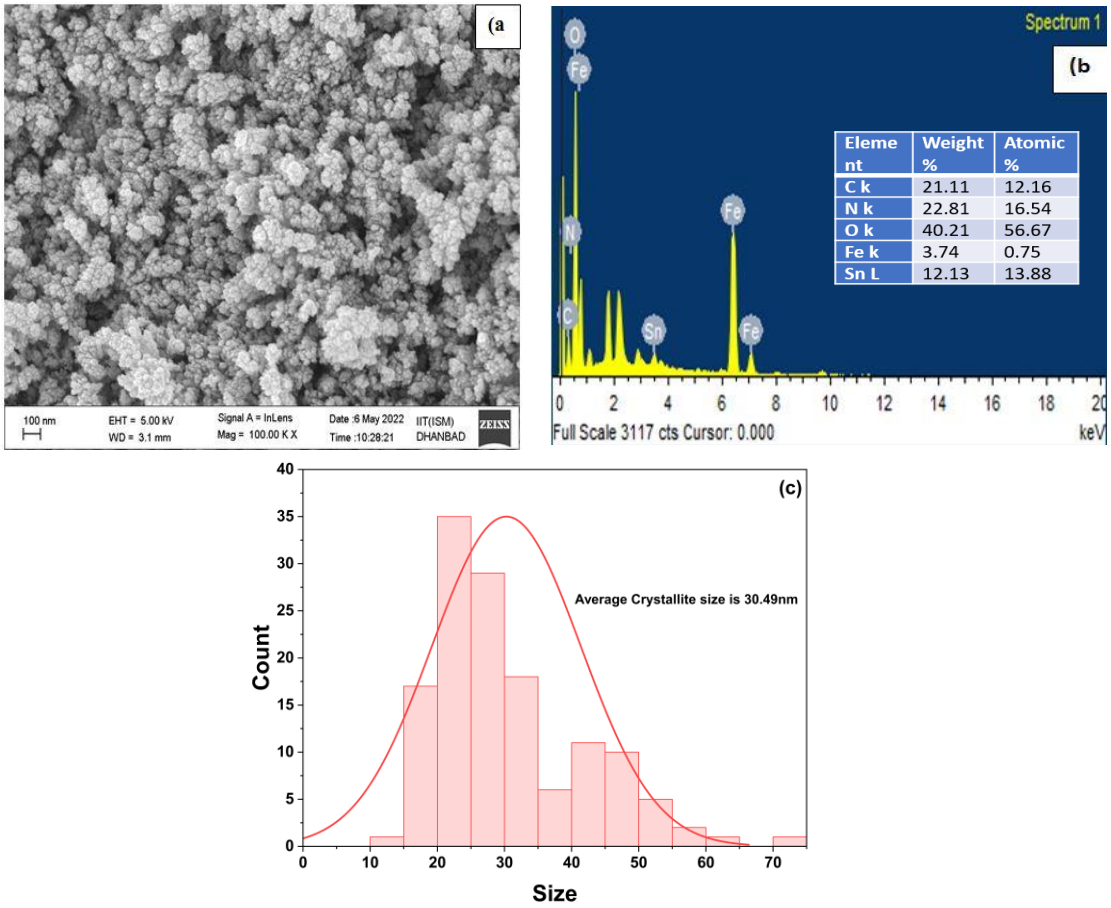

Fig. 3.1.5 (a) SEM (b) SEM-EDAX of Fe_3O_4/SnO_2/g-C_3N_4 (FSG2) (c) Average crystallite size.

3.1.5 TEM analysis

By using transmission electron microscopy, examined the nanocomposite in their native states, which is presented in Fig. 3.1.6; the transmission electron micrograph of the magnetic nanocomposite of FSG2 showed primarily spherical particles ranging in size from 200.4 to 250.5 nm. The SAED pattern, corresponding to the tetragonal phase, showed nanocrystalline features, such as scattered dots and rings. In TEM images, SnO_2 nanoparticles appeared as many little spheres. Although the hydrothermal method lowered the average size of the nanocomposite, it did not affect the sample's shape. Fe_3O_4, SnO_2, Fe_3O_4/SnO_2, $Fe_3O_4/g\text{-}C_3N_4$, and FSG2 have mean diameters of approximately (26-34), (14-32), (20-32), (31-64), (24-64), and (24-64) nm, respectively. These numbers agree with the powder XRD result, which estimated the grain size.

The HRTEM pictures of FSG2 in Fig. 3.1.6(c) showed that the SnO_2 nanoparticles were much bigger than the Fe_3O_4 nanoparticles. We have confirmed a nanoheterojunction between the components, and the $g\text{-}C_3N_4$ matrix contains Fe_3O_4 nanoparticles encased in SnO_2. In Fe_3O_4 nanoparticles, the (333) plane corresponds to an interplanar spacing of 0.161 nm. The 0.211 nm lattice fringe observations revealed the optimal development of SnO_2 nanoparticle crystals in the (210) direction. In addition, SnO_2 and $g\text{-}C_3N_4$ created a heterojunction with different energy, and it is easier for electrons and holes to migrate and separate when this heterojunction is present. Thus, not only increasing photocatalytic performance, the design of this heterojunction prevented electron-hole pair recombination. Finally, the efficient transport of electrons and holes between $g\text{-}C_3N_4$ and SnO_2 is essential for photocatalytic activities.

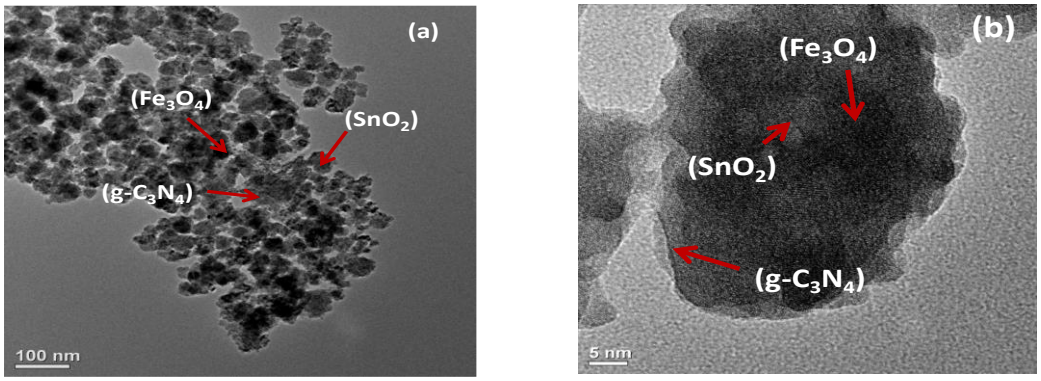

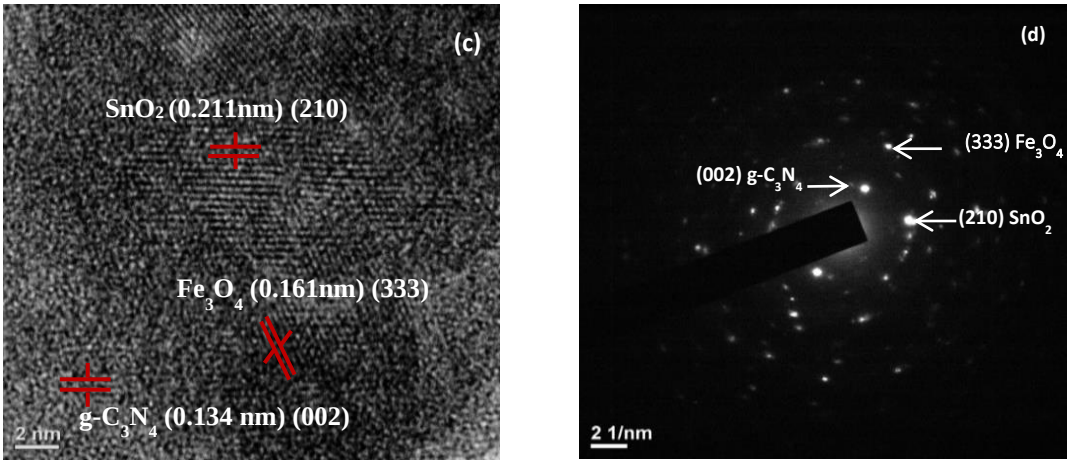

Fig. 3.1.6 (a-b) TEM Images, (c) HRTEM image and (d) SAED Image.

3.1.6 XPS studies

We examined the surface chemical composition of the FSG2 magnetic nanocomposite using X-ray photoelectron spectroscopy (XPS). The XPS spectrum analysis confirmed the presence of carbon, tin, iron, nitrogen, and oxygen (Fig. 3.1.7(a)), confirming the nanocomposite's composition as FSG2. The C1s spectra displayed two separate peaks at 285.18 and 287.4 electron volts (eV), as illustrated in Fig. 3.1.7(b). The adventitious carbon is created by the sp^2 C-C interaction, which gives the g-C_3N_4 molecule energy of 285.18 eV. The signal at 287.4 eV is due to the nitrogen-carbon interaction in the carbon-containing hexagonal ring structure of g-C_3N_4. Fig. 3.1.7(c) showed the N-atom of the carbon-nitrogen-carbon ring (at 398.78 eV) and the carbon-nitrogen-hydrogen ring (at 403.12 eV) in the presence of tertiary N-bonded groups; this area was shown to be significant according to the inquiry [Sheng *et al*., (2014)]. Fig. 3.1.7(d) revealed the detection of two peaks in the high-quality Sn3d XPS data, which correspond to SnO_2. The Sn's $3d_{5/2}$ and $3d_{3/2}$ electronic states corresponded to the peaks observed at 485.96 eV and 496.41 eV, respectively. Fig. 3.1.7(e) [Zhijie *et al*., (2018)] shown that the peak at 531.94 eV in the O1s spectra, which is caused by oxygen vacancies and strongly adsorbed oxygen species, is due to the existence of lattice oxygen in SnO_2 and Fe_3O_4. The XPS analyses showed that the Fe^{2+} and Fe^{3+} oxidation states of the Fe_3O_4 phase were responsible for the two peaks seen in the Fe2p spectra. After the restructuring, the peaks at 716.41.

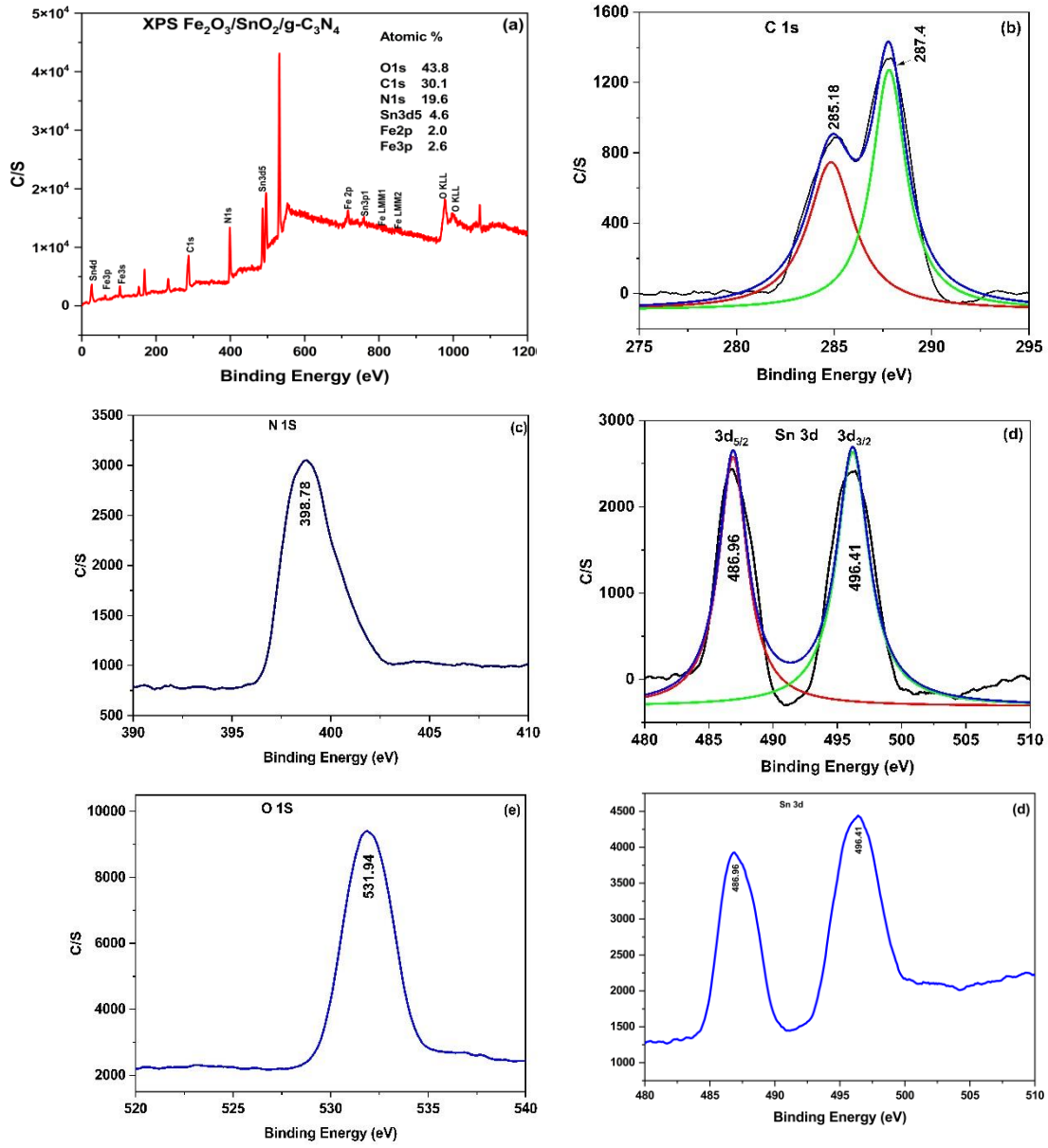

Fig. 3.1.7((a)-(e)) XPS of $Fe_3O_4/SnO_2/g\text{-}C_3N_4$ (FSG2).

3.1.7 BET surface analysis

The surface area and pore size of the $Fe_3O_4/SnO_2/g\text{-}C_3N_4$ (FSG2) nanocomposite were computed using nitrogen adsorption-desorption experiments, as seen in Fig. 3.1.8. The produced materials with percentages of Fe_3O_4/SnO_2, $Fe_3O_4/g\text{-}C_3N_4$, and $Fe_3O_4/SnO_2/g\text{-}C_3N_4$ had BJH pore diameters of 2.163, 2.446, and 2.863 nm, respectively. Summative mesopore volume for Fe_3O_4/SnO_2, $Fe_3O_4/g\text{-}C_3N_4$, and $Fe_3O_4/SnO_2/g\text{-}C_3N_4$ was 0.001, 0.032, and 0.061 cm^3/g, respectively. Table 3.1.2

displays the properties of the BET surfaces, volumes, and diameters of the Fe_3O_4/SnO_2, $Fe_3O_4/g\text{-}C_3N_4$, and $Fe_3O_4/SnO_2/g\text{-}C_3N_4$ combinations.

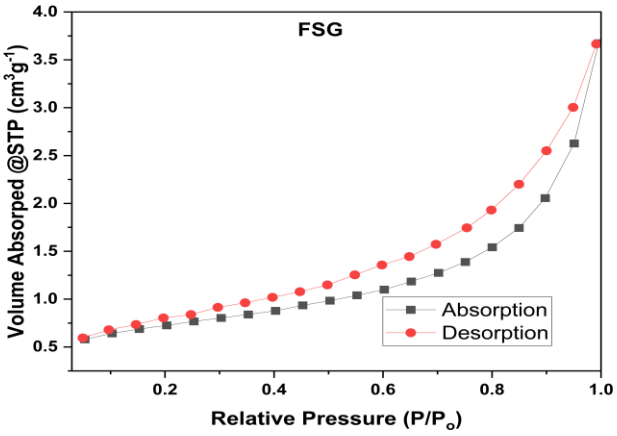

Fig. 3.1.8 Brunauer-Emmett-Teller (BET) for $Fe_3O_4/SnO_2/g\text{-}C_3N_4$ (FSG2).

Table 3.1.2 presented the characteristics of BET surface area, pore volume, and pore diameter for Fe_3O_4/SnO_2, $Fe_3O_4/g\text{-}C_3N_4$ and $Fe_3O_4/SnO_2/g\text{-}C_3N_4$ (FSG2).

Sample	S_{Bet} (m^2/g)	Pore Volume (cm^3/g)	Pore size (nm)
Fe_3O_4/SnO_2	0.356	0.001	2.163
$Fe_3O_4/g\text{-}C_3N_4$	10.957	0.032	2.446
Fe_3O_4/SnO_2/ $g\text{-}C_3N_4$ (FSG2)	22.261	0.061	2.863

3.1.8 Photoluminescence study

The use of photoluminescence measurements to learn about the effectiveness of carrier separation and the length of photoexcited charge pairs is shown in Fig. 3.1.9. We obtained the photoluminescence spectra of pure Fe_3O_4, $g\text{-}C_3N_4$, Fe_3O_4/SnO_2, and $Fe_3O_4/SnO_2/g\text{-}C_3N_4$ (FSG2) using 365 nm excitation light. It was easy to discern the broad range of wavelengths in the $g\text{-}C_3N_4$ emission spectra, which fell between 400 and 550 nm. In contrast to pure $g\text{-}C_3N_4$, the photoluminescence (PL) intensity of $Fe_3O_4/SnO_2/g\text{-}C_3N_4$ composites was noticeably lower. According to Ong *et al*. (2014), reducing the peak intensity of photoluminescence (PL) slowed down the recombination of photoexcited charge pairs. Adding SnO_2 to $Fe_3O_4/SnO_2/g\text{-}C_3N_4$ composites dramatically reduced the recombination rate of charge pairs (e^-h^+). This

was because SnO_2 have a strong affinity for the g-C_3N_4 surface. The improved segregation efficiency of photogenerated carriers causes the increased involvement of electrons (e^-) and holes (h^+) in the photocatalytic system, including Fe_3O_4/SnO_2/g-C_3N_4. The PL intensity of the Fe_3O_4/SnO_2/g-C_3N_4 nanocomposite was lower than that of g-C_3N_4 alone because it was better at separating charges and stopping electron-hole recombination. When exposed to light, g-C_3N_4 have to capture the electrons generated by SnO_2 to facilitate charge separation. The photoluminescence (PL) emission showed that the Fe_3O_4/SnO_2/g-C_3N_4 system had better light transmission, which made it easier for the generated electron-hole pairs to separate.

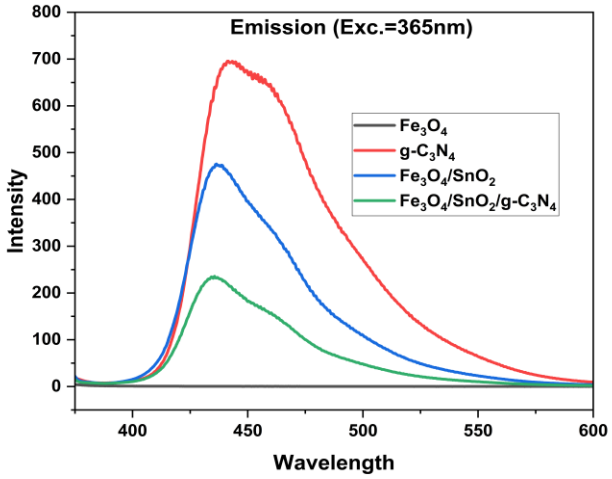

Fig. 3.1.9 PL for Fe_3O_4, g-C_3N_4, Fe_3O_4/SnO_2, Fe_3O_4/SnO_2/g-C_3N_4 (FSG2).

3.1.9 Photocatalytic Studies

The efficiency of various catalysts, including Fe_3O_4, SnO_2, g-C_3N_4, and Fe_3O_4/SnO_2/g-C_3N_4 nanocomposite, was evaluated for their ability to degrade a typical organic pollutant, specifically rhodamine B (RhB), methylene blue (MB), 2,4-DCP, and TCAA. A volume of 20 mL of treated water, with a concentration of 8 ppm of dye or pesticide, was combined with 1mg of a nanocomposite photocatalyst in each solution. The mixture was then allowed to sit in the dark for 30 min to establish equilibrium between the adsorption and desorption of the dye or pesticide. The light absorption of dye or pesticide decreased as the illumination time increased (from 0 to 180 min, at intervals of 30 min), indicating that the pollutant was decomposing on the

magnetic nanocomposite photocatalyst. We exposed the catalyst samples to visible light at various time intervals to assess the temporal disintegration of the pollutant.

$$\text{Degradation Efficiency} = \frac{C_o - C_t}{C_o} x100 \qquad (3.3)$$

The photocatalytic reaction involves visible light excitation of electrons in the $Fe_3O_4/SnO_2/g\text{-}C_3N_4$ nanocomposite valence band through the S-Scheme mechanism. Upon light absorption, the photocatalyst undergoes a process in which electrons are elevated from the valence band (VB) to the conduction band (CB), forming charge pairs. As a result, electron-hole pairs (e^-/h^+) are formed. Adsorption caused the adhesion between the photocatalyst and the pollutant molecules, with the catalyst's active sites facilitating this connection.

The redox processes occurred.

Oxidation:

When photoexcitation generates holes in the conduction band, these holes might react with water molecules or hydroxide ions (OH^-) in the vicinity, resulting in the formation of hydroxyl radicals ($\dot{O}H$).

$$h^+ + H_2O \text{ or } OH^- \rightarrow \dot{O}H \qquad (3.4)$$

a) Reduction:

Superoxide radicals ($\dot{O}_2^-$) are formed when electrons in the conduction band interact with oxygen molecules (O_2) that were deposited on the surface of the photocatalyst.

$$e^- + O_2 \rightarrow \dot{O}_2^- \qquad (3.5)$$

The degradation occurred due to the reactivity of hydroxyl and superoxide radicals (generated during a redox reaction). Dyes or pesticide molecules adsorbed on the photocatalyst can undergo oxidation by highly reactive species and decomposition, forming smaller and less hazardous constituents. The desorption and release of byproducts can effectively separate and degrade RhB byproducts from the photocatalyst. These leftovers can be used to produce non-toxic chemicals through additional reactions. The ability of the photocatalyst to produce reactive species like hydroxyl radicals ($\dot{O}H$) and superoxide radicals ($\dot{O}_2^-$), has been found to be crucial in

breaking down dyes or molecules. The photocatalyst selection, surface quality, and reaction conditions can compromise the process efficiency. The degradation products and intermediates can differ depending on the reaction conditions and the photocatalyst's features.

$$\left.\begin{array}{c} g-C_3N_4(e^-+h^+)/SnO_2(e^-+h^+) \rightarrow g-C_3N_4(e^-+e^-)/SnO_2(h^++h^+) \\ h^+ + OH^- \rightarrow OH \text{ (Oxidation)} \\ e^- + O_2 \rightarrow \dot{O}_2^- \text{ (Reduction)} \\ H_2O + \dot{O}_2^- \rightarrow O\dot{O}H + OH^- \\ 2O\dot{O}H \rightarrow \dot{O}_2^- + H_2O_2 \\ H_2O_2 + \dot{O}_2^- \rightarrow \dot{O}H + OH^- + O_2 \\ H_2O_2 + e^- \rightarrow \dot{O}H + OH^- \\ Fe^{3+} + H_2O_2 \rightarrow Fe^{2+} + O\dot{O}H + H^+ \\ Fe^{2+} + H_2O_2 \rightarrow Fe^{3+} + OH^- + \dot{O}H \\ \dot{O}H + \text{dyes/pesticides} \rightarrow \text{Decomposition products} \end{array}\right\} \quad (3.6)$$

When subjected to visible light such as LED, H_2O_2 generates two hydroxyl radicals ($\dot{O}H$), which break down RhB. Hydroxyl radical ($\dot{O}H$) is a potent oxidizing agent that break down organic contaminants. The degradation of dyes or pesticides was tracked using UV-visible spectroscopy. The catalyst effectively reduced the peak intensity at λ_{max}, indicating that it degraded a significant amount of dyes or pesticides within a time frame of around 180 min under LED light.

3.1.9.1 RhB photodegradation

As shown in Fig. 3.1.10(a) and (b), Fe_3O_4/SnO_2 (FS) and Fe_3O_4/g-C_3N_4 (FG) nanoparticles may photocatalytically removed the Rhodamine B (RhB) dye when exposed to LED light, while Fig. 3.1.10(c) for RhB degradation with an FSG2 nanocomposite photocatalyst. In the degradation of RhB, as described in studies by Soltani, (2013), He, (2009), and Diao, (2017), the hydroxyl radicals of the nanoparticles accelerated N-de-ethylation and chromophore modification (as depicted in Fig. 3.1.10(d)) and mass spectrum is shown in Fig. 3.3.10(e), and bond cleavage was induced by this mechanism, which opens molecular rings, generates oxidation products, and forms smaller RhB molecules. Mineralizing the smaller molecules is the last step in the process, producing CO_2 and H_2O.

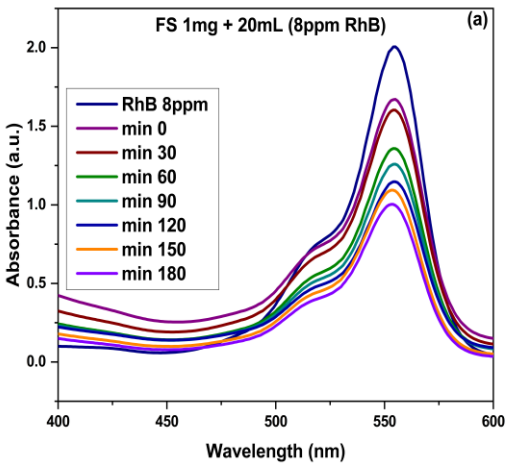
FS 1mg + 20mL (8ppm RhB)
(a)
RhB 8ppm
min 0
min 30
min 60
min 90
min 120
min 150
min 180
Absorbance (a.u.)
Wavelength (nm)

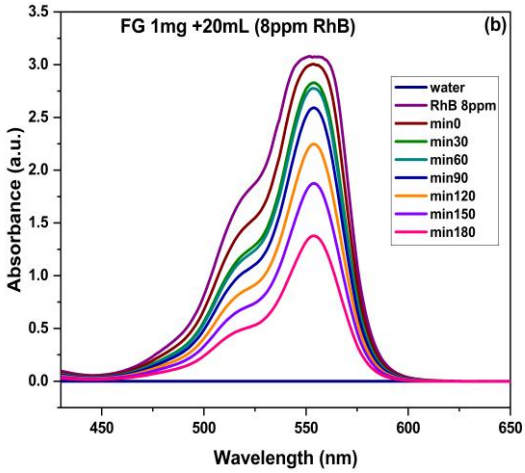
FG 1mg +20mL (8ppm RhB)
(b)
water
RhB 8ppm
min0
min30
min60
min90
min120
min150
min180
Absorbance (a.u.)
Wavelength (nm)

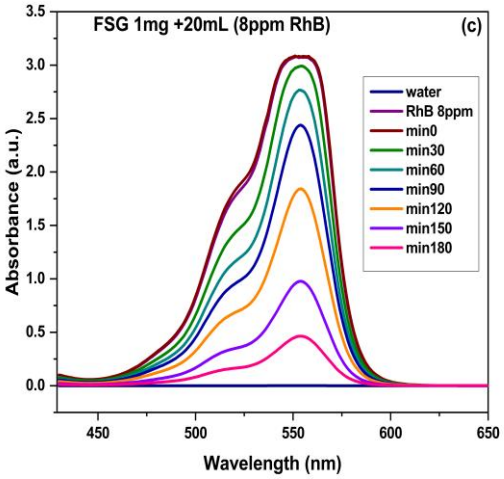
FSG 1mg +20mL (8ppm RhB)
(c)
water
RhB 8ppm
min0
min30
min60
min90
min120
min150
min180
Absorbance (a.u.)
Wavelength (nm)

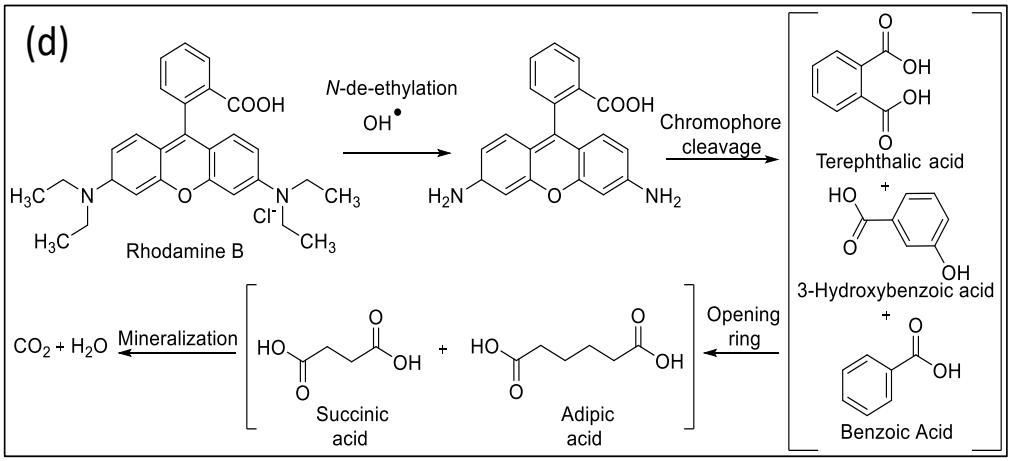
(d)
COOH
N-de-ethylation
OH•
Chromophore cleavage
Rhodamine B
Terephthalic acid
3-Hydroxybenzoic acid
Benzoic Acid
Opening ring
Succinic acid
Adipic acid
Mineralization
CO2 + H2O

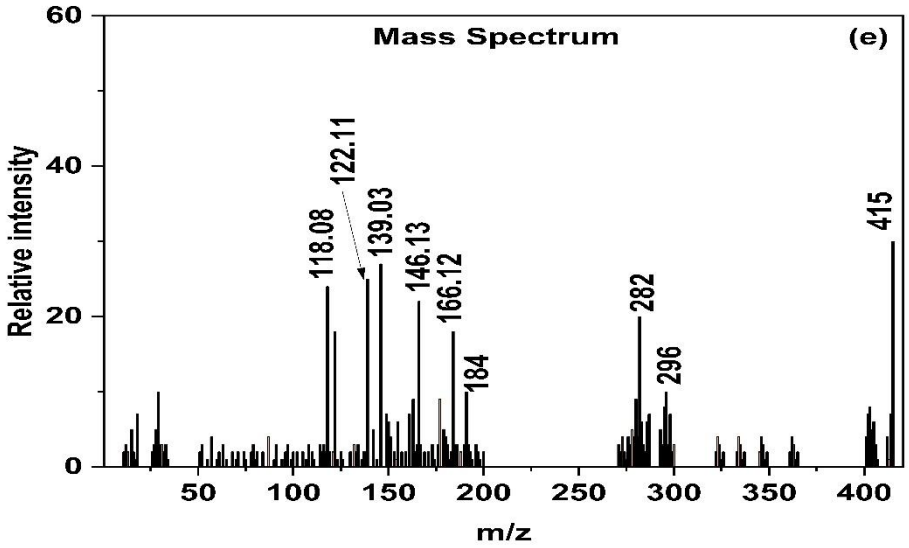

Fig. 3.1.10 RhB decomposition (a) Fe_3O_4/SnO_2 (b) Fe_3O_4/g-C_3N_4 (c) Fe_3O_4/SnO_2/g-C_3N_4 (FSG2) (d) Mineralization of RhB (e) Mass Spectrum.

The Langmuir-Hinshelwood model determined the order of rate constant (k). $kt=\ln(C_o/C_t)$, where C_o and C_t are RhB dye concentrations at 0 and t min illumination, respectively. The sample's pseudo first-order rate constant (k) from the graph of the line connecting the absorption time and the natural logarithm of C_t/C_o while for pseudo-second order rate constant (k) from the graph of the line connecting the absorption time and the natural logarithm of $1/C_t$-$1/C_o$, depicted in Fig. 3.1.11 (a) ,(b).

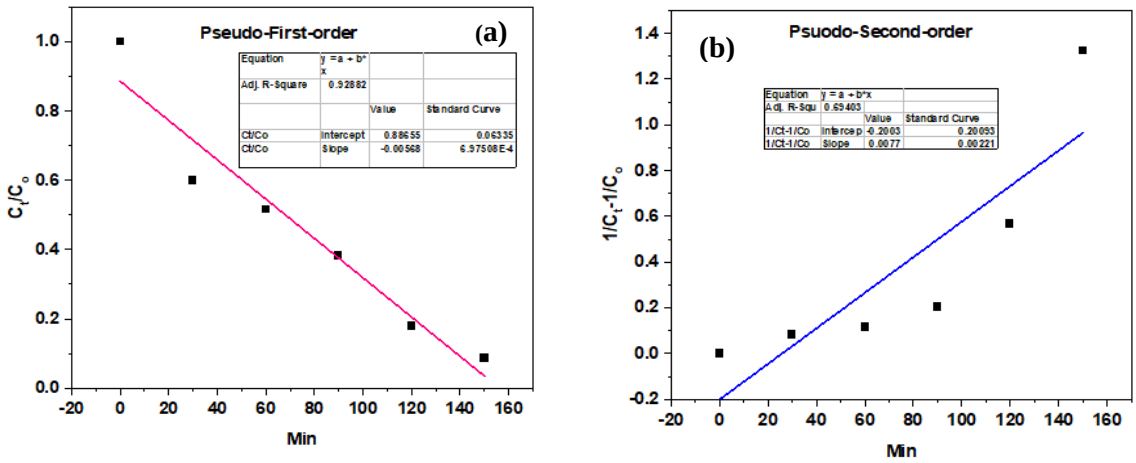

Fig. 3.1.11. Graph of absorption time Vs C_t/C_o (b) absorption time Vs $1/C_t$-$1/C_o$.

Order of Reaction	Intercept	Slope	R^2
Pseudo First order	0.88665	-0.00568	0.92882
Pseudo Second order	2.17856	0.49036	0.69403

R^2 values indicated the goodness of fit of the experimental data to these models. R^2, or the coefficient of determination, indicates how well the data fits a particular model, with values closer to 1 representing a better fit. Since the R^2 value is higher for the pseudo-first-order model (0.928) compared to the pseudo-second-order model (0.694) when RhB is treated with FSG under LED light, this suggested that the experimental data fits the pseudo-first-order kinetic model better. Therefore, we can conclude that the reaction likely follows pseudo-first-order kinetics.

3.1.9.2 MB Degradation

Fig. 3.1.12(a) illustrated the analysis results on the degradation of methylene Blue (MB) under LED light exposure. Fig. 3.1.12(b) demonstrated that the breakdown of MB occurs when the hydroxyl groups of the FSG2 nanocomposite come into contact with the MB molecules, and this interaction results in the dissociation of chemical bonds, such as sulfur-chlorine, nitrogen-methyl, carbon-sulfur, carbon-nitrogen, and carbon-oxygen. As a result, a series of reactions occurred, leading to the breakdown of intermediate substances and the opening of MB rings, ultimately producing smaller organic compounds.

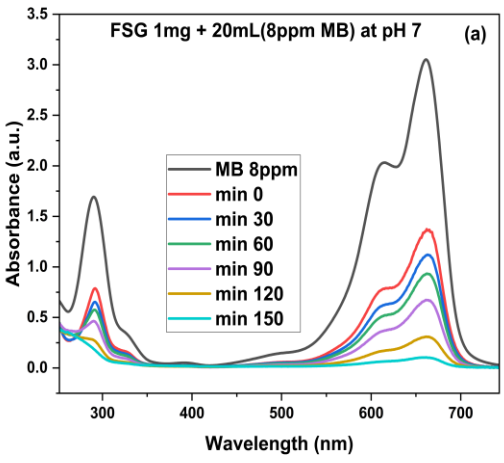

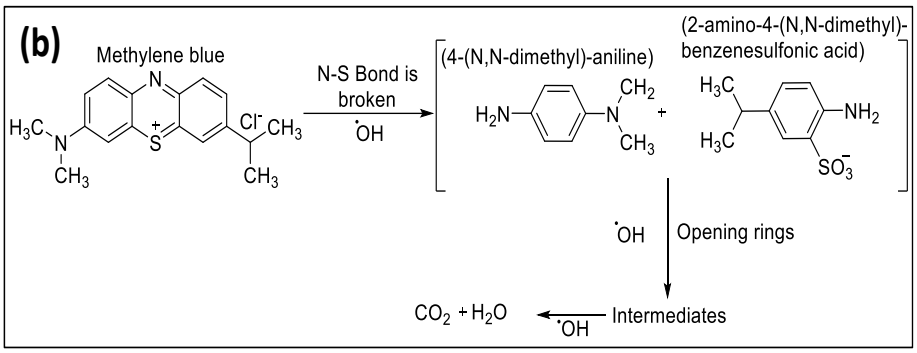

Fig. 3.1.12 (a) Degradation of MB with FSG2 (b) Mineralization of MB

3.1.9.3 MB and rhodamine (mixture) Degradation

Under LED circumstances, a mixture of 10 mL of each methylene blue (8 ppm) and rhodamine B (8 ppm) dye was analysed for degradation, as shown in Fig. 3.1.13. When combining rhodamine B (RhB) with methylene blue (MB) in water, several things could reduce their solubility, and there were several possible explanations for the observed decrease in solubility. RhB and MB molecules could vie for adsorption sites at the solvent-water interface. Combining two colours with low water solubilities might cause competing adsorption, lowering the mixture's solubility. When exposed to water, RhB and MB molecules have the potential to aggregate, and this phenomenon can also occur as a result of interactions between other dyes. Because of this aggregation, the individual colours in the combination may have less effective solubility, due to development of complexes between RhB and MB molecules.

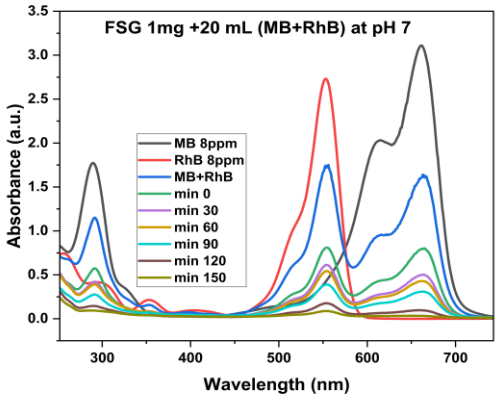

Fig. 3.1.13 Degradation of MB and RhB mixtures with FSG2.

3.1.9.4 Degradation of 2, 4-DCP

Fig. 3.1.14(a) shows the proportion of 2, 4-DCP removed by FSG nanocomposites exposed to LED irradiation. After 180 min of LED light irradiation, the FSG2 nanocomposite has the highest clearance compared to FS and FG. Fig. 3.1.14(b) shows about how the nanocomposite changed composition in a 20 mL 2,4-DCP solution. When 2, 4-DCP was started at a lower concentration, the end concentration-to-initial concentration ratio increased. A Langmuir–Hinshelwood relationship can illustrate how 2, 4-DCP degradation depends on its initial concentration [Chen and Ray, (1999)] and the reaction's surface locations may also inhibit 2, 4-DCP breakdown. At 8 ppm, 2,4-DCP degrades in 2.30 hours, and the results revealed that photocatalytic oxidation works even at low pollutant concentrations.

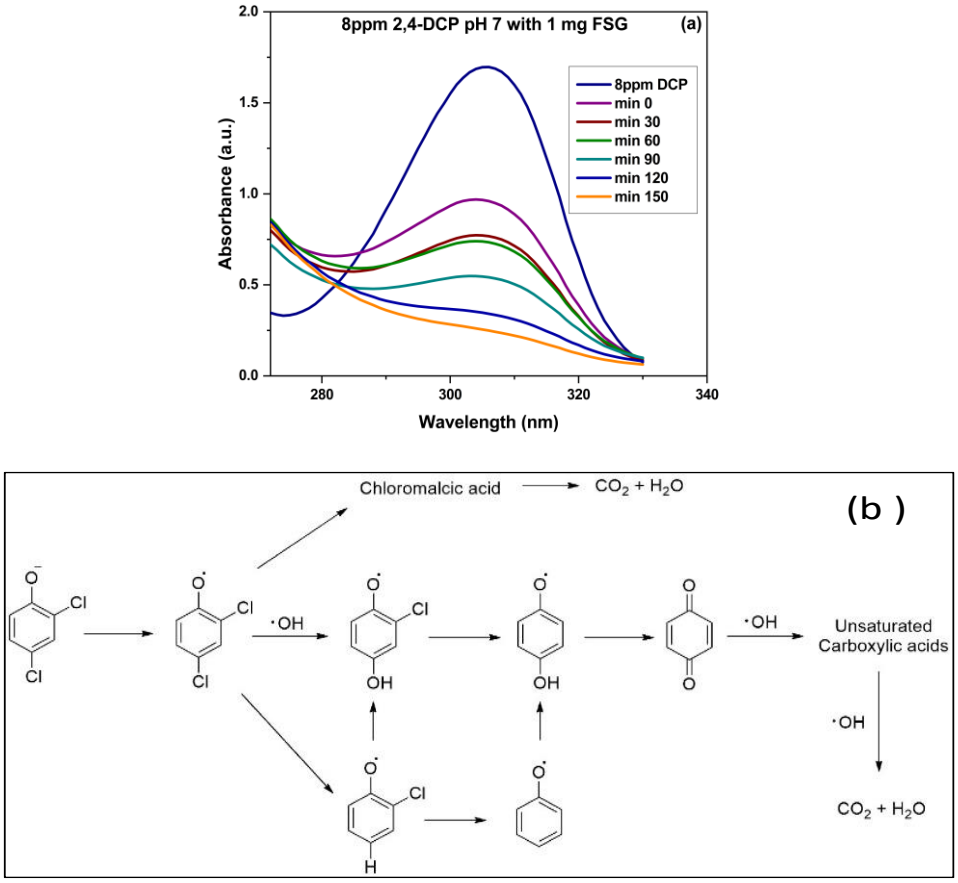

Fig. 3.1.14 (a) Degradation of 2,4-DCP with FSG2 (b) Mineralization of 2,4-DCP.

3.1.9.5 TCAA degradation

The effectiveness of FSG in mineralizing trichloroacetic acid (TCAA) was evaluated over a range of pH values (from 5 to 10) by investigating the total organic carbon (TOC) removal percentage. The resulting breakdown intermediates, designated as acetic acid, formic acid, and hydroxyacetic acids (Fig. 3.1.15 (a) and (b)), demonstrated lower toxicity than the original TCAA. Mass chromatograms indicated different intermediates such as formic acid (CH_2O_2, m/z 46, R_t=4.48 min), hydroxyacetic acid ($C_2H_4O_3$, m/z 93, R_t=4.57 min), and acetic acid ($C_2H_4O_2$, m/z 62, R_t=3.56 min). According to LCMS analysis, an intermediate with m/z 46 was identified from an intermediate with m/z 62. The data revealed that acetic acid and hydroxyacetic acid were the principal breakdown phases of TCAA, even though only formic acid was found in the LCMS analysis. Possible breakdown pathway for TCAA in the FSG process, leveraging molecular characteristics revealed from LCMS analysis and associated investigations.

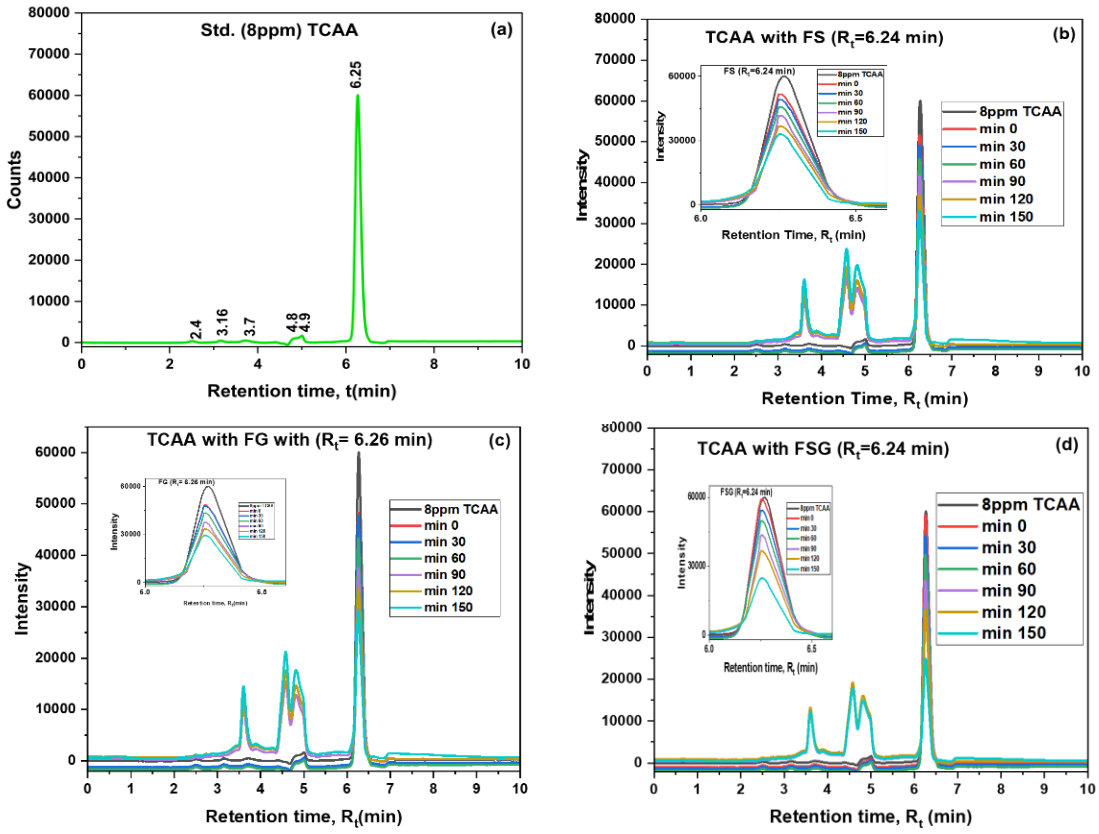

Fig. 3.1.15 (a)Standard TCAA (8ppm) (b) Degradation of TCAA with FS

(c) Degradation of TCAA with FG (d) Degradation of TCAA with FSG2.

3.1.10 TOC (total organic carbon) determination

The objective of the total carbon study was to determine RhB dye mineralization. The dye's absolute total organic carbon (TOC) value decreased by 8 ppm when 1 mg of $Fe_3O_4/SnO_2/g\text{-}C_3N_4$ (FSG2) was used, as shown in Fig. 3.1.16. This resulted in a photomineralization efficacy of 70%; however, when using Fe_3O_4/SnO_2 with the same amount of photocatalyst, there was only a slight decrease in photomineralization efficiency, reaching 48%. The limited number of active sites on the catalyst surface was responsible for impeding the desired reaction, resulting in a decrease in the absolute TOC value from 41.74 to 28.62 mg/L. Furthermore, these data provide insight into the potential presence of residual Total Organic Carbon (TOC) in each of these samples, which may be attributable to the reaction in intermediate stages before their total mineralization. We used the equation to calculate the demineralization of dyes and pesticides.

$$\alpha = \frac{TOC_{(init)} - TOC_{(eq)}}{TOC_{(init)}} x100 \qquad (3.7)$$

Here, α is the proportion of mineralization, and the initial amount of organic carbon is represented by the abbreviation $TOC_{(init)}$, while the amount of carbon in equilibrium is represented by $TOC_{(eq)}$.

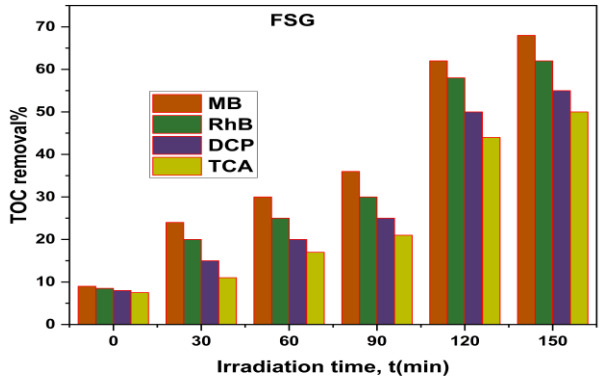

Fig. 3.1.16 TOC removal % of RhB dye with $Fe_3O_4/SnO_2/g\text{-}C_3N_4$ (FSG2).

3.1.11 Turnover number and turnover frequency

Analysing the Turnover Number (TON) and Turnover Frequency (TOF) was a

significant benchmark evaluation for establishing a catalyst's immediate effectiveness. TON is the number of substrate molecules converted into a product for every photocatalyst molecule processed in a given time interval. One way to find out is to use the following equation:

$$\text{TON} = \frac{(\%\ \text{Conversion})(\text{Number of moles of substrate})}{\text{Number of moles of Catalyst}} \quad (3.8)$$

The percentage conversion indicates the degree of degradation achieved by the photocatalyst. On the other hand, the following equation defines Turnover Frequency (TOF) as the maximum number of catalytic cycles achieved by each active site within a given unit of time:

$$\text{TOF} = \frac{\text{TON}}{\text{Time}} \quad (3.9)$$

The results obtained from the TON and TOF analyses performed during the photocatalytic degradation processes of MB, RhB, 2,4-DCP, and TCAA under the influence of LED irradiation are shown in Table 3.1.3. In the deterioration of dyes and pesticides (MB, RhB, 2,4-DCP, and TCAA) under LED radiation, the FSG nanocomposite has the most excellent TON and TOF values.

This was an awe-inspiring result, and the size reduction, which led to an increase in surface area and the number of active sites, was responsible for this improved performance, which may be linked to the previous sentence. As a consequence of this, there was an increase in the efficiency of the breakdown of organic pollutants [Kundu *et al.*, (2020); Salavati *et al.*, (2009)].

Table 3.1.3 Estimation of TOF and TON

Dyes	sample	TOF (min^{-1})	TON (min^{-1})
MB	FSG2	30.119	0.201
RhB	FSG2	22.705	0.151
2,4-DCP	FSG2	9.168	0.016
TCA	FSG2	10.189	0.067

3.1.12 Reusability

The dye or pesticide degradation efficiency of Fe_3O_4/SnO_2, $Fe_3O_4/g\text{-}C_3N_4$, and $Fe_3O_4/SnO_2/g\text{-}C_3N_4$ (FSG2) was assessed after 150 min of LED light exposure. The stability and recyclability of the photocatalyst were critical for practical application. The recycling observation demonstrated the long-lasting and reusable nature of the magnetic nanocomposite photocatalyst in its original state. Fig. 3.1.17 illustrated studies on the recycling of a nanocomposite photocatalyst for RhB, MB, 2,4-DCP, and TCAA decomposition. Following five iterations, nanocomposite photocatalysts were retrieved from the solution mixture using an external magnet. Subsequently, dye solutions were applied to nanocomposite photocatalysts. The investigation revealed that dye or pesticide degradation efficiency decreased from 96 to 85% after 150 min. We discovered a slight alteration in decomposition efficiency. The photocatalyst's adsorption capacity and decomposition performance may diminish after each usage due to the accumulation of intermediate products from the decomposition of dyes or pesticides that remain attached to its surface. As per the agreement, the nanocomposite photocatalyst efficiently decomposes dyes or pesticides through photocatalysis upon light exposure while maintaining stability and reusability. As part of a study on the factors affecting the breakdown process, the initial concentration of pollutants, the pH of the dye water, and the dosage of photocatalysts in the solution or system will be examined.

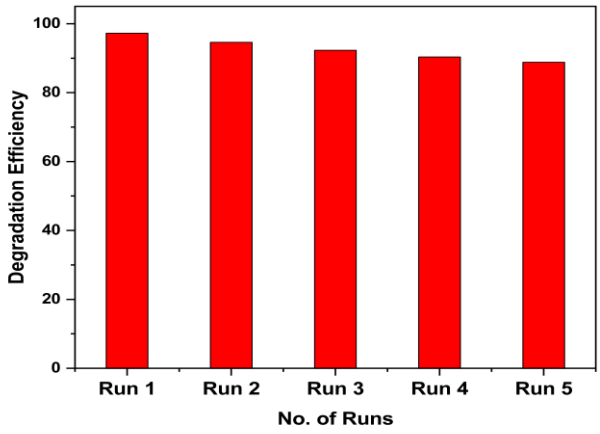

Fig. 3.1.17 Number of times of reusing of FSG2 for photodegradation

3.1.13 Dosage effect

The degradation of the dye solution necessitates the precise amount of catalyst. Fig. 3.1.18(a) and (b) illustrated the degradation of dye in a 20 mL solution containing 8 ppm of RhB, and Different amounts of photocatalyst, ranging from 0.5 to 11mg, were used in the experiment. The pH of the solution was maintained at 7.0, and examining the adsorption-desorption capacity in systems with varying catalyst dosages has verified that augmenting the catalyst dosage enhances the photocatalytic activity. This suggested that photocatalysts with a higher quantity of active sites can absorb more significant amount of RhB prior to the process of photocatalysis [Yan *et al*., (2012); Wei *et al*., (2009)]. An excessive amount of photocatalyst leads to a decrease in irradiance caused by light scattering, reducing the effectiveness of photocatalytic degradation [Jia *et al*., (2020)]. The phenomenon of cumulative effects elucidates why increasing the dose of photocatalyst does not significantly improve degradation efficiency. This method also assessed the photocatalytic degradation of the dye solution under LED illumination, which proved to be inefficient at a concentration of 8 ppm. By augmenting the quantity of photocatalyst in the system from 0.5 to 1mg, the decomposition efficiency increased from 16% to 19%. However, gradually raising the catalyst dose from 1 to 11mg only resulted in a slight alteration in the decomposition rate 30 min. After considering all of these criteria, it was concluded that the ideal quantity of nanocomposite photocatalyst to utilize was 1mg.

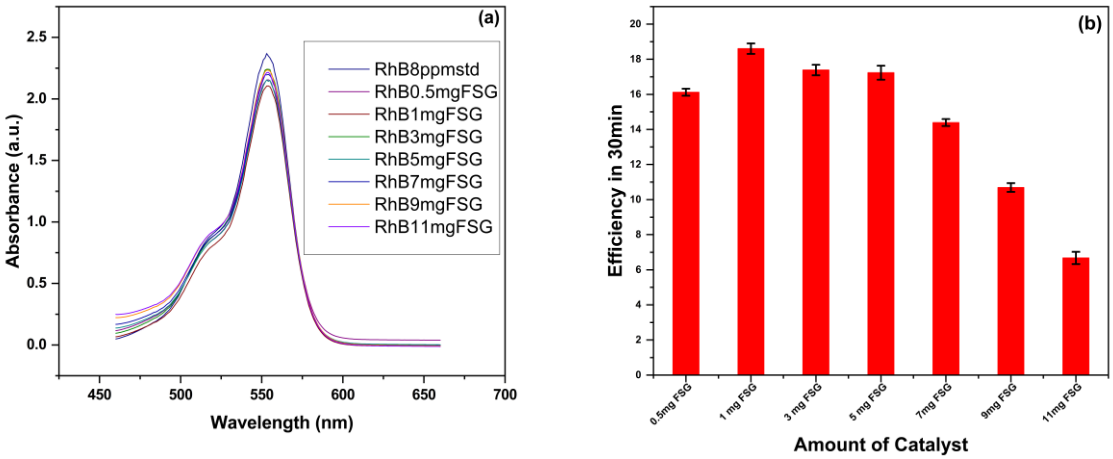

Fig. 3.1.18 ((a)-(b)) RhB degradation efficiency at various amount of prepared

photocatalyst.

3.1.14 pH effect studies

The experiment used a constant initial concentration of 8 ppm and a catalyst dose of 1mg in 20 mL of each solution. The degradation processes exhibited similarities, particularly at pH levels of 6; both very low and high pH values increase the photocatalytic degradation efficiency of dyes and pesticides, possibly due to the significant presence of hydroxyl radicals in the solution. The synthesised nanocomposite photocatalyst demonstrated the highest efficiency at a pH level between 6 and 8, as indicated by the previously mentioned.

Under acidic conditions, positive holes played a crucial role, while alkaline and neutral conditions oxidised hydroxyl radicals. The chemical composition of the environment often accelerates or retards the degradation of dyes and pesticides. Furthermore, both can undergo accelerated degradation at elevated pH values, such as pH 10, through the hydrolysis process. This phenomenon occurred when both were exposed to an alkaline environment, leading to the disassembly of the molecule. As a result, different degradation products with unique chemical properties may arise. In addition, it had a reaction with hydroxide ions, which are present in greater quantities in a solution with a higher pH. Thus, molecules can undergo degradation by the action of these ions. Increasing the pH levels generally accelerated these reactions; hence, it was crucial to regulate the pH of the surroundings. In addition, it was plausible that at elevated pH levels, the reactivity of some chemical species may undergo alterations, rendering them more prone to interacting with them. This heightened responsiveness could accelerate the demise of dyes and pesticides.

The Langmuir-Hinshelwood model ascertained the value of the first-order rate constant (K), and the equation $kt=\ln (C_o/C_t)$ represents the relationship between the rate constant K, the initial concentration C_o, the concentration C_t at time t min, and the natural logarithm function (ln). This equation is supported by references [Madkour *et al*., (2016)]. The experiment has been repeated three times to verify precision and dependability. The pseudo-first-order rate constant (K) and kinetic energy of the sample were determined by calculating the slope of the line connecting the absorption time and the natural logarithm of C_tC_o. The nanocomposite Fe_3O_4, SnO_2, g-C_3N_4, and

$Fe_3O_4/SnO_2/g\text{-}C_3N_4$ have a higher rate constant than other materials. This is because it has more surface area, and its parts worked together to make it stronger.

3.1.14.1 RhB degradation

Fig. 3.1.19((a)-(c)) displayed the UV-visible spectroscopy spectra of RhB photodecomposition at different pH levels and a graph of ln (C_o/C_t) Vs time in Fig. 3.1.18(d). As a result of RhB's cationic properties, studies on FSG2 adsorption at pH values between 5 and 10 have shown percentages of 80, 78, 72, 74, 78, and 81%, respectively. The degradation of RhB dye under LED was a modest 2% when FSG nanocomposite was not present. Similar to previous photocatalysis, the LED-RhB-FSG sample degraded 81% of the RhB after 150 min, making it the most promising of the samples.

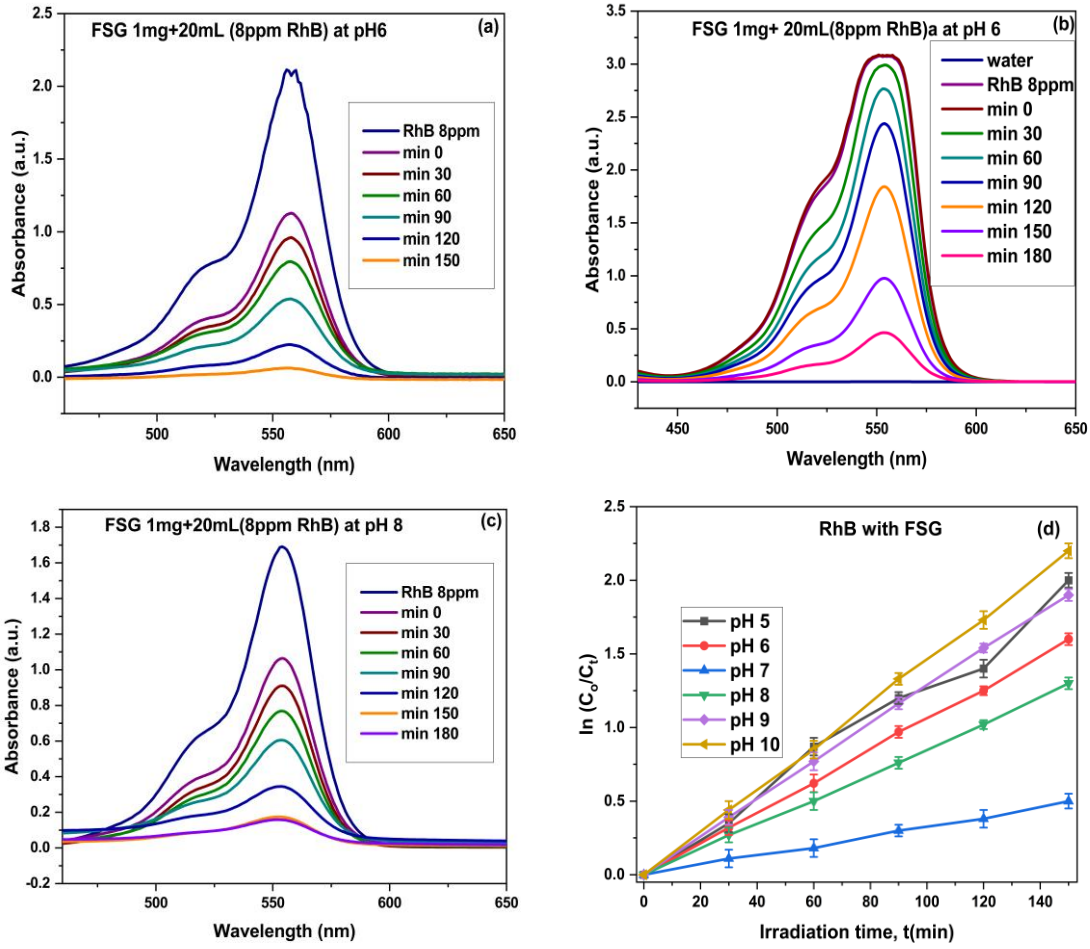

Fig. 3.1.19 (a) RhB degradation at different pH by using 1mg of prepared photocatalyst

(b) Kinetics of photodegradation.

3.1.14.2 MB degradation

Fig. 3.1.20(a)-(c) presented the UV-visible spectroscopy spectra of MB photodecomposition at various pH levels. Fig. 3.1.19(d) shown the graph of the natural logarithm of the ratio of initial concentration to current concentration (ln (C_o/C_t)) plotted against time. After 150 min, the FSG solutions at pH 5–10 showed absorptions of 85, 82, 75, 78, 82, and 88%, respectively. The positive charges inherent in the dye enhanced the absorption on the FSG surface. Significantly, the pure MB dye undergoes a 3% deterioration when subjected to LED light. The LED-MB-FSG solution exhibited the most significant deterioration, with an approximate degradation rate of 88% after 150 min of exposure to LED radiation, specifically at pH 10. The intensified deterioration was ascribed to the amplified surface area and boosted photocatalytic capability of FSG nanoparticles owing to their reduced dimensions and narrower band gap energy.

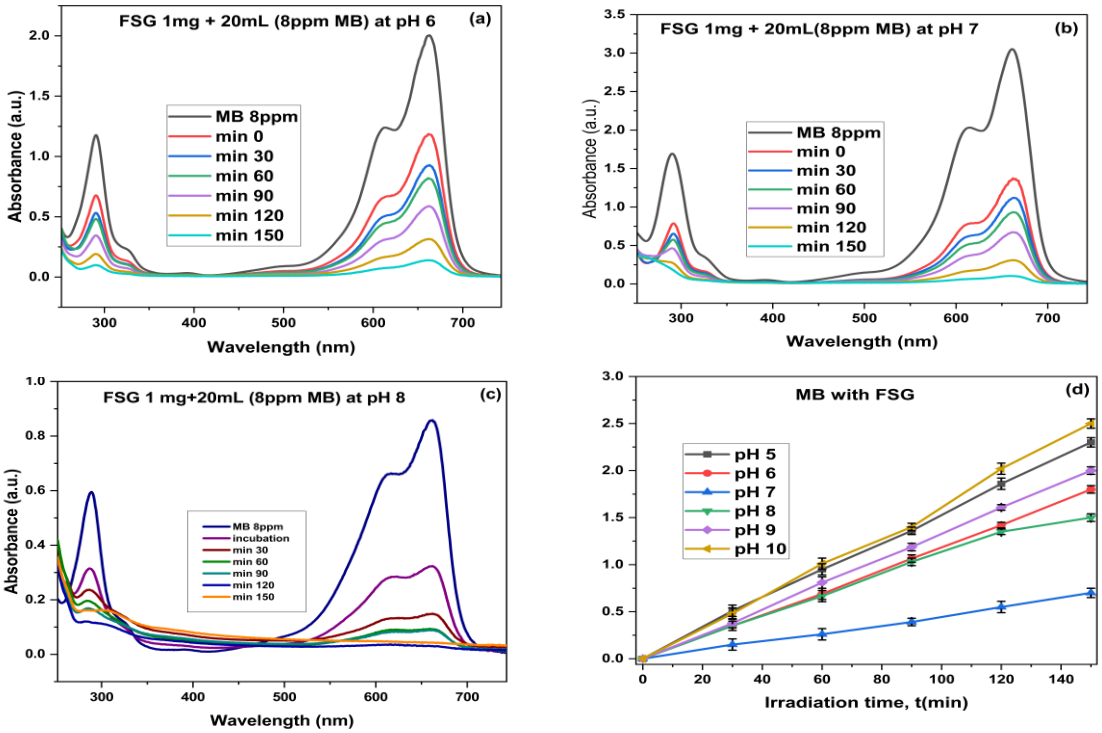

Fig. 3.1.20 (a)-(c) MB degradation at different pH by using 1mg of prepared photocatalyst (d) Kinetics of photodegradation

3.1.14.3 MB and RhB mixture degradation

The ultraviolet-visible spectroscopic spectra of MB and RhB mixture photodecomposition at a range of pH values are displayed in Fig. 3.1.21((a)-(c)). Absorption of both dyes occurred in 150 min, and at pH 7, degradation efficiencies for solutions containing FSG are 82% and 88%, respectively. The FSG surface is more easily absorbed due to the dye's positive charges. However, the MB and RhB mixture breaks down by a mere 1% under LED illumination. The LED-MB-FSG solution stands out with the most significant degradation percentage of around 88% at pH 7 after 150 min of exposure.

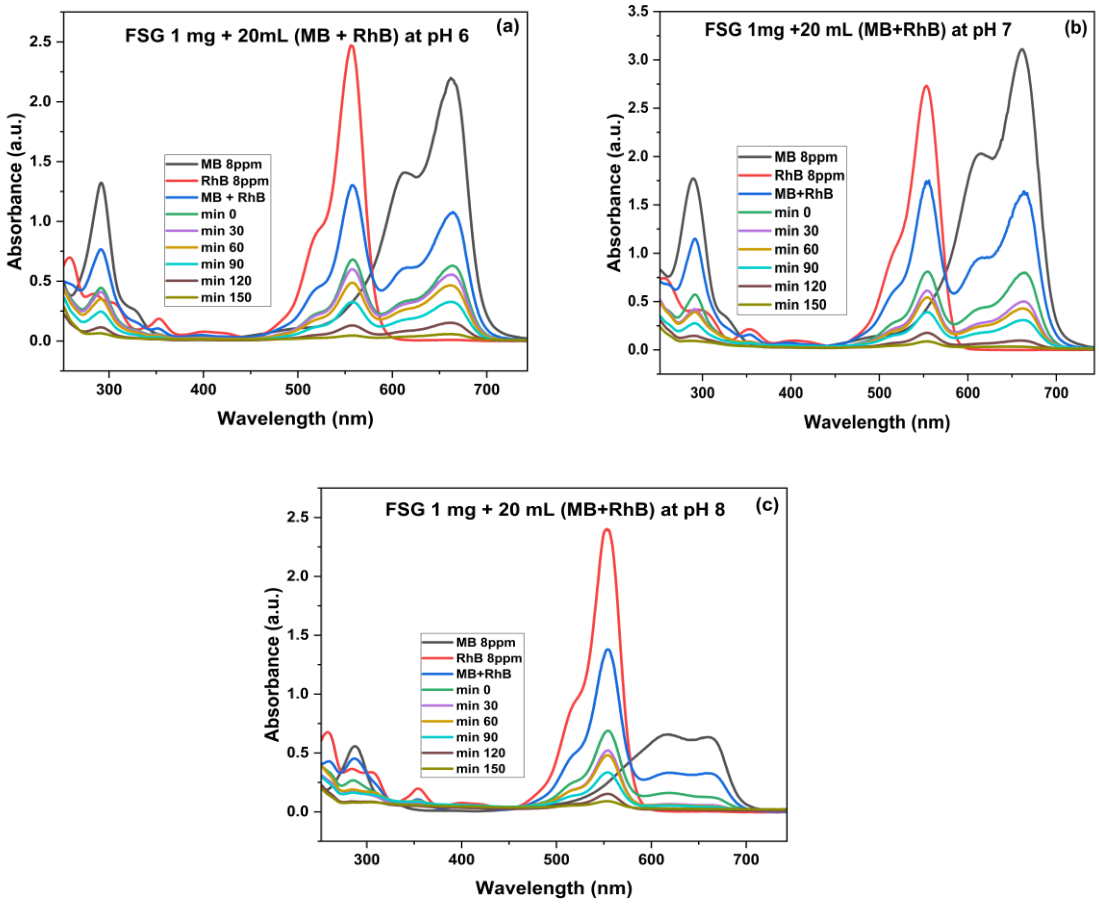

Fig. 3.1.21 ((a)-(c)) MB and RhB mixture, degradation at different pH by using 1 mg of prepared photocatalyst.

3.1.14.4 2,4-DCP and TCAA degradation

Under certain conditions, such as a catalyst concentration of 8 ppm and a contact time of 150 min, UV-visible spectroscopy spectra of the photodecomposition of 2,4-DCP at different pH levels are shown in Fig. 3.1.22((a)-(c)). As seen in Fig. 3.1.22(d)-(e), the natural logarithm of the ratio of initial to current concentrations (ln (C_o/C_t)) is shown as a function of time for 2,4-DCP and TCAA, respectively. Under these conditions, 2,4-DCP degraded at a rate of around 72%, while TCAA degraded at a rate of about 55%. Moreover, over the 150 min reaction period, the mineralization rates for 2,4-DCP varied between 8.14 and 54.78%, whereas for TCAA, the rates varied between 7.14 and 50%. This indicated a significant degradation of 2,4-DCP and TCAA into CO_2 and H_2O as the end products of mineralization. A significant discovery revealed a positive correlation between the mineralization rate and the reaction time, suggesting that a longer reaction time is essential for complete TCAA mineralization.

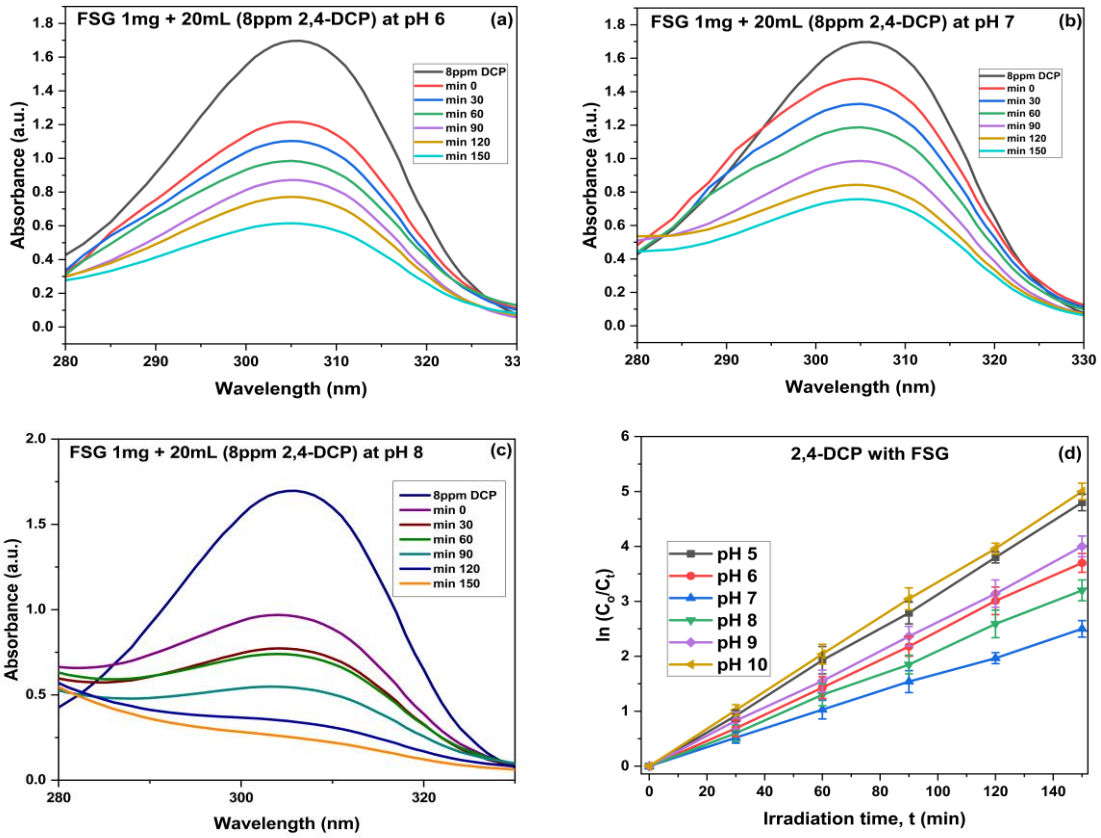

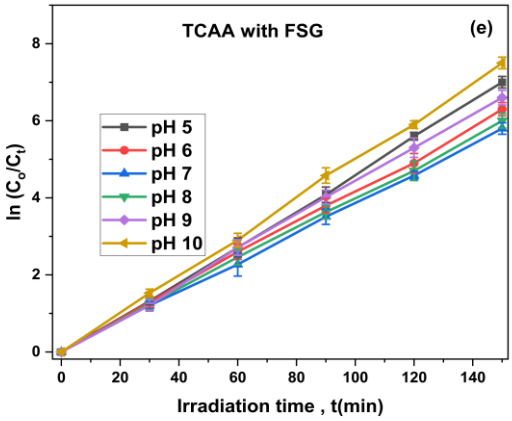

Fig. 3.1.22 (a)-(c) 2,4-DCP degradation efficiency at different pH by using 1mg of prepared photocatalyst (d) Kinetics of photodegradation of 2,4-DCP (e) Kinetics of photodegradation of TCAA.

3.1.15 Comparison

The degradation constants for this solution are shown in Table 3.1.4, which follow the same trend as the photocatalytic activity. Specifically, at pH 7, the degradation constant of the LED-MB-FSG2 sample was larger than that of the LED-RhB-FSG2 sample. In addition, the LED-MB-FSG2 (pH 7) solution deteriorated more rapidly than the LED-RhB-FSG2 solution due to the larger and more complex molecular structure of rhodamine B. Based on the findings, it appeared that the FSG2 was more efficient with 2,4-DCP than that of TCAA in mineralization, which is shown in Fig. 3.1.23.

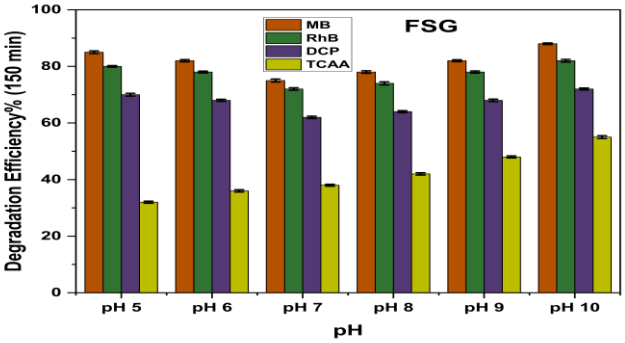

Fig. 3.1.23 Degradation efficiency with FSG2 photocatalyst.

Table 3.1.4 Estimation of rate constant for photodegradation

pH	MB		RhB		DCP		TCA	
	k (min^{-1})	R^2	k (min^{-1})	R^2	k (min^{-1})	R^2	k (min^{-1})	R^2
pH 5	0.0257	0.979	0.0317	0.956	0.0125	0.968	0.0132	0.978
pH 6	0.0225	0.979	0.0286	0.974	0.0095	0.956	0.0109	0.952
pH 7	0.0192	0.981	0.0205	0.962	0.0095	0.978	0.0068	0.954
pH 8	0.0206	0.976	0.0264	0.986	0.0178	0.958	0.0082	0.960
pH 9	0.0236	0.958	0.0308	0.952	0.0108	0.972	0.0128	0.958
pH 10	0.0278	0.962	0.0325	0.958	0.0189	0.968	0.0139	0.972

Given that the R^2 value for the pseudo-first-order model (0.974,0.948, 0.902) is greater than that for the pseudo-second-order model (0.876,0.910,0.864) when MB, 24-DCP and TCAA respectively are treated with FSG under LED light, it indicates that the experimental data aligns more closely with the pseudo-first-order kinetic model. Consequently, it can be inferred that the reaction probably follows pseudo-first-order kinetics. The process concluded with mineralization, resulting in the production of CO_2 and H_2O as the final molecules.

3.1.16 Magnetic Property

Fig. 3.1.24 depicts the magnetic response properties of Fe_3O_4 magnetic nanoparticles and $Fe_3O_4/SnO_2/g\text{-}C_3N_4$ (FSG2) ternary nanocomposite using coercivity magnitudes (MH). All Fe_3O_4 magnetic nanoparticle nanocomposites showed symmetrical hysteresis and saturation magnetization when made in their original state. The saturation magnetization values for Fe_3O_4 (F), Fe_3O_4/SnO_2 (FS), $Fe_3O_4/g\text{-}C_3N_4$ (FG), and $Fe_3O_4/SnO_2/g\text{-}C_3N_4$ were 20.70, 17.2603, 2.3087, and 1.10 emu/g, respectively. The magnetic moment of Fe_3O_4 nanoparticles may decrease as a result of their small particle size [Nurul *et al*., (2014); Ding *et al*., (2006)] and due to a spin configuration, that was not collinear at proximity to the surface. Contrary to solely SnO_2, $g\text{-}C_3N_4$ lacked magnetism due to the presence of a tri-S-triazine unit that could attract Fe_3O_4 components, resulting in a significant decrease in its magnetic properties. When the magnetic nanoparticles form, the saturation magnetization of the

Fe_3O_4/SnO_2 sample decreases compared to pure Fe_3O_4. The uniformly synthesized nanocomposite's magnetic properties effectively eliminated hysteresis, remanence, and coercivity in $Fe_3O_4/SnO_2/g\text{-}C_3N_4$. The saturation magnetization results showed that pure Fe_3O_4 has the highest value, while the $Fe_3O_4/SnO_2/g\text{-}C_3N_4$ composite has a lower value because it contained parts that were not magnetic. The sample exhibited superparamagnetic properties, and the photocatalyst's elevated saturation magnetization facilitated the process of recovery and recycling. This was made possible because an external magnetic field could separate it from the solution.

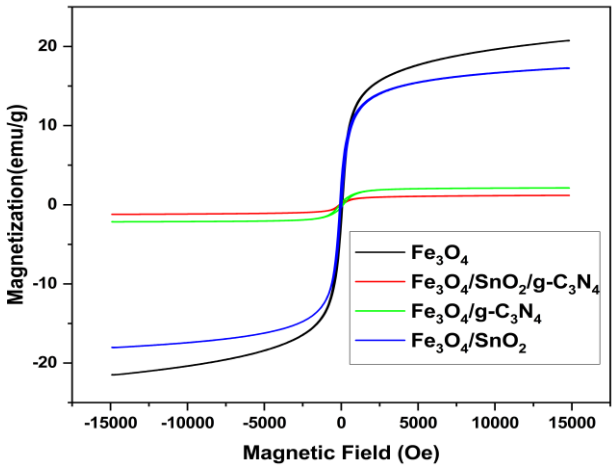

Fig. 3.1.24 VSM of Fe_3O_4, $Fe_3O_4/SnO_2/g\text{-}C_3N_4$ (FSG2), Fe_3O_4 /g-C_3N_4, Fe_3O_4/SnO_2.

3.1.17 Pathway of dyes and pesticides degradation with prepared photocatalyst

We have presented a technique for degrading RhB dye using a nanocomposite photocatalyst, as seen in Fig. 3.1.25. The energy levels of heterojunction conduction bands (CBs) in the $Fe_3O_4/SnO_2/g\text{-}C_3N_4$ system exhibited variation. Electrons undergo migration between the conduction bands of different materials. SnO_2, possessing a reduced conduction band energy, can transfer electrons to g-C_3N_4. The electrons in the conduction band of g-C_3N_4 catalyse the reduction of oxygen and other compounds. The interaction of dyes or pesticides with photoexcited electron-hole pairs in the conduction and valence bands is a complex process that involves different mechanisms. This interaction can lead to the degradation or modification of these molecules, which can have important implications for various industries such as agriculture or textiles. Understanding this process is crucial for developing more

efficient and sustainable approaches to these fields. This enhanced the chemical reaction between the dye and the pre-existing nanocomposite photocatalyst. The nanocomposite photocatalyst's enhanced photocatalytic efficiency stems from its increased absorption of visible light, reduced rate of charge pair recombination, and sustained adsorption of dye or pesticide molecules. Additionally, it can be employed as a photocatalyst due to its efficient degradation of dyes or pesticides. Further, incorporating Fe_3O_4 (magnetite) into nanocomposites enhances material recovery and reuse by adding magnetic properties, allowing easy separation from mixtures with a magnet. This simplifies the recuperation process, making it cost-effective and environmentally friendly. The nanocomposite can be reused multiple times without losing performance, reducing the need for continuous production. After catalytic reactions, it can be magnetically separated and reused with minimal purification, ensuring thorough purification of treated water. Magnetic recovery is simple and labor-efficient, reducing replacement frequency and saving materials and costs. Overall, reusing the nanocomposite promotes sustainability and efficiency in catalytic processes and environmental remediation.

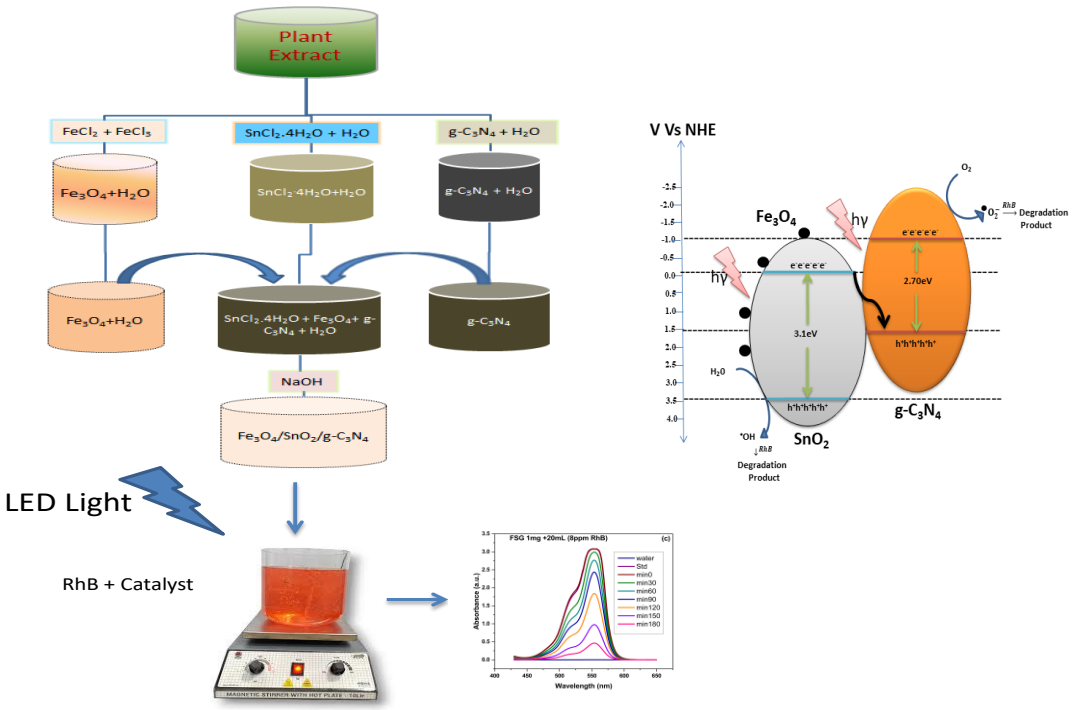

Fig. 3.1.25 Pathway of RhB degradation with prepared photocatalyst.

3.2 Effect of Silver on g-C_3N_4 in Fe_3O_4/Ag-doped g-C_3N_4 ternary nanocomposite for degradation of dyes and pesticides.

The durability and toxicity of organic dyes and pesticides pose a huge environmental threat. Environmental treatment requires photocatalysts that degrade these contaminants. Fe_3O_4/Ag-doped g-C_3N_4 nanocomposite, which contains magnetite, silver, and graphitic carbon nitride.

Silver greatly improves this composite's photocatalytic properties. Silver is a noble metal with exceptional electrical conductivity, antibacterial capabilities, and distinctive optical qualities. Localized surface plasmon resonance (LSPR) nanoparticles improve light absorption. Silver can trap electrons to reduce electron-hole pair recombination in photocatalysis and improve light absorption due to LSPR.

g-C_3N_4 is a polymer made of carbon and nitrogen atoms. It has a 2D layered structure and great thermal and chemical stability. Photocatalytic applications use its visible light absorption and electron-hole pair generation. g-C_3N_4 supports photocatalytic components well due to its stability, wide surface area, and visible light absorption. Silver sinks photogenerated electrons from g-C_3N_4. This lowers electron-hole pair recombination, enhancing photocatalytic charge carriers.

Magnetic Fe_3O_4 readily separates the photocatalyst from the reaction mixture using a magnetic field. Magnetic photocatalysts are a type of photocatalyst that can be separated from a reaction mixture using a magnetic field. These materials combine the photocatalytic properties of a semiconductor with the magnetic properties of materials like iron oxides (e.g., Fe_3O_4), offering several advantages in environmental and chemical applications.

The Fe_3O_4/Ag-doped g-C_3N_4 (FAG3) (5 wt.%) nanocomposites achieved the photodegradation of the RhB dye, as illustrated in Fig. 3.2.1. The intensity of absorption was assessed to assess the photocatalytic activity of the as-prepared ternary nanocomposite in degrading the RhB (Sigma Aldrich) dye in water.

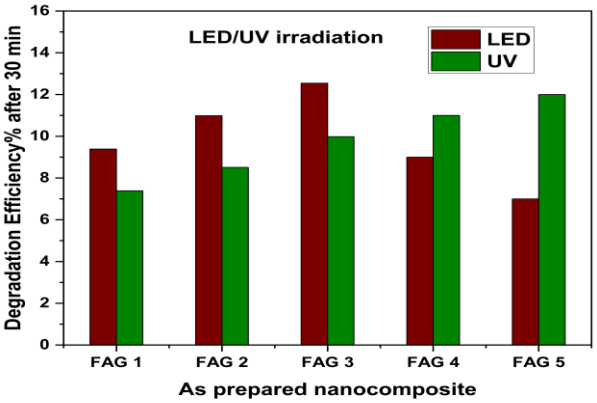

Fig. 3.2.1 The efficiency of the catalyst developed is enhanced by exposure to UV and LED light, leading to increased deterioration.

According to these experiments, the most effective ternary nanocomposite for degrading RhB under LED light having 5 wt.%. For this reason, we studied further on Fe_3O_4/Ag doped g-C_3N_4 (FAG3), which has Ag (5 wt.%).

3.2.1 X-ray Diffraction

Fig. 3.2.2 exhibited powder X-ray diffraction (XRD) patterns of the produced Fe_3O_4, g-C_3N_4 nanoparticles, and FAG3 nanocomposites from the XRD data sample crystallite size and structure using the Scherrer equation. Nanocomposite FAG3 produced a distinct diffraction pattern from pure Fe_3O_4 and g-C_3N_4.

Fe_3O_4 has a cubic inverse spinel structure with 602.101 cell volumes and lattice parameters of 8.246 Å. Diffraction peaks at 2Ɵ=29.101°, 34.983°, 36.164°, 44.112°, and 61.04° correlated to miller indices (220), (311), (222), (400), and (440), which matched this design with JCPDS no. 82-1533.

When g-C_3N_4 was in its hexagonal crystalline form, as described in JCPDS No. 87-1526, diffraction peaks at 2Ɵ=27.444° corresponded to *hkl* planes (002), lattice parameters of a=b=7.134Å, c=1.994Å, and cell volume of 93.112. The diffraction peaks observed at 2θ=38.304° in the cubic crystalline phase of Ag (JCPDS no. 87-0720) can be attributed to the *hkl* planes of 200. The lattice parameters for this phase were determined to be a=b=c=4.754Å, with a corresponding cell volume of 72.294. FAG3 diffraction patterns showed a cubic structure of Fe_3O_4, whereas Ag and g-C_3N_4

had cubic and hexagonal structures, respectively. None of the impurity peaks had phases. Ag and Fe_3O_4 in the matrix did not alter g-C_3N_4's hexagonal structure.

We used the Debye-Scherrer formula (as given in equation 3.1 under section 3.1.1) for the diffraction of Fe_3O_4 (311), g-C_3N_4 (002), and Ag (200) to determine the crystallite size of FAG3 ternary nanocomposites. Table 3.2.1 displays the sizes of the crystallites based on the full width at half maximum (FWHM) of the sharp peaks. Several factors contribute to the larger grain size change in Fe_3O_4/Ag-doped g-C_3N_4 (FAG3) composites compared to single grains of Fe_3O_4.

This variation depends on the specifics of the synthesis method and the composite's makeup. We have advanced several hypotheses to explain the observed change. Composites underwent a transformation in their overall composition upon the incorporation of Ag-doped g-C_3N_4 that could influence crystallisation and subsequent grain development. The interfaces between components of the composite, including Fe_3O_4, Ag-doped g-C_3N_4 have the potential to generate novel interactions. These interactions may affect the nucleation and development of grains, resulting in a different grain size compared to solo Fe_3O_4.

Table 3.2.1. Demonstrates the volume, lattice characteristics, and average particle size of the prepared Fe_3O_4, Fe_3O_4/g-C_3N_4, Fe_3O_4/(5 wt.%) Ag-doped g-C_3N_4 (FAG3) nanomaterials.

As-prepared photocatalyst	Crystallite Size(nm)	Lattice Parameters			Cell volume
		a (Å)	b (Å)	c (Å)	
Fe_3O_4	26.234	8.246	8.246	8.246	602.101
Fe_3O_4/g-C_3N_4 (FG)	46.241 46.268	8.415 7.134	8.415 7.134	8.415 1.994	576.212 93.112
Fe_3O_4/(5 wt.%) Ag-doped C_3N_4 (FAG3)	73.268 50.293 63.478	8.408 4.754 6.281	8.408 4.754 6.281	8.408 4.754 2.369	594.440 72.294 80.961

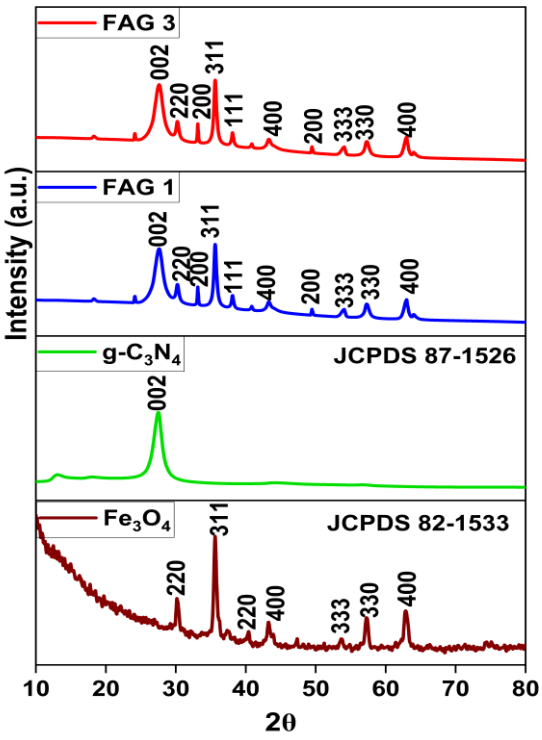

Fig. 3.2.2 Powder XRD of Fe_3O_4, g-C_3N_4 and Fe_3O_4/Ag-g-C_3N_4 (FAG1 and FAG3)

3.2.2 FT-IR studies

The FT-IR spectra of Fe_3O_4, g-C_3N_4, $AgNO_3$, and FAG3 nanocomposites are displayed in Fig. 3.2.3 (a)-(d), with each spectrum labelled as Fe_3O_4, g-C_3N_4, $AgNO_3$, and Fe_3O_4/Ag-g-C_3N_4 (FAG3), respectively. The significant absorption peaks seen in the 400 to 524 cm^{-1} spectral range were due to metal-oxygen (M-O) bond stretching. The g-C_3N_4 nanoparticles displayed characteristic peak frequencies ranging from 800 to 1200 cm^{-1}, while the 432 and 524 cm^{-1} peaks explained the Fe-O bonds in the Fe_3O_4 nanomaterial. The silver (Ag) peaks were observed at wavenumbers of 786 and 1255 cm^{-1}. The presence of hydroxyl radical groups in Fe_3O_4, which react with carboxylate ions in plant extract, was confirmed by the absorption of COO-Fe bonds at 1103 and 1357 cm^{-1}. The high absorption peaks at 1219 and 1319 cm^{-1} in g-C_3N_4 indicate the presence of different vibrations from trigonal C-N (-C)-C and bridging C-NH-C units, respectively, as observed about the chemical formula. Additionally, the presence of the N-H coupling can be determined by examining the peak at 1543 cm^{-1}. The broad

peak bands 1627–1635 cm^{-1} and 3355–3375 cm^{-1} are used to measure the water molecules' O-H bending and stretching. Results showed that the g-C_3N_4 matrix's nanomaterial characteristics were unaffected by the addition of Fe_3O_4 and Ag.

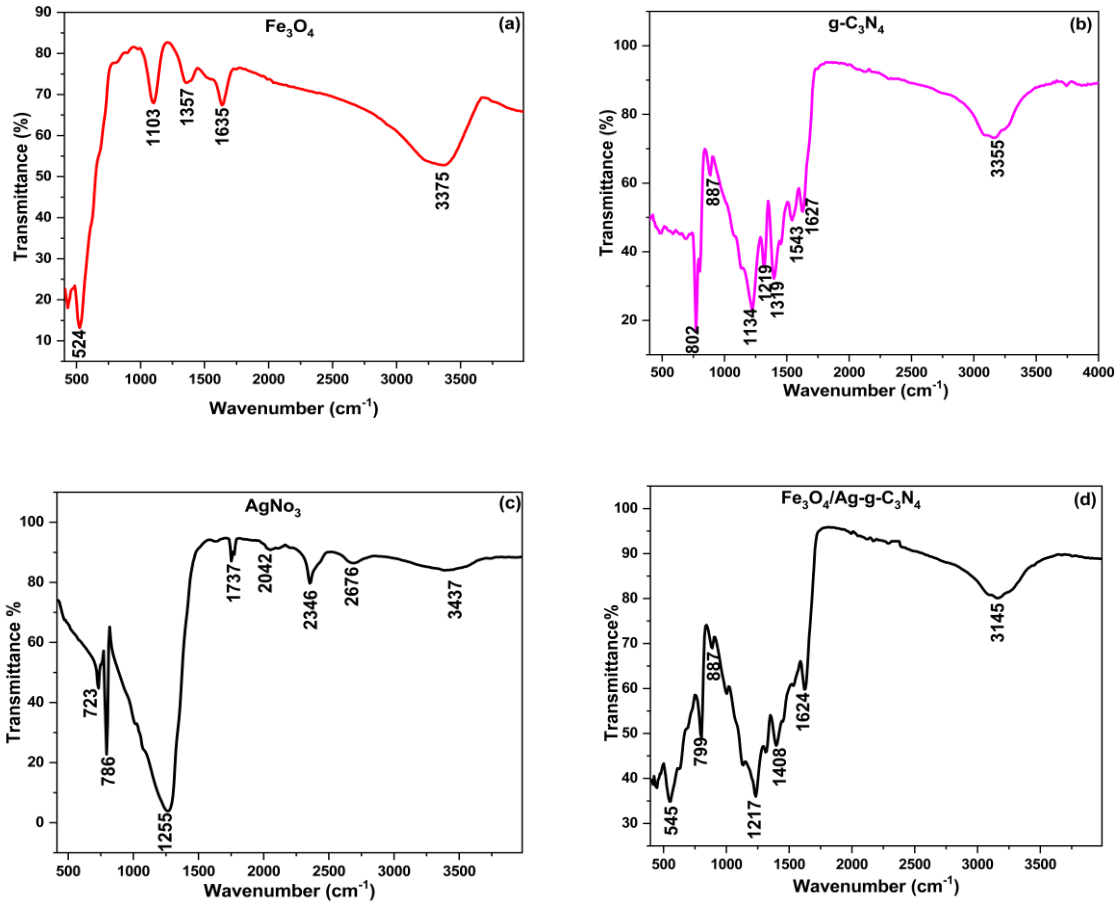

Fig. 3.2.3 FT-IR of (a) Fe_3O_4 (b) g-C_3N_4 (c) $AgNO_3$ (d) Fe_3O_4/Ag-g-C_3N_4 (FAG3)

3.2.3 UV-visible Spectroscopy

UV-Visible spectra from Thermo Scientific UV-Visible spectroscopy have been used to investigate whether the intended substance(s) were produced or not, and this analysis approximated the band-gap energy (E_g) of the prepared nanocomposite. Between 200 and 1000 nm, baseline correction was performed using double-distilled water. In order to estimate band-gap energies, the Tauc plot approach was used using data from the UV-visible spectra [Abdel-Monem *et al.*, (2017)], using the same equation (3.2), as explained in Section 3.1.9.It is estimated that the as-prepared

nanocomposite (FAG3) is a band gap energy of 3.42 eV, which has lower than the band gap energy of 3.64 eV for Ag and 2.80 eV for g-C_3N_4 as shown in Fig. 3.2.4(a)-(b).

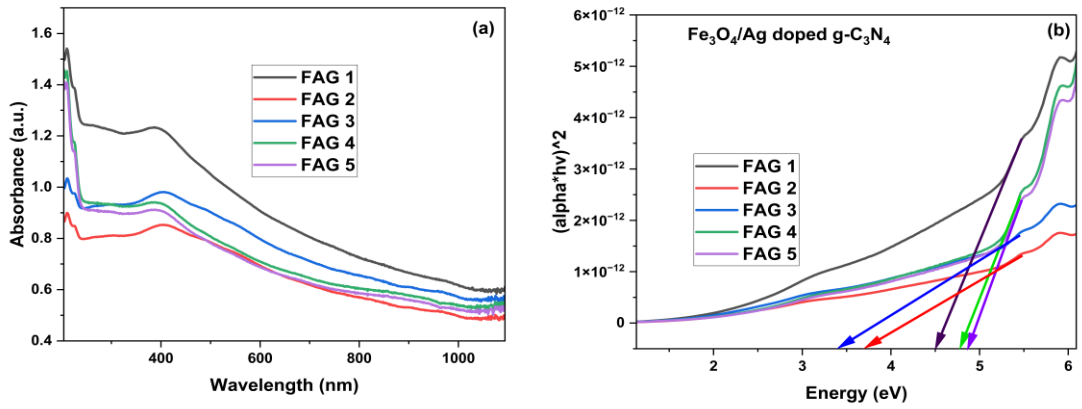

Fig. 3.2.4 (a) UV-visible spectroscopy (b) The determination of the band gap energy for Fe_3O_4/Ag-doped g-C_3N_4.

A method for separating photo-induced electrons and holes in FG and FAG was determined using the valence band spectra. In order to assess the charge transfer mechanism, this experiment aimed to synchronise the electric potentials at the E_{VB} and E_{CB} boundaries. To evaluate the E_{CB} and E_{VB}'s potential energy levels, the relationship suggested by (Hunge *et al.*, (2023) was used [Hunge *et al.*, (2023)].

$$E_{VB} = \chi - E_e + 0.5E_g \quad (3.10)$$

$$E_{CB} = E_{VB} - E_g \quad (3.11)$$

The electronegativity coefficient of g-C_3N_4 is 4.64 eV; Eg is the energy of the semiconductor's band gap; and "Ee" stands for the energy of unbound electrons on the hydrogen scale, which is 4.9 eV. When measuring Ag-doped g-C_3N_4 at 1, 3, 5, 7, and 9 wt.% concentrations, the E_{VB} values were 2.18, 1.79, 1.64, 2.32, and 2.37 eV relative to each concentration. The E_{CB} values for the sets of identical samples were -2.30, -1.91, -1.76, -2.44, and -2.49 eV, respectively. Exposure to LED light causes the excited electron to readily transition from the E_{CB} of g-C_3N_4 to the E_{CB} of Ag.

3.2.4 Scanning electron microscope (SEM) and Tanning electron Microscope (TEM) analysis.

The generated nanocomposite was examined using scanning electron microscopy (SEM). The resulting image is shown in Fig. 3.2.5(a), and the image also shows that the particles were evenly dispersed. The average size of the nanocomposite was calculated to be 22.54 nm, which is shown in Fig. 3.2.5(b).

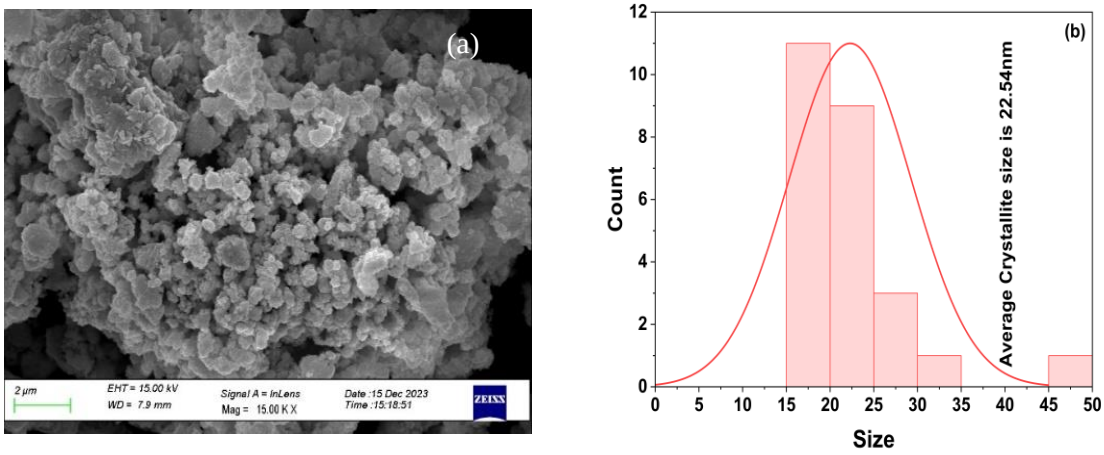

Fig. 3.2.5 (a) SEM of Fe_3O_4/Ag doped g-C_3N_4 (FAG3) (b) Average size calculation

TEM imaging measured nanoparticles, nanocomposite sizes, and morphologies, Fig. 3.2.6(a) showed the FAG3 magnetic nanoparticles through transmission electron microscopy, which revealed that they contained Fe_3O_4 and Ag nanoparticles with a mean diameter of 45–65 nm in the g-C_3N_4 matrix, which was correlated with the XRD report. The SAED pattern confirmed the nanocrystalline and tetragonal phases with diffuse patches and rings. Fe_3O_4, Fe_3O_4/g-C_3N_4, and FAG3 showed typical diameters of 26–74, 45–64, and 46–75 nm, respectively. The powder XRD study determined that the grain size was approximately within these numerical values.

Fig. 3.2.6(b) displayed an HR-TEM image of FAG3, and it showed that Fe_3O_4 nanoparticles enveloped Ag nanoparticles and dispersed in the g-C_3N_4 matrix, creating heterojunctions between particles of various components. Fe_3O_4 nanoparticles have (311) planes, g-C_3N_4 have (002) planes, and the lattice fringe crystal of Ag nanoparticle formation prefers (200) planes, as shown in Fig. 3.2.6(c). The

heterojunction formed by Ag and g-C_3N_4 has distinct energy levels. With this heterojunction, electrons and holes can migrate and separate. In addition to increasing photocatalysis efficiency, this heterojunction configuration stops electron-hole pair recombination. Overall, photocatalytic reactions involved the effectively transferring of electrons and holes between g-C_3N_4 and Ag. This composite material, when exposed to light, possesses a photocatalytic potential that enables water purification and the destruction of contaminants through the generation, separation, and participation in redox processes of electron-hole pairs.

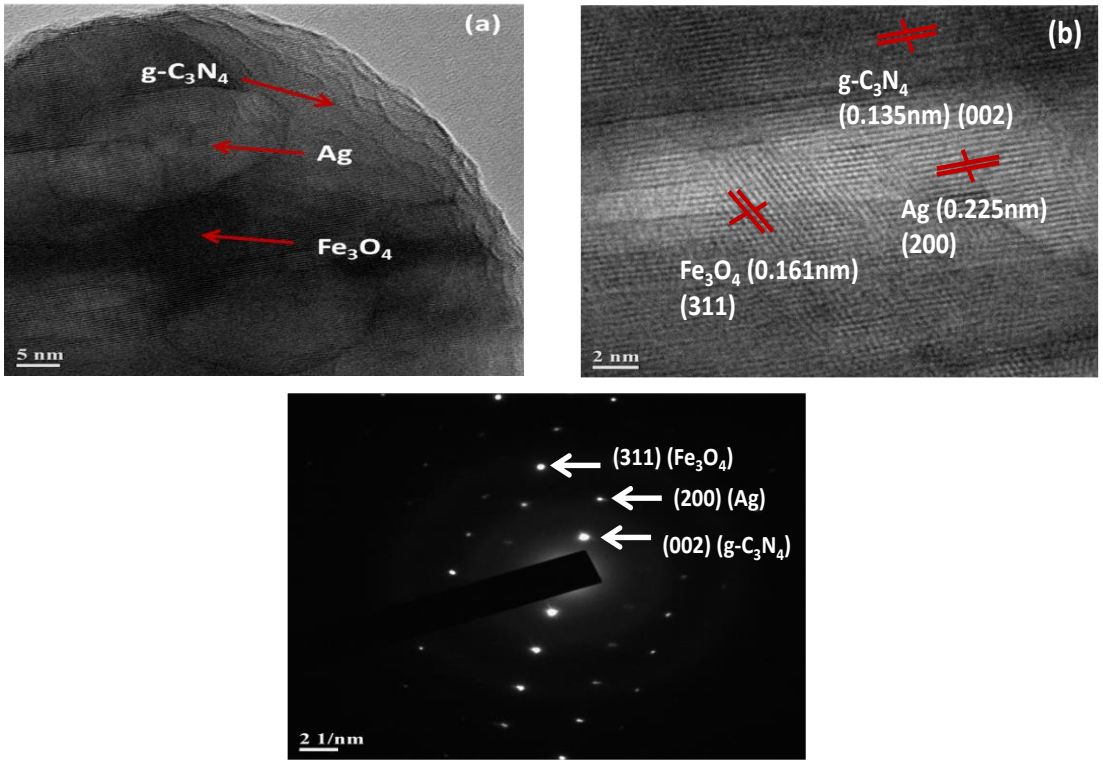

Fig. 3.2.6 Fe_3O_4/Ag-doped g-C_3N_4 (FAG3) image (a) TEM, (b) HR-TEM and (c) SAED.

3.2.5 XPS studies

The compositional components of the samples were verified using an XPS analysis of the spectra in Fig. 3.2.7. An investigation into the surface chemistry was carried out with the use of X-ray photoelectron spectroscopy (XPS) to determine the to determine the makeup of the Fe_3O_4/Ag-doped g-C_3N_4 magnetic nanocomposite that was made. Carbon, iron, silver, nitrogen, and oxygen were detected using XPS, as

depicted in Fig. 3.2.7(a). These revealed that Fe_3O_4, Ag, and g-C_3N_4 comprised the nanocomposite. Fig. 3.2.7(b) depicted that Ag 3d was studied with high-resolution XPS, and the binding energies connected with the Ag $3d_{5/2}$ and Ag $3d_{3/2}$ orbitals were responsible for the two separate peaks at 367.5 and 373.6 eV of Ag^0, respectively [Xu *et al*., (2006)].

Two distinct peaks in the C1s spectra were seen at 286.2 and 289.4 eV, which are shown in Fig. 3.2.7(c). Because of the sp^2 C-C interaction, extra carbon was added to the g-C_3N_4 molecule, which gave it a measured energy of 286.2 eV. The Fe $2p_{3/2}$ peak with excellent resolution may be separated into three separate peaks at binding energies of around 711, 717, and 724 eV, as shown in Fig. 3.2.7(d). The peaks observed at 711 eV and 717 eV can be attributed to the presence of Fe^{2+} and Fe^{3+} ions, respectively, at the octahedral sites of the spinel Fe_3O_4. On the other hand, the peak at 724 eV corresponds to Fe^{3+} ions located at the tetrahedral sites [Poulin *et al*., (2023)]. The peak at an energy level of 289.4 eV was caused by the interaction between nitrogen, carbon, and nitrogen atoms in the hexagonal ring structure of g-C_3N_4.

In particular, the N-atom held at 396.23 eV within the carbon-nitrogen-carbon ring was significant in the N1s region, as shown in Fig. 3.2.7(e). Sheng *et al.* found this especially true for tertiary N-bonded groups [Sheng *et al*., (2014)]. The O1s spectral peak at 530.34 eV was caused by lattice oxygen in Fe_3O_4 as shown in Fig. 3.2.7(f) [Brojendro Singh Shagolsem, Nongmaithem Mohondas Singh, 2024].

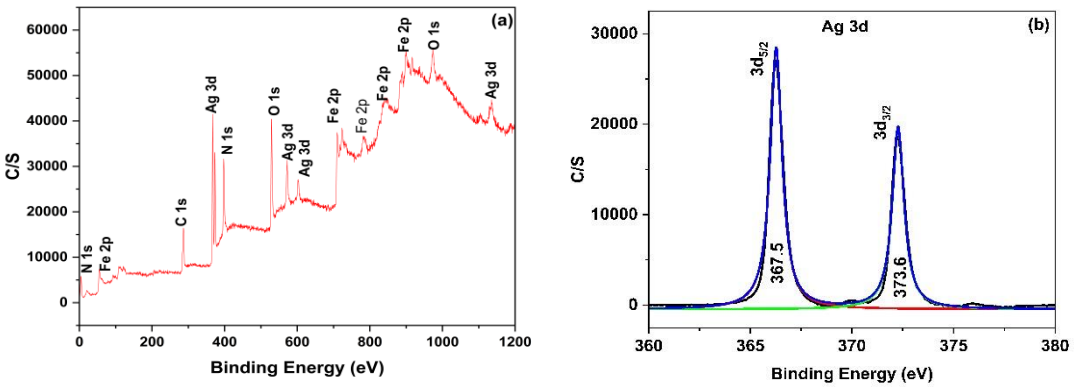

.

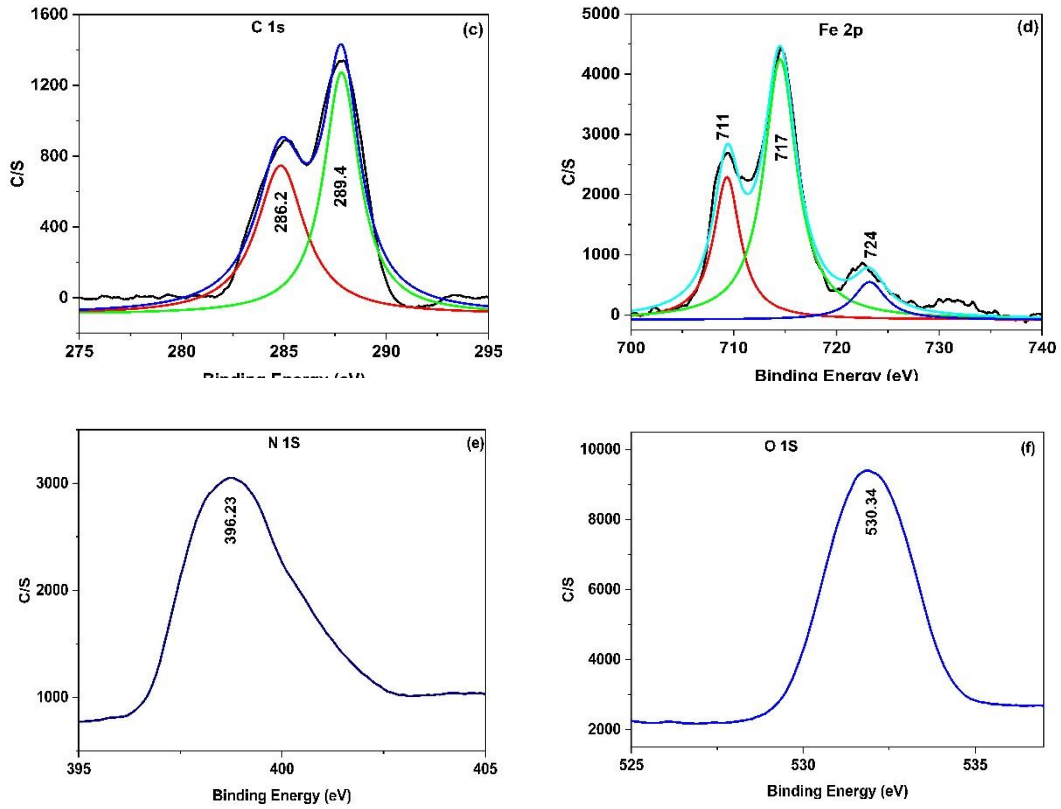

Fig. 3.2.7 XPS of (a) Fe_3O_4/Ag doped g-C_3N_4 and (b) Ag 3d (c) C 1s (d) Fe 2p (e) N 1s (f) O 1s in Fe_3O_4/Ag doped g-C_3N_4 (FAG3).

3.2.6 BET surface analysis

The surface area and pore size of the FAG3 nanocomposite were determined using nitrogen adsorption-desorption experiments, depicted in Fig. 3.2.8, and the isotherm shown in Figure is classified as type IV according to the IUPAC system. This form of isotherm is typical of materials with pores that allow gases to pass through them [Qi *et al*., (2009)]. The generated Fe_3O_4/g-C_3N_4 and FAG3 had cumulative mesopore volumes of 0.032 and 0.042 cm^3/g with BJH pore diameters of 2.446 and 2.923 nm, respectively, which are given in Table 3.2.2. The enhanced surface area and mesoporous properties of the FAG3 ternary nanocomposite facilitated photodegradation. Therefore, the addition of Ag nanoparticles to the top of the 2D g-C_3N_4 support matrix resulted in an improved photodegradation process. This improvement can be attributed to the enhanced surface area and mesoporous properties

of the FAG3 ternary nanocomposite, as discussed earlier. The results of the nitrogen adsorption-desorption experiments further support this claim, showing that the FAG3 nanocomposite has a higher cumulative mesopore volume and larger BJH pore diameter than the Fe_3O_4/g-C_3N_4 nanocomposite.

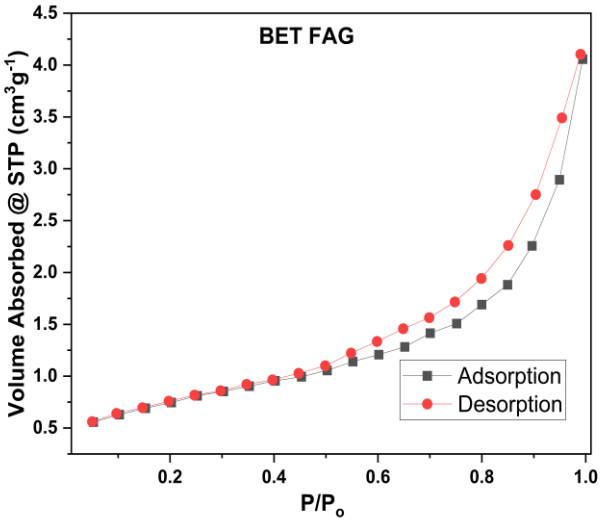

Fig. 3.2.8 Brunauer-Emmett-Teller (BET) for the compound Fe_3O_4/Ag-g-C_3N_4 (FAG3).

Table 3.2.2 gives information about the surface areas, volumes, and diameters of the pores in the Fe_3O_4/g-C_3N_4 and Fe_3O_4/Ag-g-C_3N_4 (FAG3).

As-prepared nanomaterials	S_{BET} (m^2/g)	Pore Volume (cm^3/g)	Pore Diameter (nm)
Fe_3O_4/g-C_3N_4	10.957	0.032	2.446
FAG3	13.857	0.042	2.923

3.2.7 Photoluminescence analysis.

The application of photoluminescence measurements to understand the rate of separation and the length of photoexcited charge pairs is depicted in Fig. 3.2.9. By utilising a light source with a wavelength of 375 nm excitation, it was feasible to get the photoluminescence spectra of g-C_3N_4, Fe_3O_4/g-C_3N_4, and Fe_3O_4/Ag-doped g-

C_3N_4. A wide variety of wavelengths were displayed by the emission spectra of g-C_3N_4, notably from 400 to 550nm, and these wavelengths were readily apparent. Compared with g-C_3N_4, the photoluminescence (PL) intensity of composites made of Fe_3O_4 and Ag-doped g-C_3N_4 was much lower. According to Premjit *et al.* and Ramanada *et al.*, the study revealed that a reduction in the maximum intensity of photoluminescence (PL) results in a slowdown in the recombination of charge pairs obtained through photoexcitation [Premjit *et al*., (2020); Ramananda *et al*., (2022)]. Therefore, incorporation of silver into Fe_3O_4/g-C_3N_4 composites results in a considerable decrease in the e^-/h^+ charge-recombination rate. This was because of the strong attraction between silver and the surface of g-C_3N_4. Consequently, due to the due increased separation efficiency of photoexcited charge pairs, the photocatalytic system of Fe_3O_4/Ag-doped g-C_3N_4 experiences a greater involvement of electrons (e) and holes (h^+).

In comparison to g-C_3N_4, the FAG3 nanocomposite exhibited the lowest PL intensity; this was attributed to the nanocomposite's competence in efficiently isolating charges and decreasing electron-hole recombination processes. Ag's capture of the electrons created by g-C_3N_4 when exposed to light was crucial for improving the separation of charges. This improvement in the light transmittance of the FAG3 system was one of the factors that led to the strengthened capacity of the system, such that light in the visible spectrum can be transmitted. The synthesized nanocomposite's photoluminescence (PL) light confirmed the successful separation of electron and hole pairs.

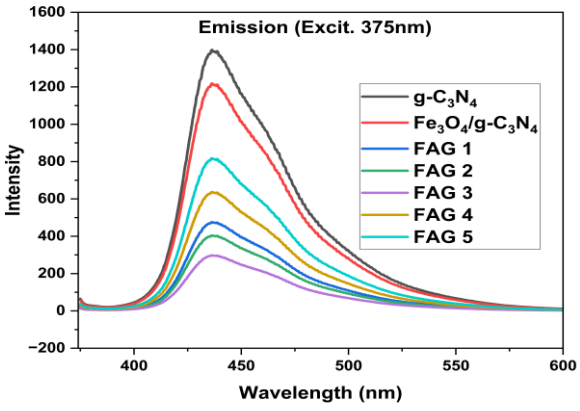

Fig. 3.2.9 PL of g-C_3N_4, Fe_3O_4/g-C_3N_4, Fe_3O_4/Ag doped g-C_3N_4.

3.2.8 Radical studies

The photocatalytic activity of many scavengers was assessed by exposing them to visible light to determine the reactive radicals accountable for the degradation of RhB using a FAG3 nanocomposite. Fig. 3.2.10(a) illustrated incorporating of scavengers and without scavengers (No S) into the photocatalytic process to neutralise the reactive radicals. This variation in scavengers resulted in a change in the C_t/C_o of the RhB dye. Scavengers like isopropyl alcohol (IPA), benzoquinone (BQ) [Bhuvaneswari *et al*., (2020)], benzoic acid (BA) [Prakash *et al*., (2016)], and ethylene diamine tetraacetic acid disodium (EDTA) [Keerthana *et al*., (2021)] were used in the catalytic process to catch superoxide radical ($\dot{O}_2^-$), holes (h^+), and hydroxyl radical ($\dot{O}H$). Fig. 3.2.10(b) showed how various scavengers affect FAG3's radiation efficiency. The degradation of RhB dye decreased from 64 to 57% and 62% when IPA and BA were present as scavengers, respectively. The data on degradation efficiency indicated that hydroxyl radicals play a crucial role in decomposing the RhB dye into water and carbon dioxide. We observed a slight degradation efficiency alteration when EDTA and BQ were added to the reaction system. Visual irradiation triggered the catalytic process of RhB, primarily engaging superoxide radicals and holes as the principal reactive species. The results indicated that FAG3 was capable of effectively expanding the LED light absorption range into the visible region due to its ability to degrade RhB dye.

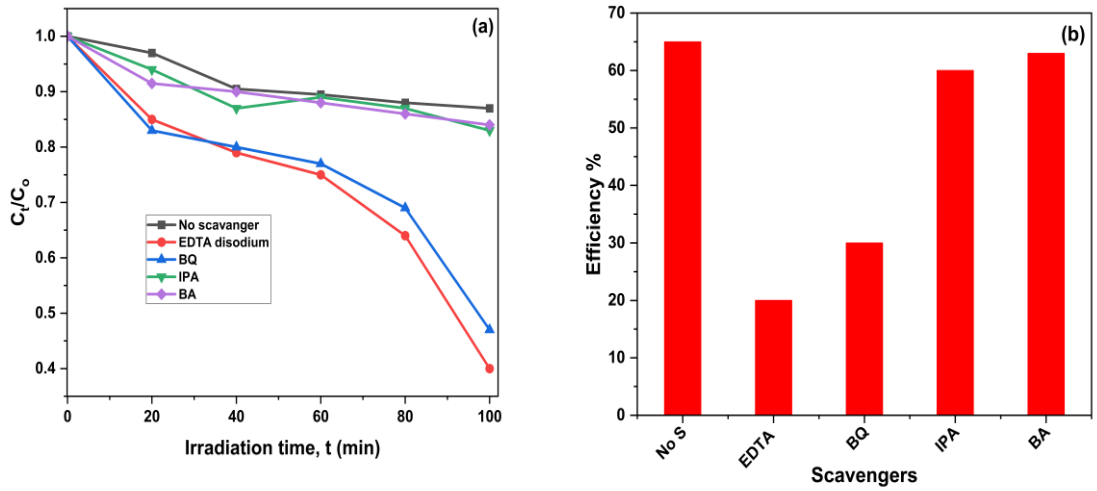

Fig. 3.2.10(a) C_t/C_o Vs Irradiation time (b) Efficiency of various Scavengers.

3.2.9 EPR studies

An EPR spectroscopy investigation determined the presence of individual captured electrons carrying oxygen vacancies. The EPR measurement revealed the presence of oxygen vacancy defects in the g-C_3N_4 system and provided a better understanding of these defects. The studies conducted by Kumar *et al.,* (2018) and Shi *et al.,* (2014) unequivocally showed that the maximum intensity of the Electron Paramagnetic Resonance (EPR) was closely correlated with the quantity of oxygen vacancies present in the nanocomposite system [Kumar *et al.,* (2018); Shi *et al.,* (2014)]. According to Kumar *et al.,* we can determine the g-value using the following relation.

The equation $g = {h\vartheta}/{\mu_B B}$ (3.12)

The electron's g factor, the Bohr magneton, the resonance frequency, and the electromagnetic pulse resonance's (EPR) resonance field are all represented by the variables μ_B, $h\vartheta$, and B, respectively. Even at room temperature, FAG3 showed EPR resonances at 2.258 mT, according to the results of the present study (Fig. 3.2.11). The high-intensity peak seen in the FAG3 nanocomposite was due, in part, to the presence of several oxygen vacancies.

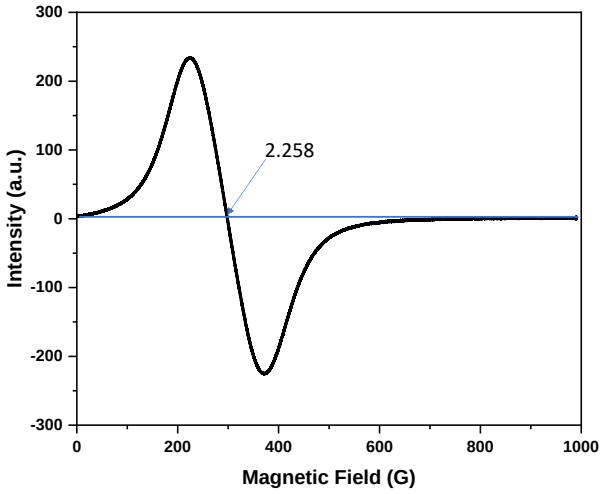

Fig. 3.2.11 Analysis of Fe_3O_4/Ag doped g-C_3N_4 (FAG3) through EPR

3.2.10 Photocatalytic Studies

The degradation of MB, RhB, 2,4-DCP, and TCAA identified the optimal catalysts among the nanocomposite catalysts consisting of Fe_3O_4/g-C_3N_4 and FAG3. The equilibrium between adsorption and desorption was assessed by exposing 20 mL of contaminated water (containing an aqueous dye or pesticide solution) to a nanocomposite photocatalyst at a concentration of 1mg for 30 min in the absence of light. The degree of degradation was evaluated by capturing spectra using UV-visible spectroscopy for RhB, MB, and 2,4-DCP, but not TCAA, by using HPLC. The dye or pesticide absorption intensity decreased as the irradiation period increased from 0 to 150 min, with measurements taken every half an hour. This suggested that the dye decomposes on the surface of the created magnetic nanocomposite photocatalyst. Visual light is used to stimulate valence band electrons that have gathered in the narrow band of the g-C_3N_4 nanocomposite. Due to the closure of the conduction bands of Ag and g-C_3N_4, the electrons were transferred to the conduction band of Ag. As a result, the reverse reaction of the photogenerated charge carriers was delayed. To determine the breakdown of RhB, the initial dye concentration (C_o) was divided by the final dye concentration (C_t) [Madkour *et al.,* (2016)]. The majority of photocatalytic redox reactions took place on the surfaces of catalysts. Specifically, the characteristics of the surfaces influenced the efficiency of the catalysts. The efficacy of dye or pesticide breakdown was determined using the formula mentioned in equation 3.3 under Section 3.1.9.

The Z-scheme arises from the transfer of electrons from the valence band to the conduction band upon light absorption by the photocatalyst. The active sites on the catalyst facilitated the efficient adsorption of dye or pesticide molecules, forming a chemical bond. When oxygen molecules (O_2) came into contact with the surface of the photocatalyst, the electrons in the conduction band interacted, leading to redox reactions and the formation of superoxide radicals ($\dot{O}_2^-$) as shown in eqn. no 3.5 under the section 3.1.9

The degradation of dyes or pesticides occurs due to the generation of hydroxyl and superoxide radicals ($\dot{O}H$ and $\dot{O}_2^-$) that takes place during the redox reaction. Using

a photocatalyst, producing these highly reactive entities through the oxidation of contaminant molecules was possible. They undergo degradation, resulting in a reduction in size and a decrease in toxicity. The desorption and release of the byproducts of degraded contaminants, which were generated by the photocatalyst, were achievable. Non-toxic compounds can trigger other reactions by utilizing the resulting substances. Substituting light sources were introduced to reinstate the photocatalyst's participation in specific degradation reactions. The photocatalyst played a crucial role in generating reactive species such as hydroxyl radicals ($\dot{O}H$) and superoxide radicals ($\dot{O}_2^-$), among others [Lallianmawii, N. Mohondas Singh, (2023)], which were necessary for the decomposition of dye molecules. Under the influence of visible light emitted by an LED, two hydroxyl radicals ($\dot{O}H$) produced from hydrogen peroxide break down pesticides or dyes. The oxidant $\dot{O}H$ showed efficacy against organic contaminants, while H_2O_2 decomposed the colour.

$$
\begin{aligned}
g-C_3N_4(e^- + h^+)/Ag(e^- + h^+) &\rightarrow g-C_3N_4(h^+ + h^+)/Ag(e^- + e^-) \\
h^+ + OH^- &\rightarrow OH \text{ (Oxidation)} \\
e^- + O_2 &\rightarrow \dot{O}_2^- \text{ (Reduction)} \\
H_2O + \dot{O}_2^- &\rightarrow O\dot{O}H + OH^- \\
2O\dot{O}H &\rightarrow \dot{O}_2^- + H_2O_2 \\
H_2O_2 + \dot{O}_2^- &\rightarrow \dot{O}H + OH^- + O_2 \\
H_2O_2 + e^- &\rightarrow \dot{O}H + OH^- \\
Fe^{3+} + H_2O_2 &\rightarrow Fe^{2+} + O\dot{O}H + H^+ \\
Fe^{2+} + H_2O_2 &\rightarrow Fe^{3+} + OH^- + \dot{O}H \\
\dot{O}H + \text{dyes/pesticides} &\rightarrow \text{Decomposition products}
\end{aligned}
\quad \Big\} \quad (3.13)
$$

3.2.10.1 RhB photodegradation

The photocatalytic removal of the Rhodamine B (RhB) dye by FG and FAG3 nanocomposite in the presence of LED light is demonstrated in Fig. 3.2.12(a) and (b), which illustrated the time-dependent optical absorption spectra of RhB's LED light, respectively. The nanocomposites' hydroxyl radicals expedite N-de-ethylation and chromophore alteration during RhB degradation, which opens molecular rings, creates smaller RhB molecules, and generates oxidation products by inducing bond cleavage. The final phase in the process, which yielded CO_2 and H_2O, is the mineralization of the smaller molecules, as explained in the previous section

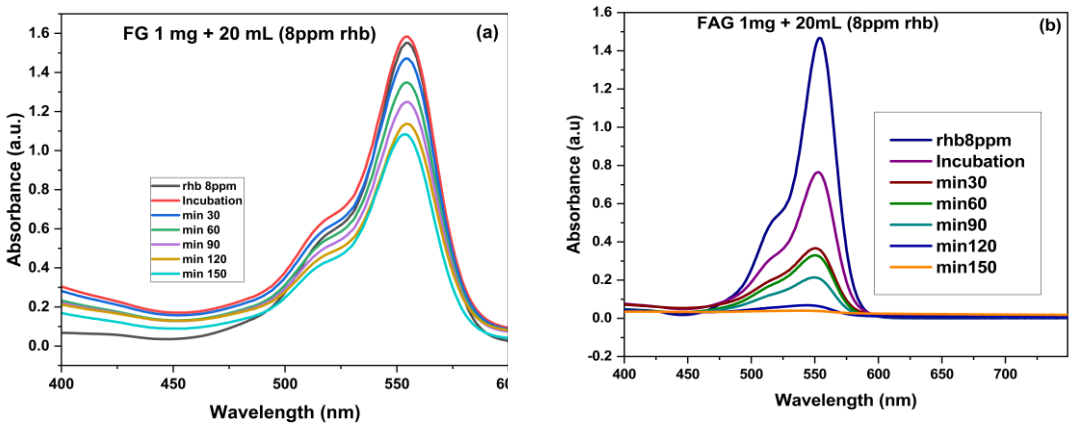

Fig. 3.2.12 RhB decomposition (a) Fe_3O_4/g-C_3N_4 (FG) (b) Fe_3O_4/Ag-g-C_3N_4 (FAG3).

3.2.11 Dosage effect

Choosing an appropriate catalyst for the dye solution decomposition was of the utmost importance. Fig. 3.2.13(a) illustrated the variation in dosage from 1 to 11mg in a 20 mL solution containing 8 ppm of RhB at a pH of 7.00±0.38. We examined various systems to assess their adsorption-desorption performance at varied catalyst dosages before activating the light. It was found that extra photocatalysts made there be more active sites, and more RhB could be absorbed before the photocatalytic process. This implies that employing more catalysts would enhance the degradation process [Brojendro Singh Shagolsem, N. Mohondas Singh, (2024)]. Increased concentrations of photocatalysts resulted in the deflection of light and decreased penetration of irradiation, hence restricting the efficiency of degradation [Huang *et al*., (2020); Farzaneh *et al*., (2016)]. The results elucidated the reason behind the lack of improvement in degradation efficiency with an increase in photocatalyst dose. Surprisingly, augmenting the quantity of photocatalyst from 0.5 to 1mg led to enhanced system breakdown efficiencies, rising from 16 to 19%. Fig. 3.2.13(b) demonstrated that the breakdown rate was modified when the catalyst dosage was raised from 1 to 11mg, resulting in a decrease. We evaluated all these factors and determined that precisely 1 mg was the ideal amount of nanocomposite photocatalyst to use in the procedure. The experiment was replicated three times to ensure its precision and reliability.

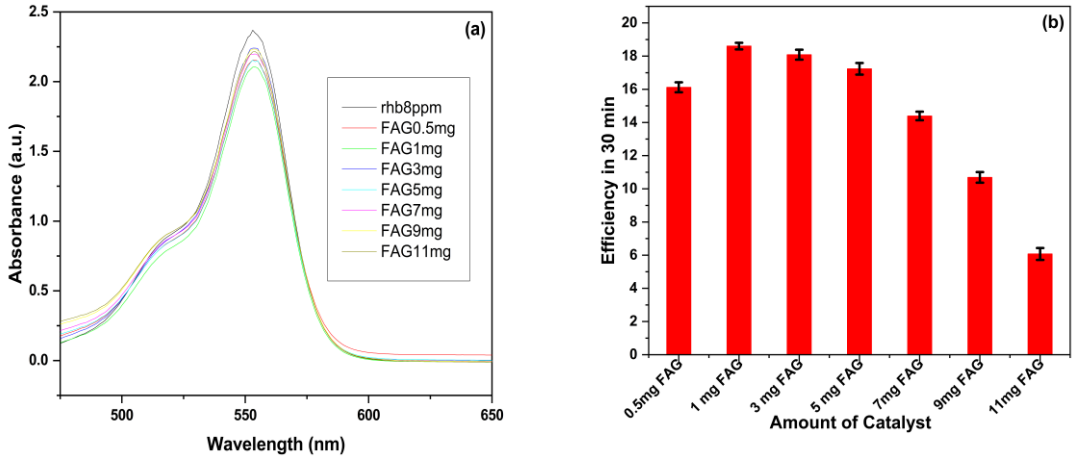

Fig. 3.2.13((a)-(b)) The effectiveness of RhB degradation at different concentrations of the photocatalyst in its various forms.

3.2.12 pH effect

Dye or pesticides exhibited greater absorption at high pH levels compared to low pH levels due to the presence of a higher concentration of hydroxyl radicals in the solution. The solubility and photocatalytic degradation of the substance exhibited an upward trend when the pH level rose from 5 to 10. These radicals were the predominant oxidative species at neutral or alkaline pH levels. However, the positive holes took precedence at acidic or basic pH levels. The chemical makeup of the surroundings often hastened or slowed down the degradation of dyes and pesticides. They can experience an expedited breakdown at higher pH levels, such as pH 10, via hydrolysis. The phenomenon occurred when a dye or pesticide was exposed to an alkaline environment, causing the molecule to break apart.

Consequently, many decomposition byproducts with distinct chemical characteristics can be generated. In addition, it reacted with hydroxide ions, which increase in concentration as the pH increases. The dye or pesticide molecules undergo degradation due to the influence of these ions, resulting in an overall acceleration of these reactions when the pH levels increase. Therefore, it was imperative to control the pH of the environment. Furthermore, the responsiveness of particular chemical species is expected to change when the pH level increases, hence enhancing the

likelihood of their interaction with dye or pesticide. This heightened sensitivity could accelerate the rapid deterioration of RhB. Upon evaluating the aforementioned impacts at a pH range of 6–8, it was inferred that the nanocomposite photocatalyst exhibited exceptional performance. Langmuir-Hinshelwood derived the first-order rate constant, k, using the following equation: $kt = \ln(C_o/C_t)$, where C_o and C_t represent the concentrations of RhB dye at 0 and t minutes of irradiation, respectively. We can obtain the value of k by dividing the logarithm of the ratio of C_o to C_t by t min. As a result, we successfully determined both the sample's kinetic energy and the first order rate constant. We performed a linear regression using the logarithm of the ratio C_t/C_o to estimate the rate constant k and find the slope of the line for fitting absorption time. In order to guarantee the accuracy and reliability of the experiment, we conducted it on three separate occasions. The nanocomposite of Fe_3O_4 and Ag-g-C_3N_4 has a much higher rate constant than other materials. This is because it has a lot of surface area and the Fe_3O_4, Ag, and g-C_3N_4 worked well together.

3.2.12.1 RhB degradation

UV-visible spectra of RhB photodecomposition at various pH levels, using specific experimental parameters, and the adsorption studies for FAG3 at pH values ranging from 5 to 10 reveal percentages of 77.30, 75.28, 68.52, 70.87, 74.34, and 78.56%, respectively. When FAG3 nanocomposite was absent, the degradation of RhB dye under LED was very small, about 2%. The most promising sample was the LED-RhB-FAG3, which, like prior photocatalysis, degraded 78.56% of the RhB after 150 min. In order to estimate the rate constant k for fitting absorption time, a linear regression was performed using the logarithm of the ratio C_o/C_t to find the slope of the line, as shown in Fig. 3.2.14(a). After the removal of the ethyl groups, the resultant products have the potential to undergo subsequent reactions, ultimately culminating in the creation of less complex molecules, such as m/z (terephthalic acid) = 166.12, m/z (3-hydroxybenzoic acid) =122.11, m/z (benzoic acid) =122.11, m/z (succinic acid) =118.08, m/z (adipic acid) = 146.13, and carbon dioxide. The process described is known as mineralization, in which organic substances are decomposed into their most basic inorganic forms, including CO_2, water, and mineral ions, as shown in Fig. 3.2.14(b).

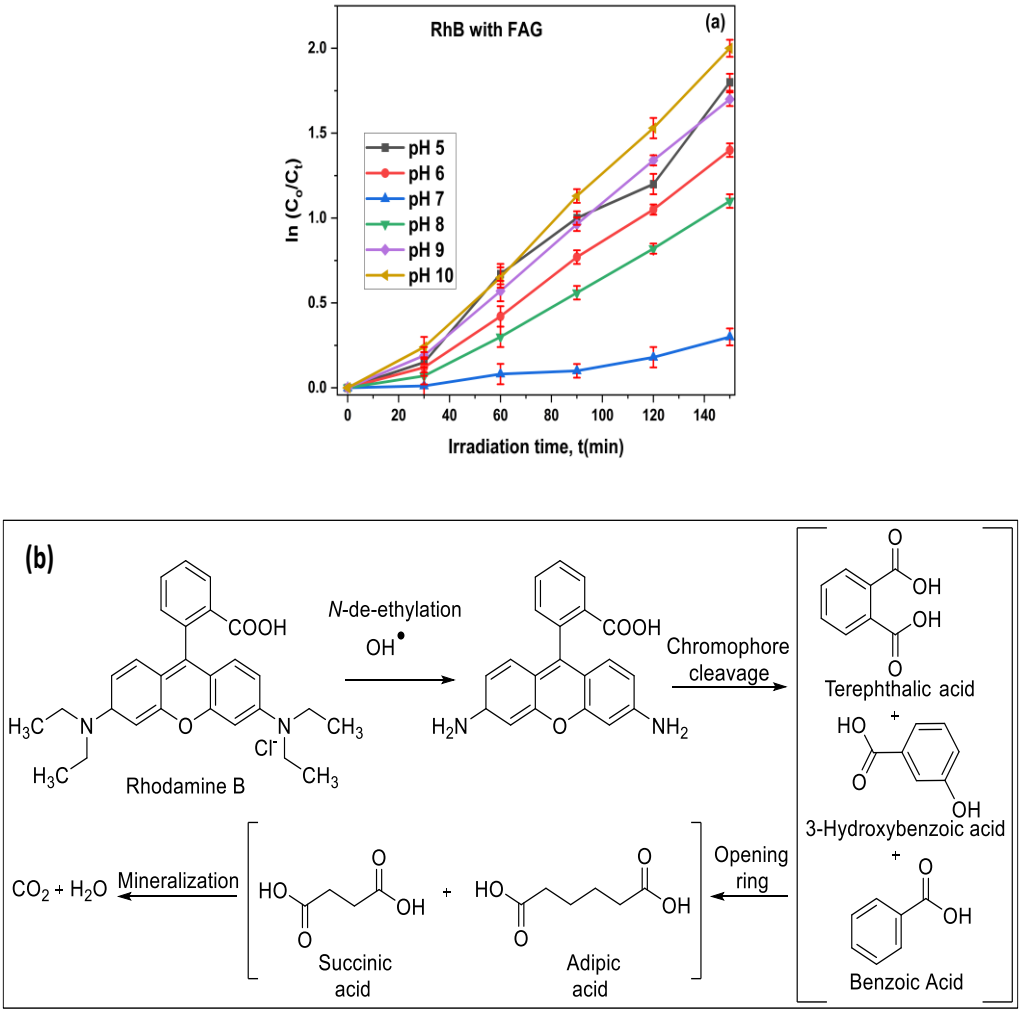

Fig. 3.2.14 (a) Kinetics of photodegradation (b) Mineralization of RhB.

3.2.12.2 MB degradation

After 150 min, the FAG solutions with pH values ranging from 5 to 10 showed respective absorption rates of 81.84, 79.04, 71.32, 74.83, 78.78, and 85.09%. The pure MB dye degrades by 3% when exposed to LED light, which is a significant decrease. At pH 10, the LED-MB-FAG3 solution degrades at an estimated rate of 85.09% after 150 min of exposure to LED radiation, making it the most severely degraded. Since FAG nanocomposite is smaller and has a shorter energy gap, its increased surface area and photocatalytic capacity are thought to be responsible for the accelerated degradation. Fig. 3.2.15(a) showed the linear regression results that used the logarithm of the ratio C_o/C_t ratio to determine the line's slope. As a result, we could estimate the

rate constant k for fitting absorption time. Due to this interaction, chemical bonds like sulfur-chlorine, nitrogen-methyl, carbon-sulfur, carbon-nitrogen, and carbon-oxygen dissociate. Ultimately, a chain reaction breaks down intermediate components and opens MB rings, producing smaller organic molecules. The process is complete at mineralisation, and the end molecules are CO_2 and H_2O, as shown in Fig. 3.2.15(b).

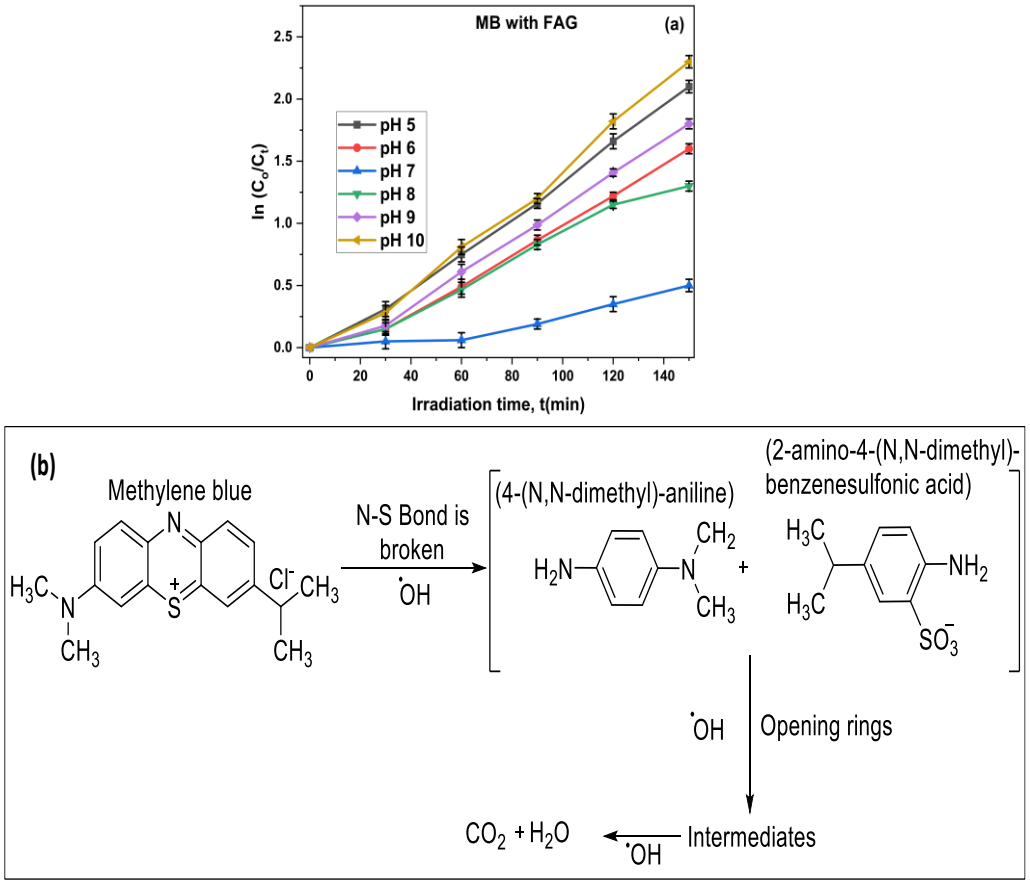

Fig. 3.2.15 (a) Kinetics of photodegradation (b) Mineralization of MB.

3.2.12.3 MB and RhB Mixture degradation

MB and RhB dyes are absorbed after 150 min, and at pH 7, FAG3 containing solutions degrade with a rate of 74.08 and 70.36% efficiency, respectively, which are shown in Fig. 3.2.16(a) and (b). This was because the dye's positive charges made the FAG surface more absorbent. With LED light, however, the MB and RhB combination degrades by only 1%. After 150 min of exposure, the LED-MB-FAG3 solution exhibited the highest degradation percentage of around 74.08% at pH 7. The decreased size and band gap of FAG3 nanoparticles lead to an increase in surface area and an

improvement in photocatalytic activity. Many things could decrease the solubility of rhodamine B (RhB) and methylene blue (MB) when combined in water. The observed drop in solubility could be due to several things, like the solvent-water interface being a potential adsorption location where RhB and MB molecules may compete. If we blended two colours that were not very water-soluble, we run the risk of competing adsorption, which would make the mixture less water-soluble. RhB and MB molecules can cluster when exposed to water; this can also happen when other colours interact. This aggregation reduced the effective solubility of the individual colours in the mixture. Their solubility can influence complex formation between RhB and MB molecules. The creation of complexes might reduce solubility because the species that are complexed with them may precipitate out of the solution. Electrostatic interactions or hydrogen bonding between RhB and MB molecules can reduce RhB's solubility. These interactions may induce complex or cluster formation, leading to a decrease in dye solubility in water.

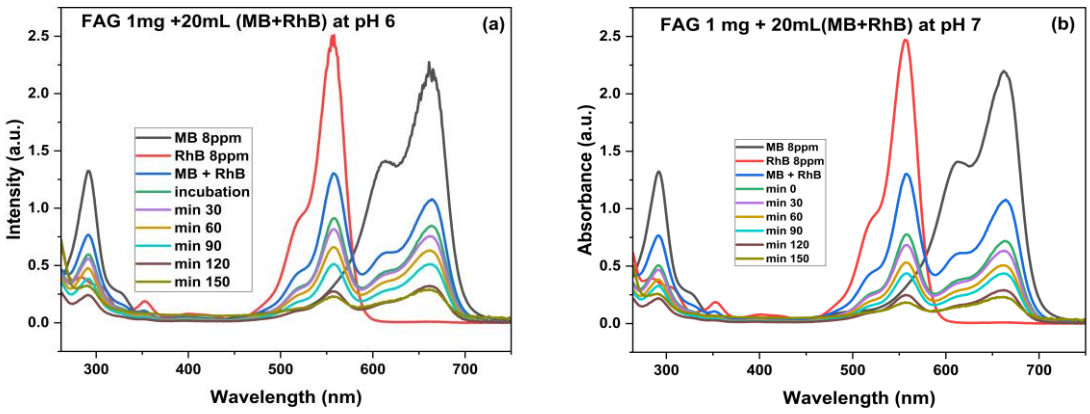

Fig.3.2.16 (a)-(b)MB and RhB mixture degradation at different pH.

3.2.12.4 Degradation of 2, 4-DCP under LED irradiation

The UV-visible spectra of 2,4-DCP photodecomposition at different pH levels, employing specified experimental conditions and studies on FAG3 adsorption at pH levels between 5 and 10, yielded percentages of 67, 65, 59, 61, 65, and 69%, in that order. A linear regression was performed, and the logarithm of the ratio C_o/C_t was used

to calculate the slope of the line for 2,4-DCP. The regressions are displayed in Fig. 3.2.17(a). Because of this, we could calculate an estimate of the rate constant k for the absorption rate. In addition, throughout the 150 min response time, the mineralization rates for 2,4-DCP ranged from 5 to 52%, and this indicated that the final products of mineralization include the considerable degradation of 2,4-DCP and TCAA into CO_2 and H_2O, which is shown in Fig. 3.2.17(b).

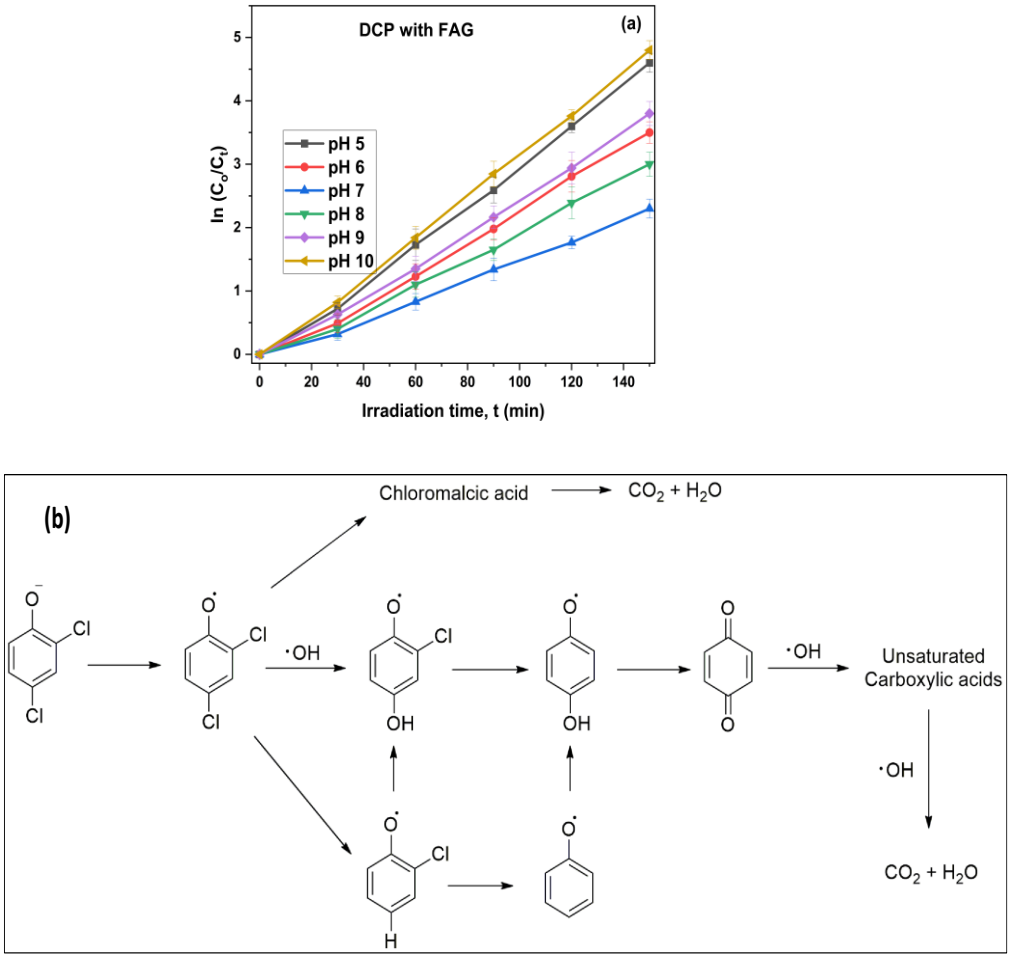

Fig. 3.2.17 (a) Kinetics of photodegradation of 2,4-DCP (b) Mineralization of 2,4-DCP

3.2.12.5 TCAA degradation

The UV-visible spectra of 2,4-DCP photodecomposition were analyzed at various pH levels using specific experimental settings. Additionally, we studied the adsorption of FAG3 at pH levels ranging from 5 to 10. The results showed 29, 33, 35, 39, 45, and 52% percentages in sequential sequence. A chromatogram of 8 ppm TCAA

analysis through HPLC is shown in Fig. 3.2.18(a). TCAA mineralization and degradation by FAG under specific circumstances, such as an 8 ppm catalyst concentration and 150 min contact duration, which were analyzed through HPLC, are shown in Fig. 3.2.18(b). A linear regression was conducted using the logarithm of the ratio C_o/C_t to determine the slope of the line for 2,4-DCP, and the results of the regression can be seen in Fig. 3.2.18(c). Consequently, we could compute an approximation of the rate constant k for the absorption rate. The breakdown intermediates of TCAA, namely hydroxyacetic, formic, and acetic acids, are less hazardous than the initial TCAA. The mass chromatograms showed that the mixtures included formic acid (CH_2O_2, m/z 46, R_t 4.36 min), hydroxyacetic acid ($C_2H_4O_3$, m/z 93, R_t 4.52 min), and acetic acid ($C_2H_4O_2$, m/z 62, R_t 3.42 min). An intermediate with m/z 46 was found by LCMS analysis. This intermediate was produced from an intermediate with m/z 62. Although LCMS analysis only detected formic acid, the data showed that acetic acid and hydroxyacetic acid were the primary breakdown phases of TCAA, Fig. 3.2.18(d).

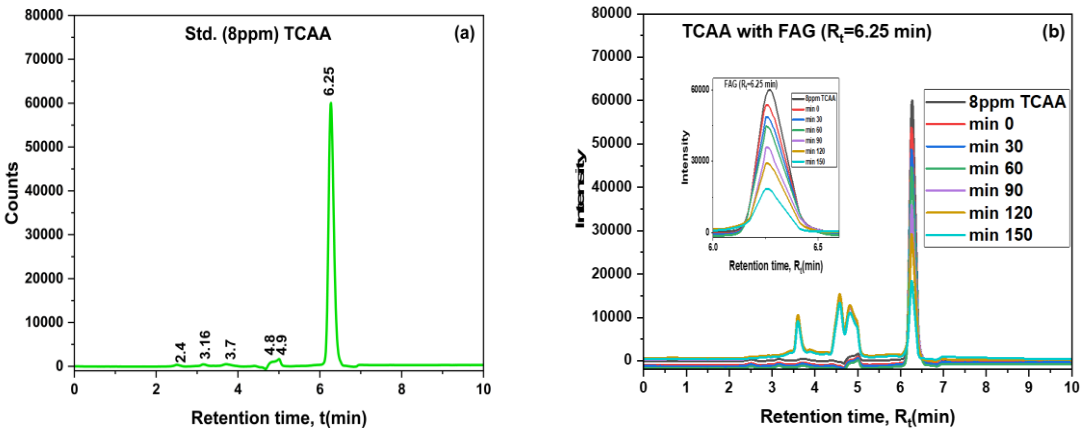

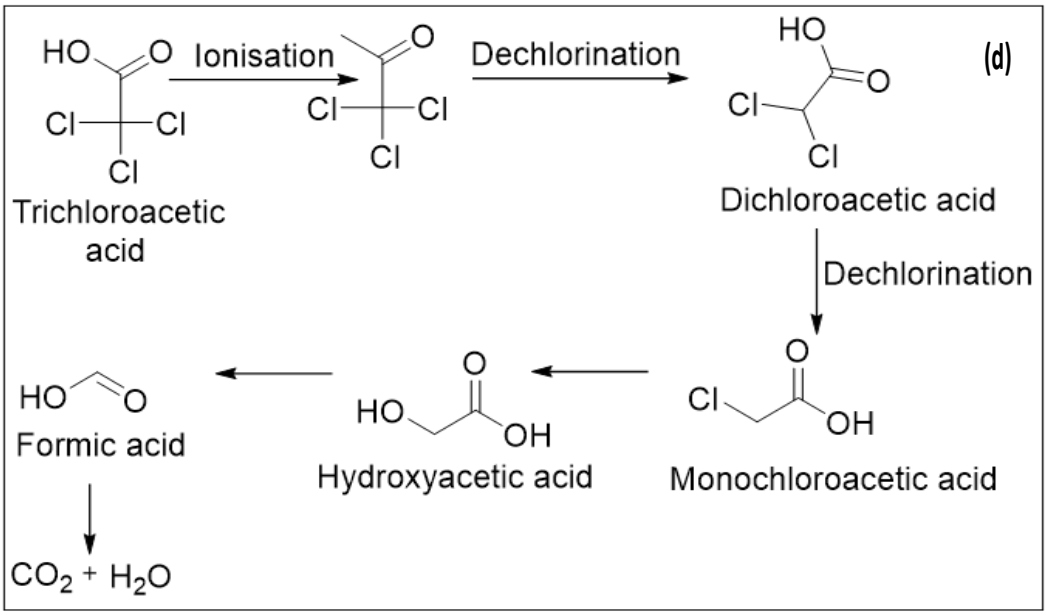

Fig. 3.2.18(a) Standard TCAA (8ppm) (b)TCAA decomposition with 1mg of FAG3 (c) Kinetics of photodegradation of TCAA (d) Mineralization of TCAA.

3.2.13 TOC (total organic carbon) determination

The primary goal of the carbon investigation was to identify mineralization resulting from dyes and pesticides. The percentage of total organic carbon (TOC) removal for MB, RhB, 2,4-DCP, and TCAA using 1mg of FAG3 was 6, 5.5, 5, and 4.5%, respectively, after incubation. The exposure to LED light for 150 min improved the TOC removal percentages to 65, 59.034, 52, and 47%, respectively. Fig. 3.2.19 shows a decrease in the dye's absolute total organic carbon (TOC) value after adding 1mg of Fe_3O_4/Ag-g-C_3N_4 (FAG3). The photomineralization efficacy was 59.034%. However, when we used the same amount of photocatalyst with Fe_3O_4/g-C_3N_4, the efficacy dropped to 40.128%. This indicates a slight decrease in photomineralization efficiency due to insufficient active sites on the catalyst's surface, which hindered the desired reaction. Moreover, these findings provide insight into the presence of Total Organic Carbon (TOC) in both samples, potentially originating from a chemical process occurring prior to mineralization. We computed the demineralisation of dye or pesticide degradation by employing the same equation (3.7 under Section 3.1.10). We replicated the experiment three times to confirm its correctness and dependability.

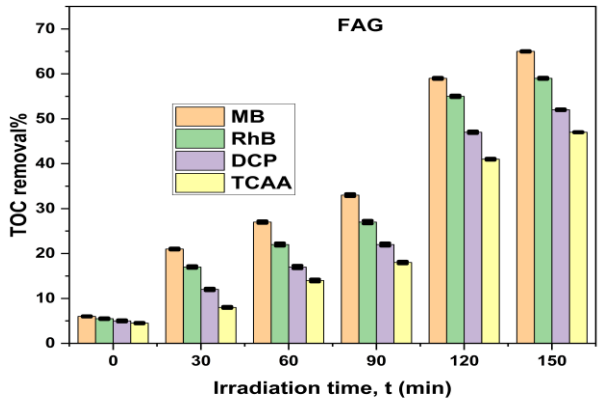

Fig. 3.2.19 RhB dye's total organic carbon removal percentage using Fe_3O_4/Ag doped g-C_3N_4 (FAG3)

3.2.14 Turnover number and turnover frequency

Analysing the Turnover Number (TON) and Turnover Frequency (TOF) is a big deal for determining the immediate efficacy of a catalyst. The "TON" value represents the product conversion rate from substrate molecules per photocatalyst molecule processed within a specific time frame. A possible approach to determining this is by applying the same equation 3.8 presented in Section 3.1.11, while the percentage conversion shows how much deterioration the photocatalyst accomplished. Conversely, Turnover Frequency (TOF) is defined as the maximum number of catalytic cycles executed by each active site within a given time unit according to equation 3.9, as given in Section 3.1.11. Table 3.2.3 presents the outcomes of the TON and TOF investigations conducted on methylene blue (MB), rhodamine B (RhB), 2,4-DCP, and TCAA during their photocatalytic degradation processes in the presence of LED light.

When exposed to LED radiation, the FAG nanocomposites exhibited the highest TON and TOF values in the degradation of both MB and RhB colourants. This enhanced performance, likely related to the preceding statement, is the result of the shrinkage, which increased the surface area and quantity of active sites. As a result, organic contaminants are degraded more efficiently.

Table 3.2.3 Estimation of TOF and TON

Dye	sample	TOF (min^{-1})	TON (min^{-1})
MB	FAG3	58.339	0.388
RhB	FAG3	34.662	0.231
2,4-DCP	FAG3	10.504	0.07
TCA	FAG3	6.434	0.042

3.2.15 Reusability

The breakdown efficiencies of MB, RhB, 2,4-DCP, and TCAA for FG and FAG were determined following exposure to visible light for 150 min. Stability and recyclability were essential requirements for practical photocatalysts. We investigated the photocatalytic stability and reusability of the magnetic nanocomposite following recycling. The process of recycling the dyes or pesticides that break down nanocomposite photocatalysts is illustrated in Fig 3.2.20.

The investigative study showed that RhB decreased from 83% to 75% over 150 minutes. We found a modest variation in the decomposition efficiency. We can attribute the poor performance of the used-by-used nanocomposite photocatalysts to the presence of intermediate RhB compounds, which remain adsorbed on the surface after a partial breakdown. This leads to a reduction in both photocatalyst adsorption and degradation. Therefore, the process of degrading RhB using nanocomposite photocatalysts under visible light was both consistent and repeatable.

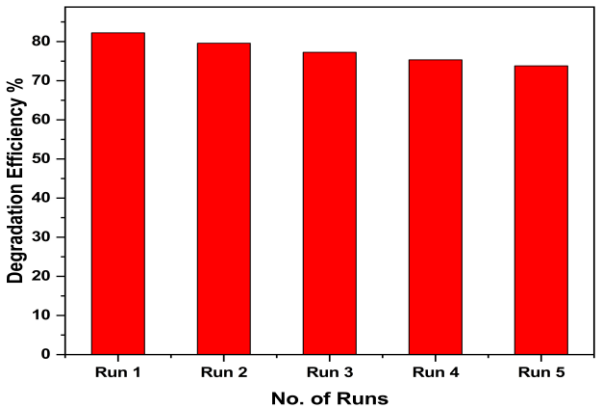

Fig. 3.2.20 Number of recycles for reusing FAG3.

3.2.16 Comparison

As with the photocatalytic activity, Table 3.2.4 displays the degradation constants for these materials. Under more basic solution conditions, with a higher concentration of hydroxyl ions, the degradation rate constants of both dyes increase. The degradation constant of the LED-MB-FAG3 solution was higher than that of the LED-MB-FG solution at pH 7. Moreover, the LED-MB-FAG3 (pH 7) solution degrades faster than the LED-RhB-FAG3 sample. Chemical structure was the primary differentiator between the two chemicals; more significantly, Rhodamine B's more prominent and more intricate molecular structure was the cause of its distinctiveness.

We measured the degradation percentage for both the MB and RhB solutions exposed to LED radiation after 150 min. Thus, FAG3 nanocomposite has been proven to be a highly efficient photocatalyst for the fast degradation of pollutants. Among them, the FAG3 containing solution with a pH of 10 works the best, as depicted in Fig. 3.2.21. This was because smaller diameters result in a higher surface area and a higher concentration of hydroxy ions.

This study verified that FAG3 nanocomposites biosynthesized with *Atocarpus heterophyllus* L effectively aid in the photocatalytic degradation of MB. The chemical differences between rhodamine B and methylene blue are the root cause of this incongruity.

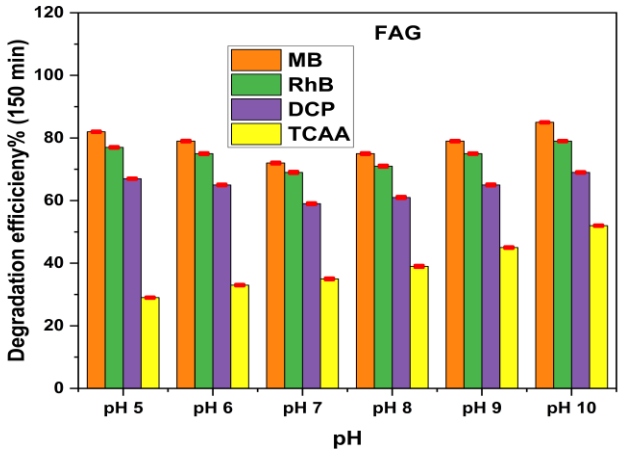

Fig. 3.2.21 Degradation efficiency of dyes and pesticides with FAG3 photocatalyst at different pH.

Depending on their structural properties, dye molecules are photocatalytically degradable to different degrees. Our results show that FAG3 nanocomposite manufactured utilising an environmentally safe method using *Atocarpus heterophyllus* extract outperforms results published in earlier literature and performs better overall. This technology is particularly effective in water pollutant degradation.

Table 3.2.4 Determination of rate constant at different pH

pH	MB k (min^{-1})	R^2	RhB k (min^{-1})	R^2	DCP k (min^{-1})	R^2	TCAA k (min^{-1})	R^2
pH 5	0.038	0.966	0.044	0.943	0.024	0.955	0.025	0.965
pH 6	0.034	0.966	0.040	0.961	0.021	0.943	0.023	0.939
pH 7	0.031	0.968	0.032	0.949	0.021	0.965	0.019	0.941
pH 8	0.032	0.963	0.038	0.973	0.030	0.945	0.020	0.947
pH 9	0.035	0.945	0.043	0.939	0.023	0.959	0.025	0.945
pH 10	0.040	0.949	0.044	0.945	0.031	0.955	0.026	0.959

The pseudo-first-order model (R^2=0.916, 0.966,0.884, 0.842) shows greater agreement with experimental data than the pseudo-second-order model (0.714, 0.862, 0.768, 0.744) for RhB, MB, 24-DCP, and TCAA treated with FAG under LED light. The reaction likely follows pseudo-first-order kinetics.

3.2.17 Property of magnetism

The coercivity magnitudes (MH) were employed to evaluate the magnetic response characteristics of magnetic nanoparticles made of Fe_3O_4 and a magnetically active nanocomposite made of FAG3 (Fig. 23). All Fe_3O_4 nanocomposites have ferrimagnetic properties and demonstrated symmetric hysteresis. The magnetic saturation magnetization of Fe_3O_4, FG, and FAG3 was measured to be 20.72, 8.63, and 4.59 emu/g, respectively. The magnetic moment of Fe_3O_4 nanoparticles was reduced by a noncollinear spin arrangement near the surface, accounting for the little impact of particle size. Due to the lack of magnetism in Ag and the presence of tri-S-triazine units as basic components in g-C_3N_4, Fe_3O_4 elements became contaminated,

which made them less magnetic. Therefore, FG exhibited a lower saturation magnetization compared to Fe_3O_4. In addition, FAG3 exhibited no hysteresis, remanence, or coercivity and this nanocomposite photocatalyst exhibited high saturation magnetization, enabling its magnetic separation from the solution, hence enhancing recovery and recycling efficiency.

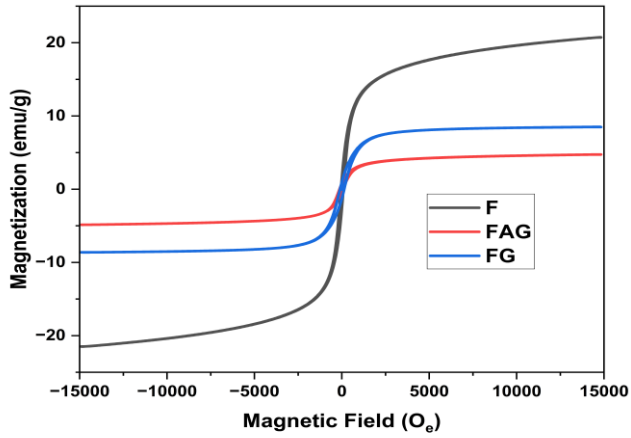

Fig. 3.2.22 VSM of Fe_3O_4 (F), Fe_3O_4/g-C_3N_4 (FG), FAG3.

3.2.18 Degradation pathway utilizing a photocatalyst

Fig. 3.2.23 illustrates our proposed approach for decomposing RhB dye using nanocomposite photocatalysts. Heterojunctions, like the Ag/g-C_3N_4 system, can exhibit diverse energy levels in their conduction bands (CBs). Electrons traverse the conduction bands of various materials. Silver (Ag) could acquire electrons from graphene-like carbon nitride (g-C_3N_4), which possessed a lower energy level in its conduction band. The electrons underwent a reduction of oxygen and other molecules in the conduction band of Ag. The dyes or pesticides reacted with photoexcited electron and hole pairs in the conduction and valence bands.

These substances enhanced the chemical interaction of the dye with the pre-made nanocomposite photocatalyst. The nanocomposite photocatalyst's enhanced photocatalytic efficacy stems from its increased absorption of visible light, reduced rate of charge pair recombination, and continuous adsorption of dye or pesticide molecules. Its efficacy in decomposing dyes implies its potential application as a photocatalyst.

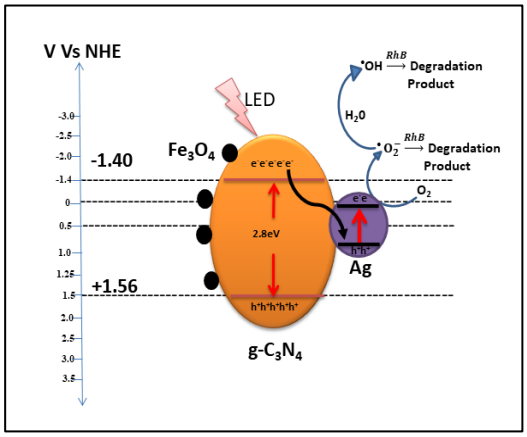

Fig. 3.2.23 RhB degradation pathway utilizing a photocatalyst

3.3 Effect of Silver on SnO_2 in Fe_3O_4/SnO_2 ternary nanocomposite for degradation of dyes and pesticides.

Photocatalysts that degrade organic contaminants like dyes and insecticides is crucial to environmental remediation research. Fe_3O_4/Ag_x-Sn_yO_2 is a nanocomposite of magnetite, silver, and tin oxide. Silver improves this composite's photocatalytic activity since silver is a noble metal with exceptional electrical conductivity, and distinctive optical qualities. However, its broad band gap hinders visible light absorption. Under UV light, SnO_2 generates electron-hole pairs, and its high electron mobility aids photocatalytic processes. It creates nanoparticles with high surface areas and localized surface plasmon resonance (LSPR), which improves light absorption. In photocatalysis, silver has many uses like as an electron sink, it traps electrons to minimize electron-hole pair recombination and improves composite light absorption due to LSPR. Magnetic Fe_3O_4 readily separates the photocatalyst from the reaction mixture using a magnetic field, which is easy recovery and photocatalytic. Thus, Ag absorbs photogenerated electrons from SnO_2.

The photocatalytic process has more charge carriers because electron-hole pair recombination is reduced. A Schottky barrier separates charge carriers at the Ag-SnO_2 contact in which holes persist in SnO_2, electrons can move to Ag, improving photocatalytic efficiency.

The study investigates the photodegradation of Rhodamine B using the Fe_3O_4/Ag_x-Sn_yO_2 (FAS3) (x:y = 1:1, 1:3, 3:1) nanocomposite. The experiment maintains a consistent reaction temperature, agitation, distance from the LED light, and pollutant solution. A concentration of 8 parts per million (ppm) of RhB was subjected to a 150 min exposure to examine the durability of the dye under LED light. The examination of the structural stability of the dye revealed that only 5% of the dye had undergone degradation after 150 min. When the LED light is on, the transition of electrical charge from the valence band to the conduction band in the two semiconductors results in energy absorption. Electrons emitted by LEDs generate positive holes and negative electrons within semiconductors. The nanocomposite Fe_3O_4/Ag_x-Sn_yO_2 (FAS3) (with a ratio of x:y = 3:1) exhibited effective

photodegradation of RhB dye, as demonstrated in Fig. 3.3.1. The absorption intensity was evaluated to assess the photocatalytic efficiency of the produced ternary nanocomposite for degrading RhB (Sigma Aldrich) dye in an aqueous solution. Before radiation exposure, 5 mg of the Fe_3O_4/Ag_x-Sn_yO_2 (FAS3) magnetic ternary nanocomposite was introduced into a solution containing 20 mL of rhodamine B with a concentration of 8 ppm.

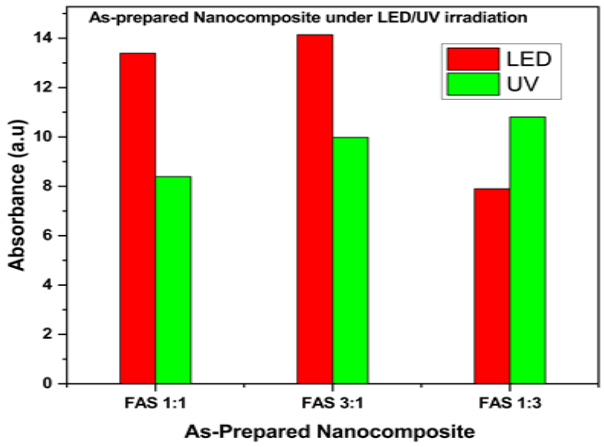

Fig. 3.3.1 Degradation efficiency of as-prepared catalyst by exposing to UV and LED light.

The findings showed that the ternary nanocomposite FAS3 with x:y=3:1 was very good at breaking down RhB when it came in contact with LED light, as seen in Fig. 3.3.1. Therefore, we will focus on characterising and investigating the potential applications of Fe_3O_4/Ag_x-Sn_yO_2 (FAS3) with a ratio of x:y = 3:1.

3.3.1 X-ray diffraction

Powder XRD was used to characterise the grain size and structure of Fe_3O_4, Fe_3O_4/SnO_2, and Fe_3O_4/Ag_x-Sn_yO_2 (FAS3, having 3:1 ratio of Ag:SnO_2) nanoparticles and nanocomposites. Fig. 3.3.2(a)–(c) displays the X-ray diffraction patterns of Fe_3O_4, SnO_2, and Fe_3O_4/Ag-SnO_2 nanocomposite, respectively. The size and structure of the crystallites were determined using the Scherrer equation. diffraction pattern of a nanocomposite of Fe_3O_4, Ag, and SnO_2 (FAS3) was compared to that of pure Fe_3O_4 and SnO_2. With lattice parameters a, b, and c equal to 8.184Å, the cubic and inverse spinel structure of the Fe_3O_4 compound was observed. The cell volume, which could

be calculated using Miller indices (220), (311), (222), (400), and (440), was 582.438. The pattern was matched by JCPDS No. 82-1533. Diffraction peaks at 2θ angles of 25.522°, 32.124°, 37.232°, 52.532°, and 64.121° were observed in the tetragonal rutile phase, which was found to be a crystal phase of SnO_2 according to JCPDS No. 41-1445. The *hkl* planes (110), (101), (111), and (310), in that order, were corresponding to these peaks. In the cubic crystalline phase of Ag (JCPDS 87-0720), the diffraction peaks observed at an angle of 2θ=38.304° may be caused by the *hkl* planes (111). The lattice constants for this phase were found to be 4.582 Å, with a cell volume of 75.384 matching this. Table 3.3.1 shows that although Ag and Fe_3O_4 were cubic, SnO_2 was tetragonal. The XRD pattern of the Fe_3O_4/Ag-SnO_2 nanocomposites shows that the tetragonal structure of SnO_2 was unaffected by the presence of Fe_3O_4 and Ag in the matrix, as shown by their (311) and (110) diffraction peaks. The Debye-Scherrer formula was used to determine how big the crystallites were in Fe_3O_4/Ag_x-Sn_yO_2 ternary nanocomposites. The Debye-Scherrer equation (equation 3.1 in the section 3.1.1) was used to forecast the average crystallite sizes of purified Fe_3O_4, SnO_2, and ternary nanocomposite Fe_3O_4/Ag_x-Sn_yO_2.

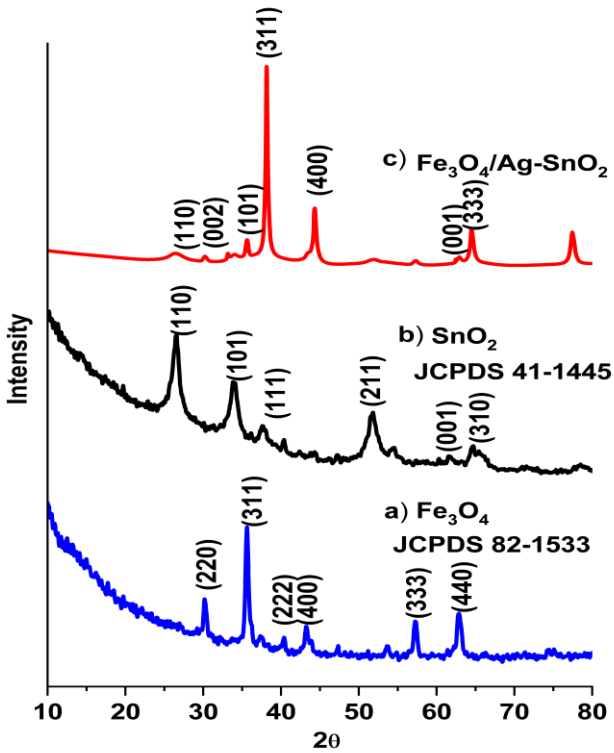

Fig. 3.3.2 X-ray diffraction of (**a)** Fe_3O_4 (**b)** SnO_2 (**c)** Fe_3O_4/Ag_x-Sn_yO_2 (FAS3)

Table 3.3.1 The generated Fe_3O_4, SnO_2, Fe_3O_4/SnO_2, and Fe_3O_4/Ag_x-Sn_yO_2 nanocomposite was examined to determine its average grain size, lattice characteristics, and volume.

As-prepared	Average crystallite Size (nm)	Lattice Parameters			Cell volume
		a (Å)	b (Å)	c (Å)	
Fe_3O_4	26.232	8.184	8.184	8.184	582.438
SnO_2	15.621	5.354	5.354	3.203	69.251
Fe_3O_4/ SnO_2 (FS)	61.921 25.103	8.438 4.730	8.438 4.730	8.438 3.178	600.805 81.125
Fe_3O_4/Ag_x-Sn_yO_2 (x:y=3:1)	42.153 18.247 24.126	8.325 4.582 7.344	8.325 4.582 7.344	8.325 4.582 2.452	602.210 75.384 83.568

3.3.2 FT-IR analysis

Performing Fourier-transform infrared spectroscopy (FTIR) analysis on a composite material like Fe_3O_4/Ag_x-Sn_yO_2 can provide valuable information about the chemical bonds and interactions within the material. This type of composite typically combines magnetic Fe_3O_4 (magnetite), silver (Ag), and tin oxide (SnO_2), each of which has characteristic infrared absorption features

As-prepared nanomaterials Fe_3O_4, SnO_2, $AgNO_3$, and Fe_3O_4/Ag_x-Sn_yO_2 (FAS3) were shown in Fig. 3.3.3((a)-(d) FT-IR spectra, respectively. The absorption peak between 400 and 524 cm^{-1} was caused by this type of M-O stretching [Brojendro Singh Shagolsem, Nongmaithem Mohondas Singh, (2024)].

Nanomaterials made of Fe_3O_4 and SnO_2 exhibited corresponding peaks at 786 and 462 cm^{-1}, for the light absorption peaks caused by the Fe-O link. Absorption bands at 1103 cm^{-1} and 1357 cm^{-1} suggest that the COO-Fe bond may be created when the carboxylate anion of the plant extract reacts with hydroxyl radical groups [Soto-Robles *et al*., (2019)]. Water molecule stretching in Fe_3O_4, SnO_2, and FAS3 nanocomposites led to large absorption bands at 1633–1670 cm^{-1} and 3364–3424 cm^{-1}, respectively.

Evidence from this experiment suggests that adding Fe_3O_4 and Ag to the SnO_2 matrix did not alter the nanomaterial's properties.

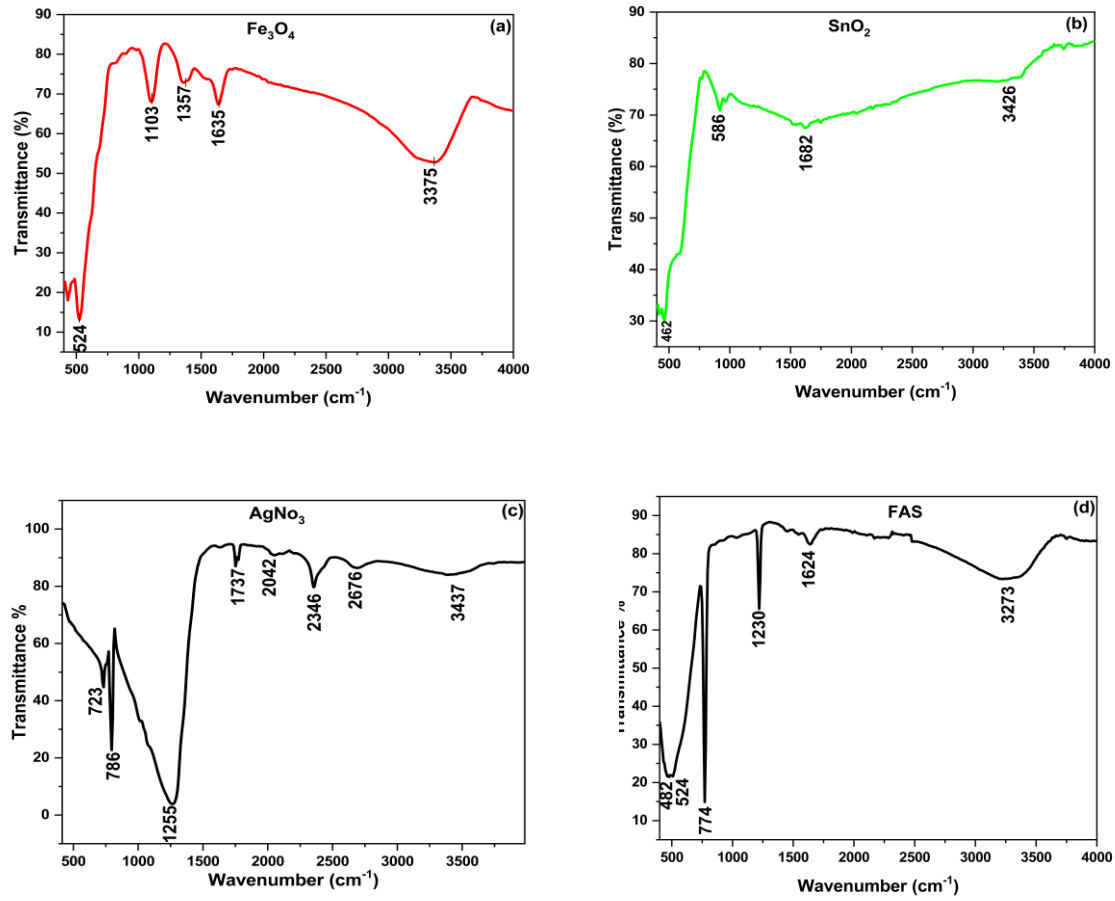

Fig. 3.3.3 FT-IR of a) Fe_3O_4 b) SnO_2 c) $AgNO_3$ d) Fe_3O_4/Ag-SnO_2 (FAS3).

3.3.3 Optical Properties

We evaluated the necessary material(s) synthesis using UV-visible spectroscopy (Thermo Scientific). Fig. 3.3.4(a) presented the results for Fe_3O_4/Ag_x-Sn_yO_2, using these data, we are able to determine their band gap energy using the same equation provided in 3.1 under Section 3.11, which is depicted in Fig. 3.3.4(b). The band gap energies of nanocomposites having ratios of Ag and SnO_2, x:y = 1:1, 1:3, 3:1 were determined to be 3.2, 3.4, and 3.7 eV respectively.

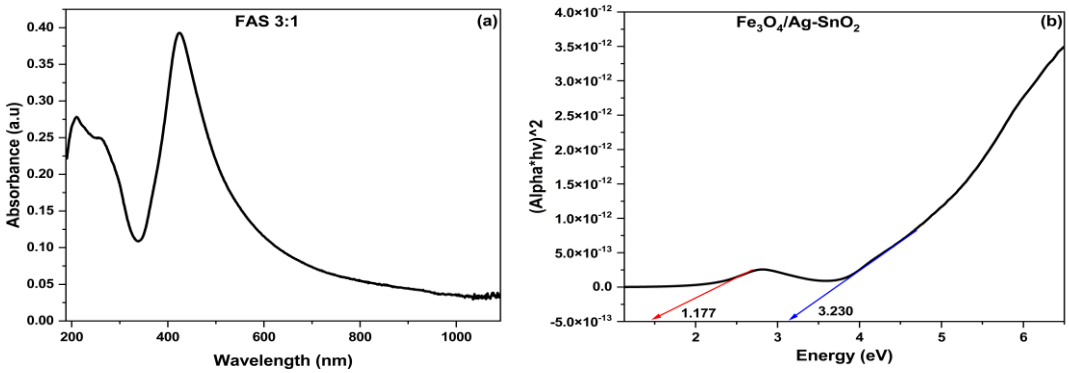

Fig. 3.3.4 (a) UV-Visible spectrum (b) the calculation of the band gap energy for Fe_3O_4/Ag_x-Sn_yO_2 (FAS3).

3.3.4 SEM and TEM analysis

Fig. 3 .3.5 (a) displays the scanning electron microscopy (SEM) imaging findings of the Fe_3O_4/Ag-SnO_2 nanoparticles. The scanning electron micrographs revealed that the particles formed a well-organised nanostructure. The particles seemed almost spherical in the images, and their size was determined to be 25.44 nm, comparable to that of a normal crystal (Fig. 3.3.5(b)).

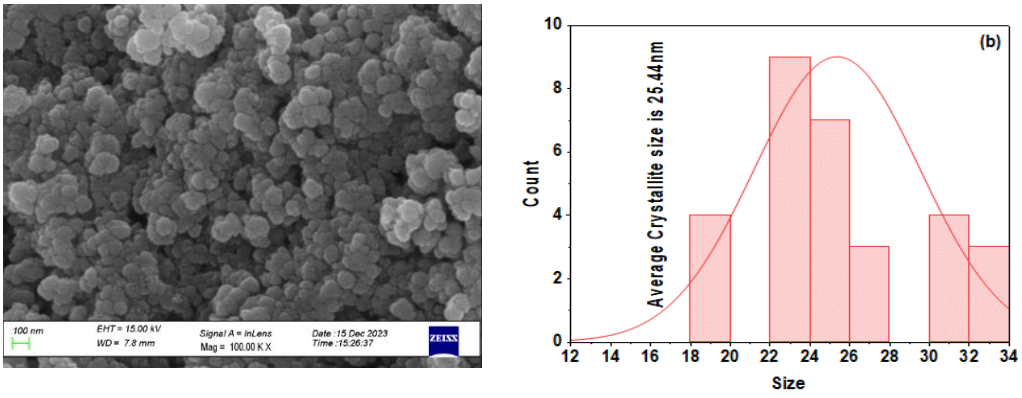

Fig. 3.3.5 (a) SEM image of Fe_3O_4/Ag_x-Sn_yO_2 (b) Average crystallite size

Magnetic nanoparticles made of Fe_3O_4/Ag_x-Sn_yO_2 are displayed in TEM images in Fig. 3.3.6(a). The difference in concentrations of Fe_3O_4 and SnO_2 nanoparticles identifies these particles. Regarding size, both Fe_3O_4 and SnO_2 nanoparticles were almost rounding, with SnO_2 being somewhat more extensive and smaller than Fe_3O_4 -

the difference in density of Fe_3O_4/Ag nanoparticles allowed for their identification. SnO_2 contained dispersed Fe_3O_4 and Ag nanoparticles that were nearly round in shape. Additionally, it had a large collected zone of particles averaging 17–35 nm in diameter and was primarily spherical.

Powder XRD's grain size computation was in agreement with the average crystallite size of Fe_3O_4/Ag_x-Sn_yO_2 (FAS3), which was 25.44 nm. Figure 3.3.6(b) displays HRTEM images of FAS3. High-resolution transmission electron microscopy revealed that the Fe_3O_4 nanoparticles were dispersed across the matrix and formed a heterojunction with the SnO_2 nanoparticles. Ag nanoparticles exhibited (111) planes, SnO_2 nanoparticles had (110), and Fe_3O_4 nanoparticles had (333) planes, all of which pointed to crystal growth in the same direction.

Combining Ag with SnO_2 resulted in an energy-varying heterojunction. This heterojunction allowed for the separation and movement of electrons and holes. The heterojunction structure enhanced the photocatalytic effectiveness by inhibiting the recombination of electron-hole pairs. The ability to efficiently transmit electrons and holes between SnO_2 and Ag allows for photocatalytic reactions. Because it produces, separates, and is involved in redox reactions involving electron-hole pairs, this composite material could purify water and destroy pollutants by light absorption. As diffuse patches and rings, SAED's tetragonal phase and nanocrystalline structure were visible in Fig. 3.3.6(c).

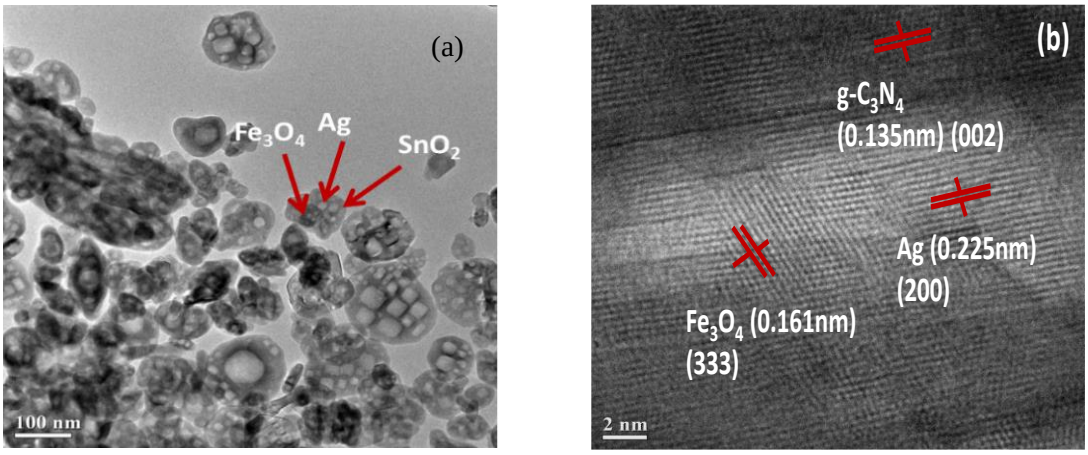

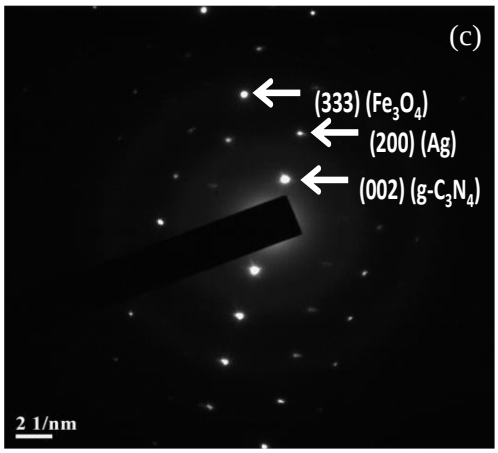

Fig. 3.3.6 Fe_3O_4/Ag_x-Sn_yO_2 (FAS3) (a) TEM Images, (b) HRTEM image and (c) SAED Image.

3.3.5 XPS studies

X-ray photoelectron spectroscopy (XPS) was used to analyze the elemental composition and oxidation state of the materials in their as-synthesized condition. According to Fig. 3.3.7(a), in the survey spectrum, the nanocomposite was composed of the components Sn, Fe, O, and Ag. The Ag 3d region was analysed using X-ray photoelectron spectroscopy (XPS), and the findings were presented in Fig. 3.3.7(b). The spectral data analysis indicated the existence of two separate peaks at energy levels of 366 and 372 electron volts (eV), respectively. The peaks observed may be attributed to the binding energies of the $3d_{5/2}$ and $3d_{3/2}$ orbitals in the silver (Ag) atom. Fig. 3.3.7(c) displayed the Sn 3d spectrum with high resolution, showing two distinct spin-orbit doublet peaks. The electronic states of Sn $3d_{5/2}$ and $3d_{3/2}$ were represented by peaks at 484 and 494 eV, respectively. According to Chen *et al*. (2020), the presence of oxygen from the air caused a rise in the binding energy of tin (Sn), as indicated by the appearance of peaks at 485.0 and 493eV for Sn^{2+}. According to reference [Zhang *et al*., (2011)], it was verified that the $2p_{3/2}$ state have a peak energy of 716 eV for Fe ions, while the $2p_{1/2}$ state have a high energy of 723 eV, depicted in Fig. 3.3.7(d). The presence of lattice oxygen in SnO_2 and Fe_3O_4 was responsible for the peak in the O1s spectra that occurred at 527 eV, whereas the peaks at 531.94 and 533.0 eV were created by oxygen vacancies and heavily adsorbed oxygen species, as can be seen in Fig. 3.3.7(e) [Zhijie *et al*., (2018)].

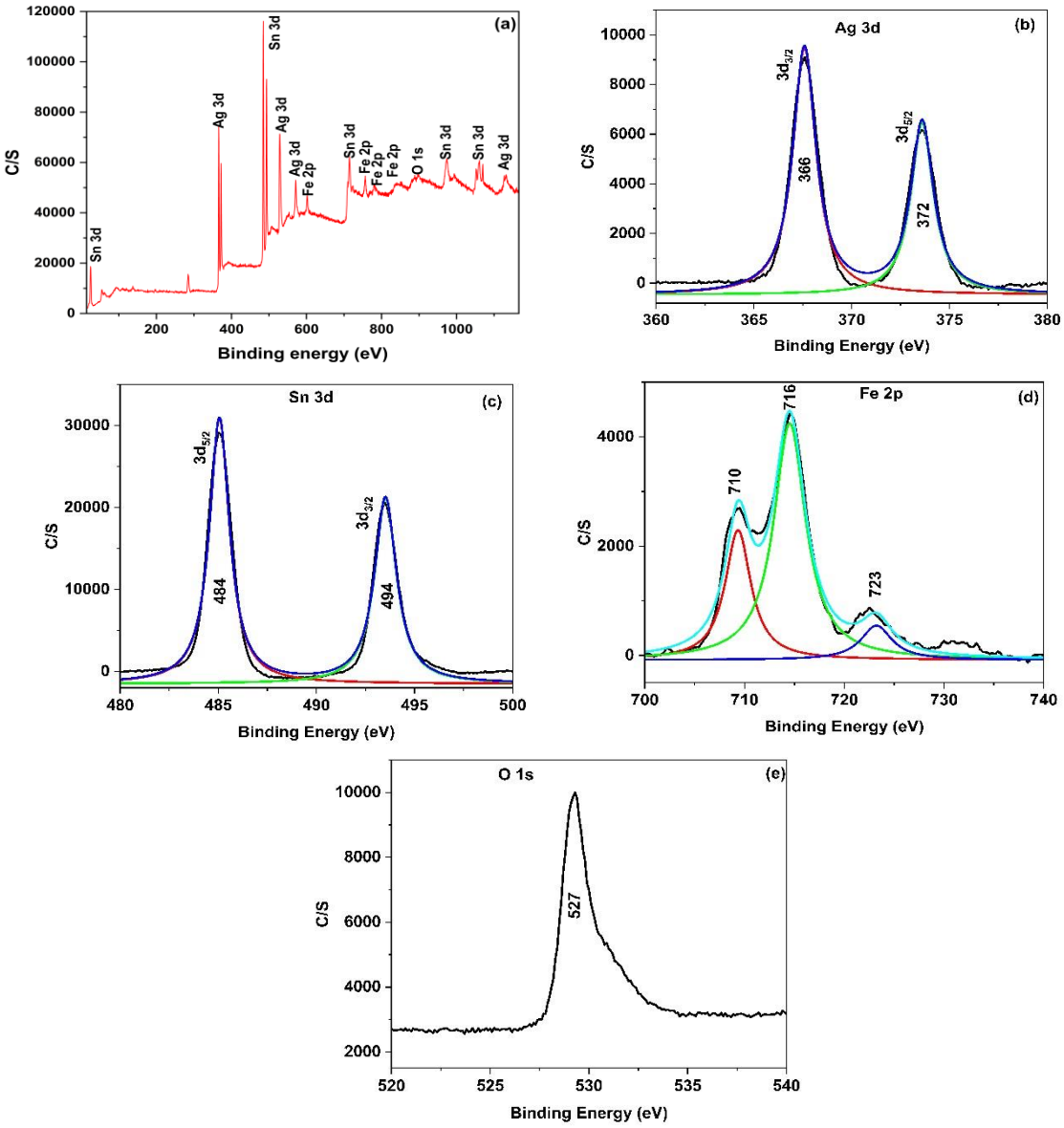

Fig. 3.3.7 XPS of (a) Fe_3O_4/Ag_x-Sn_yO_2 (FAS3) and (b) Ag 3d (c) Sn 3d (d) Fe 2p (e) O 1s in Fe_3O_4/Ag_x-Sn_yO_2.

3.3.6 Photoluminescence analysis

Fig. 3.3.8 displays the photoluminescence spectra of metallic SnO_2 and ferroelectric FAS3. Comprehensive and robust emission peaks in the visible area (454 nm and 468 nm) were typically associated with SnO_2's luminous properties in its photoluminescence spectra. These peaks may be attributed to a variety of factors, including material flaws and the unique crystal structure of SnO_2. Crystallographic defects in Sn-O-Sn, which occurred during expansion, were the cause of this emission.

Oxygen vacancies or dense tin interstitials contaminated the band gap of SnO_2, generating a fault level. The presence of O vacancies or Sn interstitials created an abundance of trapped states or metastable energy levels, leading to a notable release of photoluminescence [Bouras *et al*., (2014)].

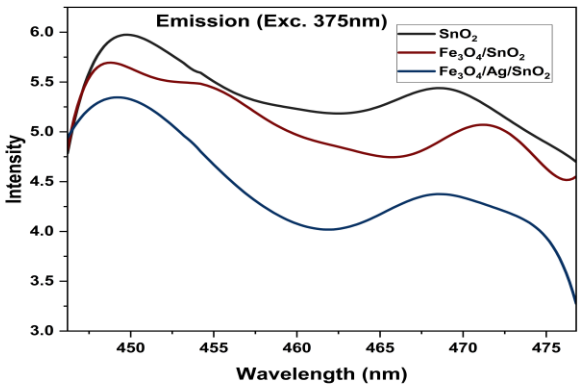

Fig. 3.3.8 PL spectra of SnO_2, Fe_3O_4/SnO_2, FAS3.

According to Xu *et al*., (2011), photogenerated carrier recombination can happen very efficiently close to the numerous minute grain boundaries. Compared to the prepared SnO_2, the FAS3 nanocomposite had a lower PL intensity, which showed that the charges were separated successfully and that electron-hole recombination was stopped. The collection of photogenerated electrons from SnO_2 was an essential step in permitting charge separation, and Ag played a key role in this process. This led to an enhancement in the visible light performance of the FAS3 system. The photoluminescence (PL) output of the FAS3 material demonstrated the effective separation of the produced electron-hole pairs.

3.3.7 Radical studies

It was possible to identify the reactive radicals in the FAS3 nanocomposite that degraded the dye or pesticide by studying the photocatalytic activity of several scavengers when exposed to visible light. It is shown in Fig. 3.3.9(a) that the reactive radicals can be neutralised by either one or more scavengers in the photocatalytic process. These modifications to scavengers caused changes to the RhB dye's C_t/C_o. We employed scavengers such as isopropyl alcohol (IPA), benzoquinone (BQ),

benzoic acid (BA), and ethylene diamine tetraacetic acid disodium (EDTA) in the catalytic procedure to capture the superoxide radical ($\dot{O}_2^-$), holes (h^+), and the hydroxyl radical (ȮH) [Bhuvaneswari *et al*., (2020); Prakash *et al*., (2016); Keerthana *et al*., (2012)]. Various scavengers affect FAS radiation efficiency differently, as shown in Fig. 3.3.9(b). The catalytic reaction degraded the RhB dye material by 57% in BA and 54% in IPA, a scavenger. According to the data on degradation efficiency, H_2O_2 and water were the end products of the RhB dye's breakdown. The addition of EDTA and BQ slightly altered the degradation efficiency of the reaction system. For the most part, holes and superoxide radicals were involved in the catalytic activity that RhB started when exposed to light. Evidence showed that by degrading RhB dye, FAS3 successfully expanded the visible light absorption range of the LED.

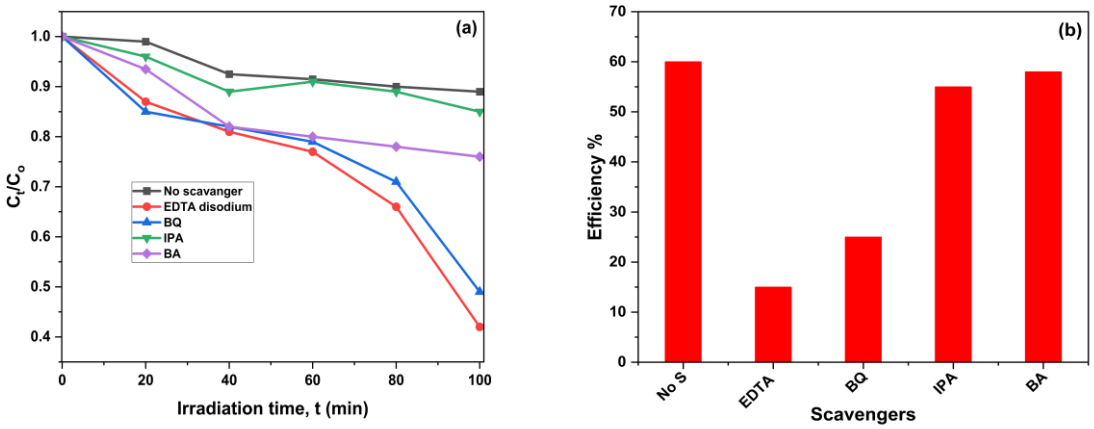

Fig. 3.3.9 (a) C_t/C_o Vs Irradiation time (b) Efficiency of different Scavengers.

3.3.8 EPR studies

The presence of solitary electrons bearing oxygen vacancies was investigated using the EPR spectroscopy technique. The EPR measurement improved our understanding of oxygen vacancy defects, and we discovered that the SnO_2 system included. This was in contrast to the lattice oxygen vacancies in Fig. 3.3.7 (XPS) and the surface oxygen vacancies in Fig. 3.3.8 (PL). Research by Kumar *et al*., (2018) and Shi *et al*., (2014) established a clear correlation between the peak intensity of the EPR and the presence of oxygen vacancies in the SnO_2 nanoparticle. The present study's results reveal resonances at 312.45 mT in the EPR spectra of FAS3 at ambient temperature (Fig. 3.3.10). The g-value of 2.160 was determined for FAS3 by the following equation, 3.12, which is presented in Section 3.2.9. In this case, the resonant

magnetic field proved it. Free electrons have a g-value of 2.099, which is nearly identical. The high-intensity peak found in the reported Fe_3O_4/Ag_x-Sn_yO_2 (FAS3) nanocomposite occurred for multiple reasons, and an abundance of oxygen vacancies was one of these causes.

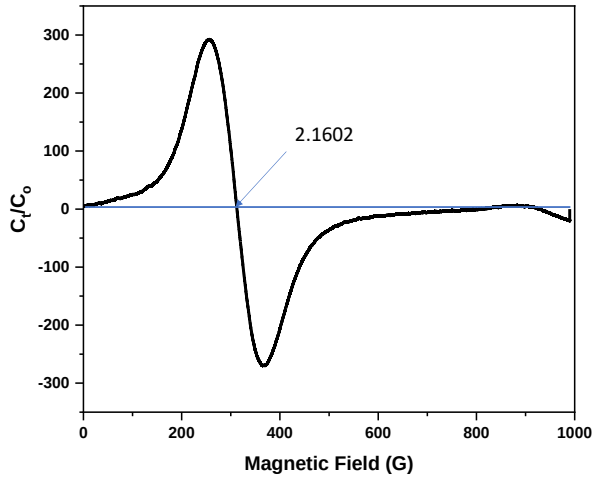

Fig. 3.3.10 EPR spectrum of FAS3, C_t/C_o Vs magnetic field (G)

3.3.9 Brunauer-Emmett-Teller (BET)

In the adsorption-desorption isotherms of FAS3, shown in Fig. 3.3.11, a monolayer of N_2 was adsorbed onto the mesoporous structure walls when the relative pressure was less than 0.4. The adsorption plot showed considerable variation due to the strong upward slope between 0.4 and 0.98. These variations are due to the tin mesoporous material's high capillary density. Particles outside surfaces undergo adsorption by many layers, which accounts for the upper part of the 0.48 value. Based on the results from the BET approach [Tao *et al*., (2013); Chen *et al*., (2014)], Table 3.3.2 records the particular surface area, dimensions, and volume of the cavities. FAS3 exhibited a higher specific surface area (5.877 m^2/g) compared to Fe_3O_4/SnO_2 (0.356 m^2/g). One possible explanation for this variation is that the metal nanoparticle structure effectively reduced the buildup of Fe_3O_4/SnO_2. According to the BJH pore size distribution plot, the aperture's more exceleent radius distribution was between 1 and 4 nm.

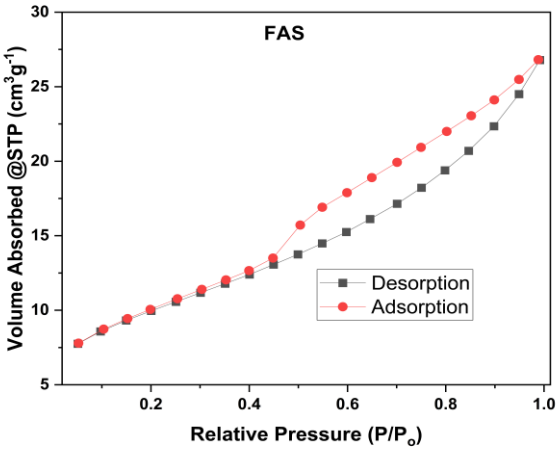

Fig. 3.3.11 Analysis of Brunauer-Emmett-Teller (BET) for Fe_3O_4/Ag_x-Sn_yO_2 (FAS3).

Table 3.3.2 lists the properties of the BET surfaces, volumes, and diameters for Fe_3O_4/SnO_2 and FAS3.

As-prepared	S_{Bet} (m^2/g)	Pore Volume (cm^3/g)	Pore Size (nm)
Fe_3O_4/SnO_2	2.142	0.132	2.058
Fe_3O_4/Ag_x-Sn_yO_2 (FAS3)	5.877	0.890	2.723

3.3.10 Photocatalytic Studies

Each experiment involved using 20 mL of wastewater containing an aqueous RhB solution with a concentration of 8 ppm. Additionally, 5mg of the prepared nanocomposite photocatalyst was subjected to sonication in complete darkness for 30 min to establish equilibrium between adsorption and desorption. In order to evaluate the extent of degradation, we obtained absorption spectra at different time intervals while exposing it to visible light. During this study, it was seen that as the duration of illumination grew from 0 to 150 min at intervals of 30 min, there was a decrease in the level of dye or pesticide absorption. This indicates that the pollutant was degraded by the photocatalyst composed of magnetic nanocomposite materials. Extended exposure to LED lights can cause organic colours to fade naturally.

The degradation of colourants was more pronounced when exposed to LED light than other types of light, mostly because of the substantial band gap energy and wide range of wavelengths emitted by LEDs. Following 150 min, we evaluated the extent

of deterioration expressed as a percentage for dyes and pesticide solutions that were exposed to LED radiation. We estimated it using the same formula that is mentioned in equation 3.3 under Section 3.1.9. Photocatalytic light absorption caused electron migration from the valence band (VB) to the conduction band (CB), resulting in the Z-Scheme. Active areas on the catalyst triggered the attachment of dye or pesticide molecules to the photocatalyst during adsorption. Below are the details of Fe_3O_4/Ag-SnO_2 photocatalysis.

$$\left.\begin{array}{c} Ag(e^- + h^+)/SnO_2(e^- + h^+) \rightarrow g - C_3N_4(e^- + e^-)/SnO_2(h^+ + h^+) \\ h^+ + OH^- \rightarrow OH \text{ (Oxidation)} \\ e^- + O_2 \rightarrow \dot{O}_2^- \text{ (Reduction)} \\ H_2O + \dot{O}_2^- \rightarrow O\dot{O}H + OH^- \\ 2O\dot{O}H \rightarrow \dot{O}_2^- + H_2O_2 \\ H_2O_2 + \dot{O}_2^- \rightarrow \dot{O}H + OH^- + O_2 \\ H_2O_2 + e^- \rightarrow \dot{O}H + OH^- \\ Fe^{3+} + H_2O_2 \rightarrow Fe^{2+} + O\dot{O}H + H^+ \\ Fe^{2+} + H_2O_2 \rightarrow Fe^{3+} + OH^- + \dot{O}H \\ \dot{O}H + RhB \rightarrow \text{ Decomposition products} \end{array}\right\} \quad (3.14)$$

Fig. 3.3.12(a) and (b) illustrated the utilization of Fe_3O_4/SnO_2 (FS) and FAS3 nanocomposite respectively to eliminate the rhodamine B (RhB) dye through photocatalysis under LED.

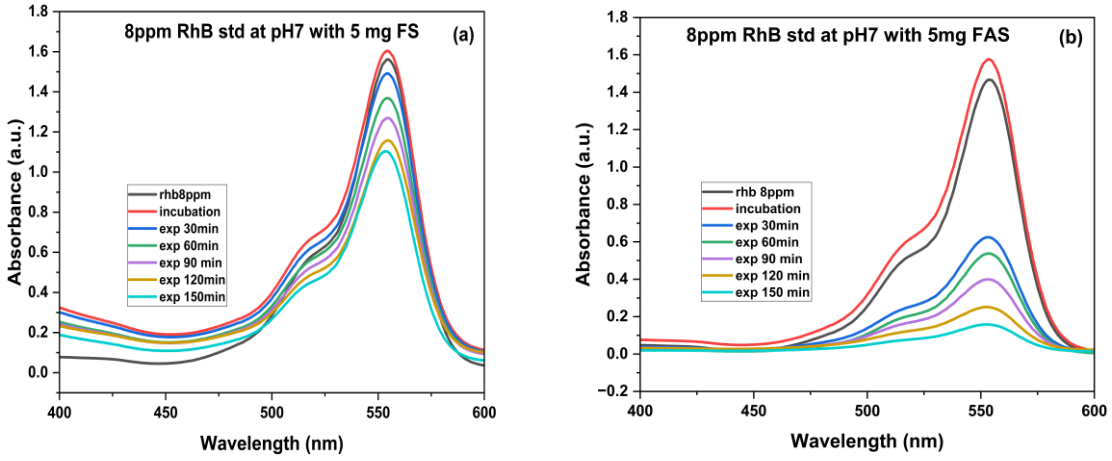

Fig. 3.3.12 Degradation RhB with (a) FS (b) FAS3.

3.3.11 Dosage effect

Determining the right amount of catalyst to degrade the dye solution was of utmost importance. We added 0.5–11mg of a manufactured catalyst to a 20 ml solution with 8 ppm of RhB and a pH of 7.38 before we turned on the light. Next, we examined the adsorption-desorption properties of the catalyst. More photocatalysts allowed for better absorption of RhB before the photocatalytic process since there were more active sites. This clarifies why increasing the dosage of the catalyst resulted in an increase in photocatalytic activity [Chen *et al*., (2016)]. According to An *et al*., (2013) and Yan *et al*., (2012), degradation efficiency is reduced when there is an excess of photocatalyst, which leads to more light scattering and less irradiation penetration. Even with larger quantities of photocatalysts, the efficiency of photocatalytic degradation has not increased noticeably. This is because of cumulative effects. Under LED light, the 8 ppm dye solution photocatalytically degraded without any effect from the device. We increased the catalyst quantity from 0.5 to 5 mg, which surprisingly positively affected decomposition efficiency from 4.6% to 10.6%. We observed this improvement across different systems. We observed this improvement across different systems. After increasing the catalyst dosage to 11 mg, the decomposition rate in 30 min changed, becoming slower, as shown in Fig. 3.3.13(a) and (b). After taking all of these factors into account, the best dosage of nanocomposite photocatalyst was found to be 5 mg.

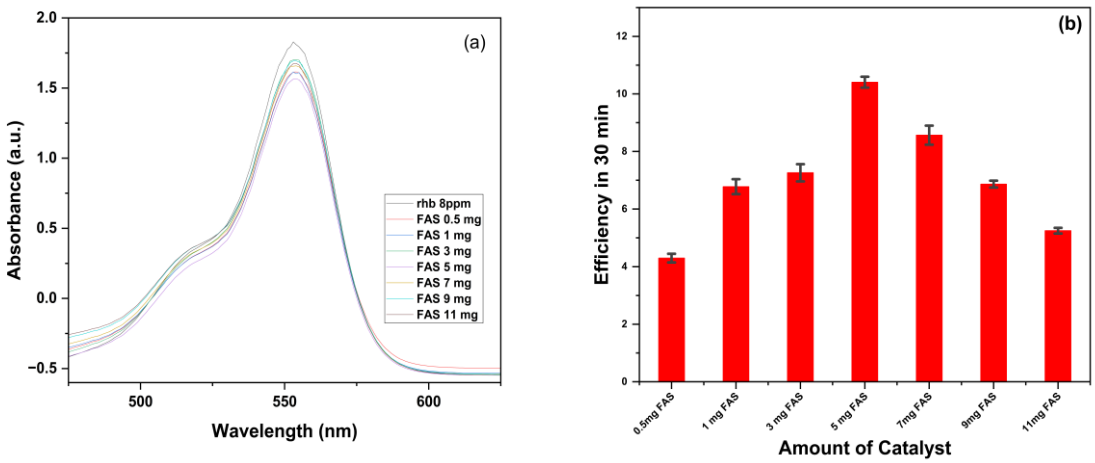

Fig. 3.3.13 ((a)-(b)) Different amounts of produced photocatalyst were used to determine the effectiveness of RhB degradation.

3.3.12 pH effect

In 20 mL of dye or pesticide solution, the initial concentration was 8 ppm, and the catalyst dose was 5mg. We determined that the breakdown mechanisms remained consistent across pH values ranging from 6 to 8. As the pH rose from 5 to 9, dyes and pesticides' solubility and photocatalytic degradation declined. The instability of the nanocomposite photocatalyst in an acidic solution may have distorted the heterojunction and diminished photocatalytic activity. The pH-dependent redox species similarly affected catalytic pollutant adsorption. According to Wei *et al.,* (2009) and Pouretedal *et al.,* (2009), hydroxyl radicals were more prevalent at neutral and alkaline pHs, while positive holes were more prevalent at lower pHs. It was typical for the chemical makeup of the surrounding environment to either hasten or slow down the degradation of pollutants. Rapid hydrolysis can accelerate the decomposition of dyes or pesticides at high pH values, such as pH 10. Exposure to an acidic environment causes the dye or insecticide to break down into its component elements. New degradation products with unique chemical properties might be formed due to this. Another solution with a higher pH likewise showed an interaction with hydroxide ions, although in much smaller amounts. When exposed to these ions, the pollutant molecules could degrade; hence, raising pH levels usually quickens these processes. Therefore, controlling the environmental pH was of utmost importance. The results thus far indicate that a pH of 6–8 was optimal for the nanocomposite photocatalyst. At irradiation times of 0 and t min, the concentration of RhB dye was determined using the equation $kt=\ln (C_o/C_t)$, which is based on the Langmuir-Hinshelwood model. So that we could be sure it was accurate and trustworthy, we ran the experiment three times.

3.3.12.1 MB Degradation

Following 150 min of exposure to LED light, the respective degradation efficiencies of 72.56, 70.42, 62.07, 66.04, 69.30, and 75.06% were observed in the FAS3 solutions with pH values ranging from 5 to 10. The pure MB dye degrades by 3% when exposed to LED light, a negligible decrease. At pH 10, the LED-MB-FAS3 solution degrades at an estimated rate of 75.06% after 150 min of exposure to LED radiation, making it the most severely degraded. Taking the logarithm of the ratio C_o/C_t

allowed us to do a linear regression and estimate the rate constant (k) for fitting absorption time, and Fig. 3.3.14(a) shows the line's resultant slope. Due to this interaction, chemical bonds like sulphur-chlorine, nitrogen-methyl, carbon-sulphur, carbon-nitrogen, and carbon-oxygen dissociate. In the end, smaller organic molecules were produced after a chain reaction broke down intermediate components and opened MB rings. The process is complete at mineralisation, and the end molecules are CO_2 and H_2O, presented in Fig. 3.3.14(b).

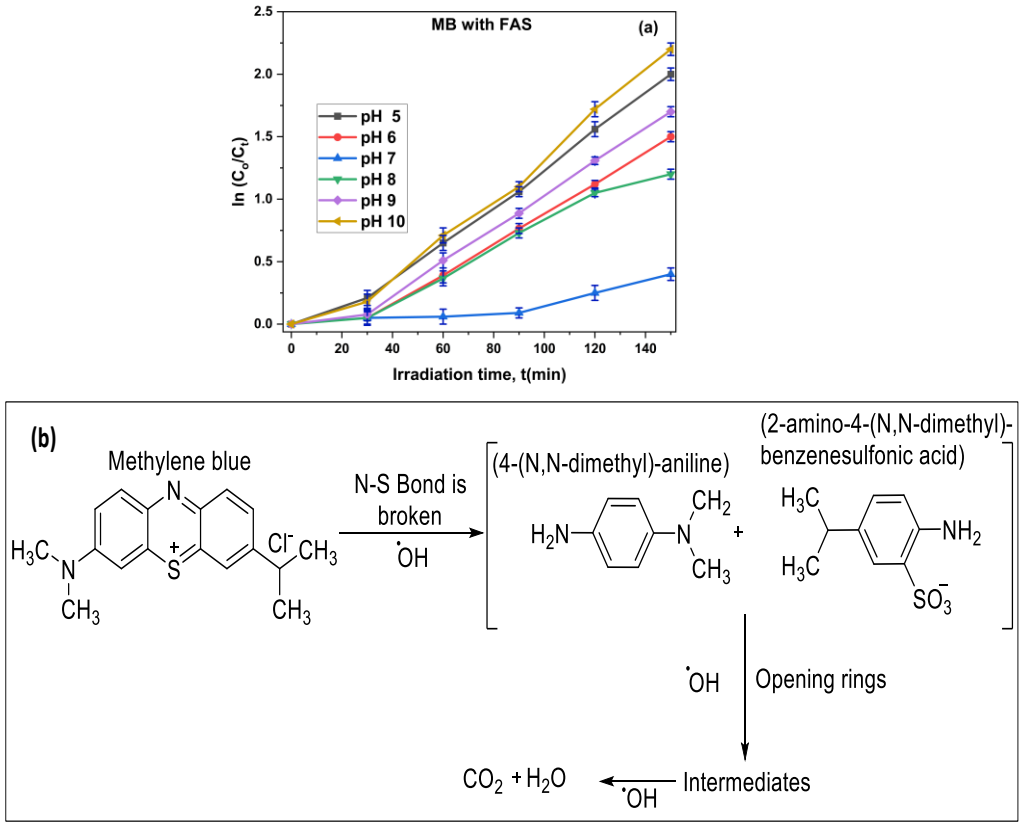

Fig. 3.3.14 (a) Kinetics of photodegradation (b) Mineralization of MB.

3.3.12.2 RhB Degradation

The adsorption investigation for FAS3 at pH values ranging from 5 to 10 demonstrates the cationic character of RhB, with degradation efficiencies of 67.83, 65.86, 59.85, 61.82, 65.86, and 70.07%, respectively. In the absence of FAS3 nanocomposite, RhB dye degradation under LED illumination is only 2%, which is considered minimal. Confirming prior research, these rates of degradation have been

established, and the LED-RhB-FAS3 sample showed the most potential, as it successfully decomposed 70.07% of the RhB compound during a duration of 150 min, similar to previous photocatalysis experiments. We performed a linear regression and calculated the slope of the line using the logarithm of the ratio C_o/C_t. The results of this regression are displayed in Fig. 3.3.15 (a). Because of this, we were able to calculate an estimate of the rate constant k for the absorption rate. Upon the elimination of the ethyl groups, the resulting products possess the capability to undergo subsequent reactions, ultimately leading to the formation of simpler molecules, including m/z (terephthalic acid) =166.12, m/z (3-hydroxybenzoic acid) =122.11, m/z (benzoic acid) =122.11, m/z (succinic acid) =118.08, m/z (adipic acid) =146.13, and carbon dioxide. The abovementioned process is referred to as mineralization, when organic compounds undergo decomposition into their fundamental inorganic forms, such as CO_2, water, and mineral ions, as seen in Fig. 3.3.15 (b).

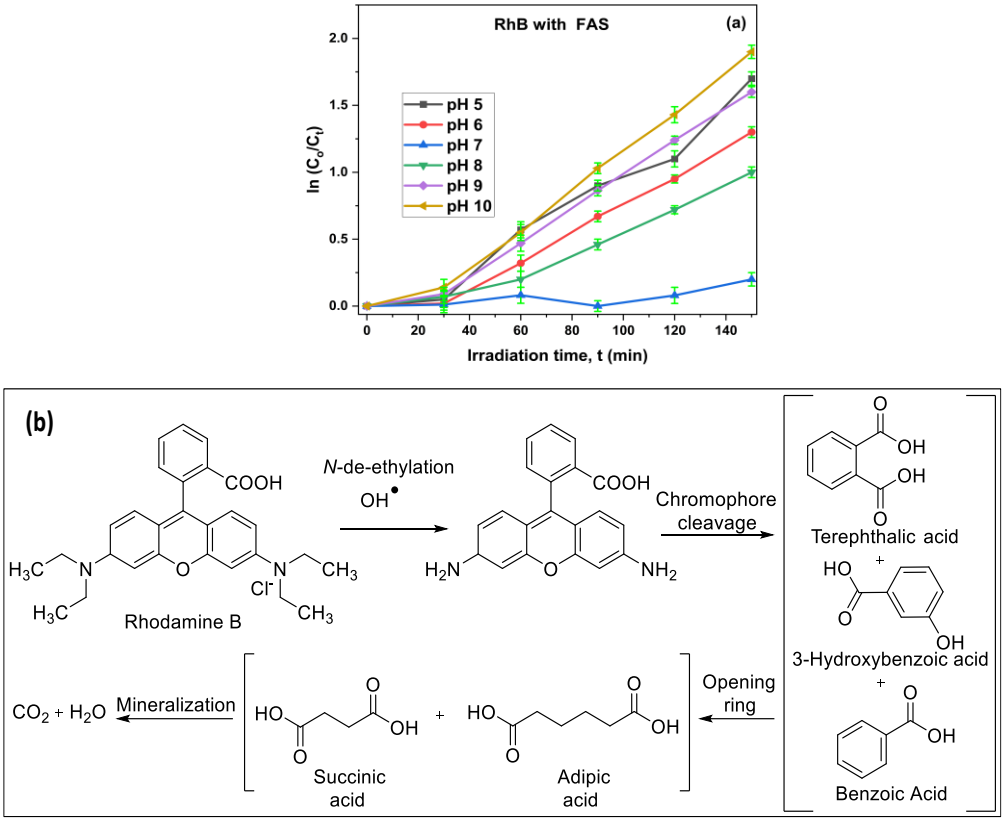

Fig. 3.3.15 (a)) Kinetics of photodegradation (b) Mineralization of RhB.

3.3.12.3 MB and rhodamine (mixture) Degradation

At pH 7, both colours are absorbed within 150 min under LED light solutions containing FAG degradation, with an efficiency rate of 62.46 and 59.08%, respectively. This occurred because of the electrostatic attraction between the positively charged dye molecules and the FAS3 surface, resulting in increased absorbency. However, only 1% of the MB and RhB mixture is degraded when using LED light.

The LED-MB-FAS3 solution showed a maximum degradation percentage of around 62.46% after being exposed for 150 min at a pH of 7, as shown in Fig. 3.3.16((a)-(c)). The reduction in size and band gap of FAS3 nanoparticles results in an augmentation of surface area and an enhancement of photocatalytic performance. When mixed in water, several factors can diminish the solubility of rhodamine B (RhB) and methylene blue (MB).

Possible factors contributing to the observed decrease in solubility, such as the interface between the dyes and water, were a possible area for adsorption where RhB and MB molecules may compete. Blending two colours with low water solubility may result in competitive adsorption, reducing the overall water solubility of the mixture. RhB and MB molecules can form clusters in water. This phenomenon can also occur when different hues come into contact. The aggregation process decreases the overall solubility of each particular hue in the combination. The development of complexes between RhB and MB molecules can affect their solubility.

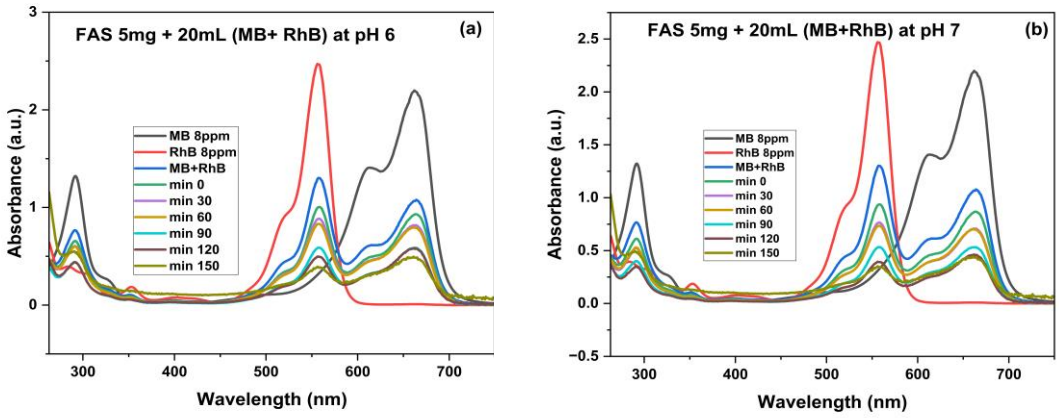

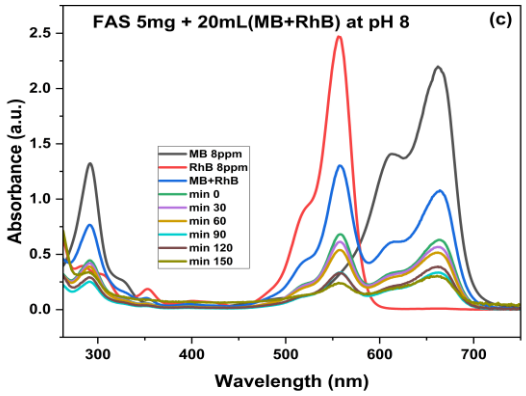

Fig. 3.3.16 Degradation of MB and RhB mixtures with FAS3

3.3.12.4 Degradation of 2, 4-DCP under LED irradiation

The UV-visible spectra of 2,4-DCP photodecomposition under the condition specified for the experiment were obtained at various pH values. Studies conducted on the adsorption of FAS3 at pH values ranging from 5 to 10 produced degradation efficiency percentages of 86.40, 83.56, 77.44, 72.98, and 70.86%, respectively with 5 mg of FAS3. We carried out a linear regression and used the logarithm of the ratio C_o/C_t in the regression analysis to determine the slope of the line for 2,4-DCP. The outcomes of these regressions are presented in Fig. 3.3.17 (a) with the respective results. As a result, we were able to compute an estimate of the rate constant k when it comes to the rate of absorption. Furthermore, the mineralization rates for 2,4-DCP varied between 3% and 43% over the course of 150 min. As shown in Fig. 3.3.17(b), this suggests that one of the final effects of mineralization is the breakdown of 2,4-DCP into CO_2 and H_2O.

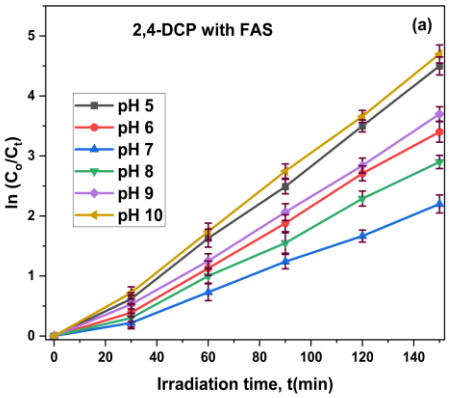

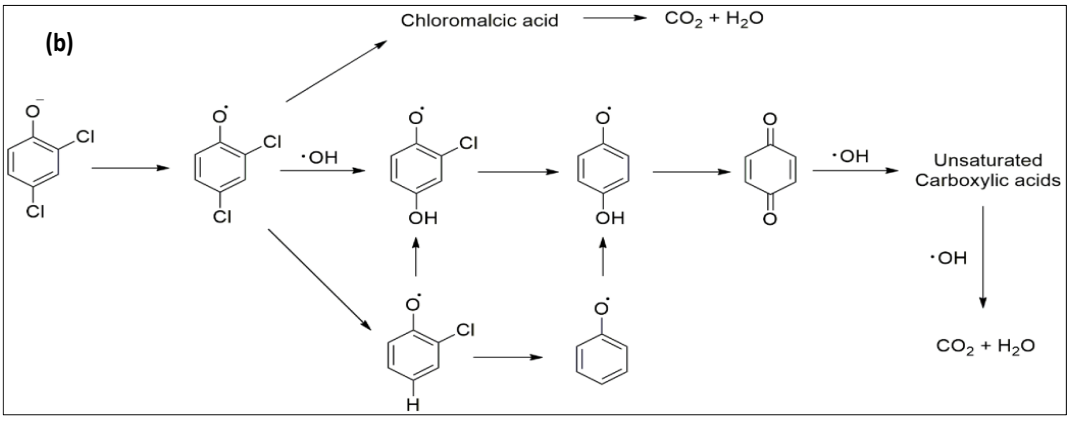

Fig. 3.3.17 (a) Kinetics of photodegradation of 2,4-DCP (b) Mineralization of 2,4-DCP

3.3.12.5 TCAA degradation

The study aimed to determine how well FAS mineralized trichloroacetic acid (TCAA) within a pH range of 5 to 10, emphasizing total organic carbon (TOC) removal. The analysis of 8 ppm standard TCAA was done through HPLC; the chromatograph is shown in Fig. 3.3.18(a). Using an 8 ppm concentration of TCAA and 5mg of FAS3, which have a 150 min contact duration, was evaluated using HPLC and revealed the mineralization and degradation of TCAA by FAS3, as depicted in Fig. 3.3.18(b). At the same time, Fig. 3.3.18(c) displayed the results of a linear regression that was performed to ascertain the slope of the line for TCAA, the logarithm of the ratio C_o/C_t was used in this process. Using numerical calculations, this allowed us to approximate the absorption rate's rate constant, k.

We discovered that the breakdown intermediates of hydroxyacetic acids, formic acid, and acetic acid were not as dangerous as the initial TCAA. Mass chromatograms showed the breakdown of TCAA to include formic acid (CH_2O_2, m/z 46, R_t 4.53 min), hydroxyacetic acid ($C_2H_4O_3$, m/z 93, R_t 4.57 min), and acetic acid ($C_2H_4O_2$, m/z 62, R_t 3.43 min). LCMS studies confirmed these acids. LCMS analysis detected formic acid as the primary compound, even though it formed from an intermediate with m/z 62. According to the findings, acetic acid and hydroxyacetic acid were the primary byproducts of TCAA degradation. Fig. 3.3.18(d) shows a possible route for TCAA

degradation in the FAS process based on molecular characteristics determined by LCMS and related studies.

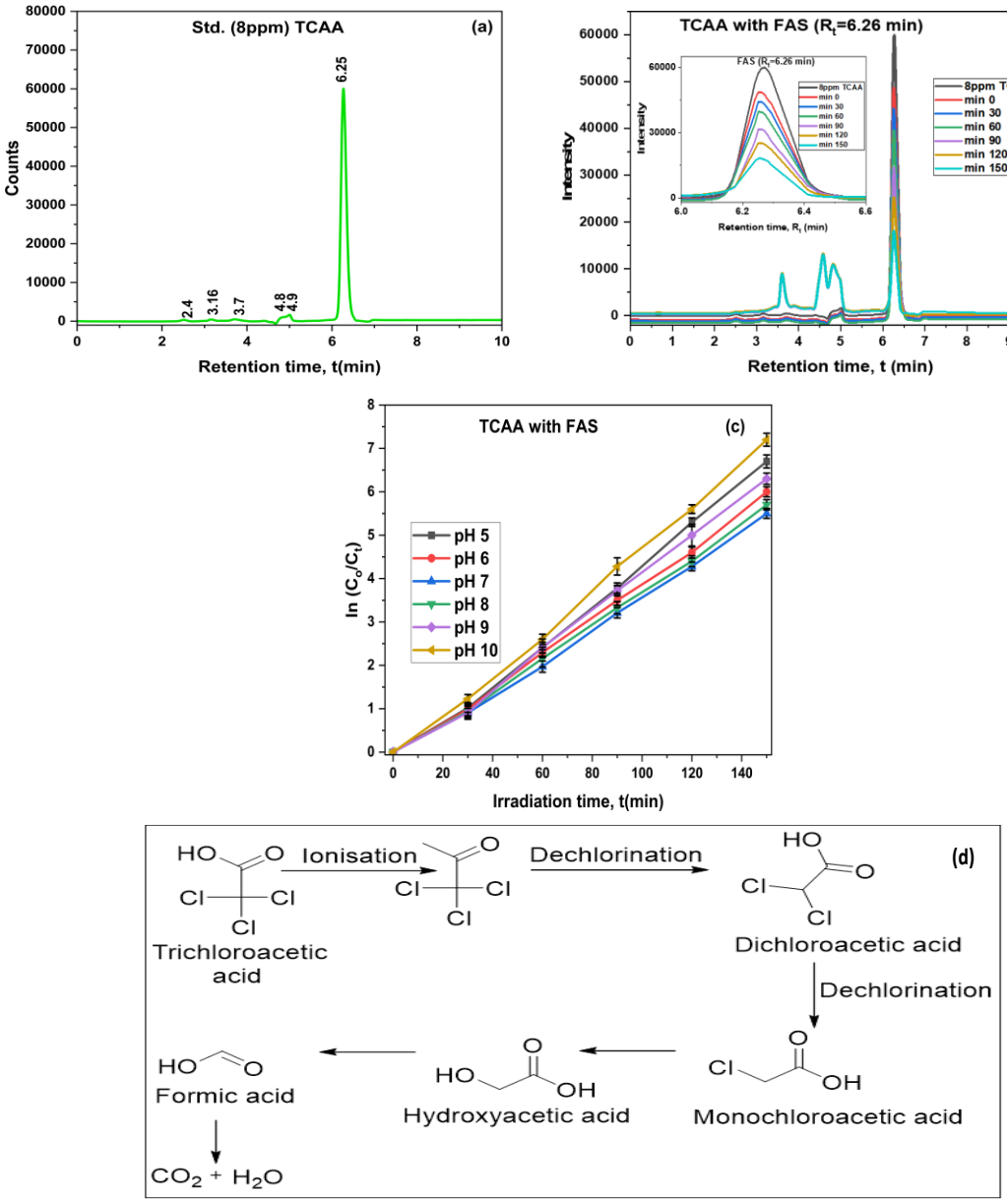

Fig. 3.3.18 (a)Standard TCAA (8ppm) (b)TCAA decomposition with 5mg of FAS3 (c) Kinetics of photodegradation of TCAA (d) Mineralization of TCAA.

3.3.13 TOC (total organic carbon) determination

The rhodamine B mineralization method was determined by measuring the total carbon content. According to Fig. 3.3.19, the addition of 5mg of FAS3 to the dye resulted in a decrease in its absolute total organic carbon (TOC) value when the

concentration was 8 ppm. The efficacy of photomineralization was 53%. The efficacy of photomineralization was 61%. The photomineralization efficiency decreased to 43% when using Fe_3O_4/SnO_2 with an equivalent amount of photocatalyst. The restricted number of operational sites on the catalyst surface hindered the predicted reaction, decreasing the absolute total organic carbon (TOC) removal value from 53 to 43%.

Moreover, these findings offer a valuable understanding of the possibility of connecting the residual total organic carbon (TOC) in these samples to the reaction that took place between complete mineralization and the intermediate stages. The RhB degradation due to demineralization was precisely determined using equation 3.7, mentioned under Section 3.1.10. In order to ensure the accuracy and reliability of the experiment, we conducted it three times separately.

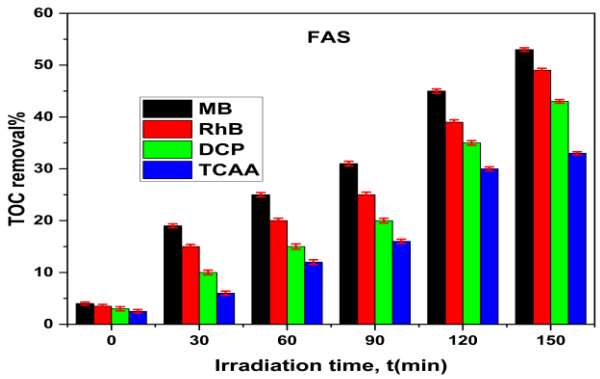

Fig. 3.3.19 TOC removal% of MB, RhB, 2,4-DCP and TCAA with Fe_3O_4/Ag_x-Sn_yO_2 (FAS3).

3.3.14 Turnover number and turnover frequency

Evaluating the Turnover Number (TON) and Turnover frequency (TOF) is crucial in assessing the immediate effectiveness of a catalyst. The TON value quantifies the efficiency of converting substrate molecules into product molecules per photocatalyst molecule during a given period. One potential method for finding this is by utilizing the formula given in 3.8 in Section 3.1.11, while the percentage conversion quantifies the extent of degradation achieved by the photocatalyst. On the other hand, Turnover Frequency (TOF) is determined as the highest number of catalytic cycles

performed by each active site within a specified period, as expressed by equation 3.9, section 3.1.11. Table 3.3.3 presents the results of the TON and TOF experiments carried out on methylene blue (MB) and rhodamine B (RhB) during their degradation processes using sunlight and UV light as catalysts.

When subjected to LED radiation, the FAS3 nanocomposite demonstrated the highest TON (Turnover Number) and TOF (Turnover Frequency) values in the degradation of both the MB (methylene blue) and RhB (rhodamine blue) colourants. We were impressed by this result for the improved performance, presumably attributed to the previous statement, as a consequence of the reduction in size, which has led to an increase in both the surface area and the number of active sites. This phenomenon leads to an enhanced breakdown of organic pollutants.

Table 3.3.3 Determination of TOF and TON

Dyes	Photocatalyst	TOF (min^{-1})	TON (min^{-1})
MB	FAS3	28.374	0.189
RhB	FAS3	48.378	0.322
2,4-DCP	FAS3	8.769	0.058
TCAA	FAS3	4.492	0.029

3.3.15 Reusability

Fe_3O_4/SnO_2 and FAS3 broke down dyes and pesticides after 150 min of irradiation under LED light. The most important photocatalyst qualities were stability and recyclability, and we learned how stable and reusable the magnetic nanocomposite photocatalyst was by watching it in action during recycling. Nanocomposite photocatalyst recycling for RhB breakdown is shown in Fig. 3.3.20, and an external magnet separates the nanocomposite photocatalyst from a mixed solution every five cycles. Reused nanocomposite photocatalysts were mixed with a new dye solution, and RhB's breakdown efficiency dropped from 70 to 63% in 150 min. Decomposition efficiency varied slightly because used-by-used nanocomposite photocatalyst performance might diminish due to intermediate products from degraded RhB

adhering to the surface and not breaking down completely. However, the nanocomposite photocatalyst decomposed RhB under visible light with outstanding stability and reusability.

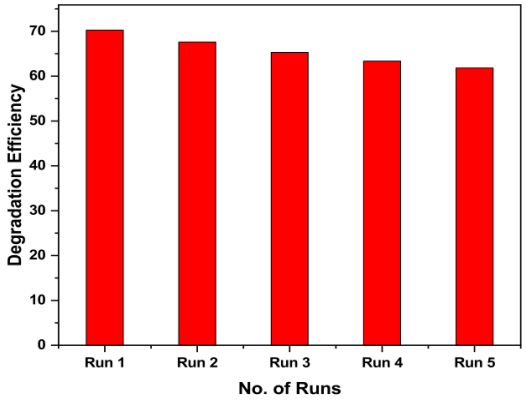

Fig. 3.3.20 Number of recycles for reusing of FAS3.

3.3.16 Magnetic Quality

Fig. 3.3.21 shows the results of a study into the magnetic response of Fe_3O_4 nanoparticles and the magnetically active ternary nanocomposite FAS3, which was conducted by assessing the magnitudes of coercivity (MH). All magnetic Fe_3O_4 nanocomposites had symmetric hysteresis and saturation magnetization. Pure Fe_3O_4, Fe_3O_4/SnO_2, and FAS3 showed saturation magnetizations of 20.70, 17.23, and 8.34 emu/g, respectively. The surface noncollinear spin arrangement might decrease magnetic moment in Fe_3O_4 nanoparticles with small particle size [Farzaneh *et al*., (2016); Mohammed, (2021)]. Fe_3O_4 might have reduced its magnetic properties since SnO_2 and Ag were non-magnetic. From this study, it was revealed that the ternary nanocomposite composite photocatalyst exhibited high saturation magnetization in order to improve recovery and recyclability by isolating it from the solution using an external magnetic field.

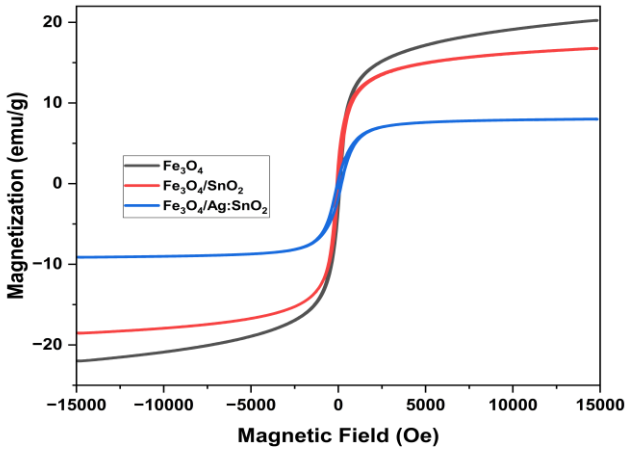

Fig. 3.3.21 VSM of Fe_3O_4, Fe_3O_4/SnO_2, Fe_3O_4/Ag_x-Sn_yO_2 (FAS3)

3.3.17 Developing a Photocatalyst for the Degradation of RhB

Fig. 3.3.22 shows that we developed a strategy for RhB dye degradation using nanocomposite photocatalysts. The conduction band (CB) energy levels in heterojunctions, like the Ag/SnO_2 system, can be varied. An electron moving through a material would traverse its conduction band. SnO_2 has lower conduction band energy, making it a potential electron donor for Ag. Dyes could react with electrons located in the conduction band of silver. This expedited the dye-to-nanocomposite photocatalyst chemical process. The nanocomposite photocatalyst's higher photocatalytic efficacy was due to several factors, including increased visible light absorption, slowing down the rate of charge pair recombination, and keeping RhB dye molecules adsorbed.

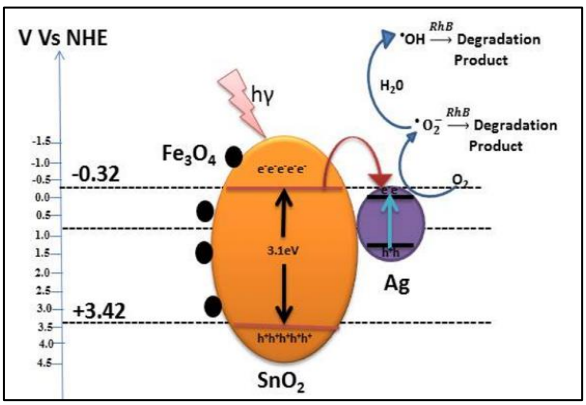

Fig. 3.3.22 Photocatalyst for the Degradation of RhB

3.3.18 Comparison

Table 3.3.4 presents the degradation constants for various materials, which indicate their photocatalytic activity. Under conditions of greater alkalinity, characterized by a higher concentration of hydroxyl ions, both dyes' degradation rate constants increased. The degradation constant of the LED-MB-FAS3 solution exhibited a more excellent value than that of the LED-RhB-FAS3 solution, specifically at pH 7. Furthermore, the LED-MB-FAS3 (pH 7) solution undergoes degradation more rapidly than the LED-RhB-FAS3 solution.

The key distinguishing factor between the two compounds is their chemical structure. Specifically, Rhodamine B's more extensive and complex molecular structure was responsible for its uniqueness. Photocatalysis can degrade dye molecules to varying extents depending on their structural features. The outcomes of our study demonstrate that FAS nanocomposite produced using an ecologically benign process employing Parkia speciosaextract not only surpasses the findings reported in previous literature but also exhibits superior overall performance. This method is highly efficient in the breakdown of water pollutants. The study looked at how well FAS3 broke down 2,4-dichlorophenol (2,4-DCP) and trichloroacetic acid (TCAA) by checking how much total organic carbon (TOC) was removed over a pH range of 5 to 10. Fig. 3.3.23 shows a direct comparison of the degradation of 2,4-DCP and TCAA by FAS3 under particular conditions, including an 8 ppm catalyst concentration and a 150 min contact period. Given these conditions, the rates at which 2,4-DCP and TCAA degraded were approximately 63 and 47%, respectively.

Furthermore, throughout the 150 min period, the rates of mineralization for 2,4-DCP varied between 3 and 43%, whereas for TCAA, the rates ranged from 2.5 to 33%. This suggested that the mineralization end products involve the significant breakdown of 2,4-DCP and TCAA into carbon dioxide (CO_2) and water (H_2O). The observed positive association between the rate of mineralization and the duration of the reaction is a noteworthy finding, as it implies that a longer reaction time is necessary for the complete mineralization of TCAA. The findings indicate that the FAS3 nanocomposite outperformed the degradation of RhB, MB, 2,4-DCP, and TCAA.

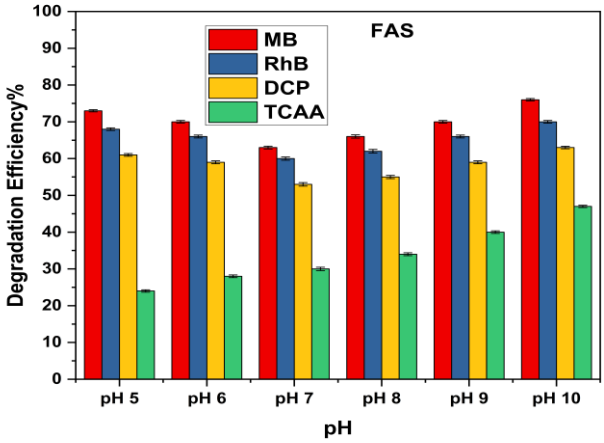

Fig. 3.3.23 Degradation efficiency with FAS3 photacatalyst

Table 3.3.4 Estimation of Rate constant for photodegradation

pH	MB		RhB		DCP		TCA	
	k (min^{-1})	R^2	k (min^{-1})	R^2	k (min^{-1})	R^2	k (min^{-1})	R^2
pH 5	0.0498	0.9549	0.0558	0.9319	0.0366	0.9439	0.0373	0.9539
pH 6	0.0466	0.9549	0.0527	0.9499	0.0336	0.9319	0.035	0.9279
pH 7	0.0433	0.9569	0.0446	0.9379	0.0336	0.9539	0.0309	0.9299
pH 8	0.0447	0.9519	0.0505	0.9619	0.0419	0.9339	0.0323	0.9359
pH 9	0.0477	0.9339	0.0549	0.9279	0.0349	0.9479	0.0369	0.9339
pH 10	0.0519	0.9379	0.0566	0.9339	0.043	0.9439	0.038	0.9479

For RhB, MB, 24-DCP, and TCAA treated with FAS under LED light, the pseudo-first-order model (R^2 = 0.936, 0.952, 0.916, 0.876) aligns better with experimental data than the pseudo-second-order model (0.766, 0.824, 0.882, 0.764), This reaction may follow pseudo-first-order kinetics.

3.4 Effect of Pr^{3+} on SnO_2 in Fe_3O_4/Pr^{3+}-doped SnO_2 ternary nanocomposite for degradation of dyes and pesticides.

Pr^{3+} doping introduces intermediate energy levels in SnO_2's band gap, improving visible light absorption. This makes the Fe_3O_4/Pr^{3+}-doped SnO_2 nanocomposite more effective in visible light than pure SnO_2, which absorbs UV light. Pr^{3+} ions trap electrons, slowing electron-hole pair recombination. More charge carriers are available for photocatalytic processes. Pr^{3+} enhances charge carrier mobility, boosting composite electron transfer. Fe_3O_4 and Pr^{3+}-doped SnO_2 synergistically boost photocatalytic activity. Fe_3O_4 adds magnetic characteristics and photocatalytic activity to SnO_2, while Pr^{3+} doping improves light absorption and charge separation. Pr^{3+} broadens the composite's absorption spectrum, allowing it to use more solar spectrum. Fe_3O_4 makes the nanocomposite magnetic, making photocatalyst recovery and reuse easier using a magnetic field.

The nanocomposite Fe_3O_4/Pr^{3+}: SnO_2 (FPS1) (with Pr^{3+} 1 at.%) exhibited excellent photodegradation of RhB dye, as depicted in Fig. 3.4.1. We evaluated absorption intensity as a means of assessing the photocatalytic efficiency of the ternary nanocomposite we prepared, with the aim of degrading RhB (Sigma Aldrich) dye in an aqueous solution.

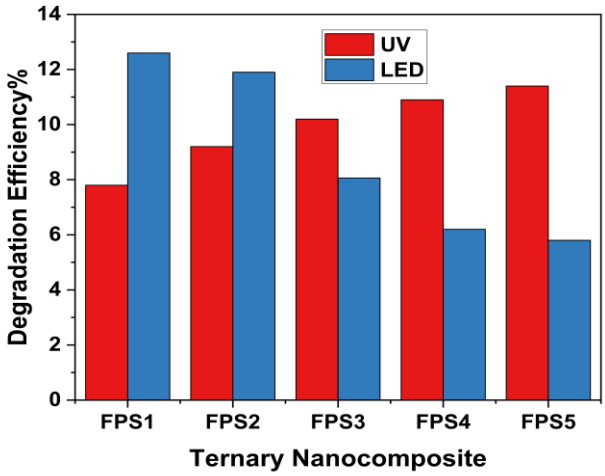

Fig. 3.4.1 The efficiency of the catalyst developed is enhanced by exposure to UV and LED light, leading to increased deterioration.

Based on these investigations, we found that ternary nanocomposite containing Fe_3O_4/(1 at.%) Pr^{3+}:SnO_2 (FPS1) is highly effective in degrading RhB when exposed to LED light. We focused on characterising and exploring the applications of FPS1, which has 1 at.% of Pr^{3+}.

3.4.1 X-ray Diffraction analysis

Nanocomposite was created by combining Fe_3O_4, SnO_2, and praseodymium ions. The X-ray diffraction patterns of Fe_3O_4/ Pr^{3+}: SnO_2 nanocomposite with 1, 5, and 9 at.% Pr^{3+} are depicted in Fig. 3.4.2. The catalyst exhibited diffraction peaks at specific angles, namely 18.27°, 26.32°, 29.80°, 33.43°, 36.74°, 50.34°,57.29°, 62.65° and 65.01° among others. The 2θ values of 18.27°, 29.80°, 36.74°, 57.29° and 62.65° for Fe_3O_4 correspond to the *hkl* planes (111), (220), (311), (330), and (440), respectively, and this alignment has been confirmed by JCPDS 41-1445.

Further, SnO_2 was described by looking at its *hkl* planes (110), (101), (211), and (310), and finding that their 2θ, values are 26.32°, 33.43°,50.34° and 65.01° respectively. These values were then compared with the JCPDS 82-1533 database for matching purposes. Incorporating praseodymium into SnO_2 will have an effect on the crystal structure of the material, as seen by the XRD patterns of 1%, 5%, and 9% Pr-doped tin dioxide. As the doping levels increased, we noticed a shift in peak positions towards a lower 2θ value, changes in peak strength, and broadening of peaks. These observations suggest that there were changes in lattice characteristics, crystallite size, and strain inside the crystal structure.

The leftward shift of the 2θ angle in X-ray Diffraction (XRD) patterns for praseodymium (Pr)-doped SnO_2 can be attributed to the following factors like Praseodymium ions (Pr^{3+}) ion replace some of the tin ions (Sn^{4+}) in the SnO_2 lattice when integrated. The higher ionic radius of Pr^{3+} ions (about 0.99 Å) compared to Sn^{4+} ions (0.71 Å) lead to an expansion of the SnO_2 lattice when Pr^{3+} ions are incorporated into it. This expansion causes an increase in the distance between the crystal planes (interplanar spacing or d-spacing) in the crystal structure. As a result, the peaks observed for (110), (101), (211), and (310) in X-ray diffraction (XRD) shift towards lower 2θ values, in accordance with Bragg's law. In addition, the addition of Pr^{3+} to SnO_2 might result in the presence of imperfections, such as oxygen vacancies or

interstitials, inside the crystal structure and these imperfections can cause the lattice to become distorted and expand. The existence of these imperfections alters the lattice parameters, resulting in a displacement of the diffraction peaks towards the left (lower 2θ values). The effective preparation of nanocomposites FPS was confirmed by XRD analysis, and the addition of Fe_3O_4, Pr^{3+} to SnO_2 did not alter the tetragonal structure.

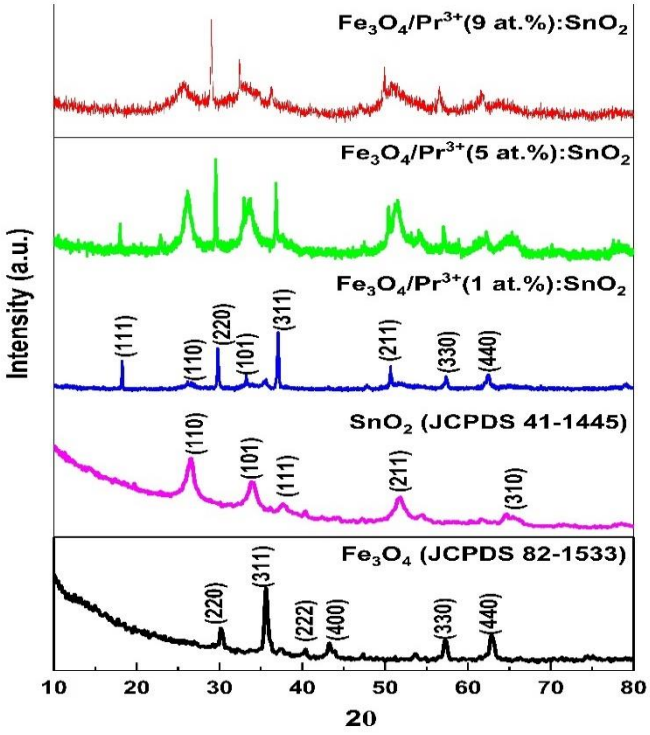

Fig. 3.4.2 XRD pattern of Fe_3O_4/Pr^{3+}: SnO_2 (1, 5 and 9 at.%).

The Scherrer formula (3.1 under Section 3.1.1) was utilised to ascertain the average particle size (D). Table 3.4.1 presented about the details of average grain size that was estimated using Scherrer's method.

Table 3.4.1 The synthesized nanocomposite(s) were measured for their average crystallite size, parameters, and cell volume.

Sample	Crystallite Size(nm)	Lattice Parameters			Cell volume
		a (Å)	b (Å)	c (Å)	
Fe_3O_4	76.708	8.284	8.284	8.284	582.325
SnO_2	53.066	4.564	4.564	3.023	69.924

Praseodymium	32.489	3.562	3.562	10.744	140.42
Fe_3O_4/SnO_2(FS)	54.224	4.826	4.826	3.266	73.468
Fe_3O_4/Pr^{3+}:SnO_2(FPS1)	30.310	3.604	3.604	11.220	142.08

3.4.2 FT-IR Spectroscopy analysis

Fig.3.4.3 displayed the X-ray diffraction patterns of Fe_3O_4/Pr^{3+}:SnO_2 nanocomposite, where the SnO_2 was doped with 1, 3, 5, 7, and 9 at.% of Pr^{3+} ions. An extensive absorption band ranging from 400 to 600 cm^{-1} was detected, corresponding to the stretching vibration mode of the metal-oxygen (Fe-O) connection. The stretching and vibration band corresponding to the metal in the octahedral or tetrahedral oxide structure revealed the crystalline lattice of the Fe_3O_4 molecule in the (Fe-O) link. At the same time, the peak at 771.52 cm^{-1} indicated the presence of irregular SnO_2. Conversely, the subtle peak observed at wavelengths ranging from 1219.01 to 1519.90 cm^{-1} can be attributed to the vibrations caused by the bending of OH groups [Brojendro Singh Shagolsem, Nongmaithem Mohondas Singh, (2024)]. SnO_2 can be synthesised to yield several types of hydroxyl hybrid groups, as shown by the absorption bands observed in the range of 1060 to 1500 cm^{-1}. The presence of water molecules caused the absorption of particular vibrations related to the bending and stretching movements of the hydroxyl group, resulting in peaks at 1651.06 cm^{-1} and 3140.11 cm^{-1}, respectively [Hunge *et al*., (2023); Fageria *et al*., (2015)].

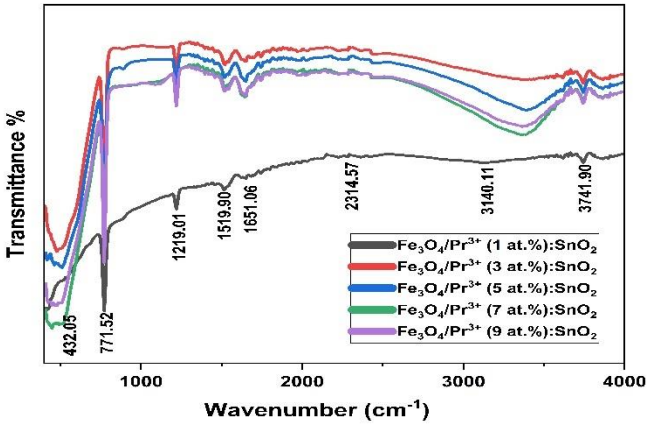

Fig. 3.4.3 FT-IR Spectrum of 1, 3, 5, 7 and 9 at.% of the Fe_3O_4/Pr^{3+}: SnO_2.

3.4.3 UV-visible spectroscopy analysis

We examined the UV-visible spectra of the synthesised nanocomposite, which has different atomic percentages of praseodymium ions. Light absorption in the 200–1000 nm region was seen in the synthesised magnetically active Fe_3O_4, and the band gap energy of Fe_3O_4 was determined to be 1.726 eV [Brojendro singh Shagolsem, Nongmaithem Mohondas Singh, (2024)].

Further, UV-visible spectra and band gap energy calculations of ternary nanocomposite having various atomic percentages of praseodymium doped SnO_2 are shown in Figs. 3.4.3(a) and (b), respectively. Out of the different amounts of doping catalysts, FPS1, which is 1 at.% of Pr^{3+}-doped SnO_2, showed the lowest band gap energy value. We will use this specific catalyst for future analysis and dye breakdown.

By examining the data from the UV-visible spectra and using the Tauc relation (3.2 under Section 3.1.3), the optical band gap energy was determined. The band gap energy of the Fe_3O_4/Pr^{3+}: SnO_2 having1, 3, 5, 7 and 9 at.%) composite was determined to be 2.56, 3.01, 3.25, 3.4, and 3.6 eV respectively.

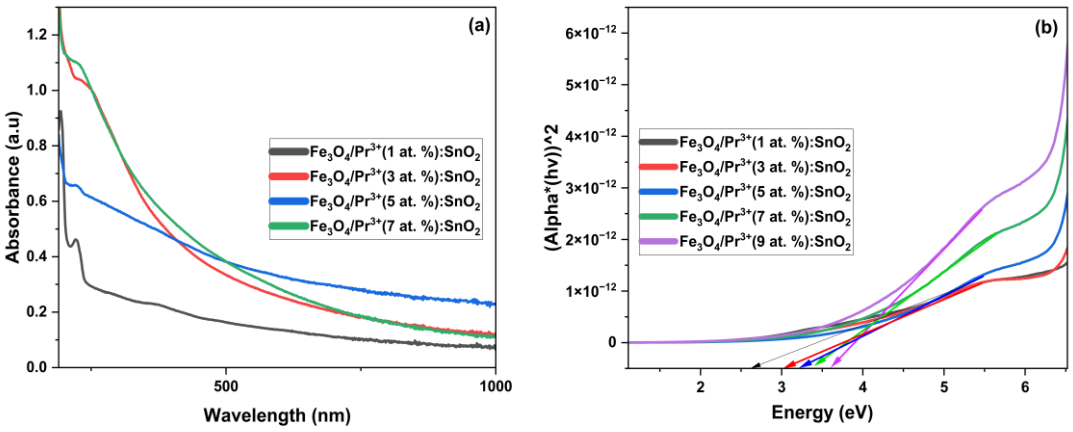

Fig. 3.4.4(a) UV-visible spectrum and (b) Fe_3O_4/Pr^{3+}: SnO_2 band gap energy calculation.

The valence band spectra were utilized to ascertain the optimal mechanism for separating photo-induced electrons and holes in Fe_3O_4/SnO_2 (FS) and Fe_3O_4/(1

at.%)Pr^{3+}: SnO_2 (FPS1). The objective of this experiment was to synchronise the electric potentials at the boundary of the conduction band (E_{CB}) and the valence band (E_{VB}) and to evaluate the process of charge transfer. The relationship proposed by reference [Haque *et al*. (2011)] can be utilized to assess the potential energy level of the E_{CB} and E_{VB} (equations 3.9 and 3.10 under Section 3.2.3).

The energy band gap (E_{VB}) values for SnO_2 and Pr-doped SnO_2 at various concentrations (1, 3, 5, 7, and 9 at.%) were measured and found to be 3.59, 3.58, 3.57, 3.56, 3.54, and 3.51 electron volts (eV), respectively, which is presented in Fig. 3.4.5. The E_{CB} values for the identical samples were -0.09, -0.08, -0.075, -0.07, -0.064, -0.073, and -0.074 electron volts, respectively. This clarifies why, upon exposure to visible light, the excited electron readily jumps from SnO_2's electron conduction band (E_{CB}) to the CB of a Pr^{3+}-doped SnO_2 nanoparticle. As a result, the SnO_2 and Pr^{3+}-doped SnO_2 nanoparticles can absorb light within the visible light spectrum, reducing recombination. Reactive hydroxyl and superoxide radicals are critical for enhancing the pathways of photocatalytic reactions. This was demonstrated by the band edge potential of photocatalysts consisting of SnO_2 and Pr^{3+}-doped SnO_2 nanoparticles.

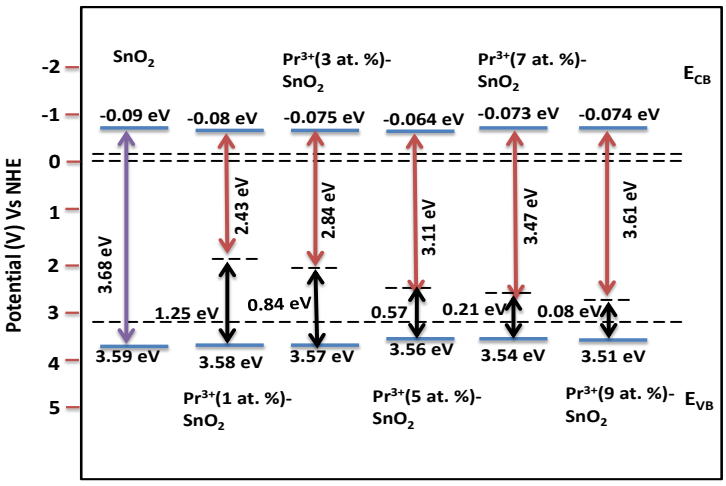

Fig. 3.4.5 Conduction and Valence band calculation of various prepared Fe_3O_4/Pr^{3+}: SnO_2.

3.4.4 Scanning electron microscope (SEM) studies

The Fe_3O_4/Pr^{3+}: SnO_2 (1 at.%) (FPS1) nanoparticles were imaged using a scanning electron microscope (SEM), and the image is illustrated in Fig. 3.4.6(a). Based on the scanning electron microscope (SEM) image, it was evident that the particles exhibited a well-organised nanostructure. The particles' images exhibited a near-spherical shape and were approximately the size of a normal crystal. Its average crystallite size is determined to be 27.48 nm, which is being calculated using ImageJ software (Fig. 3.4.6(b)).

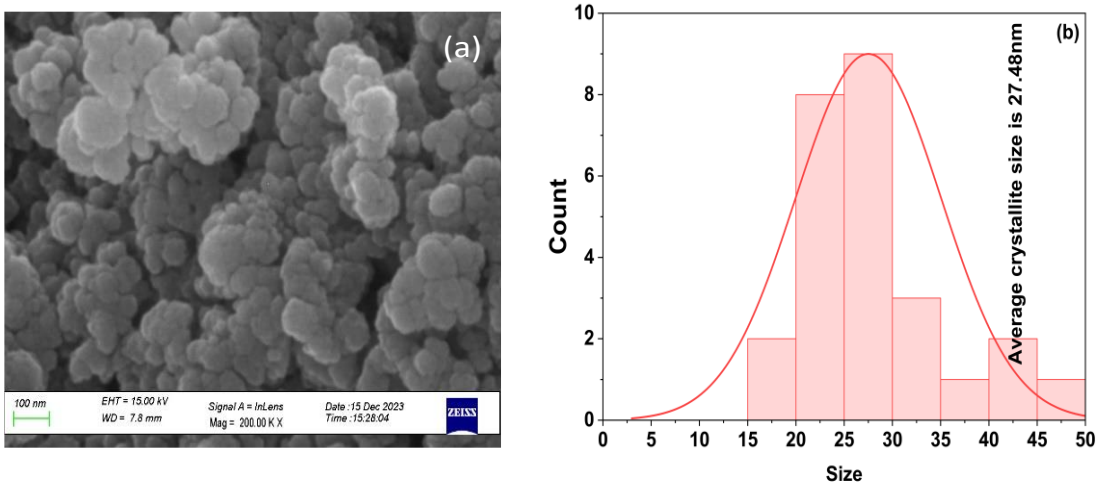

Fig. 3.4.6 (a)SEM Image of Fe_3O_4/Pr^{3+}: SnO_2 (FPS1) (1 at.%) (b) Calculation of average crystallite size.

3.4.5 Tanning electron microscope (TEM) studies

In order to obtain a more distinct understanding of the microstructure of the FPS nanocomposite, we used TEM, HRTEM, and SAED (selected area electron diffraction) imaging. Fig. 3.4.7(a) displayed a transmission electron micrograph of a nanocomposite of FPS1 to validate the grain sizes of the fabricated nanocomposite, which exhibited an average grain size of around 21.8nm. The HRTEM picture is shown in Fig. 3.4.7(b), which is used to estimate the d-spacing and assign its corresponding miller indices of the fabricated nanocomposite, which exhibited lattice distances of 0.252, 0.326, and 0.159nm; the corresponding miller indices are (101), (110) and (211), respectively, of the rutile (tetragonal) SnO_2 structure. The scanning electron diffraction (SAED) pictures, depicted in Fig. 3.4.7(c), clearly demonstrated

that the FPS nanocomposite is composed of many crystals and displayed diffraction circles. This tiny, porous SnO_2 structure improved the dye adsorption and desorption process and the number of active sites for surface-contact reactions. Additionally, it exhibited less diffusion resistance and a significantly larger contact area. This substance's properties make it a promising option for dye breakdown.

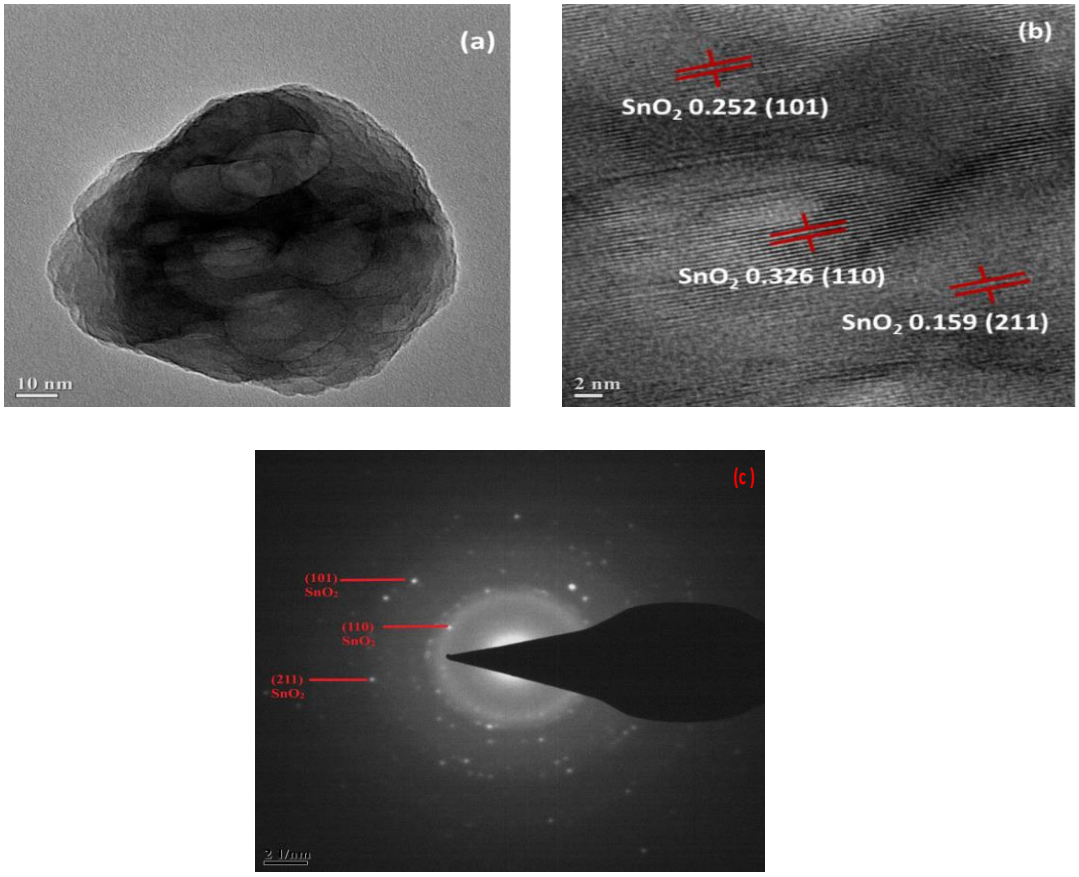

Fig. 3.4.7(a) TEM (b) HRTEM (c) SAED of Fe_3O_4/Pr^{3+}: SnO_2 (FPS1)

3.4.6 XPS analysis

XPS measurement can determine the chemical compositions and bonding states of the FPS1 nanocomposite with a 1 at.% praseodymium ion concentration, which is presented in Fig. 3.4.8(a). Although the spinel structure was clearly shown by the XRD pattern of the samples (Fig. 3.4.1), the occurrence of a γ-Fe_2O_3 phase in the nanoparticles is still possible. This is because the Fe_3O_4 and γ-Fe_2O_3 phases share

similar properties. Since X-ray photoelectron spectroscopy (XPS) is very sensitive to Fe^{2+} and Fe^{3+} cations, it is a great tool for differentiating between the two phases. Fig. 3.4.8(b) shows that the energy values of the $Fe2p_{3/2}$ and $Fe2p_{1/2}$ levels are 716 and 724 eV, respectively. Based on the reported $Fe2p_{3/2}$ and $Fe2p_{1/2}$ levels at 711 and 725.0 eV, respectively, for γ-Fe_2O_3, this indicates that the sample is actually Fe_3O_4, not γ-Fe_2O_3. The peaks in Fe_3O_4 broaden and trend towards higher binding energies, as observed in the literature [Zhang *et al*., (2020); Wang *et al*., (2005)]. This is because $Fe^{3+}(2p_{3/2})$ and $Fe^{2+}(2p_{1/2})$ are present, so the produced nanoparticles should be in the magnetite (Fe_3O_4) phase.

The examination of the relative O 1s spectra at 530 eV is presented in Fig. 3.4.8(c). The subsequent analysis displayed the outcomes of decomposing the O1s spectrum into its three discernible peak locations. The oxygen-tin metal bond was thought to be responsible for the low binding energy peak of 530 eV. At 524 eV, the initial peak was detected, indicating the presence of a Sn-O-Sn bond. The second peak was observed at 537 eV, corresponding to the Pr-O-Pr bond and aligning with the binding energy of Pr_2O_3. Fig. 3.4.8(d) shows that a peak at 486.96 eV is ascribed to Sn $3d_{5/2}$ of Sn^{4+} and a peak at 496.4 eV to Sn $3d_{3/2}$ of Sn^{4+} [Ogasawara *et al*., (1991); Li *et al*., (2008)].

The Pr 3d spectra of a nanocomposite of SnO_2 doped with 1 at.% Pr were thoroughly analyzed. Substituting Pr ion with a valence state of 3+ into SnO_2 leads to peak positions of Pr 3d. Consistent with previous studies, the Pr dopant in our nanocomposite, which is doped with 1 at.% of Pr^{3+}, is expected to function as Pr^{3+} ions at Sn sites, as illustrated in Fig. 3.4.8(e). As evident from the aforementioned outcome, the incorporation of Pr^{3+} ions into the SnO_2 nanocomposite was satisfactorily accomplished and further confirmed the successful integration of Pr^{3+} ions into the SnO_2 crystal structure by the $3d_{3/2}$ and $3d_{5/2}$ peaks, which are at 953 eV and 933 eV, respectively, and corresponded to the expected binding energy of Pr.

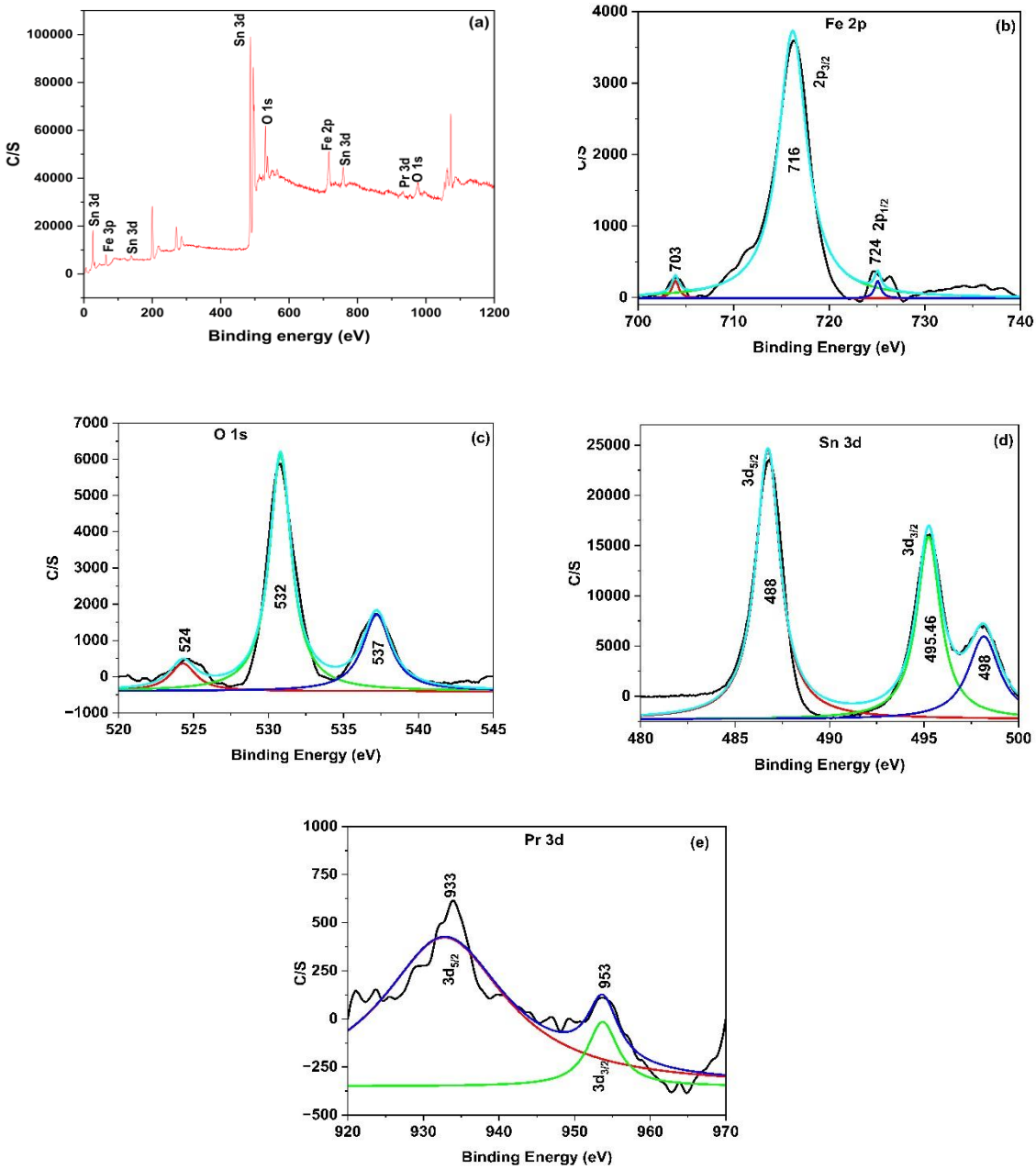

Fig. 3.4.8 XPS of (a) Fe_3O_4/Pr^{3+}: SnO_2 and (b) Fe 2P (c) O 1s (d) Sn 3d (e) Pr 3d in Fe_3O_4/Pr^{3+}: SnO_2 (FPS1).

3.4.7 Brunauer-Emmett-Teller (BET)

Fig. 3.4.9 shows the FPS1 adsorption-desorption isotherm and the monolayer of N_2 adsorbed onto the walls of the mesoporous structure is shown when the relative pressure is less than 0.4. The steep and increasing slope of the adsorption plot explains

the significant oscillations observed between 0.4 and 0.48. These fluctuations indicate changes in capillary density within the tin mesoporous material. According to Tao *et al*., 2015, the 0.45 value (p/p_o) is primarily due to the adsorption of several layers onto the surface of particles [Tao *et al*., (2015)]. Table 3.4.2 displayed the BET method, as described by Xiangyu *et al*., 2017, to calculate the exact surface area, dimensions, and cavity capacity [Xiangyu *et al*., (2017)]. According to the analysis results, the specific surface area of FPS is 43.753 m^2/g, whereas that of FS is 23.134 m^2/g. The arrangement of the metal nanoparticles induces this modification, which reduces FS accumulation. The arrangement of the metal nanoparticles induces this modification, which reduces FS accumulation.

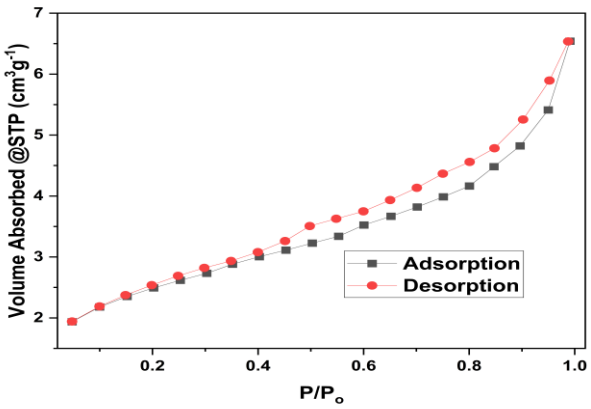

Fig. 3.4.9 Brunauer-Emmett-Teller (BET) for Fe_3O_4/Pr^{3+}: SnO_2 (FPS1)

Table 3.4.2 details outlining the features of BET surface area, pore volume, and pore diameter for both FS and FPS1.

As-prepared nanocomposite	S_{Bet} (m^2/g)	Pore Volume (cm^3/g)	Pore size (nm)
Fe_3O_4/SnO_2 (FS)	23.134	0.052	1.524
Fe_3O_4/Pr^{3+}: SnO_2 (FPS1)	43.753	0.074	2.463

3.4.8 Photoluminescence study

A more comprehensive understanding of the recombination rate and transfer behaviour of electron-hole pairs created by light can be achieved through the study of

photoluminescence (PL) [Premjit *et al*., (2020); Ramananda *et al*., (2022)]. Fig. 3.4.10 displayed the photoluminescence spectra of different FPS. The emission spectrum spans a wide range of wavelengths, specifically from 700 to 720 nm, when excited at 471nm. Particularly noticeable were the prominent peaks at approximately 709 nm, which were commonly linked to its brilliant characteristics. Crystallographic mistakes made during the expansion process, material flaws, and the unusual crystal structure of SnO_2 were all possible explanations for the occurrence of these peaks and the emission they produced. Oxygen vacancies or tin interstitials caused defects within the band gap when the density of SnO_2 was high. The presence of oxygen vacancies or silver interstitials caused a significant photoluminescence emission, which in turn caused the creation of many trapped states or metastable energy levels. Photogenerated carrier recombination can also occur efficiently in close near several tiny grain boundaries. The FPS nanocomposite lowered the PL intensity compared to the original SnO_2. This shows that the charges are effectively separated and electron-hole recombination is stopped. Gathering photogenerated electrons from SnO_2 can enhance the accessibility of charge separation, with praseodymium playing a pivotal role in facilitating this process. Consequently, the visible light performance of the FPS system was enhanced. The FPS1 nanocomposite's photoluminescence (PL) output clearly showed that the electron-hole pairs were separated compared to others.

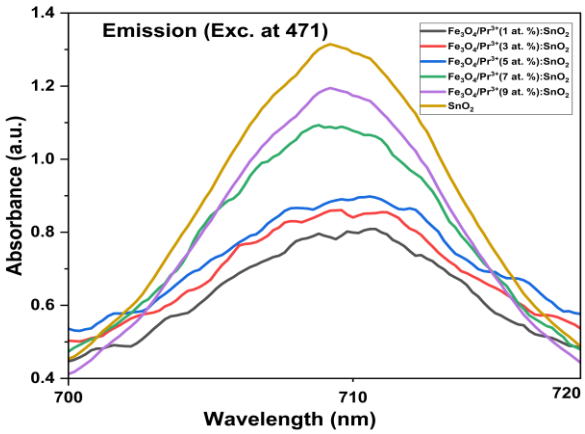

Fig. 3.4.10 PL emission spectrum SnO_2 and Fe_3O_4/Pr^{3+}: SnO_2 (1,3,5,7 and 9 at.%).

3.4.9 Radical Study

The photocatalytic activity of various scavengers was evaluated by utilizing light to detect the reactive radicals responsible for the breakdown of RhB. This was accomplished utilizing a nanoparticle of tin dioxide (SnO_2) doped with 1 at.% of praseodymium (Pr). Fig. 3.4.11(a) depicted the introduction of scavengers, alongside the absence of scavengers (No S), in the photocatalytic process aimed at neutralising highly reactive radicals. Variations among scavengers altered the concentration ratio (C_t/C_o) of RhB dye at time t compared to its initial concentration. To capture superoxide radicals ($\dot{O}_2^-$), holes (h^+), and hydroxyl radicals ($\dot{O}H$), the catalytic process utilized scavengers such as isopropyl alcohol (IPA), benzoquinone (BQ) [Bhuvaneswari *et al*., (2020)], benzoic acid (BA) [Prakash *et al*., (2016)], and ethylene diamine tetraacetic acid disodium (EDTA) [Keerthana *et al*., (2021)]. The impact of various scavengers on the radiation efficiency of SnO_2 doped with 1 at.% praseodymium is illustrated in Fig. 3.4.11(b). During the catalytic reaction phase, using IPA as a scavenger increased the degradation efficiency of RhB dye to 67%, while BA resulted in a 69% enhancement. The degradation efficiency results indicate the decomposition of RhB dye's hydroxyl radicals into carbon dioxide and water, a crucial step. Adding EDTA and BQ to the reaction system changed the degradation efficiency to some extent, and according to the research, when exposed to visible light, RhB's catalytic activity was mediated mainly by superoxide radicals and holes.

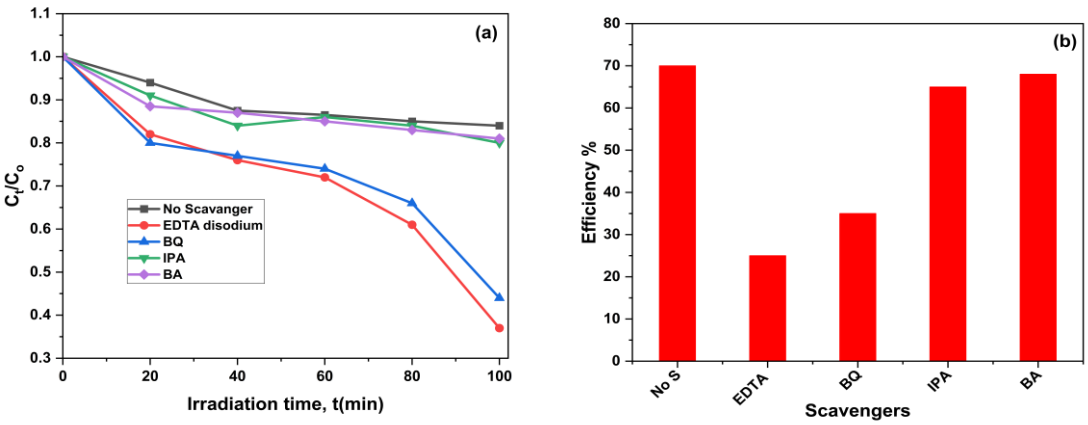

Fig. 3.4.11 (a) The relation between C_t/C_o and Irradiation time (a) The effectiveness of FPS1 using modified scavengers.

3.4.10 EPR studies

Using EPR spectroscopy to identify individual electrons bound to oxygen vacancies was the primary goal of this research. The SnO_2 system, was found, and EPR measurements provided more information about oxygen vacancy defects. Oxygen vacancies on the surface and in the lattice were also shown in Figs. 3.4.8 (XPS) and 3.4.10 (PL). The EPR investigation directly correlates the peak strength with the occurrence of oxygen vacancies in SnO_2 nanoparticles [Kumar *et al*., (2018); Shi *et al*., (2014)]. The analysis revealed that SnO_2 doped with 1 at.% of praseodymium exhibited resonances at 312.45 mT in the Electron Paramagnetic Resonance (EPR) spectrum, as illustrated in Fig. 3.4.12. We employ the same equation, i.e., equation no. 3.12, which is mentioned in Section 3.2.9, is used to calculate the g-value. Resonant magnetic field analysis showed that 2.003 was the g-value for SnO_2 doped with 1 at.% Pr^{3+} ions. The g-value of a free electron is 2.009, which is very close to this value. The prominent peak observed in 1 at.% Pr-doped SnO_2 nanoparticles can be attributed to the substantial presence of oxygen vacancies.

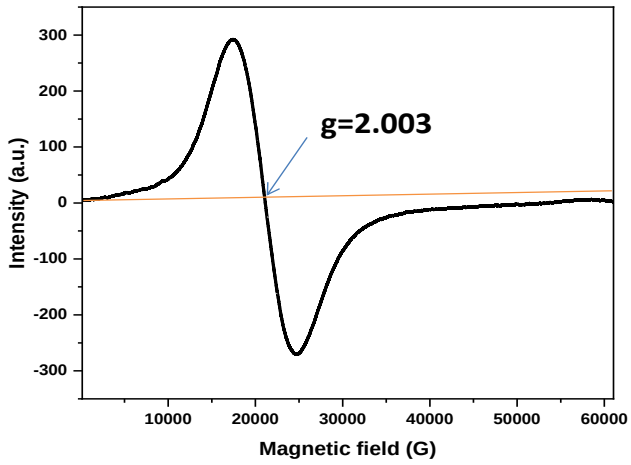

Fig. 3.4.12 EPR spectrum of FPS1

3.4.11 Study of photocatalytic activity

The hydroxyl radicals (ȮH) were produced in the aqueous solution of dye by the interaction between holes and H_2O molecules, together with the existence of hydroxyl

radicals that were adsorbed on the surface [Lallianmawii, N. Mohondas Singh, (2023)]. The electrons generated by the photochemical reaction reacted with the oxygen present in the surrounding environment, forming superoxide anions ($\dot{O}_2^-$). The superoxide anion species ($\dot{O}_2^-$) and the hydroxyl radical ($\dot{O}H$) was showed reactivity towards the oxidant. They both showed reactivity in the presence of dye on FS and FPS (1 at.%) nanoparticles. The reaction resulted in the liberation of water and carbon dioxide through the degradation of the dye. Below is a concise depiction of the observable response process:

$$\left.\begin{array}{c} SnO_2 + h\nu \rightarrow SnO_2 + h^+ + e^- \\ Pr:SnO_2 + h\nu \rightarrow Pr:SnO_2 + h^+ + e^- \\ h^+ + dye \rightarrow dye^{\bullet+} \rightarrow \text{Oxidation products} \\ e^- + dye \rightarrow dye^{\bullet-} \rightarrow \text{Reduction products} \\ h^+ + H_2O\,(ads) \rightarrow H^+(ads) + \dot{O}H \\ e^- + O_2\,(ads) \rightarrow \dot{O}_2^- \\ RhB + \dot{O}H \rightarrow CO_2 + H_2O \rightarrow \text{Degradation products} \end{array}\right\} \quad (3.15)$$

We mixed 20 mL of a solution containing dye or pesticide in water, which has a concentration of 8 ppm each, and added 1mg of a photocatalyst as prepared. After achieving equilibrium between the adsorption and desorption processes, the mixture was further subjected to a 30 min period in a lightless environment. The deterioration rate was determined by monitoring the absorption spectrum of RhB at its peak wavelength (λ_{max}=554 nm) after exposure to LED light. The photocatalytic degradation process endured 150 min while being exposed to illumination. Over the initial 150 min, measurements were collected every 30 min, indicating a progressive decline in dye or pesticide absorbance. Hence, it was confirmed that the magnetic nanocomposite photocatalyst efficiently disintegrated the dye. The equation that is provided in Section 3.1.9 was used to calculate the decomposition efficiency.

3.4.12 RhB Degradation

Fig. 3.4.13(a) and (b) depicted the process of photocatalytic dye degradation utilising FS and FPS nanocomposite, respectively, as indicated by the data. The decline outcome was found to be most favourable when SnO_2 was doped with 1 at.% Pr^{3+}. The hydroxyl radicals speed up the processes of N-de-ethylation and chromophore

alteration during the degradation of RhB, which was outlined in the research conducted by [Yadav *et al*., (2023)]. More information about how the hydroxyl radicals in the nanocomposite hasten the degradation of RhB, as well as the N-de-ethylation and chromophore change processes. Through this process, molecular rings are opened, smaller RhB molecules are formed, and oxidation products are produced by breaking chemical bonds; LCMS tests confirmed the following m/z values: adipic acid = 146.13, terephthalic acid = 166.12, 3-hydroxybenzoic acid = 122.11, benzoic acid = 122.11, and succinic acid = 118.08. This process initiated the opening of molecular rings, forming smaller RhB molecules and producing oxidation products by breaking chemical bonds. The next step of the process was to mineralize the smaller molecules, which produced CO_2 and H_2O, as shown in Fig. 3.4.13(c).

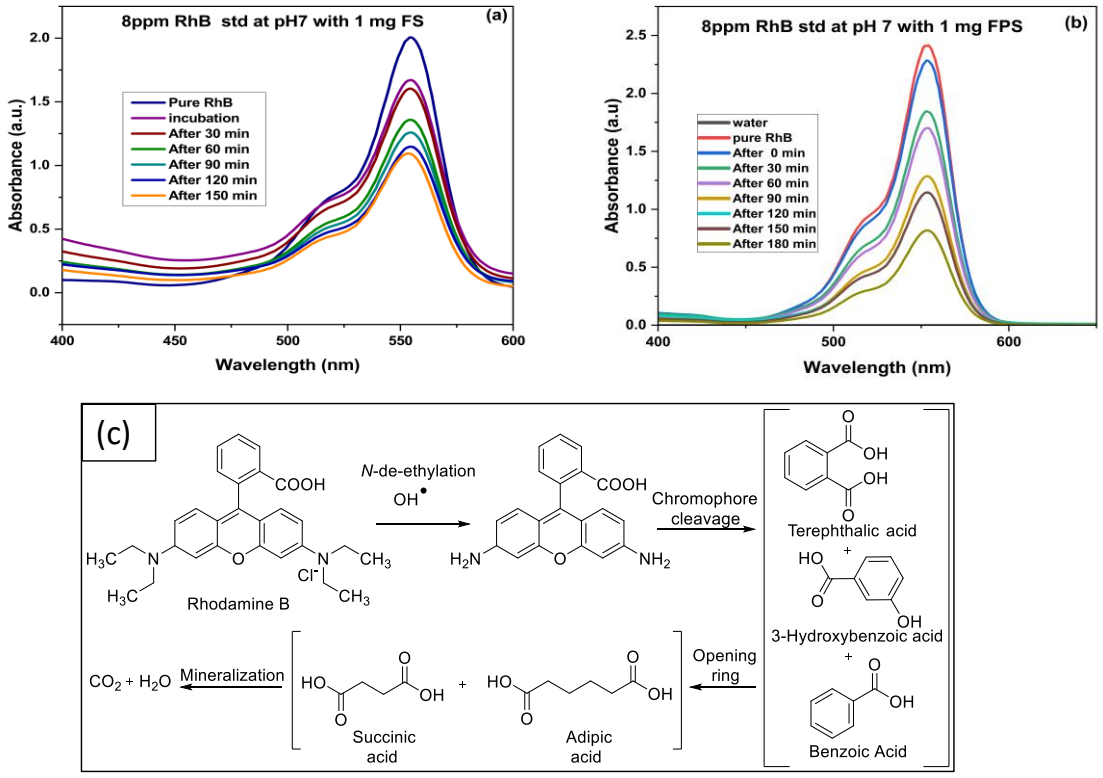

Fig. 3.4.13 RhB decomposition (a) Fe_3O_4/SnO_2 (b) Fe_3O_4/(1 at.%)Pr^{3+}: SnO_2 (FPS1) (c) Mineralization of RhB

3.4.13 Dosage effect

Increasing the catalyst dosage enhances the rapid breakdown of dye solutions. Fig. 3.4.14 (a) and (b) demonstrate that the concentration of RhB in a 20 mL solution,

initially containing 8 ppm and with a pH of 7, increased from 0.5 to 11mg following a 30 min exposure to LED illumination. In order to understand the observed enhancement in photocatalytic activity with increasing catalyst quantity, it was necessary to investigate the adsorption and desorption processes in systems with different catalyst concentrations. Increasing the number of photocatalysts makes more photocatalytically active sites available, which makes it easier to absorb RhB. Increased concentrations of photocatalysts lead to decreased irradiance as a result of light dispersion, resulting in less efficient photocatalytic breakdown [Brojendro Singh Shagolsem, N. Mohondas Singh, (2024)]. The augmentation of the photocatalyst's concentration did not enhance the photocatalytic degradation since the decisive factor was the total effect. The technique examined dye solutions' photocatalytic degradation under LED light. The initial concentration of 8 ppm produced unfavourable outcomes. The breakdown rate was increased by 10%, rising from 60 to 70%, by increasing the quantity of photocatalyst from 0.5 to 1mg. The decomposition rate and degradation efficiency exhibited no variation when the catalyst dosage was augmented within the 1 to 11mg range. Upon careful evaluation of these criteria, it has been determined that the optimal dosage for the nanocomposite photocatalyst is 1 mg. Based on the plotted graph; it is evident that the utilisation of 1mg of catalyst resulted in the attainment of the optimal peak.

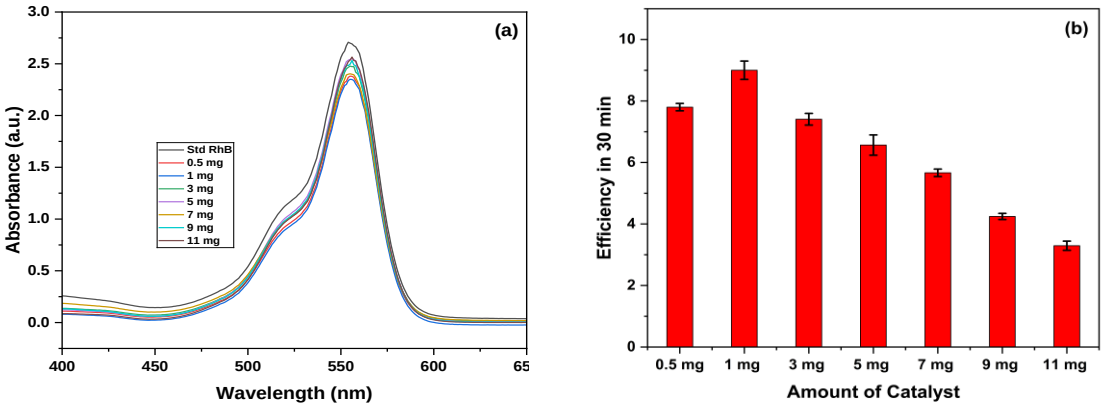

Fig. 3.4.14 (a) Degradation spectrum of RhB (b) The effectiveness of degradation at different quantities of the produced photocatalyst.

3.4.14 pH EFFECT

The initial concentration of pollutant was maintained at a constant level of 8 ppm, and a catalyst weighing 1mg was introduced into a 20 ml solution of dye or pesticide. The acidic solution utilized in the production of the nanocomposite photocatalyst may contain defects, which have the potential to alter the doping structure and diminish the efficiency of the photocatalyst.

The pH of the environment impacted the redox species and their ability to adhere to catalysts. Hydroxyl radicals were the main factors responsible for oxidation in alkaline or neutral pH conditions, whereas positive holes significantly affected acidic pH conditions. The examination of these results indicated that the nanocomposite photocatalyst exhibited the most advantageous performance within a pH range of 5 to 7. The graph illustrates the correlation between time and the (C_o/C_t) ratio, demonstrating the photodegradation process of RhB dye in FS and FPS1 nanoparticles.

The Langmuir-Hinshelwood kinetic model, $kt = \ln (C_o/C_t)$ as described in reference [Hirami *et al*., (2023)], was employed in combination with the provided equation to represent the degradation of RhB through pseudo-first-order kinetics accurately.

3.4.14.1 RhB Degradation

The adsorption examination for FPS1 at pH values ranging from 5 to 10 reveals the cationic nature of RhB, with degradation efficiency percentages of 54.59, 53.09, 46.99, 48.83, 53.09, and 56.79%, respectively. When the FPS nanocomposite was absent, RhB dye degradation under LED illumination was approximately 2%. The most promising sample was the LED-RhB-FPS1 mix at pH 10. It broke down 56.79% of the RhB molecule in 150 min, which aligns with previous studies that used photocatalysis.

A linear regression was performed with the logarithm of the ratio C_o/C_t to get the slope of the line shown in Fig. 3.4.15. This was done to estimate the rate constant k for fitting absorption time.

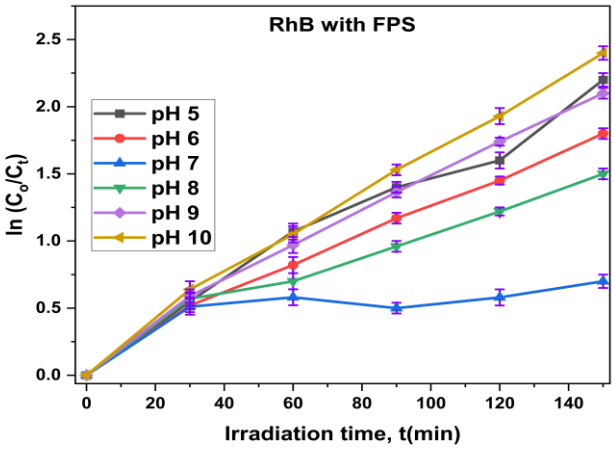

Fig. 3.4.15 Kinetics of photodegradation.

3.4.14.2 MB Degradation

After 150 min, the FPS1 solutions with pH values ranging from 5 to 10 showed respective absorption rates of 59.90, 57.01, 49.98, 52.87, 56.79, and 62.89%. The pure MB dye degrades by 3% when exposed to LED light, which is a significant decrease. At pH 10, the LED-MB-FPS1 solution degrades at an estimated rate of 62.89% after 150 min of exposure to LED radiation, making it the most severely degraded compared to RhB.

We performed a linear regression using the logarithm of the ratio C_t/C_o to determine the slope of the line, as illustrated in Fig. 3.4.16(a). In order to suit the absorption time, we were able to estimate the rate constant k. This interaction dissolves sulfur-chlorine, nitrogen-methyl, carbon-sulfur, carbon-nitrogen, and carbon-oxygen chemical bonds. Breaking down intermediate components and opening MB rings led to forming smaller organic compounds. LCMS investigations confirmed the following: m/z (4-(N, N-dimethyl)-aniline) =136.22, m/z (2-amino-4-(N, N-dimethyl) benzene sulfonic acid) =231.26. Fig. 3.4.15(b) shows the final molecules produced during mineralization, which are CO_2 and H_2O.

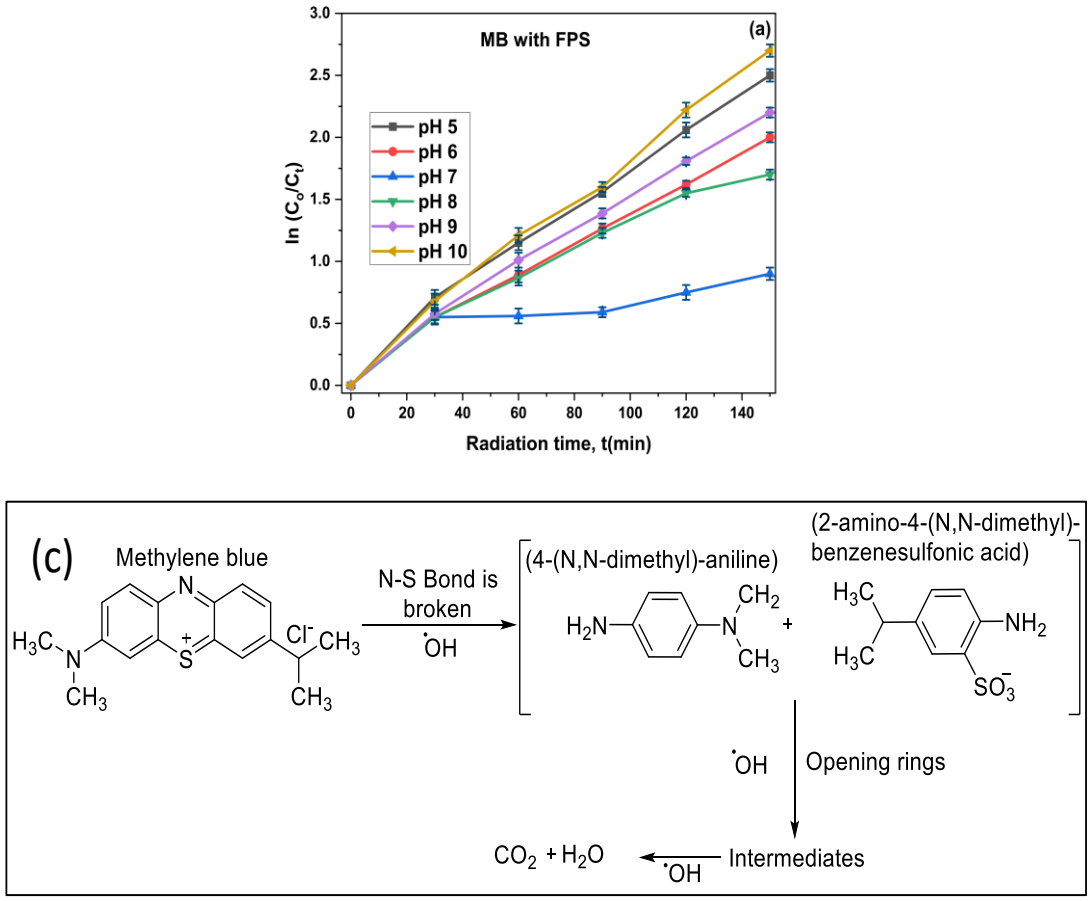

Fig. 3.4.16 (a) Kinetics of photodegradation of MB (b) Mineralization of MB

3.4.14.3 MB and rhodamine (Mixture) Degradation

As shown in Fig. 3.4.17((a)-(c)), the MB and RhB dye mixtures are absorbed after 150 minutes, and solutions containing FPS1 deteriorate at a rate of 58.72% and 52.64% efficiency, respectively, at pH 7. An electrostatic attraction develops because the FPS surface is positively charged and the dye molecules are negatively charged, leading to enhanced absorption. Nevertheless, when illuminated by LED light, the MB and RhB combination degrades by a mere 1%. After 150 minutes of exposure to the LED-MB-FPS1 solution at pH 7, the maximum degradation percentage was approximately 58.72%.

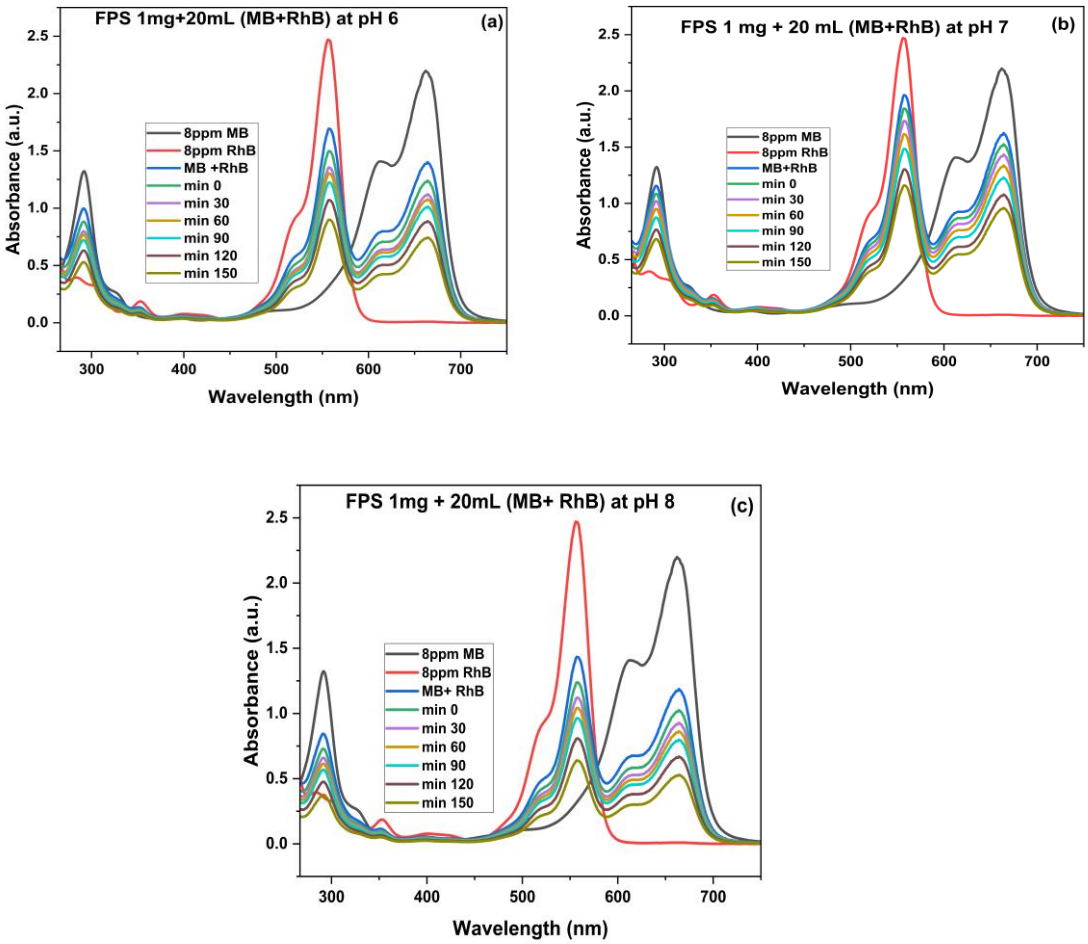

Fig. 3.4.17 (a)-(c) MB and RhB mixture degradation at different pH values.

3.4.14.4 Degradation of 2, 4-DCP under LED irradiation

The breakdown efficiency of the FPS1 nanocomposite was 45% at pH 5 and 56.79% at pH 10 when exposed to light-emitting diode radiation at a dosage of 1mg. Chen and Ray (1999) discovered a Langmuir-Hinshelwood relationship that indicates the degradation of 2, 4-DCP is influenced by its concentration. Some surfaces may exhibit resistance to hydrolysis by 2, 4-DCP. In our linear regression analysis, we calculated the slope of the line by taking the logarithm of the ratio C_o/C_t for 2,4-DCP. Fig. 3.4.18(a) presented the study findings in their original formats and this method enabled us to estimate the rate constant (k) for the photocatalytic degradation of 2,4-DCP using the nanocomposite prepared in advance. Fig. 3.4.18(b) provided information on the mineralization of 2,4-DCP, specifically the m/z values of 147.48

for Chloromalcic acid and 72.05 for unsaturated carboxylic acid, both of which were verified through LCMS studies.

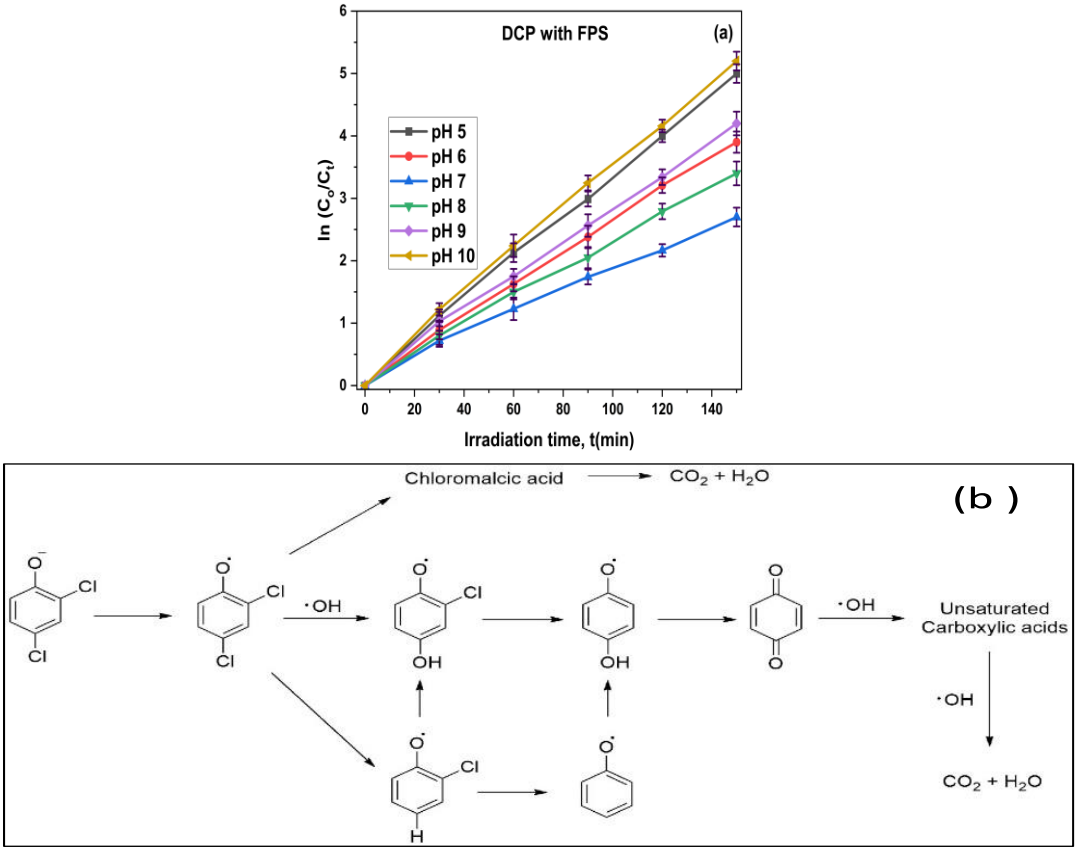

Fig. 3.4.18 (a) Kinetics of photodegradation of 2,4-DCP (b) Mineralization of 2,4-DCP

3.4.14.5 Trichloroaceticacid (TCAA) degradation

The experiment aimed to determine how well FPS1 mineralized trichloroacetic acid (TCAA) to remove total organic carbon (TOC) at a pH of 7. The research examined the mineralization and degradation of TCAA under defined conditions, such as an 8 ppm catalyst concentration and a 150 min contact time, utilising HPLC, as shown in Fig. 3.4.19(a). The breakdown intermediates, including hydroxyacetic acids, formic acid, and acetic acid, were determined to be less dangerous than the original TCAA. Fig. 3.4.19(b) illustrates the results of TCAA mineralization and degradation, including particular information gathered from HPLC analysis. whereas details of photodegradation kinetics are shown in Fig. 3.4.19(c), LCMS studies showed the existence of one or two intermediates in the process of TCAA decomposition.

Mass chromatograms displayed intermediate compounds such as formic acid (CH_2O_2, m/z 46, retention time 4.59 min), hydroxyacetic acid ($C_2H_4O_3$, m/z 93, retention time 4.81 min), and acetic acid ($C_2H_4O_2$, m/z 62, retention time 3.61 min). An intermediate compound with a mass-to-charge ratio of 46 was detected using chromatography-mass spectrometry analysis, derived from an intermediate compound with a mass-to-charge ratio of 62. Fig. 3.4.19(d) illustrates a possible breakdown pathway for TCAA in the FPS process based on molecular characteristics identified by LCMS analysis and related studies.

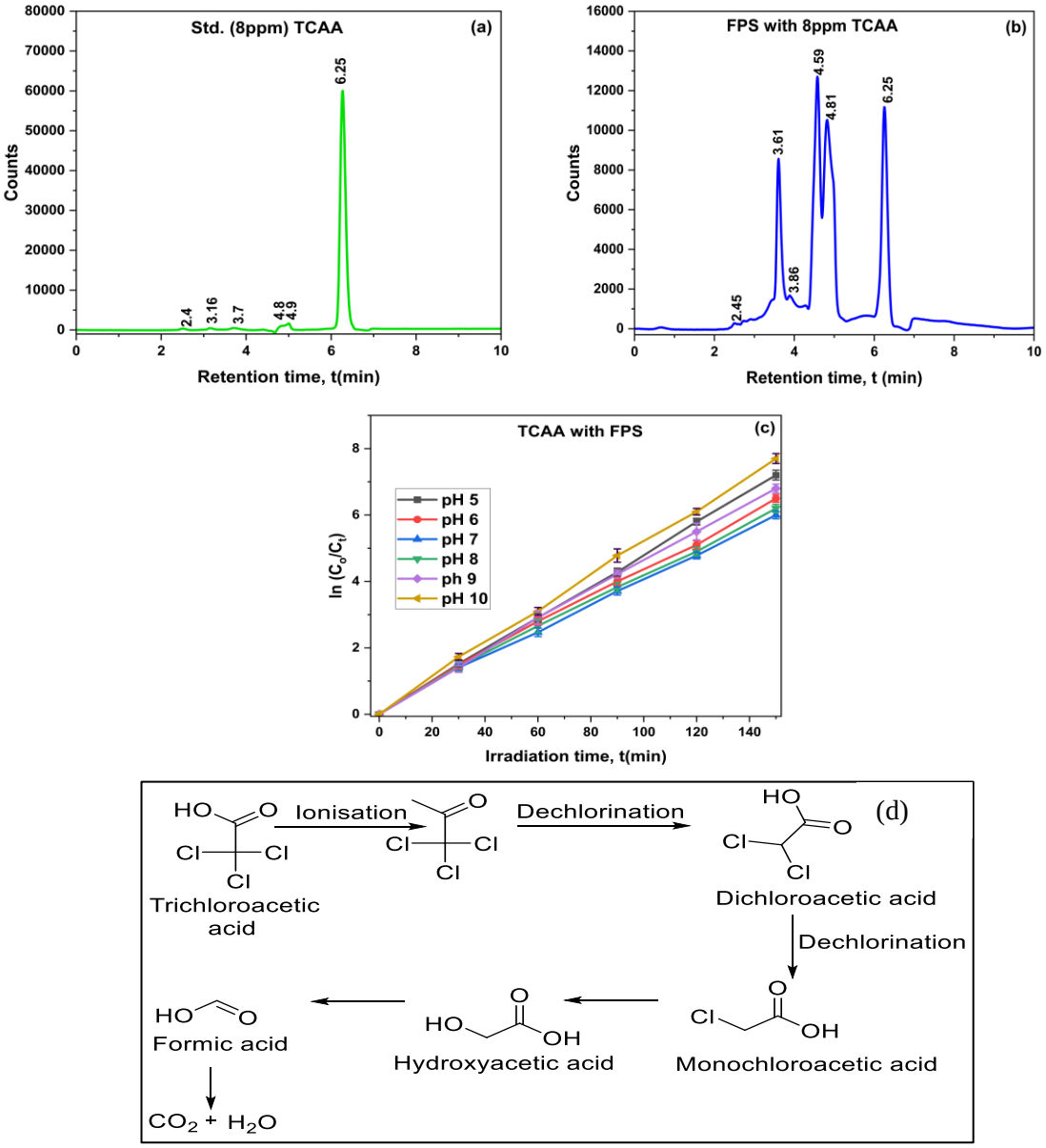

Fig. 3.4.19 (a)Std TCAA (b)TCAA decomposition with 1mg of FPS1 (c) Kinetics of

Photodegradation (d) Mineralization of TCAA.

3.4.15 TOC (Total Organic Carbon) determination

We employed total carbon analysis to ascertain the mineralization of the RhB dye. Upon adding 1mg of FPS1, the dye's absolute total organic carbon (TOC) value fell at a concentration of 8 ppm, as illustrated in Fig. 3.4.20. The outcome had a photomineralization efficiency of 55%. The photomineralization efficiency slightly dropped to 32% when using FS with the same amount of photocatalyst. The restricted number of active sites on the catalyst's surface hindered the reaction, decreasing in the absolute total organic carbon value from 55% to 32%.

Moreover, this data provides insight into the potential presence of residual Total Organic Carbon (TOC), a form of carbon in organic substances, in each of these samples. This phenomenon could be ascribed to the response occurring during the transitional phases of the specimens before the completion of mineralization. Using equation 3.7 mentioned in Section 3.1.10, we accurately calculated the demineralization of a dye or pesticide following its degradation. We ran the experiment three times to verify its accuracy and reliability.

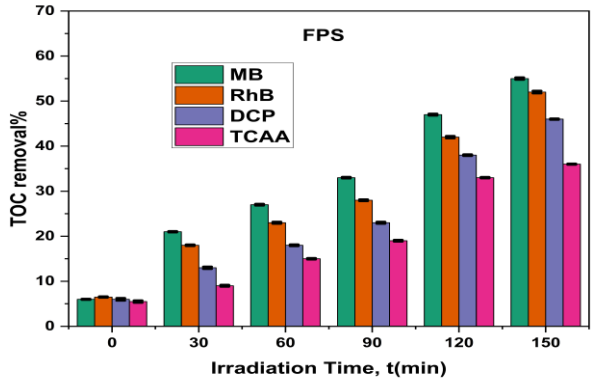

Fig. 3.4.20 TOC removal % of dyes and pesticides dye with FPS1.

3.4.16 Comparison

Degradation constants, which measure a material's photocatalytic activity, are shown in Table 3.4.3. When subjected to 1 mg of light-emitting diode radiation, the

FPS1 nanocomposite broke down MB, RhB, 2,4-DCP, and TCAA with an efficiency of 49.98, 46.99, 37, and 27%, respectively, at pH 7, which is shown in Fig. 3.4.21. When the pH was higher, both dyes and pesticides showed an increase in their degradation rate constants, caused by a higher concentration of hydroxyl ions. At pH 7, the degradation constant for the LED-MB-FPS1 solution was higher than that for the LED-RhB-FPS1 solution.

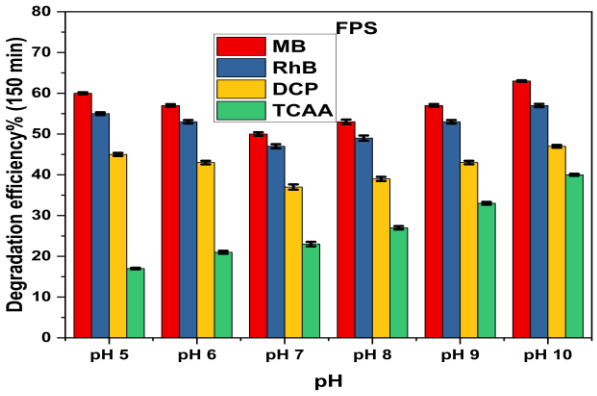

Fig. 3.4.21 Degradation efficiency of RhB, MB, 2,4-DCP and TCAA

Our research found that FPS1 nanocomposite made with an environmentally friendly method using *Artocarpus heterophyllus* L. extract, function better than that of FS i.e. breaking down contaminants in water using this process is incredibly efficient.

Table 3.4.3 Estimation of Rate constant for photocatalytic degradation

pH	MB		RhB		DCP		TCAA	
	k (min^{-1})	R^2	k (min^{-1})	R^2	k (min^{-1})	R^2	k (min^{-1})	R^2
pH 5	0.0558	0.9489	0.0618	0.9259	0.0426	0.9379	0.0433	0.9479
pH 6	0.0526	0.9489	0.0587	0.9439	0.0396	0.9259	0.041	0.9219
pH 7	0.0493	0.9509	0.0506	0.9319	0.0396	0.9479	0.0369	0.9239
pH 8	0.0507	0.9459	0.0565	0.9559	0.0479	0.9279	0.0383	0.9299
pH 9	0.0537	0.9279	0.0609	0.9219	0.0409	0.9419	0.0429	0.9279
pH 10	0.0579	0.9319	0.0626	0.9279	0.049	0.9379	0.044	0.9419

This study measured the efficacy of FPS1 in mineralizing 2,4-dichlorophenol (2,4-DCP) and trichloroacetic acid (TCAA) at pH 7. Their total organic carbon (TOC) removal percentages were calculated to observe the mineralization and degradation of 2,4-DCP and TCAA by FPS1 under certain conditions, such as an 8 ppm catalyst concentration and a 150 min contact period. It was found that the mineralization rates for TCAA ranged from 5.5 to 36% during the 150 min period, while for 2,4-DCP, they ranged from 6 to 46%. Mineralization results in the significant breakdown of 2,4-DCP and TCAA into CO_2 and H_2O. For RhB, MB, 24-DCP, and TCAA treated with FPS under LED light, the pseudo-first-order model (R^2 = 0.942, 0.958, 0.914, 0.866) better matches experimental data than the pseudo-second-order model (0.752,0.802, 0.842, 0.798), suggesting pseudo-first-order kinetics.

3.4.17 VSM CURVE

An investigation of the magnetic responses of Fe_3O_4 and the magnetically active quaternary compound FPS1 (1 at.%) - a based magnetic nanoparticle was conducted. The study used coercivity magnitudes (MH), as shown in Fig. 3.4.22. All nanocomposites using Fe_3O_4 magnetic nanoparticles exhibited ferrimagnetic characteristics, such as symmetrical hysteresis and saturation magnetization. The saturation magnetizations of Fe_3O_4, FS, and FPS1 were determined to be 20.70, 17.260, and 2.10 emu/g, respectively. The reduction in magnetic moment of Fe_3O_4 nanoparticles was the cause of the decrease in particle size. A noncollinear spin configuration was commonly seen on the surface. As the size of Fe_3O_4 magnetic nanoparticles increases, the saturation magnetization of the FS sample falls compared to pure Fe_3O_4. The FPS1 hysteresis loop exhibited no remaining magnetism or coercive force, and saturation magnetization of Fe_3O_4 exceeded that of FPS1 because it contained non-magnetic components, leading to the sample exhibiting superparamagnetic properties. The studies demonstrated that the photocatalyst exhibited substantial saturation magnetization, facilitating its efficient reusability. This was achieved due to the magnetic field surrounding it, offering a shield against the solution.

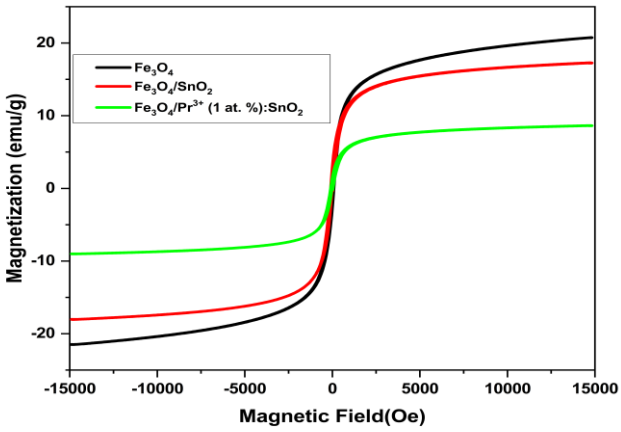

Fig. 3.4.22 VSM curve of Fe_3O_4, FS and FPS1.

3.4.18 Reusability

The deterioration of RhB occurred due to the presence of FS and FPS1 during a 150 min exposure to visible light. The main attributes of the photocatalyst were its durability and its capacity to be reused. In order to assess the stability and reusability of the magnetic nanocomposite photocatalyst, we investigated its recycling performance. Fig. 3.4.23 illustrates the recycling process of nanocomposite photocatalysts for the degradation of RhB. Throughout the five cycles, an external magnet was used to separate the nanocomposite photocatalyst from the mixture. Recycled nanocomposite photocatalysts decomposed the dye solution. The RhB breakdown efficiency showed a decrease within 150 min, declining from 70% to 63%. The decomposition efficiency showed negligible variability. The reduced efficacy of nanocomposite photocatalysts may be attributed to the incomplete degradation of the intermediate products clinging to the surface. On the other hand, the nanocomposite photocatalyst was very stable and could be used repeatedly because it consistently and effectively broke down dyes or pesticides with visible light.

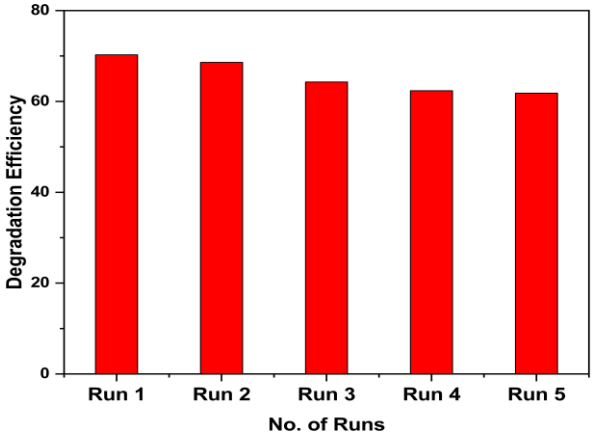

Fig. 3.4.23 Number of recycles of using FPS1

3.4.19 Mechanism of RhB decomposition using the synthesized photocatalyst

Fig. 3.4.24 illustrated the development of nanocomposite photocatalysts specifically intended to decompose RhB dye, demonstrating the progress of a degradation method. The degradation of RhB utilizing a photocatalyst doped with Pr^{3+} ions and SnO_2 (tin dioxide) was a complex process involving multiple sequential reactions dependent on the fundamental principles of photocatalysis. Doping SnO_2 with praseodymium resulted in an augmentation of its photocatalytic activity. Upon exposure to light, the Pr^{3+}: SnO_2 photocatalyst generates charge pairs by absorbing photons, facilitating the transfer of electrons from the valence band to the conduction band. Incorporating Pr^{3+} ions into the SnO_2 structure facilitated effective charge separation, hindering rapid charge pair recombination. Hydrogen ions in the valence band of Pr^{3+}-doped SnO_2 could directly oxidise RhB molecules that have stuck to the surface of the catalyst. The interaction between electrons in the conduction band and oxygen molecules adsorbed on the catalyst's surface may lead to the formation of superoxide radicals ($\dot{O}_2^-$). When light and water molecules create holes, a catalyst's surface can generate highly reactive oxygen species (ROS), specifically hydroxyl radicals ($\dot{O}H$). Reactive species, like hydroxyl radicals and valence band holes, work together to make it easier for dye or pesticide molecules to come off the photocatalyst's surface. During the breakdown process, simpler and more easily degradable intermediate molecules were produced, unlike the original molecule. Using

mineralization, the photocatalytic method was developed to transform pollutants into non-reactive inorganic compounds, such as carbon dioxide, water, and mineral ions. Adding Pr^{3+} ions to the SnO_2 lattice made it more photocatalytic by changing the band structure and active sites that help with adsorption and catalysis.

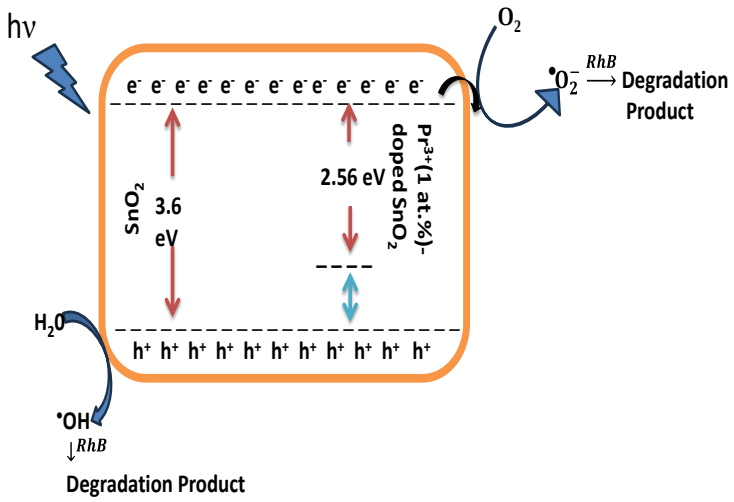

Fig. 3.4.24 Photocatalytic degradation of RhB using a synthesized catalyst

3.5 Effect of Pr^{3+},Y^{3+} co-doped on SnO_2 in Fe_3O_4/Pr^{3+},Y^{3+}:SnO_2 ternary nanocomposite for degradation of dyes and pesticides.

Intermediate energy levels from Pr^{3+} and Y^{3+} ions extend SnO_2's visible spectrum light absorption. This maximizes solar energy for photocatalytic processes compared to pure SnO_2.The electron-hole pair recombination rate is reduced by Pr^{3+} and Y^{3+} ions. This increases charge carrier lifespan and photocatalytic efficiency. Co-doping promotes quicker charge transfer and photocatalytic activity by increasing electron and hole mobility in the SnO_2 matrix. Fe_3O_4, Pr^{3+}, and Y^{3+} ions in SnO_2 synergistically boost nanocomposite photocatalytic capabilities. Pr^{3+} and Y^{3+} doping improves light absorption and charge separation, while Fe_3O_4 recovers magnetically.

As shown in Fig. 3.5.1, Fe_3O_4/Pr^{3+},Y^{3+}: SnO_2 (FPYS3 (5 at.%)) photodegraded RhB dye more effectively than any other nanocomposites that were prepared. The photocatalytic efficacy of the ternary nanocomposite in its as-prepared state was assessed by measuring the intensity of absorption, which was used to degrade RhB (Sigma Aldrich) dye in an aqueous solution.

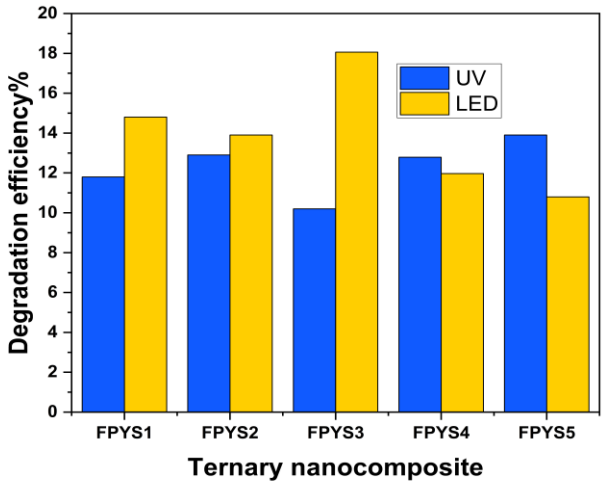

Fig. 3.5.1 The efficiency of the catalyst developed is enhanced by exposure to UV and LED light, leading to increased deterioration.

According to the results of these investigations, a ternary nanocomposite consisting of Pr^{3+}, Y^{3+}, and SnO_2 has 5 at.% (Pr^{3+},Y^{3+}) exhibited remarkable efficacy

in the degradation of RhB when exposed to LED light. Consequently, our attention was directed towards $Fe_3O_4/Pr^{3+},Y^{3+}$: SnO_2 (FPYS3 (5 at.%)) in order to characterise and explore its potential applications.

3.5.1 X-ray diffraction studies

The grain size and structure of aged nanoparticles and nanocomposites were evaluated using powder X-ray diffraction (XRD). The X-ray diffraction patterns of pure Fe_3O_4, SnO_2, Fe_3O_4/SnO_2 (FS), and $Fe_3O_4/Pr^{3+},Y^{3+}$: SnO_2 (5 at.%)(FPYS3) nanocomposites are shown in Fig. 3.5.2. The crystal sizes were calculated using the Debye-Scherrer equation based on the XRD observations.

The diffraction patterns of FPYS3 (5 at.%) nanocomposites were compared to those of Fe_3O_4 and SnO_2. The diffraction peaks of cubic inverse spinel Fe_3O_4 were found to correlate with JCPDS No. 82-1533 at specific angles of $2\theta = 30.11°$, 35.65°, 40.39°, 43.55°, and 62.96°. These angles corresponded to the Miller indices (220), (311), (222), (400), and (440). As shown in JCPDS No. 41-1445, the tetragonal rutile crystalline structure of SnO_2 has a cell volume of 69.924 and diffraction peaks at 2θ angles of 26.64°, 33.91°, 51.59°, and 54.28° corresponded to the Miller indices 110, 101, 211, and 001, respectively. No distinct impurity peaks were found in the different phases.

The leftward shift of the 2θ angle in X-ray Diffraction (XRD) patterns for $Fe_3O_4/Pr^{3+},Y^{3+}$: SnO_2 (5 at.%)(FPYS3) can be attributed to several factors like Praseodymium (Pr^{3+}) and yttrium (Y^{3+}) ions replace some of the tin ions (Sn^{4+}) in the SnO_2 lattice, their larger ionic radii about 0.99 Å for Pr^{3+} and 0.90 Å for Y^{3+} compared to 0.71 Å for Sn^{4+} which caused the SnO_2 lattice to expand. This expansion increases the distance between the crystal planes (d-spacing), leading to a shift of the XRD peaks for the 110, 101, and 211 planes towards lower 2θ values, in line with Bragg's law. XRD analysis confirmed the successful preparation of the nanocomposites FPYS3, and the tetragonal structure of SnO_2 remained unchanged with the inclusion of Fe_3O_4, Y^{3+}, and Pr^{3+}.The dimensions of the crystallites in the $Fe_3O_4/Pr^{3+},Y^{3+}$: SnO_2 nanocomposites were determined using the Debye-Scherrer formula (equation 3.1, mentioned in Section 3.1.1). The formula utilised the diffraction peaks (110) for SnO_2, (311) for Fe_3O_4. Table 3.5.1 provides the average grain size of Fe_3O_4, SnO_2, FS, and

FPYS3.

Table 3.5.1 Average Crystallite size, Parameters and cell volume of prepared nanocomposite(s).

As-prepared photocatalyst	Crystallite Size (nm)	Lattice Parameters			Cell volume
		a (Å)	b (Å)	c (Å)	
Fe_3O_4	28.014	8.284	8.284	8.284	546.325
SnO_2	15.128	4.564	4.564	3.023	69.924
Praseodymium	32.489	3.562	3.562	10.744	140.42
Yttrium	28.612	3.492	3.492	6.218	69.292
Fe_3O_4/SnO_2 (FS)	38.103	4.826	4.826	3.266	73.468
$Fe_3O_4/Pr^{3+},Y^{3+}:SnO_2$ (5 at.%)(FPYS3)	46.163	5.040	5.040	3.602	74.012

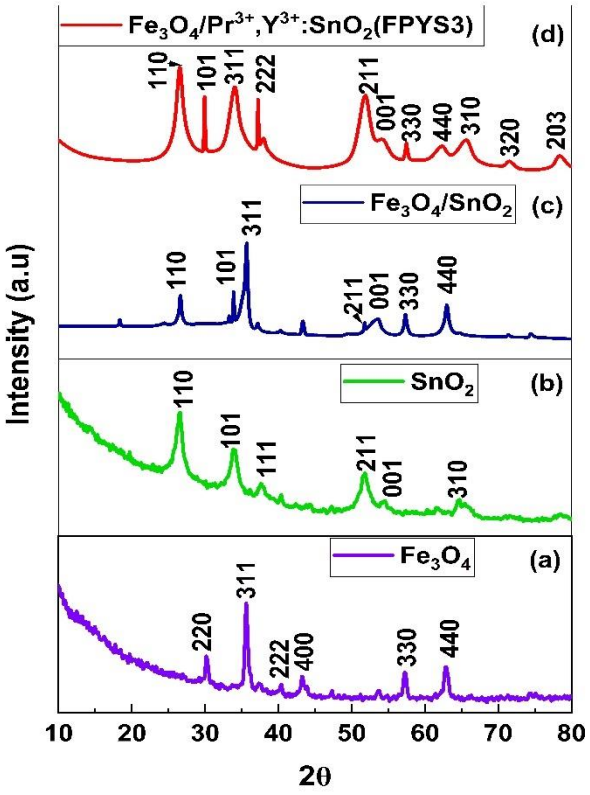

Fig. 3.5.2 X-ray diffraction for (a) Fe_3O_4, (b) SnO_2, (c) Fe_3O_4/SnO_2 (FS) and (d) FPYS3 (5 at.%).

3.5.2 FTIR studies

Fig. 3.5.3 depicts the Fourier transform infrared (FT-IR) spectra of nanocomposites that is $Fe_3O_4/Pr^{3+},Y^{3+}$ (5 at.%) co-doped with SnO_2 in the presence of a plant extract as well as Fe_3O_4 and SnO_2. In magnetite (Fe_3O_4), the stretching vibration of Fe-O occurs at 510 cm^{-1}, while the stretching vibration of Sn-O occurs at 764 cm^{-1}. There is a possibility that a peak anywhere between 1218 -1512 cm^{-1} could be caused by the presence of organic molecules or surface functional groups, such as C-O stretching and C-O-C stretching vibrations from ester groups or others can take place in this region as a result of the utilization of plant extract in the process of manufacturing the nanocomposite. Adsorbed water molecules exhibit an H-O-H bending vibration at a frequency of 1646 cm^{-1} while at 3400 cm^{-1}, vibration is produced by O-H stretching from water molecules that have been adsorbed. A further factor that can contribute to O-H stretching vibrations at 3750 cm^{-1} is the presence of hydroxyl groups that are bound to metal ions, such as Sn or Fe.

Moreover, there is a possibility that the unique FTIR peaks for Pr^{3+} and Y^{3+} ions co-doping in SnO_2 will not be easily discernible if they are present in very low concentrations. It has the ability to affect the SnO_2 lattice also, which can cause minor alterations in the Sn-O stretching vibrations. Further, the introduction of new vibrational modes or the modification of existing ones can also be accomplished through co-doping.

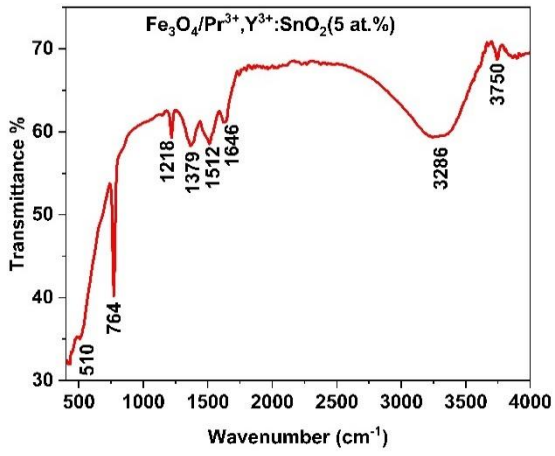

Fig. 3.5.3 FT-IR spectrum of Fe_3O_4/(1,3,5,7 and 9 at.%) Pr^{3+},Y^{3+}: SnO_2.

3.5.3 UV-visible spectroscopy

An investigation using a Thermo Scientific UV-visible spectrophotometer, as depicted in Fig. 3.5.4(a), was conducted to assess the band-gap energies of the fabricated ternary nanocomposite. Additionally, a preliminary examination was performed to verify the production of the intended substance. The baseline was calibrated using double-distilled water across the 200 to 1000 nm wavelength range. The Tauc plot method (presented in 3.2 under Section 3.1.2) was employed to calculate the band gap energy of FPYS nanocomposite with varying atomic percentages. The UV-visible spectrum data illustrating this calculation is presented in Fig. 3.5.4 (b) FPYS3 presents the UV-visible spectrum data illustrating this calculation. The nanocomposite FPYS has 1, 3,5,7, and 9 at.% displayed a band gap of 2.44, 2.90, 3.30, 3.31, and 3.7 electron volts (eV), respectively, indicating the observable activity of the photocatalyst as a compound.

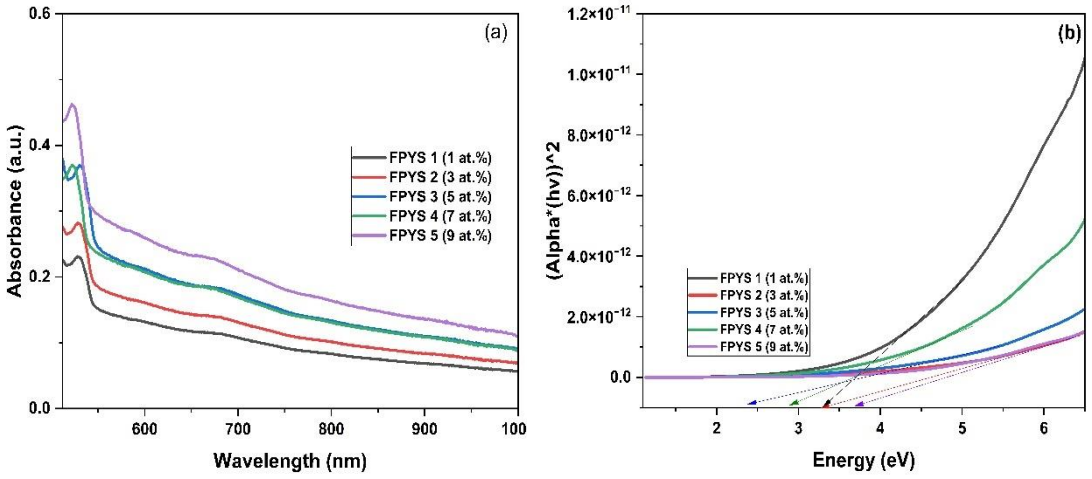

Fig. 3.5.4 (a) Fe_3O_4 UV-visible analysis (b) $Fe_3O_4/Pr^{3+},Y^{3+}$: SnO_2 band gap energy calculation

SnO_2, in this scenario, mitigates the recombination of charge carriers, serving as a valuable strategy to enhance the efficiency of charge transfer and photocatalytic degradation processes. A highly effective separation of photo-excited electrons and holes was accomplished by calculating the spectra of the valence band in FPYS3 (5 at.%). This was conducted to synchronise the electric potentials at the edges of the

conduction band (E_{CB}) and the valence band (E_{VB}) and to evaluate the charge transfer process. The provided connection enables the determination of the potential energy level of the E_{CB} and the E_{VB} by using equations 3.9 and 3.10, respectively, which are mentioned in Section 3.2.3 [Hunge *et al*., (2023)]. The energy band gap (E_{VB}) values for SnO_2 and SnO_2 co-doped with Pr^{3+} and Y^{3+} at various concentrations (1, 3, 5, 7, and 9 at.%) were as follows: 3.60, 3.59, 3.58, 3.57, 3.55, and 3.52 eV, respectively, while E_{CB} values for the identical samples are as follows: -0.08, -0.07, -0.065, -0.06, -0.054, and -0.063 eV, respectively. These results are illustrated in Fig. 3.5.5, and this explains why the excited electron easily moves from the electron conduction band (E_{CB}) of SnO_2 to the conduction band (CB) of the (Pr^{3+},Y^{3+}) co-doped SnO_2 nanoparticle when exposed to LED light. Consequently, the SnO_2 nanoparticles doped with (Pr^{3+},Y^{3+}) could absorb visible light, leading to a reduction in recombination. Reactive hydroxyl and superoxide radicals were essential for facilitating the photocatalytic reaction pathways. This was demonstrated by the band edge potential of photocatalysts, comprised of SnO_2 and SnO_2 nanoparticles co-doped with (Pr^{3+},Y^{3+}).

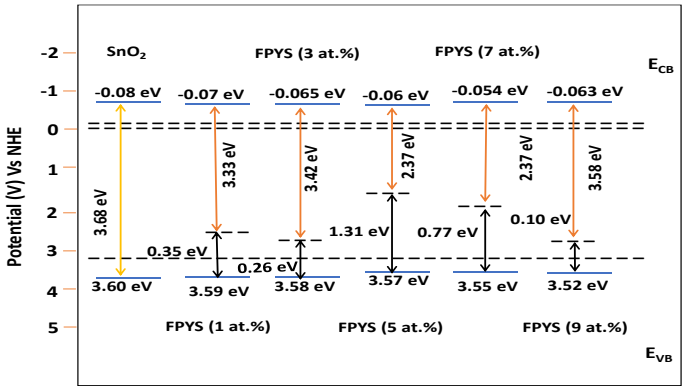

Fig. 3.5.5 Conduction and valence band calculation of various prepared Fe_3O_4/Pr^{3+},Y^{3+}: SnO_2.

3.5.4 SEM studies

After annealing to remove organic components, Fig. 3.5.6(a) presented scanning electron microscopy (SEM) pictures of a SnO_2 nanocomposite co-doped with 5 at.% of Pr^{3+} and Y^{3+}. The SnO_2 nanoparticles co-doped with Pr^{3+} and Y^{3+} (5 at.%) have outer diameters ranging from 29 to 71 nm. The average crystallite size of the nanocomposite was found to be 45.10 nm, as depicted in Fig. 3.5.6(b).

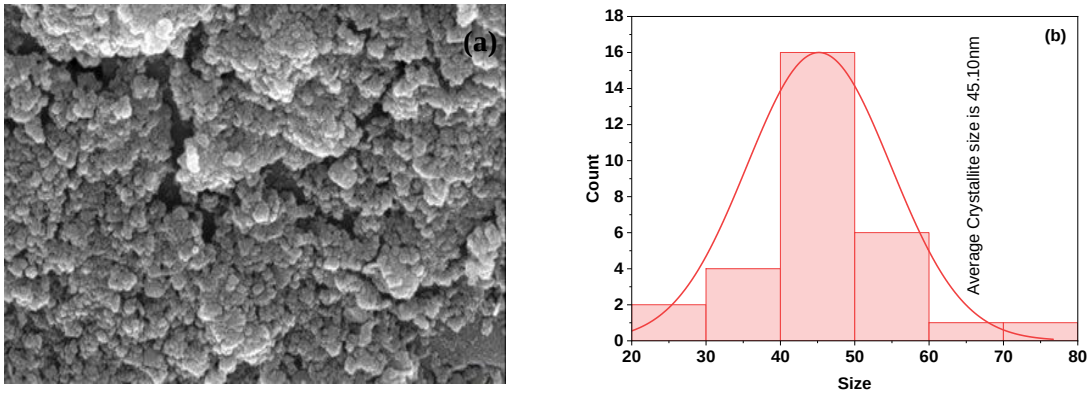

Fig. 3.5.6 (a) SEM image of $Fe_3O_4/Pr^{3+},Y^{3+}$: SnO_2 (FPYS3) (b) Calculation of average crystallite size.

3.5.5 TEM studies

We performed TEM, HRTEM, and SAED analyses on FPYS3 (5 at.%) nanocomposite to understand the microstructure further. The transmission electron microscopy (TEM) image is shown in Fig. 3.5.7(a), which illustrated a nanocomposite material consisting of FPYS3 (5 at%) with a co-doping concentration of 5 at% and Fig. 3.5.7(b) shown a high-resolution transmission electron microscopy (HRTEM) picture, which was used to confirm the d-spacing of the produced nanocomposite.

The average grain size was found to be approximately 44.08 nm, and the HRTEM image revealed the rutile (tetragonal) SnO_2 structure with lattice distances of 0.254 nm, 0.309 nm, and 0.35 nm. Fig. 3.5.7(c) shows the selected area electron diffraction (SAED) images, which clearly show the diffraction circles. This proved that the FPYS3 (5 at.%) nanocomposite has a polycrystalline structure.

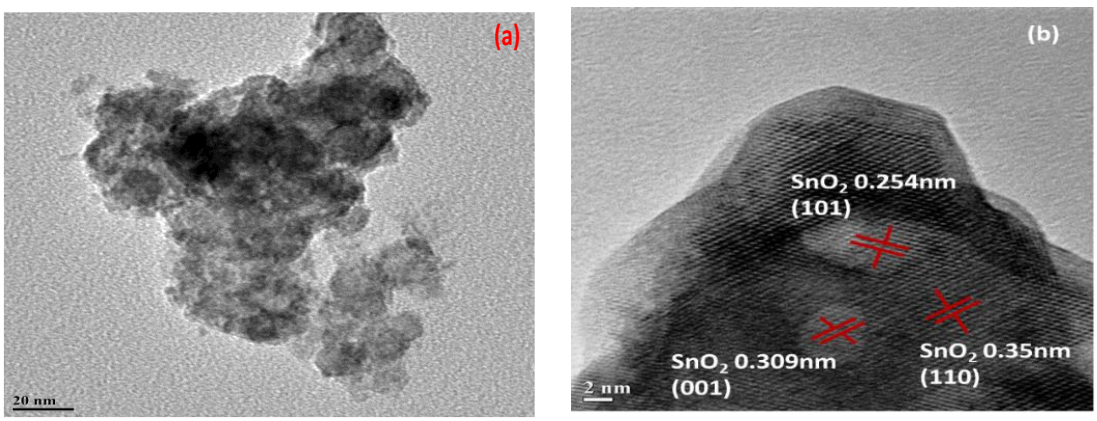

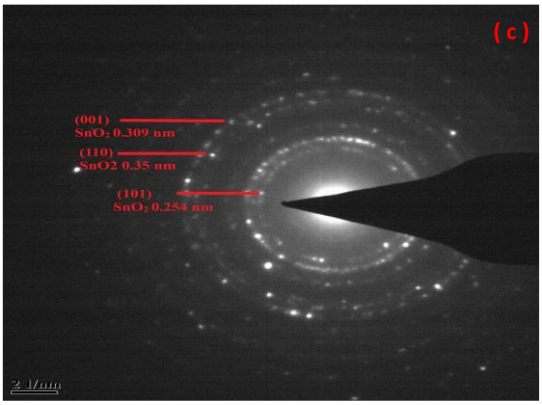

Fig. 3.5.7(a) TEM (b) HRTEM (c) SAED of $Fe_3O_4/Pr^{3+},Y^{3+}$: SnO_2 (FPYS3).

3.5.6 XPS studies

As illustrated in Fig. 3.5.8(a), the chemical compositions and bonding states of a SnO_2 nanocomposite co-doped with 5 at.% Pr^{3+} and Y^{3+} were investigated using X-ray photoelectron spectroscopy (XPS). With a spin-orbit splitting of 2 eV, the Y-doped SnO_2 complexes have binding energy values of Y $3d_{5/2}$ of about 157.17 eV and Y $3d_{3/2}$ of around 159.3 eV, which is shown in Fig. 3.5.8(b). It is clear from these findings that trivalent oxidation states are most common for yttrium ions [Baoping *et al*., (2020)]. While the XRD pattern of the samples (Fig. 3.5.1) clearly indicated the presence of the spinel structure, it is still possible that there may be some γ-Fe_2O_3 phase in the nanoparticles. This is because the γ-Fe_2O_3 and Fe_3O_4 phases have comparable characteristics. Because it is so sensitive to Fe^{2+} and Fe^{3+} cations, X-ray photoelectron spectroscopy (XPS) is a great way to tell the difference between the two phases. The $Fe2p_{3/2}$ and $Fe2p_{1/2}$ levels in Fig. 3.5.8(c), have energy values of 710 and 723 eV, respectively. This suggested that the sample is Fe_3O_4, rather than γ-Fe_2O_3 (the $Fe2p_{3/2}$ and $Fe2p_{1/2}$ levels are measured at 711 and 725.0 eV, respectively, for γ-Fe_2O_3). The literature [Wang *et al*., (2005); Brojendro Singh Shagolsem, Nongmaithem Mohondas Singh, (2024)] confirms that the peaks in Fe_3O_4 shift towards greater binding energy. And become wider, which can be attributed to the presence of $Fe^{3+}(2p_{3/2})$ and $Fe^{2+}(2p_{1/2})$. Thus, it indicated that the nanoparticles generated should be in the magnetite (Fe_3O_4) phase.

The spectrum of Pr 3d, as shown in Fig. 3.5.8(d), comprises Pr $3d_{5/2}$ at 931.7 eV and Pr $3d_{3/2}$ at 954.7 eV, which represent Pr^{3+} and Pr^{4+} ions, respectively [Ogasawara

et al., (1991)]. The SnO_2 lattice was validated by the O1s spectra analysis, which showed a peak at 531.94 eV, respectively, which is shown in Fig. 3.5.8(e). These peaks correspond to the M-O bond, the Sn-O-Sn bond, and the Pr-O-Pr bond, respectively. Fig. 3.5.8(f) shows that Sn $3d_{5/2}$ of Sn^{4+} is allocated a peak at 486.96 eV, while Sn $3d_{3/2}$ of Sn^{4+} is assigned a peak at 496.4 eV [Li *et al*., (2008); Brojendro Singh Shagolsem, N. Mohondas Singh, (2024)]. The SnO_2 nanocomposite, co-doped with 5 at.% (Pr^{3+},Y^{3+}), showed the presence of Y^{3+},Pr^{3+} ions at the Sn sites.

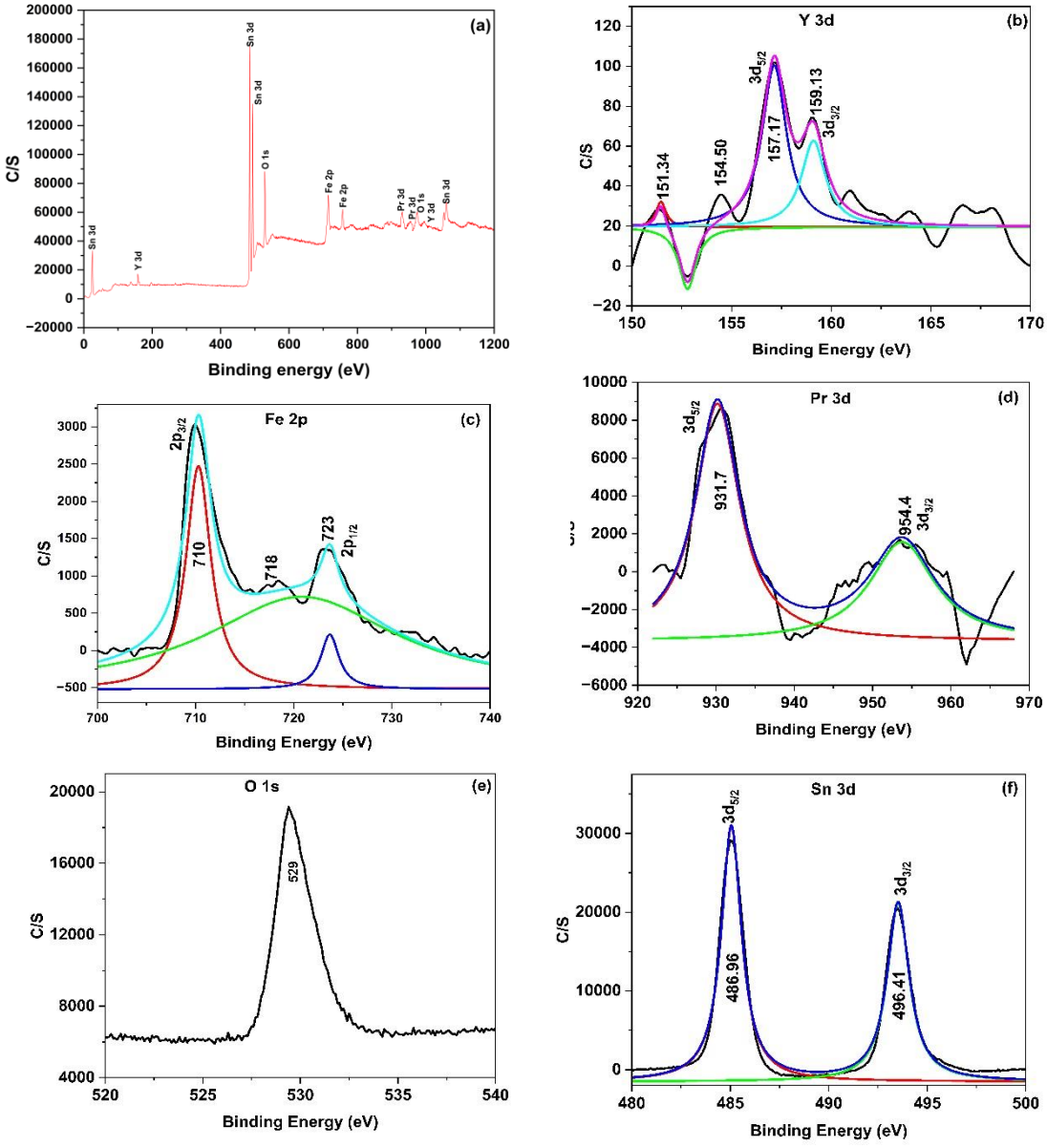

Fig. 3.5.8 XPS of (a) Fe_3O_4/Pr^{3+},Y^{3+}: SnO_2 (b) Y 3d (c) Fe 2p (d) Pr 3d (e) O 1s (f) Sn

3d in $Fe_3O_4/Pr^{3+},Y^{3+}$: SnO_2 (FPYS3)

3.5.7 Brunauer-Emmett-Teller (BET) studies

The FPYS3 (5 at.%) adsorption-desorption isotherms are shown in Fig. 3.5.9. When the relative pressure is less than 0.4, the mesoporous structure displays a monolayer of N_2 adsorbed onto its walls. Because of the increased capillary density in the tin mesoporous material, the adsorption plot oscillates between 0.4 and 0.48 on account of a sharp and increasing slope. According to Tao *et al.*, the bulk of the 0.5 value is linked to the adsorption of several layers on the surface of the particles [Tao *et al*., (2015)]. Table 3.5.2 presents the findings of using the BET approach to measure the surface area, dimensions, and cavity capacity by the details given by Chen *et al*. [Chen *et al*., (2017)]. When compared to FS (0.356 m^2/g), FPYS3 (5 at.%) has a much higher specific surface area (25.468 m^2/g). This shift occurred because of a rearrangement of metal nanoparticles, which significantly decreased FS buildup. According to Fig. 3.5.9, which showed the BJH pore size distribution plot of FPYS3 (5 at.%), the apertures have a maximum radius distribution that ranges from 1 to 4 nm, and the IUPAC classification classifies the isotherm displayed in Figure as type IV. Pores in a substance are characteristic of materials with this type of isotherm [Qi *et al.*, (2009)]. The porous SnO_2 nanostructure improved the dye adsorption-desorption process and increased the number of active sites for surface contact reactions. Furthermore, it provided a considerably greater surface for contact and minimal obstruction to the spread of particles. These features suggest its potential application in dye degradation.

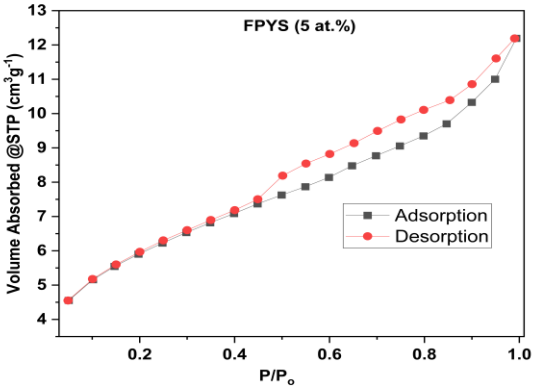

Fig. 3.5.9 Application of the Brunauer-Emmett-Teller (BET) method to

$Fe_3O_4/Pr^{3+},Y^{3+}$: SnO_2 (FPYS3).

Table 3.5.2 Provides details on BET surface area, pore volume, and pore size attributes for FS and FPYS3 (5 at.%).

Sample	S_{Bet} (m^2/g)	Pore Volume (cm^3/g)	Pore size (nm)
Fe_3O_4/SnO_2 (FS)	0.356	0.031	2.136
$Fe_3O_4/Pr^{3+},Y^{3+}$:SnO_2 (FPYS3 (5 at.%))	25.468	0.052	2.878

3.5.8 Photoluminescence studies

Investigating photoluminescence (PL) [Premjit *et al*., (2020); Ramananda *et al*., (2022)] has provided a clearer insight into the recombination rate and transfer behaviour of electron-hole pairs generated by light. In Fig. 3.5.10, the photoluminescence spectra of various FPYS3 (5 at.%) are presented. The photoluminescence spectrum of pristine SnO_2 revealed prominent emission peaks in the visible spectrum, notably at wavelengths of 454 nm and 468 nm, characteristic of its luminous qualities. The existence of these peaks can be attributed to various factors, including material defects, the distinctive crystal structure of SnO_2, and crystallographic imperfections resulting from the expansion process, leading to such emission. An elevated concentration of oxygen vacancies or tin interstitials creates a defect level within the band gap of SnO_2, causing significant photoluminescence emission due to the presence of O vacancies or Sn interstitials. As a result, numerous trapped states or metastable energy levels are formed. Additionally, efficient photogenerated carrier recombination can occur close to several small grain boundaries. FPYS3 (5 at.%) nanocomposite exhibited diminished photoluminescence (PL) intensity in comparison to unmodified SnO_2, indicating effective separation of charges and suppression of electron-hole recombination. To enhance the separation of charges, capturing the electrons created by SnO_2 was necessary. The presence of (Pr^{3+},Y^{3+}) ions was essential for this process, and consequently, the visible light performance of the FPYS3 (5 at.%) system was enhanced. The FPYS3 (5 at.%)

material's photoluminescence (PL) output proved that the electron-hole pairs were successfully separated.

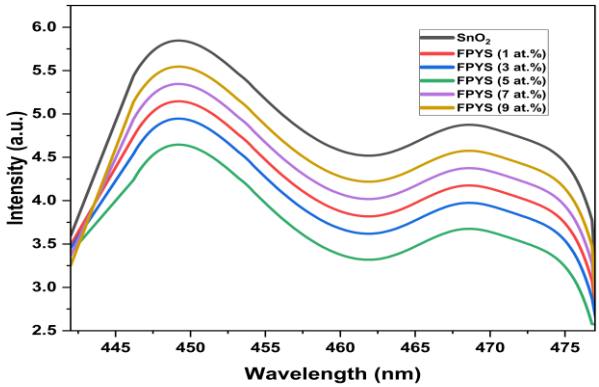

Fig. 3.5.10 Photoluminescence of $Fe_3O_4/Pr^{3+},Y^{3+}$: SnO_2 having different co-doping atomic percentage.

3.5.9 Radical studies

Visible light exposure was employed to assess the photocatalytic effectiveness of various scavengers, aiming to identify the reactive radicals responsible for the degradation of dyes and pesticides in a 5 at.% (Pr^{3+},Y^{3+}) co-doped SnO_2 nanocomposite. Fig. 3.5.11(a) illustrated incorporating without Scavenger (No S) and with different scavengers into the photocatalytic process to neutralise the reactive radicals. This variation in scavengers resulted in a change in the C_t/C_o of the dye or pesticide. The catalytic procedure involved employing scavengers such as isopropyl alcohol (IPA), benzoquinone (BQ) [Bhuvaneswari *et al*., (2020)], benzoic acid (BA) [Prakash *et al*., (2016)], and ethylene diamine tetraacetic acid disodium (EDTA disodium) [Keerthana *et al*., (2021)] to trap hydroxyl radicals (ȮH), superoxide radicals ($\dot{O}_2^-$) and holes (h^+) respectively. Fig. 3.5.11(b) demonstrated the influence of various scavengers on the radiation efficiency of SnO_2 co-doped with 5 at.% (Pr^{3+},Y^{3+}).The degradation of MB dye decreased from 70 to 67 and 69% when IPA and BA were present as scavengers, respectively. The data on degradation efficiency indicated that hydroxyl radicals play a crucial role in decomposing the MB dye into water and carbon dioxide. A slight degradation efficiency alteration was observed upon adding EDTA and BQ to the reaction system. These data indicate that the main reactive species participating in the visible irradiation catalytic process of MB are

superoxide radicals and holes. The results indicated that SnO_2 doped with (Pr^{3+},Y^{3+}) at concentrations of 5 at.% could effectively expand the LED light absorption range into the visible region due to their ability to degrade MB dye.

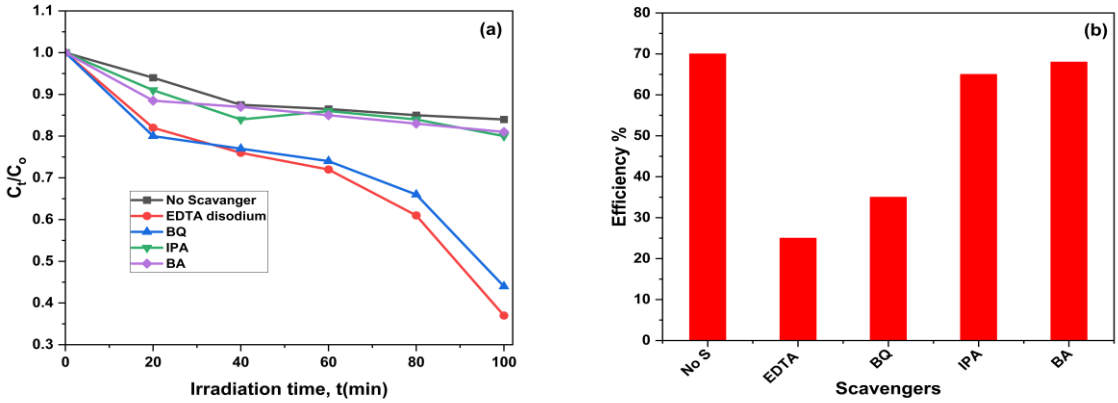

Fig. 3.5.11 (a) Relationship between C_t/C_o and Irradiation time (b) Efficiency using various Scavengers.

3.5.10 EPR studies

The study focused on the detection of individual electrons with oxygen vacancies through the use of EPR spectroscopy. Oxygen vacancies were discovered in the SnO_2 system, and the electron paramagnetic resonance (EPR) measurement enhanced the comprehension of oxygen vacancy defects. The presence of oxygen vacancies in the SnO_2 nanoparticle is directly correlate with the peak intensity seen in the EPR analysis [Kumar *et al*., (2018)].

The current work found that at ambient temperature, SnO_2 co-doped with 5 at.% (Pr^{3+},Y^{3+}) displayed resonances at 312.45 mT in the EPR spectrum (Fig. 3.5.12), and to determine the g-value, use the same equation 3.12, given in Section 3.2.9. The study of resonant magnetic fields showed that the g-value of SnO_2 doped with 5% Pr^{3+},Y^{3+} is 2.003, which is very close to the g-value of a free electron (2.009). The significant increase in energy level noted in the SnO_2 nanoparticle doped with Pr^{3+},Y^{3+} at 5 at.% is due to the profusion of oxygen vacancies.

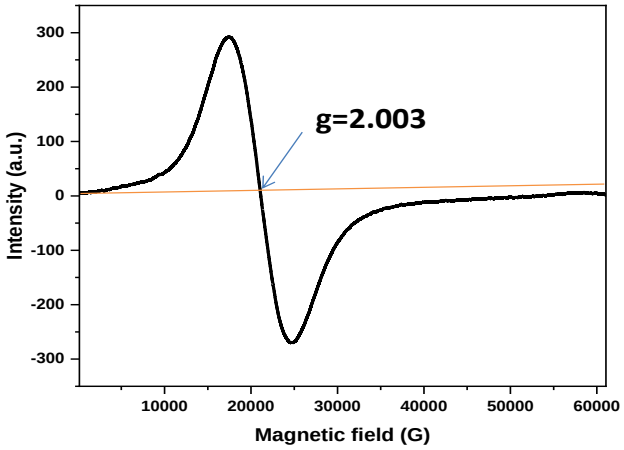

Fig. 3.5.12 EPR of $Fe_3O_4/Pr^{3+},Y^{3+}$ (5 at.%):SnO_2 (FPYS3)

3.5.11 Photocatalytic studies

In each experiment, 20 mL of contaminated water containing an aqueous solution of dye or pesticide with a concentration of 8 ppm was mixed with 3 mg of FPYS3 nanocomposite photocatalyst. This mixture was left in the dark for 30 min to allow adsorption and desorption equilibrium. The degradation rate was determined by monitoring the absorption spectrum of MB at its maximum wavelength (λ_{max}=664nm) while exposing it to LED light. The photocatalytic degradation process continued for 150 min under light exposure. The results of the study revealed a gradual decrease in the light absorption of MB over the 0 to 150 min period, with measurements taken at 30 min intervals. Subsequently, the magnetic nanocomposite photocatalyst initiated the breakdown of the dye, and its decomposition efficiency was calculated using equation 3.3 mentioned in Section 3.1.9. Electrons in an elevated energy state within the conduction band have the potential to engage with oxygen molecules, resulting in the generation of superoxide radical anions ($\dot{O}_2^-$) [Yadav *et al.*, (2023)]. Molecules creating holes in the valence band reacted with water molecules to produce hydroxyl radicals (ȮH) [Hirami *et al.*, (2023); Lallianmawii, N. Mohondas Singh, (2023)].

Subsequently, the methylene blue dye was adsorbed onto the catalytic surface composed of FS and FPYS3 (5 at.%) nanocomposite. Following this, the catalyst surface underwent light absorption, generating photogenerated electron (e^-) and hole

(h^+) pairs. Oxidation products formed upon hole interaction with MB dye were $MB^{\bullet+}$. Conversely, electron interaction with MB dye led to the formation of a reduction product known as $MB^{\bullet-}$. The generated electrons and holes fully covered the surface of the FS and FPYS3 (5 at.%) nanocomposite. Hydroxyl radicals ($\dot{O}H$) were generated in the aqueous MB dye solution through a hole reaction with H_2O molecules, and hydroxyl radicals were adsorbed on the surface. Electrons produced from the photochemical reaction are combined with surrounding oxygen and the MB aqueous solution, producing superoxide anions ($\dot{O}_2^-$). Both hydroxyl radical ($\dot{O}H$) and superoxide anion species ($\dot{O}_2^-$) could undergo reactions in the presence of the MB dye on FS and FPYS (5 at.%) nanoparticles. This reaction led to the release of water and carbon dioxide due to the breakdown of the MB dye. In summary, the reaction process can be represented as follows:

$$\left.\begin{array}{c} SnO_2 + h\nu \rightarrow SnO_2 + h^+ + e^- \\ Pr^{3+}/Y^{3+} : SnO_2 + h\nu \rightarrow Pr^{3+}/Y^{3+} : SnO_2 + h^+ + e^- \\ h^+ + \text{dye} \rightarrow \text{dye}^{\bullet+} \rightarrow \text{Oxidation products} \\ e^- + \text{dye} \rightarrow \text{dye}^{\bullet+} \rightarrow \text{Reduction products} \\ h^+ + H_2O\,(ads) \rightarrow H^+(ads) + \dot{O}H \\ e^- + O_2\,(ads) \rightarrow \dot{O}_2^- \\ MB + \dot{O}H \rightarrow CO_2 + H_2O \rightarrow \text{Degradation products} \\ MB + \dot{O}_2^- \rightarrow CO_2 + H_2O \rightarrow \text{Degradation products} \end{array}\right\} \quad (3.16)$$

3.5.11.1 MB degradation

Fig. 3.5.13(a) illustrates the degradation of Methylene Blue (MB) under LED light exposure, representing the analysis's findings. FPYS3 nanocomposites are thought to have a higher surface area and better photocatalytic ability because they are smaller and have a smaller energy gap. This makes degradation happen faster. As shown in Fig. 3.5.13(b), the breakdown of MB is caused by the interaction between MB molecules and the hydroxyl groups of FPYS nanocomposites. As a result of this interaction, chemical bonds such as sulfur-chlorine, Nitrogen-Methyl, Carbon-Sulfur, Carbon-Nitrogen, and Carbon-Oxygen dissociate. Ultimately, smaller organic molecules were formed through a chain reaction that breaks down intermediate components and opens MB rings, which confirmed from LCMS studies that m/z (4-(N, N-dimethyl)-aniline)=136.22 and m/z (2-amino-4-(N, Ndimethyl)

benzenesulfonicacid) = 231.26. The process is completed during mineralization, resulting i n the end molecules CO_2 and H_2O, as depicted in Fig. 3.5.13(c).

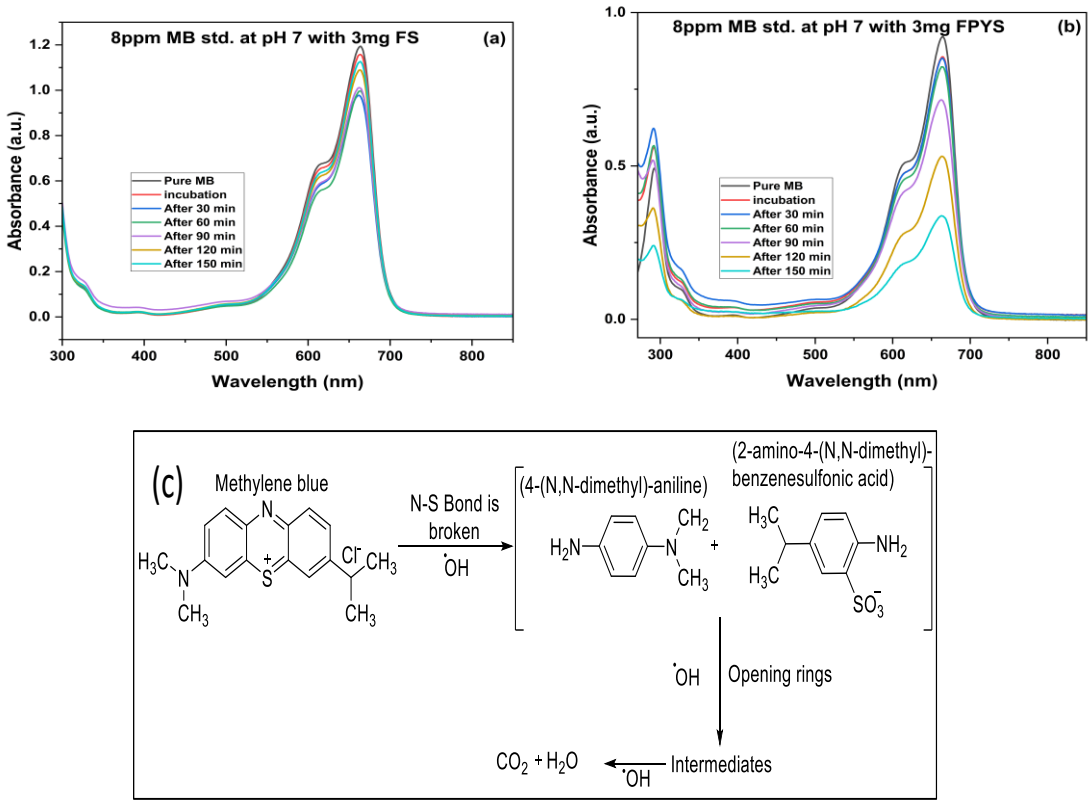

Fig. 3.5.13 MB degradation with prepared nanocomposite (a) FS (b) FPYS3 (5 at.%) (c) Mineralization of MB.

3.5.12 Dosage effect studies

The appropriate amount of catalyst was utilized for faster breakdown of the dye solution. Fig. 3.5.14((a)-(b)) demonstrates that exposing an 8 ppm, 20 mL, pH 7 solution to LED light for 30 min results in a rise in MB concentration from 1 to 11mg. By studying adsorption and desorption in systems with varying catalyst concentrations, it became clear why photocatalytic activity increases as the catalyst quantity increases. As a result, an increased number of photocatalysts resulted in a higher quantity of active sites, enabling a greater absorption of MB prior to photocatalysis. High levels of photocatalysts result in a decrease in irradiance due to light scattering. The photocatalytic degradation exhibited reduced efficacy. The

overall impact was substantial; hence, augmenting the photocatalyst did not enhance the process of photocatalytic breakdown. The investigation of the degradation of photocatalytic dye solutions under LED light was also conducted in this experimental arrangement. The original concentration of 8 ppm produced disappointing outcomes. The breakdown rate showed a 10% augmentation, escalating from 60% to 70%, with an increase in the quantity of photocatalyst from 1 to 3mg. The degradation efficiency of the breakdown rate did not improve when the catalyst dose increased from 3 to 11mg. After considering all of these elements, it was concluded that the most favourable quantity of nanocomposite photocatalyst to utilise was 3mg. The graph shows that the use of 3 mg of catalyst resulted in achieving the optimal peak.

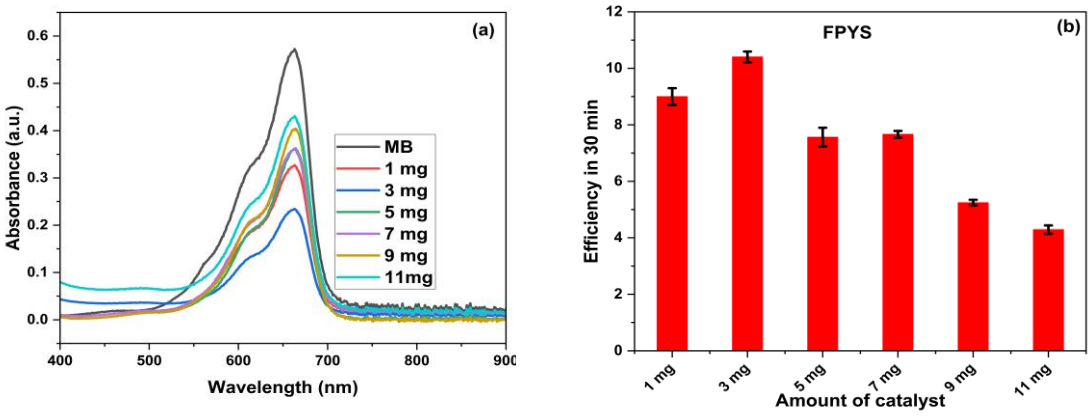

Fig. 3.5.14 (a) MB degradation (b) Efficiency of degradation at various amount of prepared photocatalyst.

3.5.13 pH effect studies

The UV-visible spectra of dye or pesticide photodecomposition at various pH levels while maintaining a consistent beginning concentration of 8 ppm and a catalyst concentration of 3mg in 20 ml of pollutant solution are presented below. According to the study, pollutants readily decompose at various pH values. The acidic solution utilized to produce the nanocomposite photocatalyst may exhibit flaws, leading to alterations in the doping structure and a decrease in photocatalytic efficiency.

The pH of the environment impacted the redox species and their ability to adhere to catalysts. Hydroxyl radicals were the predominant oxidising agents under alkaline

or neutral conditions, but positive holes played a key role under acidic conditions. The comparison of these findings indicates that the nanocomposite photocatalyst exhibits optimal performance within the pH range of 5 to 7. The Langmuir-Hinshelwood kinetic model and the provided equation were employed to linearly fit the degradation of dyes or pesticides according to pseudo-first-order kinetics. The equation relates the starting concentration of dye or pesticide (C_o), the pseudo-first-order rate constant (k), and the concentration of dye or pesticide at a given time (C_t).

3.5.13.1 MB Degradation

For pH values between 5 and 10, the FPYS3 solutions showed absorption rates of 65.90, 62.82, 55.91, 58.75, 63.18, and 68.74% after 150 minutes of exposure to the treated dye solution with the chemical. Exposure to LED light significantly reduces the degradation of the pure MB dye, which is 3%. The LED-MB-FPYS3 solution, which is the most severely damaged after 150 min of exposure to LED radiation at pH 10, has an estimated degradation rate of 68.74%. The results of a linear regression are shown in Fig. 3.5.15. The rate constant (k) for fitting absorption time was determined by taking the logarithm of the ratio C_t/C_o and using it to estimate the slope of the line.

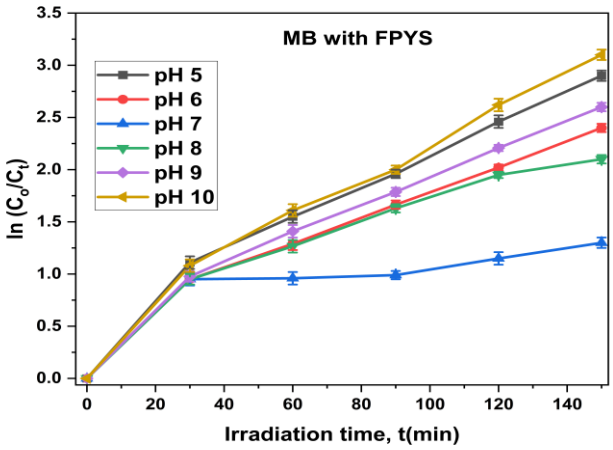

Fig. 3.5.15 Kinetics of photodegradation.

3.5.13.2 RhB Degradation

In the adsorption study for FPYS3 at pH values ranging from 5 to 10, the results show that RhB is cationic, with adsorption percentages of 60.59, 58.98, 52.68, 54.91,

58.85, and 62.93%, respectively. The degradation of RhB dye under LED light is practically nonexistent (less than 2%) in the absence of FPYS3 nanocomposite. The LED-RhB-FPYS3 nanocomposite showed the most promise. It degraded 62.93% of the RhB molecule in 150 minutes, consistent with previous photocatalysis trials. The linear regression analysis in Fig. 3.5.16 (a) used the logarithm of the ratio C_t/C_o to determine the line's slope. Because of this, we were able to approximate the fitting absorption time's rate constant, k. Fig. 3.5.16(b) showed more details on the degradation of RhB, which is accelerated by the hydroxyl radicals of the nanocomposite, which also speeds up the processes of N-de-ethylation and chromophore change.

The mechanism initiates the opening of molecular rings, forming smaller RhB molecules, and producing oxidation products by breaking chemical bonds. LCMS investigations validated the following m/z values: Terephthalic acid = 166.12, 3-hydroxybenzoic acid = 122.11, benzoic acid = 122.11, succinic acid = 118.08, and adipic acid = 146.13. Mineralization into smaller molecules, which resulted in the production of CO_2 and H_2O, was the subsequent phase in the process.

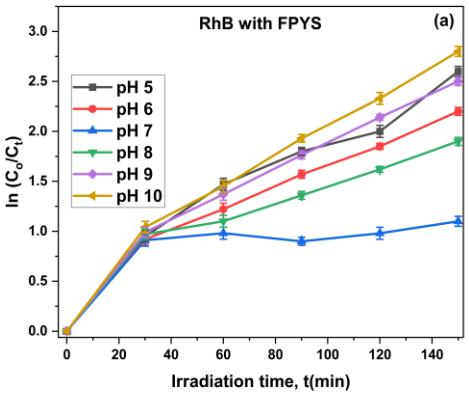

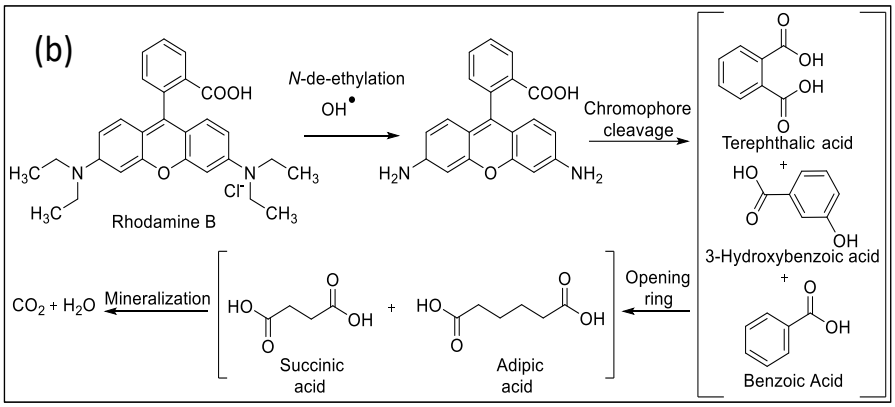

Fig. 3.5.16 (a) Kinetics of photodegradation (b) Mineralization of RhB.

3.5.13.3 MB and rhodamine (mixture) Degradation

At pH 7, solutions containing FPYS3 have a degradation efficiency of 50.86% and 44.42%, respectively, and both hues have an absorption time of 150 min. An electrostatic interaction formed between the positively charged FPYS3 surface and the negatively charged dye molecules, which increases absorption. However, the combination of MB and RhB, only degrades 1% when exposed to LED light. Fig. 3.5.17((a)-(c)) shows that after 150 min of exposure to the LED-MB-FPYS3 solution at pH 7, the maximum degradation percentage reached about 50.86%. The smaller size and band gap of FPYS3 nanocomposites allow for increased surface area and improved photocatalytic efficacy. There are a variety of possible explanations for why rhodamine B (RhB) and methylene blue (MB) become less soluble when mixed with water. Some of these explanations include: The interface between solvents and water is one possible location for adsorption of RhB and MB molecules. Combining two colours that aren't very water-soluble can reduce the overall water solubility of the mixture through competing adsorption. When exposed to water, RhB and MB molecules can aggregate, thereby lowering the combined solubility of the colors. When RhB and MB molecules come together to form complexes, the solubility of the molecules involved can change due to the species' tendency to precipitate out of solution during complex formation.

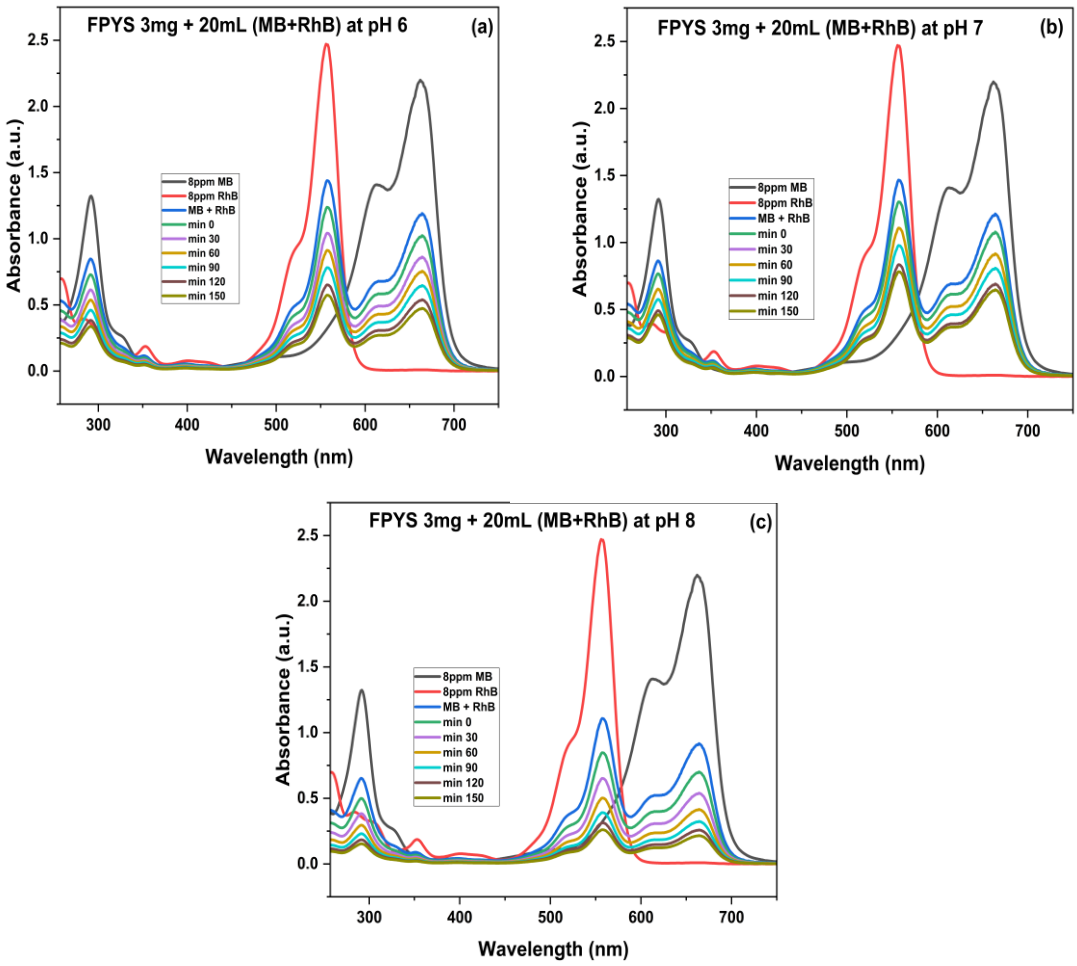

Fig. 3.5.17 (a)-(c) Degradation of MB and RhB mixtures with FPYS3.

3.5.13.4 Degradation of 2, 4-DCP under LED irradiation

The degradation efficiency was 51% at pH 5 and 53% at pH 10, respectively, when 3 mg of FPYS3 nanocomposite were subjected to light-emitting diode radiation. One of the Langmuir-Hinshelwood connections Chen and Ray (1999) found states that 2, 4-DCP degradation is concentration-dependent. There may be some surfaces that are resistant to 2,4-DCP hydrolysis. Our linear regression study used the logarithm of the ratio C_t/C_o to determine the line slope for both 2,4-DCP. Fig. 3.5.18(a) displayed the study results in their original formats. This method allowed us to approximate the rate constant (k) for the photocatalytic degradation of 2,4-DCP using the as-prepared nanocomposite, while Fig. 3.5.18(b) presented the mineralization of 2,4-DCP:

chloromalcic acid has a m/z of 147.48 and unsaturated carboxylic acid has a m/z of 72.05, both of which were confirmed by the LCMS studies.

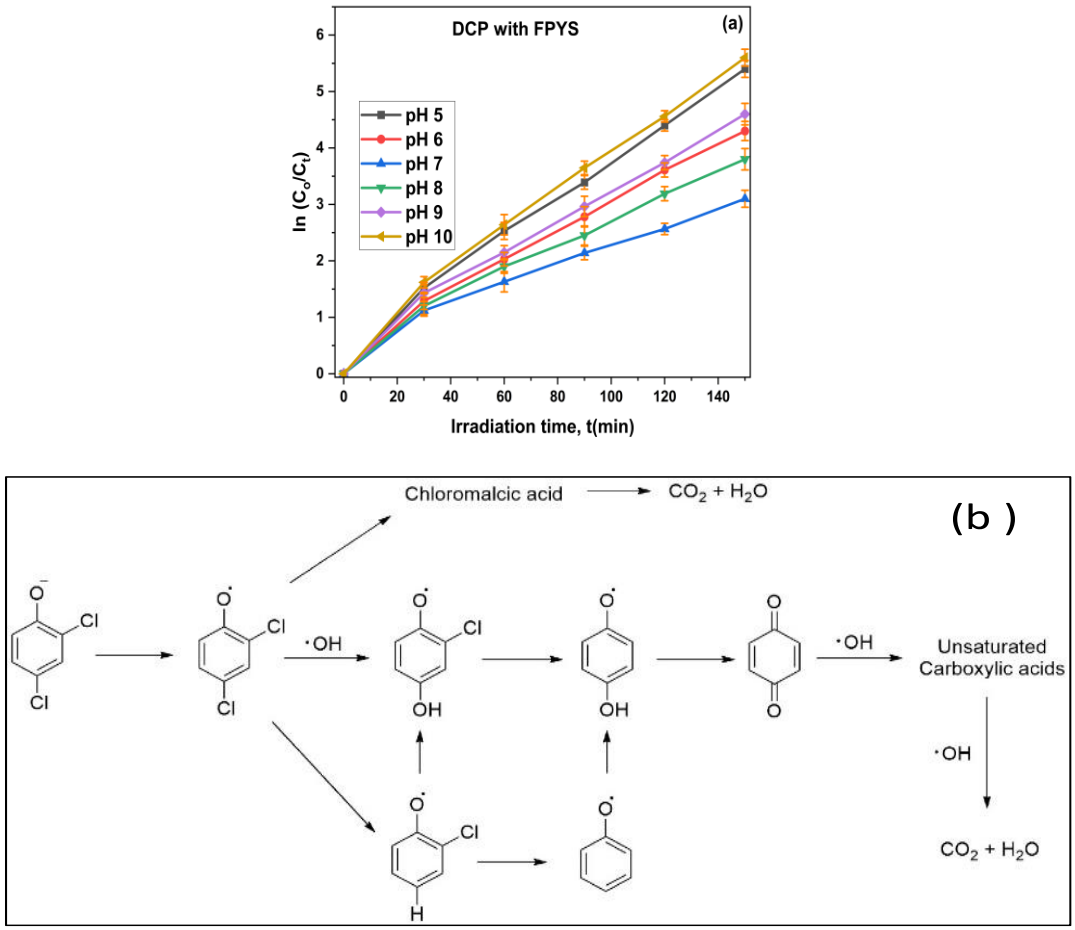

Fig. 3.5.18(a) Kinetics of 2,4-DCP photodegradation, (b) Mineralization of 2,4-DCP photodegradation.

3.5.13.5 TCAA degradation

The HPLC chromatograph of the 8 ppm Standard TCAA is shown in Fig. 3.5.19(a), and the study used a pH spectrum of 5 to 10 to measure the proportion of total organic carbon (TOC) eliminated, which allowed researchers to examine FPYS3's capacity to mineralize trichloroacetic acid (TCAA). Under regulated conditions, such as an 8 ppm catalyst concentration and a 150 min contact period, the mineralization and degradation of TCAA by FPYS3 were examined using high-performance liquid

chromatography (Waters HPLC, C18 column), as shown in Fig. 3.5.19(b). We found that the breakdown intermediates, hydroxyacetic acid, formic acid, and acetic acid—were less harmful than the initial TCAA. The LCMS assay identified one or two intermediates during the breakdown of the TCAA as CH_2O_2, hydroxyacetic acid ($C_2H_4O_3$, m/z 93, R_t 4.9 min), and acetic acid ($C_2H_4O_2$, m/z 62, R_t 3.63 min) in the mass chromatograms. The LCMS analysis identified an intermediate with m/z 46, originating from another intermediate with m/z 62. Even though acetic acid and hydroxyacetic acid were the key players in the breakdown of TCAA, the LCMS analysis only showed formic acid as an intermediary. LCMS and other studies found molecular features that pointed to a possible way for TCAA to break down in the FPYS3 process, as shown in Fig. 3.5.19(c).

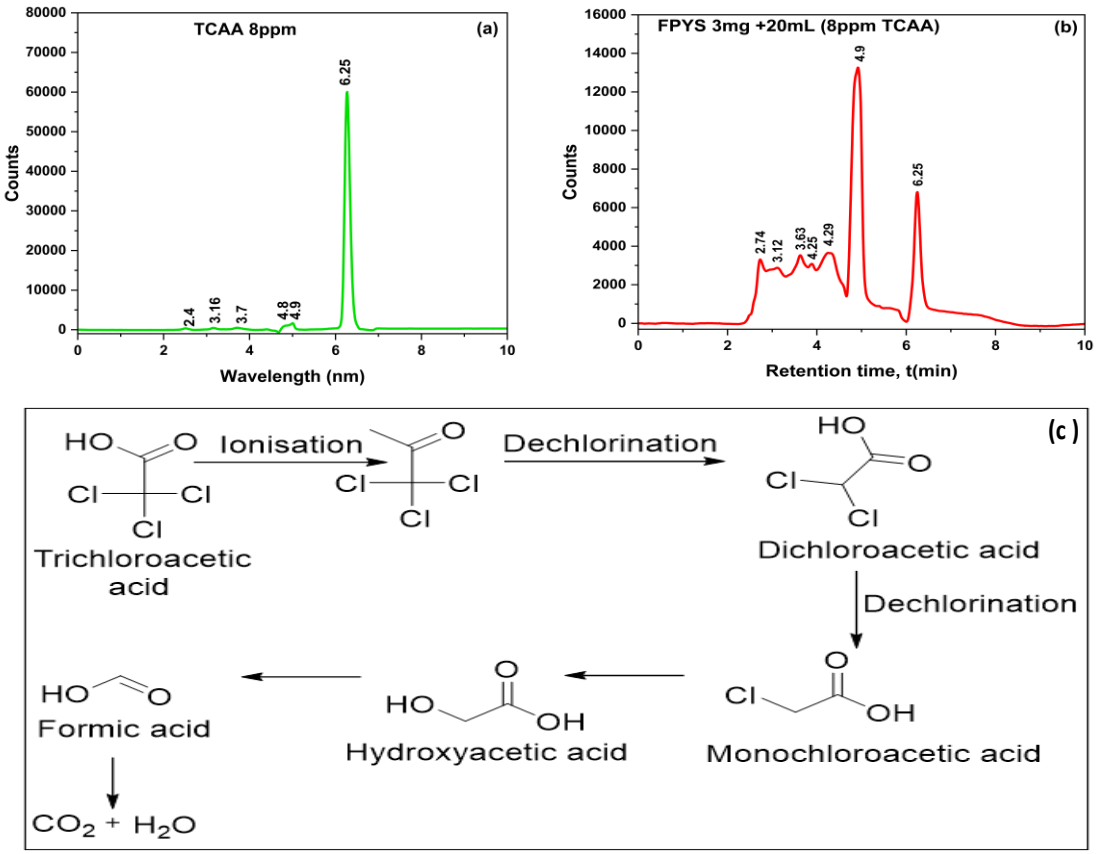

Fig. 3.5.19 (a) Std TCAA(8ppm) (b) TCAA decomposition with 3mg of FPYS3 (c)Mineralization of TCAA.

3.5.14 TOC (Total Organic Carbon) determination

The main aim of the thorough carbon investigation was to understand the mineralization processes of dyes and pesticides. When 3 mg of FPYS3 (5 at.%) was employed, the TOC removal percentage for dyes or pesticides at an 8 ppm concentration decreased, as depicted in Fig. 3.5.20, indicating a photo-mineralization efficiency of 57%. Conversely, when using FS with an equivalent amount of photocatalyst, there was only a slight decrease in photomineralization efficiency, reaching 32%. The limited presence of active sites on the catalyst surface hindered the expected reaction, decreasing the absolute TOC value from 57 to 32%. Additionally, this data provides valuable insights into the potential presence of residual Total Organic Carbon (TOC) in each solution, attributed to reactions occurring during intermediate phases before complete mineralization. Equation no. 3.7, which is given under Section 3.1.10, was utilised to calculate the degrading demineralization of dyes or pesticides. In order to ensure the experiment's accuracy and reliability, we have conducted it on three separate occasions.

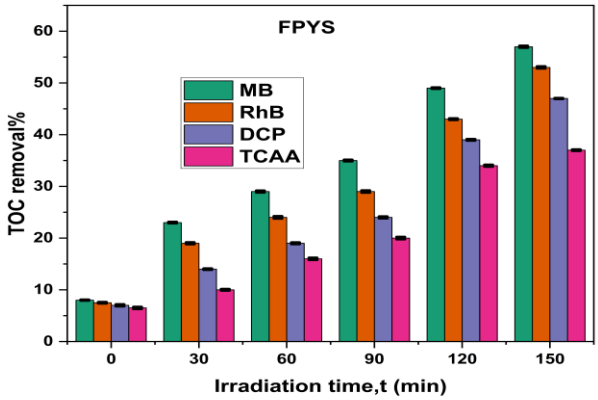

Fig. 3.5.20 TOC removal% of MB, RhB, 2,4-DCP and TCAA with FPYS3 (5 at.%).

3.5.15 Comparison

Table 3.5.3 displays degradation constants, which quantify the photocatalytic activity of a substance. Due to an increase in the quantity of hydroxyl ions, the degradation rate constants of dyes increased as the pH rose. At pH 7, both the LED-MB-FPYS3 and LED-RhB-FPYS3 solutions degrade at different rates. Furthermore, compared to the LED-RhB-FPYS3 solution, the LED-MB-FPYS3 (pH 7) sample deteriorated at a faster pace, which is shown in Fig. 3.5.21 and We repeated the

experiment three times to make sure it was accurate and reliable. The primary distinction between the two molecules was their chemical composition. In particular, Rhodamine B's larger and more complex molecular structure was responsible for its uniqueness. The structural features of dye molecules dictated how photocatalysis could degrade them. Our findings demonstrate that the FPYS nanocomposite produced using a green process with Parkia speciosa extract performs as well as, if not better than, the previously reported materials. Using this technique to break down pollutants in water was remarkably efficient.

The study looked at how well FPYS3 mineralized 2,4-DCP and TCAA across a pH range of 5 to 10 and found out what percentage of total organic carbon (TOC) was removed. Under these conditions, we found that the degradation rates for 2,4-DCP and TCAA were 53% and 44%, respectively. Moreover, whereas TCAA's mineralization rates varied between 6.5% and 37% across the 150 min period, 2,4-DCP's rates varied between 7% and 47%. One of the last results of mineralization is the significant breakdown of 2,4-DCP and TCAA into CO_2 and H_2O. The results indicate a positive correlation between the rate of mineralization and the reaction time, indicating that TCAA necessitates a longer reaction time for complete mineralization. When comparing the two methods for mineralization of 2,4-DCP, the results suggest that the FPYS3 strategy may have been superior.

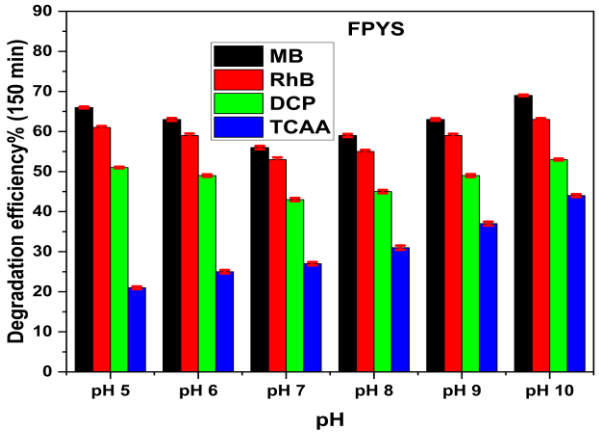

Fig. 3.5.21 Degradation efficiency of RhB, MB, 2,4-DCP and TCAA

Table 3.5.3 Determination of rate constant for photocatalytic decomposition of RhB, MB, 2,4-DCP and TCAA

pH	MB		RhB		DCP		TCAA	
	k (min^{-1})	R^2	k (min^{-1})	R^2	k (min^{-1})	R^2	k (min^{-1})	R^2
pH 5	0.067	0.936	0.073	0.913	0.054	0.925	0.043	0.935
pH 6	0.064	0.936	0.070	0.931	0.051	0.913	0.041	0.909
pH 7	0.061	0.938	0.062	0.919	0.051	0.935	0.036	0.911
pH 8	0.062	0.933	0.068	0.943	0.059	0.915	0.038	0.917
pH 9	0.065	0.915	0.072	0.909	0.052	0.929	0.042	0.915
pH 10	0.069	0.919	0.074	0.915	0.061	0.925	0.044	0.929

For RhB, MB, 24-DCP, and TCAA treated with FPYS under LED light, the experimental data aligns more closely with the pseudo-first-order model (R^2 = 0.900, 0.936, 0.896, 0.872) than with the pseudo-second-order model (R^2 = 0.784, 0.852, 0.818, 0.758), indicating that the reaction likely follows pseudo-first-order kinetics.

3.5.16 Vibrating sample magnetometry (VSM) studies

Magnetic nanocomposites synthesised from iron oxide and the magnetically active nanocomposite FPYS3 (5 at.%) were studied using magnitudes of coercivity (MH) to examine their magnetic responses; the outcomes are shown in Fig. 3.5.22. The ferrimagnetic characteristics, such as saturation magnetization and symmetric hysteresis, were demonstrated by every nanocomposite that contained Fe_3O_4 magnetic nanocomposites. 20.81, 17.27, and 5.74 emu/g were determined to be the saturation magnetization values for pure Fe_3O_4, FS, and FPYS3 (5 at.%), respectively. Miniaturization of Fe_3O_4 nanoparticles is due to a drop in magnetic moment, which is mostly brought about by the surface's noncollinear spin arrangement. Saturation magnetization in FS samples decreases relative to pure Fe_3O_4 as particle size rises. There was no remanence or coercivity observed in the hysteresis loop of the FPYS3 alloy with a 5 at.% composition. While pure Fe_3O_4 have the highest saturation magnetization, FPYS3 (5 at.%) have a lower value due to the presence of non-

magnetic components. The sample achieved superparamagnetic behaviour. The results show that the photocatalyst can be reused because of its high saturation magnetization. An external magnetic field was used to accomplish this, effectively separating it from the solution.

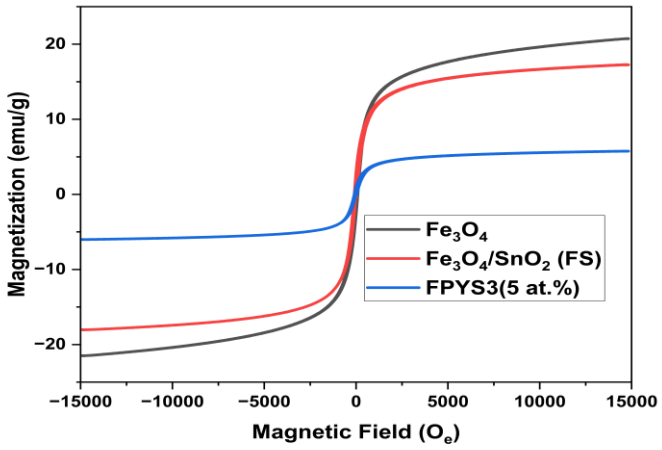

Fig. 3.5.22 VSM curve of Fe_3O_4, FS and FPYS3 (5 at.%).

3.5.17 Reusability

FS and FPYS3 (5 at.%) degraded RhB after 150 min of visible light exposure, and crucial attributes of the photocatalyst were its stability and recyclability. The stability and reusability of the magnetic nanocomposite photocatalyst were assessed using recycling observation. The process of recycling a nanocomposite photocatalyst for the breakdown of MB is illustrated in Fig. 3.5.23. When exposed to a mixed solution, a nanocomposite photocatalyst was able to be separated using an external magnet every five cycles. The recycled nanocomposite photocatalysts were blended with a fresh dye solution. The breakdown efficiency of RhB decreased from 70 to 63% after a span of 150 min. Thus, the efficiency of decomposition was slightly changed. The performance of the nanocomposite photocatalyst may be reduced due to the presence of intermediate products from degraded RhB that stick to the surface and do not fully decompose. Nevertheless, when exposed to visible light, the nanocomposite photocatalyst demonstrated remarkable durability and recyclability in the degradation of RhB.

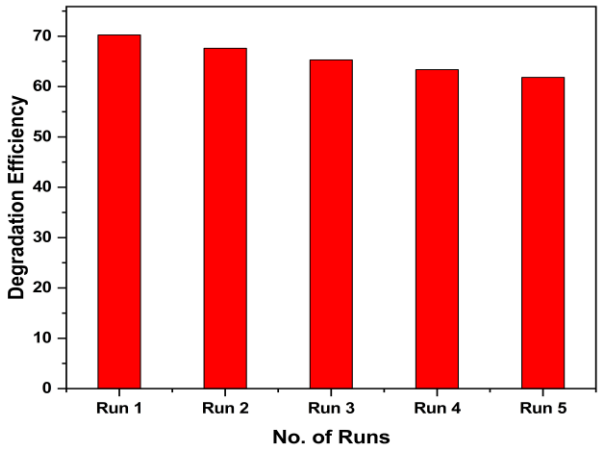

Fig. 3.5.23 Number of recycles for using FPYS3.

3.5.18 The degrading mechanism of MB using a photocatalyst that has been created

A method for the degradation of methylene blue (MB) dye was developed using nanocomposite photocatalysts (Fig. 3.5.24). An elaborate multi-step procedure dependent on photocatalytic principles is required for the degradation of MB utilising a photocatalyst Pr^{3+},Y^{3+}co-doped with SnO_2. In order to make SnO_2 a more effective photocatalyst, it is co-doped with praseodymium and yttrium ions. When SnO_2 photocatalysts are doped with Pr^{3+} and Y^{3+}, they are able to absorb light and transfer electrons from the valence band to the conduction band, resulting in the generation of electron and hole pairs. Fast electron-hole recombination was hampered by the effective charge separation made possible by the Pr and Y ions found in the SnO_2 lattice. The hydrogen ions in the valence band of SnO_2 co-doped with Pr^{3+} and Y^{3+} allow the direct oxidation of MB molecules that have stuck to the catalyst's surface. Superoxide radicals ($\dot{O}_2^-$) can be produced when electrons (e^-) in the conduction band come into contact with oxygen (O_2) that is deposited on the surface of the catalyst. Interaction between water molecules and photogenerated holes on a catalyst's surface can produce reactive oxygen species (ROS), specifically hydroxyl radicals (ȮH). Together, hydroxyl radicals and valence band holes break down MB molecules adsorbed on the photocatalyst surface. As MB broke down, it usually gave rise to smaller, more biodegradable molecules that were less complicated than the original.

The goal of the photocatalytic method was to convert the contaminants into inert inorganic molecules such as mineral ions, water, and carbon dioxide, a process known as mineralization. The presence of Pr and Y ions in the SnO_2 lattice enhanced photocatalytic activity, and co-doping enabled modifications to the band structure, surface area, and active sites for adsorption and catalysis.

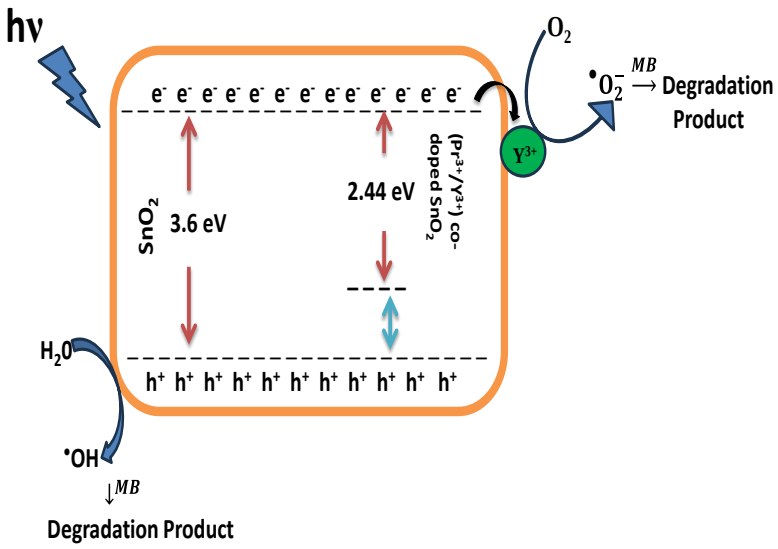

Fig. 3.5.24 Mechanism of MB degradation with prepared photocatalyst.

Chapter 4
CONCLUSIONS

Different magnetic nanocomposites were produced using several materials, such as forming heterojunctions with g-C_3N_4 and silver with SnO_2, or doping SnO_2 with silver or Praseodymium or yttrium ion. The nanocomposites mentioned are Fe_3O_4/SnO_2 (FS), Fe_3O_4/g-C_3N_4 (FG), Fe_3O_4/SnO_2/g-C_3N_4 (FSG2), Fe_3O_4/Ag-g-C_3N_4 (FAG3), Fe_3O_4/Ag_x-Sn_yO_2 (FAS3), Fe_3O_4/Pr^{3+}-doped SnO_2 (FPS1), and Fe_3O_4/Pr^{3+}, Y^{3+}co-doped SnO_2 (FPYS3). These syntheses were conducted by utilising the hydrothermal technique with the addition of plant extracts obtained from *Citrus x lemon*, *Parkia speciosa*, and *Artocarpus heterophyllus* L.

The hydrothermal method allowed for precise control over the morphology and size of the nanocomposites, leading to uniform and well-defined structures. As-prepared nanocomposites have average crystallite size of the ranged from 22.54 to 45.10 nm, and have band gaps ranging from 2.35 to 3.64 eV, which makes them very suitable for photocatalysis. This method typically results in high-purity products with excellent crystallinity, which can enhance the material's properties. It often occurred at relatively low temperatures and pressures, making it energy-efficient and cost-effective. Further, this process can be more environmentally friendly since it often uses water as the solvent, reducing the need for harmful chemicals. It can enhance the physical and chemical properties of the nanocomposites, such as improved magnetic, optical properties etc. The simplicity and efficiency of the process can lead to lower production costs compared to more complex and energy-intensive methods.

The synthesised photocatalysts undergo UV-visible spectroscopy analysis to examine in many different areas of chemistry and yields valuable information about the electronic structure of molecules and to estimate its band gap energy. Moreover, modifications were observed in the electronic band structure of the host material through the formation of heterojunctions or doping with another material. Specifically, there was a decrease in the valence band energy of the host material (SnO_2) with increasing dopant concentration, whereas the energy value of the conduction band

initially increased and then decreased as the dopant concentration increased. This can be revealed as the introduction of localised states near the valence band edge by dopant. The states of these elements can form hybridised states with the valence band states of host, resulting in a decrease in energy of the valence band or d-orbital of Ag or 4f orbitals of Pr^{3+} can interact with the O 2p orbitals in SnO_2, causing the creation of new hybridised states that have a lower energy than the original valence band edge. While the energy value of the conduction band in host material initially increased and then decreased as the concentration of praseodymium ion increased. At low concentrations of Pr^{3+}, doping can either add new energy levels or change the current energy levels in the band structure of SnO_2. This can lead to a small rise in the energy of the conduction band, as the extra electrons or holes alter the structure of the band and move the edge of the conduction band. This can boost the energy of the conduction band by adding to the states near the edge of the band that contribute to conduction.

Photocatalyst	Band gap energy (eV)	Average Crystallite Size (nm)
FSG2	2.35	30.49
FAG3	3.64	22.54
FAS3	3.23	25.44
FPS1	2.56	27.48
FPYS3	2.44	45.10

X-ray diffraction analysis to determine their crystal structures and phase purity by analysis and Fourier transform infrared spectroscopy (FT-IR) technique with the ATR method, Scanning Electron Microscope (SEM), Tanning Electron Microscope (TEM), X-ray photoelectron spectroscopy (XPS), Photoluminescence (PL), Brunauer-Emmett-Teller (BET), Total Organic Carbon (TOC) analysis, Liquid Chromatography-Mass Spectrometry (LCMS), Vibrating Sample Magnetometer (VSM), and others were used to analyse the physical properties of these novel photocatalysts.

From the photoluminescence (PL) studies revealed that intensities of the host material decrease when forming heterojunctions or doping with other materials

primarily due to introduction of dopants or forming heterojunctions can create localized energy states or traps within the host material's band structure. These traps can capture charge carriers (electrons and holes) and lead to non-radiative recombination pathways, reducing the emission of photons. Doping or heterojunction formation can alter the energy levels and electronic structure of the host material. This change can result in energy transfer processes where the energy is dissipated through non-radiative pathways rather than emitting photons. Further, the presence of dopants or the formation of heterojunctions can facilitate processes such as quenching, where the energy absorbed by the host material is transferred to the dopant or the interface region without emitting light. The presence of oxygen vacancies or silver/Praseodymium/yttrium ion interstitials caused a significant photoluminescence emission, which in turn created many trapped states or metastable energy levels. Photogenerated carrier recombination can also occur efficiently in close proximity to several tiny grain boundaries. The heterojunction or doped nanocomposite lowered the PL intensity compared to the sole or undoped SnO_2.

Since, our research is on magnetically active nanocomposite, so prepared nanocomposites were investigated through Vibrating Sample Magnetometer (VSM) in order to check their magnetic properties. The results explained that there was decrease in its value when using heterojunction or doped materials, as compared to sole or undoped materials, can be attributed to several factors related to changes in the magnetic properties and interactions of the materials. Introducing dopants into a nanocomposite can alter the magnetic domains. Dopants can disrupt the regular magnetic ordering, leading to a decrease in overall magnetization. This disruption is due to the introduction of non-magnetic or differently magnetic atoms into the lattice, which can hinder the alignment of magnetic moments. Creating a heterojunction involves combining two different materials, which can result in interfaces where magnetic interactions are altered. The magnetic properties at the interface can differ from those in the bulk materials, potentially reducing the overall magnetization. Dopants can introduce localized magnetic moments that interact with the host material's magnetic moments, often leading to complex spin interactions that reduce the net magnetization. For example, if non-magnetic or antiferromagnetic elements are

introduced, they can lead to a reduction in the overall magnetic response. At the interface of a heterojunction, the exchange coupling between different magnetic regions can be weakened or altered. This can lead to a reduction in the alignment of spins, thus decreasing the overall magnetization measured by the VSM.

Photocatalyst	Magnetization (emu/g)
F	20.70
FG	2.30
FS	17.26
FSG2	1.10
FAG3	4.59
FAS3	8.34
FPS1	2.10
FPYS3	2.04

We synthesized nanocomposite and employed it as a photocatalyst to degrade pesticides and dyes in this study. For this, the irradiation solution's absorption intensity was assessed to examine the photocatalytic efficiency of the prepared ternary nanocomposite with rhodamine B (RhB), methylene blue (MB), 2,4-dichlorophenol (2,4-DCP), and trichloroacetic acid (TCAA) were used as model pollutants. The photocatalyst impact, pH effect, and dose are just a few of the several parameters studied.

The dose of photocatalyst used in dye degradation significantly affects the degradation efficiency due to several reasons i.e. more photocatalyst means a greater surface area available for the adsorption of dye molecules. This enhances the interaction between the photocatalyst and the dye, facilitating more efficient degradation due to higher dose of photocatalyst, more light can be absorbed, generating more electron-hole pairs. This increases the number of reactive species (such as hydroxyl radicals) that participate in the degradation process. Further, larger dose of photocatalyst provides more active sites for the photocatalytic reactions, thus increasing the overall reaction rate. This leads to faster and more complete degradation of the dye molecules. However, there are also practical limitations and considerations

like beyond an optimal dose, adding more photocatalyst can lead to particle agglomeration and light scattering. This reduces the effective penetration of light into the solution, decreasing the generation of reactive species and thereby lowering the degradation efficiency.

Photocatalyst	Dose (mg/20mL)
FSG2	1
FAG3	1
FAS3	5
FPS1	1
FPYS3	3

In case of photocatalyst impact, heterojunction or doped materials has more degradation efficiency as compared to that of sole or undoped material because when two different semiconductors are combined to form a heterojunction, the interface between them can create an internal electric field. This field helps in the separation of photo-generated electron-hole pairs, reducing their recombination rate and thus enhancing the photocatalytic activity. While doping introduces additional energy levels within the bandgap of the semiconductor. These new levels can trap electrons or holes, aiding in their separation and reducing recombination. Thus, by combining materials with different bandgaps, heterojunctions can absorb a broader spectrum of light. This broadens the range of wavelengths that can be utilized for photocatalysis, improving the overall efficiency. Doping can create defect states or introduce new electronic states that allow the material to absorb visible light, extending the absorption range beyond the intrinsic bandgap of the undoped material.

Photocatalyst	Degradation % (RhB)		
		FG	FS
FSG2	72	23	26
FAG3	69	23	-
FAS3	63	-	26
FPS1	48	-	26
FPYS3	59	-	26

Photocatalyst	Degradation %			
	RhB	MB	2,4-DCP	TCAA
FSG2	72	75	72	55
FAG3	69	71	59	35
FAS3	63	68	55	29
FPS1	48	52	38	25
FPYS3	59	56	45	28

A radical test was conducted employing various scavengers to validate the presence of reactive species involved in this degradation. The report revealed that ȮH radicals are highly reactive and act as potent oxidants in these chemical reactions. Their ability to enhance the degradation of dyes and pesticides can be attributed as ȮH radicals have a very high oxidation potential, making them capable of initiating oxidation reactions with a wide range of organic compounds, including dyes and pesticides. This oxidative degradation breaks down complex molecules into simpler, less harmful substances. The introduction of scavengers, alongside the absence of scavengers (No S), in the photocatalytic process aimed at neutralising highly reactive radicals. Variations among scavengers altered the concentration ratio (C_t/C_o) of RhB dye at time t compared to its initial concentration. In order to capture superoxide radicals ($\dot{O}_2^-$), holes (h^+), and hydroxyl radicals (ȮH).

From the pH studies, between pH 8 and 10, the dye solution exhibited higher degradation efficiency during photocatalytic processes for several reasons such as the surface charge of the photocatalyst can change with pH, affecting the adsorption of dye molecules. If the dye molecules are oppositely charged to the surface of the photocatalyst at a specific pH, there will be stronger electrostatic attraction, enhancing adsorption and degradation efficiency. Conversely, if they are similarly charged, repulsion can occur, reducing adsorption and efficiency. Further, the formation of reactive species, such as hydroxyl radicals (ȮH), which are crucial for dye degradation, can be influenced by pH. For example, in the presence of water, hydroxyl radicals are

more easily formed under alkaline conditions, improving degradation efficiency. However, excessively high or low pH can also lead to the formation of other species that might not contribute as effectively to the degradation process. Not only these, the chemical structure and stability of dye molecules can change with pH. Some dyes may be more easily degraded in acidic or alkaline conditions due to the ionization state of the dye molecules. For example, certain dyes might precipitate or change their structure at specific pH levels, affecting their availability for photocatalytic degradation. The stability and activity of the photocatalyst can also be pH-dependent. Some photocatalysts might degrade or lose activity in highly acidic or alkaline conditions, thus affecting their efficiency.

pH of MB solution	FSG2	FAG3	FAS3	FPS1	FPYS3
pH 5	85	82	73	60	66
pH 6	82	79	70	57	63
pH 7	75	71	62	50	56
pH 8	78	74	66	53	59
pH 9	82	78	69	57	63
pH 10	88	85	75	63	69

Further, performing kinetics calculations for the photodegradation of dyes and pesticides with photocatalysts is crucial because kinetics studies help in elucidating the reaction mechanisms involved in the degradation process. This includes identifying the intermediate species formed during the reaction and the steps involved in their conversion to final products. Kinetics calculations provide quantitative measures of the photocatalytic efficiency. By determining the rate constants and comparing them for different photocatalysts, we are able to assess which materials are more effective in degrading specific pollutants. Kinetic parameters help in optimizing the reaction conditions, such as the concentration of the photocatalyst, the intensity of light, the pH of the solution, and the presence of other substances. This optimization is essential for achieving maximum degradation efficiency.

Photocatalyst	pH 7							
	MB		RhB		DCP		TCA	
	k (min^{-1})	R^2	k (min^{-1})	R^2	k (min^{-1})	R^2	k (min^{-1})	R^2
FSG2	0.0192	0.981	0.0205	0.962	0.0095	0.978	0.0068	0.954
FAG3	0.031	0.968	0.032	0.949	0.021	0.965	0.019	0.941
FAS3	0.0433	0.9569	0.0446	0.9379	0.0336	0.9539	0.0309	0.9299
FPS1	0.0493	0.9509	0.0506	0.9319	0.0396	0.9479	0.0369	0.9239
FPYS3	0.061	0.938	0.062	0.919	0.051	0.935	0.036	0.911

Due to the fact that the photocatalyst is exposed to LED light, the Total Organic Carbon (TOC) removal % of dye degradation with a photocatalyst normally increases with time, it continuously generates electron-hole pairs, which then produce reactive species such as hydroxyl radicals ($\dot{O}H$) and superoxide radicals ($\dot{O}_2^-$). These reactive species attack and break down the dye molecules and their intermediates over time, leading to a gradual reduction in TOC. Initially, the photocatalyst targets the dye molecules, leading to their decomposition into smaller organic intermediates. With prolonged exposure to the photocatalytic process, these intermediates are further broken down into simpler molecules, eventually leading to complete mineralization into CO_2 and H_2O, thereby reducing TOC. Over time, more dye molecules are adsorbed onto the surface of the photocatalyst, increasing the interaction between the dye and the photocatalyst. This enhanced adsorption facilitates more efficient degradation and removal of organic carbon. As the photocatalytic reaction progresses, there is an accumulation of reactive species in the solution, increasing the probability of these species encountering and degrading the organic molecules. This leads to a higher TOC removal percentage over time.

Photocatalyst	TOC removal % (pH7)			
	RhB	MB	2,4-DCP	TCAA
FSG2	64	69	55	48
FAG3	60	64	54	48
FAS3	50	54	45	35
FPS1	52	55	46	37
FPYS3	61	66	51	46

Among synthesized nanocomposites in this study, $Fe_3O_4/SnO_2/g\text{-}C_3N_4$ (FSG2) exhibited the most effective response in degrading dyes and pesticides as compared to that of others nanocomposite. Because SnO_2 exhibited a substantial surface area, which facilitates the presence of several active sites for the adsorption of dye molecules. It exhibited chemical stability and improves the overall stability of the composite, rendering it ideal for several uses. Additionally, $g\text{-}C_3N_4$ is a photocatalyst that is responsive to LED light, enabling it to harness sunshine or LED light for photocatalytic processes. This characteristic enhanced the energy efficiency and cost-effectiveness of the process. When exposed to LED light, $g\text{-}C_3N_4$ produced electron-hole pairs that contribute to the creation of reactive species such hydroxyl radicals ($\dot{O}H$) and superoxide anions ($\dot{O}_2^-$). These highly reactive organisms have the ability to break down a variety of organic contaminants, such as dyes and insecticides. Further, heterojunctions are formed at the interfaces when Fe_3O_4, SnO_2, and $g\text{-}C_3N_4$ are combined which provided effective separation and transmission of charges, minimizing the recombination of electron-hole pairs and increasing the photocatalytic activity. The incorporation of a composite structure could enhance the efficiency of light absorption and use, hence increasing the number of photons accessible to facilitate the photocatalytic reactions.

The degradation efficiency for the LED-MB-FSG2 nanocomposite solution is higher than that for the LED-RhB-FSG2 nanocomposite solution, because the chemical structures of the two molecules are very different. Rhodamine B's

distinctiveness stems from its larger and more complex molecular structure than methylene blue. The extent to which dye molecules can be degraded through photocatalysis is contingent upon their structural attributes. When rhodamine B (RhB) and methylene blue (MB) are combined in water, their solubility decreases for various reasons. Several possible factors contributing to the reduction in solubility have been identified like the presence of adsorption sites at the interface between the solvent and water, where molecules of RhB and MB may conflict for available space. Moreover, if two colours with low water solubility are mixed together, the overall water solubility of the combination can be reduced due to competitive adsorption. Not only this, RhB and MB molecules have the ability to form clusters when they come into contact with water. This effect can also appear when colours come into contact with each other. Thus, aggregation decreases the overall solubility of each individual colour in the mixture. Consequently, the solubility of RhB and MB molecules can be modified as complexes are formed between them due to the tendency of the participating species to precipitate out of the solution or the solubility of RhB can be decreased by hydrogen bonding or electrostatic interactions between RhB and MB molecules.

Our study revealed that TCAA requires a more extended period to mineralize fully. The data shows that the ternary nanocomposite method was more effective than TCAA in the mineralization of 2,4-DCP.

REFERENCES

Abbas Sadeghzadeh-Attar, (2019). Preparation and enhanced photocatalytic activity of Co/F codoped tin oxide nanotubes/nanowires: a wall thickness-dependence study. *Appl. Phys A* **125**: 768-772.

Abdel Messih, M.F., Ahmed, M.A., Ayman Soltan, Samy S. Anis, (2017). Facile approach for homogeneous dispersion of metallic silver nanoparticles on the surface of mesoporous titania for photocatalytic degradation of methylene blue and indigo carmine dyes. *J. Photochem. Photobiol. A: Chem.,* **335**: 40-51.

Abdel Messih, M.F., Ahmed, M.A., Ayman Soltan, Samy Sobhy Anis, (2019). Synthesis and characterization of novel Ag/ZnO nanoparticles for photocatalytic degradation of methylene blue under UV and solar irradiation. *J. Phys. Chem. Solids*, **135**:109086.

Abdel-Messih, M.F., Ahmed, M.A., El-Sayed, A.S., (2013). Photocatalytic decolorization of Rhodamine B dye using novel mesoporous SnO_2–TiO_2 nano mixed oxides prepared by sol–gel method. *Journal of Photochemistry and Photobiology A: Chemistry,* **260**: 1-8.

Abdel-Monem K., Emam S.M., Okda, H.M.Y., (2017). Solid state thermal decomposition synthesis of CuO nanoparticles from coordinated pyrazolopyridine as novel precursors. *J. Mater. Sci.,* **28**: 2923–2934.

Abdullah, A.H., Mun, L.K., Zainal, Z., Hussein, M.Z., (2013). Photodegradation of Chlorophenoxyacetic Acids by ZnO/γ -Fe_2O_3 Nanocatalysts: A Comparative Study. *Inter J Chem.,* **5**: 56-66.

Abe, R., Higashi, M., Sayama, K., Abe, Y., Sugihara, H., (2006). Photocatalytic Activity of R_3MO_7 and $R_2Ti_2O_7$ (R = Y, Gd, La; M = Nb, Ta) for Water Splitting into H_2 and O_2. *J Phys Chem B,* **110**: 2219-2226.

Abou-Gamra, Z.M., M.A. Ahmed, (2016). Synthesis of mesoporous TiO_2–curcumin nanoparticles for photocatalytic degradation of methylene blue dye. *J. Photochem. Photobiol. B: Biology*, **160**:134-141.

Ahmed, M.A., Abou-Gamra, Z.M., ALshakhanbeh, M.A., Medien, H., (2019). Control synthesis of metallic gold nanoparticles homogeneously distributed on hexagonal ZnO nanoparticles for photocatalytic degradation of methylene blue dye. *Environ. Nanotechnol. Monitor, Manag.*, **12:** 1-41.

Ahmed, M.A., Abou-Gamra, Z.M., Medien, H.A.A., Hamza, M.A., (2017). Effect of porphyrin on photocatalytic activity of TiO_2 nanoparticles toward Rhodamine B photodegradation. *J. Photochem. Photobiol. B: Biology.*, **176**: 25-35.

Ahmed, M.A., Abou-Gamra, Z.M., Salem, A.M., (2017). Photocatalytic degradation of methylene blue dye over novel spherical mesoporous Cr_2O_3/TiO_2 nanoparticles prepared by sol-gel using octadecylamine template. *J. Environ. Chem. Engin.*, **5**: 4251-4261.

Ahmed, S., Rasul, M., Martens, W.N., Brown, R., Hashib, M., (2011). Advances in heterogeneous photocatalytic degradation of phenols and dyes in wastewater: a review. *Water Air Soil Poll.*, **215**: 3-29.

Ai Z., Ho W., Lee S., Zhang L., (2009). Efficient photocatalytic removal of NO in indoor air with hierarchical bismuth oxybromide nanoplate microspheres under visible light. *Environ. Sci. Technol.*, **43**: 4143–4150.

Ai-Hsuan Lee, Yi-Chuen Wang, Chiing-Chang Chen, (2019). Composite photocatalyst, tetragonal lead bismuth oxyiodide/bismuth oxyiodide/graphitic carbon nitride: Synthesis, characterization, and photocatalytic activity. *Journal of Colloid and Interface Science*, **533**: 319-332.

Alanko, G.A., Thurber, A., Hanna, C.B., Punnoose, A., (2012). Size, surface structure, and doping effects on ferromagnetism in SnO_2. *J Appl Phys.*, **111**: 07C321.

Al-Hamdi, A.M., Sillanpää, M., Dutta, J., (2014). Photocatalytic degradation of phenol in aqueous solution by rare earth-doped SnO_2 nanoparticles. *Journal of Materials Science,* **49**: 5151-5159.

Al-Hamdi, A.M., Sillanpää, M., Dutta, J., (2015). Gadolinium doped tin dioxide nanoparticles: an efficient visible light active photocatalyst. *Journal of Rare Earths,* **33**: 1275-1283.

Al-Hamdi, A.M., Sillanpää, M., Dutta, J., (2016). Intermediate formation during photodegradation of phenol using lanthanum doped tin dioxide nanoparticles. *Research on Chemical Intermediates,* **42**: 3055- 3069.

Ali Baig Ameer Baig, Vadamalar Rathinam, Jayanthi Palaninathan, (2020). Photodegradation activity of yttrium-doped SnO_2 nanoparticles against methylene blue dye and antibacterial effects. *Applied Water Science,* **10**:76-83.

Alikarami, S., Soltanizade, A., Rashchi, F., (2022). Synthesis of CdS-SnS photocatalyst by chemical co-precipitation for photocatalytic degradation of methylene blue and rhodamine B under irradiation by visible light. *J. Physics and chemistry of solids*, **171**:110993.

An, C.H., Jiang, W., Wang, J.Z., Wang, S.T., Ma, Z.H., Li, Y.P., (2013). Synthesis of three-dimensional AgI@TiO_2 nanoparticles with improved photocatalytic performance. *Dalton Transactions,* **42**: 8796–8801.

Anandan, K., Rajendran, V., (2015). Influence of dopant concentrations (Mn= 1, 2 and 3mol%) on the structural, magnetic and optical properties and photocatalytic activities of SnO_2 nanoparticles synthesized via the simple precipitation process. *Superlattice Microst.,* **8**: 185-197.

Anju, S., Yesodharan, S., Yesodharan, E., (2012). Zinc oxide mediated sonophotocatalytic degradation of phenol in water. *Chem Eng J.,* **189**: 84-93.

Aristi, I., von Schiller, D., Arroita, M., Barceló, D., Ponsatí, L., García-Galán, M. J., Sabater, S., Elosegi, A., & Acuña, V., (2015). Mixed effects of effluents from a wastewater treatment plant on river ecosystem metabolism: Subsidy or stress?. *Freshwater Biology,* **60(7)**:1398–1410.

Baoping Zhang, Bo Li, Shuting Gao, Yiting Li, Rui Cao, Jingyang Cheng, Ruiping L i, Errui Wang, Yumeng Guo, Kailiang Zhang, Jun Liang, Bin Liu, (2020). Y-doped TiO_2 coating with superior bioactivity and antibacterial property prepared via plasma electrolytic oxidation. *Mater. Des.*, **192**: 108758.

Bartolomeu, M., Neves, M. G. P. M. S., Faustino, M. a. F., & Almeida, A., (2018). Wastewater chemical contaminants: Remediation by advanced oxidation processes. *Photochemical & Photobiological Sciences,* **17(11)**:1573–1598.

Bayal, N., Jeevanandam, P., (2013). Sol–gel synthesis of SnO_2–MgO nanoparticles and their photocatalytic activity towards methylene blue degradation. *Mater. Res. Bull.*, **48**: 3790–3799.

Beydoun, D., Amal, R., Low, GKC., McEvoy, S. (2000) Novel photocatalyst: titania-coated magnetite. Activity and photodissolution. *J Phys Chem B,***104**: 4387-4396.

Bhuvaneswari, K., Pazhanivel, T., Palanisamy, G., Bharathi, G., (2020). CTAB-aided surface-modified tin oxide nanoparticles as an enhanced photocatalyst for water treatment. *J Mater Sci: Mater Electron,* **31**: 6618–6628.

Bian, Z. F., Zhu, J., Wang, S. H., Cao, Y., Qian, X. F., Li, H. X., (2008). Self-assembly of active Bi_2O_3/TiO_2 visible photocatalyst with ordered mesoporous structure and highly crystallised anatase. *J. Phys. Chem. C.,* **112**: 6258-6262.

Bouras, K., Rehspringer, J.L., Schmerber, G., Rinnert, H., Colis, S., Ferblantier, G., Balestrieri, M., Ihiawakrim, D., Dinia, A., Slaoui, A., (2014). Optical and structural properties of Nd doped SnO_2 powder fabricated by the sol–gel method. *J Mater Chem C*, **2**: 8235-8243.

Brojendro Singh Shagolsem, N. Mohondas Singh, (2024). Ternary photocatalyst of

Fe_3O_4/Ag-SnO_2 with Parkia speciosa extract improves visible-light-driven photocatalytic degradation of dye. *Inorganic Chemistry Communications,* **162**: 112245.

Brojendro Singh Shagolsem, Nongmaithem Mohondas Singh, (2024). Green synthesis and magnetically separable Fe_3O_4/SnO_2/g-C_3N_4 ternary nanocomposite for degradation of Rhodamine B. *Inorganic Chemistry Communications,* **160**: 111877.

Cao Y. Q., He T., Chen Y. M., Cao, Y. A., (2010). Fabrication of Rutile TiO_2-Sn/Anatase TiO_2-N Heterostructure and Its Application in Visible-Light Photocatalysis. *J. Phys. Chem. C.*, **114**: 3627-3633.

Cao, D., Wang, Q., Liu, Z., Zhang, H., Wang, Y., Jin, R., Gao, S., (2020). Enhanced the photoelectrocatalytic performance of TiO_2 nanotube arrays by the synergistic sensitization of Ag–AgBr nanospheres. *Spectrochimica Acta A*, **227**:117674.

Cao, J.Q., Wang, Y.X., Yu, J.F., Xia, J.Y., Zhang, C.F., Yin, D.Z., Hafeli, U.O., (2004). Preparation and radiolabeling of surface-modified magnetic nanoparticles with rhenium-188 for magnetic targeted radiotherapy. *J Magn Magn Mate.,* **277**:165-174.

Cao, S.W., Zhu, Y.J., Ma, M.Y., Li, L., Zhang, L., (2008). Hierarchically Nanostructured Magnetic Hollow Spheres of Fe_3O_4 and γ-Fe_2O_3: Preparation and Potential Application in Drug Delivery. *J. Phys. Chem. C.*, **112**: 1851.

Carreño, N., Maciel, A., Leite, E., Lisboa-Filho, P.N., Longo, E., Valentini, A., Probst, L., Paiva-Santos, C., Schreiner, W., (2002). The influence of cation segregation on the methanol decomposition on nanostructured SnO_2. *Sensor Actuat B-Chem.,* **86**: 185-192.

Changlin, Y., Zhou, Wanqin, Y., Jimmyc, Cao, Fangfang, L., Xin, (2012). Thermal Stability, Microstructure and Photocataytic Activity ofthe Bismuth Oxybromide Photocatalyst. *Chin. J. Chem.*, **30**:721-726.

Che H.L., Liu F.Y., Lin Y.Y., Zuo Z., Wu W.T., Qi Q., Peng Z., Zou D., Chen C.C., (2023). Photocatalytic CO_2 reduction to C1–C5 hydrocarbons using $K_2Fe_2O_4$/g-C_3N_4 as coupling photocatalyst. *Materials Today Sustainability*, **23:** 100430.

Chen W. J., Tsai P. J., Chen Y. C., (2008). Functional Fe_3O_4/TiO_2 Core/Shell Magnetic Nanoparticles as Photo killing Agents for Pathogenic Bacteria. *Small*, **4**: 485−491.

Chen, H., Chen, J., Si, J., Hou, Y., Zheng, Q., Yang, B., Li, Z., Gao, L., Lei, L., Wen, Z., Feng, X., (2020). Ultrathin tin monosulfide nanosheets with the exposed (001) plane for efficient electrocatalytic conversion of CO_2 into formate. *Chem. Sci.*, **11**: 3952-3958.

Chen, H., Gu, M., Pu, X., Zhu, J., Cheng, L., (2016). Fabrication of SnO_2@ SnS_2 heterostructure with enhanced visible light photocatalytic activity. *Mater. Res. Exp.*, **3(6)**: 065-068.

Chen, H., Yan, T., Jiang, F., (2014). Adsorption of Cr (VI) from aqueous solution on mesoporous carbon nitride. *J Taiwan Inst Chem Eng.*, **459**: 1842–1849.

Chin-Tsung Yang, Wenlian William Lee, Ho-Pan Lin, Yong-Ming Dai, Han-Ting Chi, Chiing-Chang Chen, (2016). A novel heterojunction photocatalyst, Bi_2SiO_5/g-C_3N_4: synthesis, characterization, photocatalytic activity, and mechanism. *RSC Advances*, **6**: 40664-40675.

Chunping Xu, Prasaanth Ravi Anusuyadevi, Cyril Aymonier, Rafael Luque and Samuel Marre, (2019). Nanostructured materials for photocatalysis. *Chem. Soc.Rev.*, **48**: 3868-3902.

Comini, E. C., Baratto, G., Faglia, M., Ferroni, A., Vomiero, G., Sberveglieri, (2009), Quasi-one-dimensional metal oxide semiconductors: Preparation, characterization and application as chemical sensors. *Prog. Mater. Sci.*, **54**:1–67.

Cristante, V.M., Jorge, S.M., Valente, J.P., Saeki, M.J., Florentino, A.O., Padilha, P.M., (2007). TiO_2 films organofunctionalized with 2-aminothiazole ligand and

adsorbed Pd (II) ions applied in the photocatalytic degradation of phenol in an aqueous medium. *Thin Solid Films,* **515**: 5334-5340.

Cui, Y.H., Feng, Y.J., Liu, J., Ren, N., (2012). Comparison of various organic compounds destruction on rare earths doped Ti/Sb-SnO_2 electrodes. *J Hazard Mater.*, **239**: 225-232.

Dechmongkhon Kaewsuwan, Thipusa Wongpinij, Chanan Euaruksakul, Narong Cha nlek, Narit Triamnak, Tossaporn Lertvanithphol, Mati Horprathum, Jakrapong K aewkhao, Prapun Manyum, Rattikorn Yimnirun, Saroj Rujirawat, (2023). Photoluminescence of tin dioxide (SnO_2) nanostructure grown on Si (001) by thermal evaporation technique. *Radiation Physics and Chemistry,* **206**: 110805.

Diallo, A., Manikandan, E., Rajendran, V., Maaza, M., (2016). Physical & enhanced photocatalytic properties of green synthesized SnO_2 nanoparticles via Aspalathus linearis. *J Alloy Compd.,* **681**: 561-570.

Ding, Y., Hu, Y., Zhang, L.Y., Chen, Y., Jiang, X.Q., (2006). Synthesis and Magnetic Properties of Biocompatible Hybrid Hollow Spheres. *Biomacromolecules,* **7**: 1766-1772.

Dong, G., Ho, W., Zhang, L., (2015). Photocatalytic NO removal on BiOI surface: The change from nonselective oxidation to selective oxidation. *Appl. Catal. B Environ.,* **168**: 490–496.

Du, M., Zhang, S., Xing, Z., Li, Z., Yin, J., Zou, J., Zhu, Qi., Zhou, W., (2020). All-Solid Z-Scheme Bi–BiOCl/AgCl Heterojunction Microspheres for Improved Electron–Hole Separation and Enhanced Visible Light-Driven Photocatalytic Performance. *J. Hazard. Mater*, **384**: 7887-7895.

Eghbali-Arani, M., A., Sobhani-Nasab, M., Rahimi-Nasrabadi, S., Pourmasoud, (2018). Green Synthesis and Characterization of $SmVO_4$ Nanoparticles in the Presence of Carbohydrates as Capping Agents with Investigation of Visible-Light Photocatalytic Properties. *J. Electron. Mater.,* **47(7)**: 3757–3769.

El-Katori, E.E., Ahmed, M.A., El-Bindary, A.A., Aly M. Orab, (2020). Impact of CdS/SnO_2 heterostructured nanoparticle as visible light active photocatalyst for the removal methylene blue dye. *J. Photochem. Photobiol. A.*, **392**:112403.

Entradas, T., Cabrita, J., Dalui, S., Nunes, M., Monteiro, O., Silvestre, A., (2014). Synthesis of sub-5 nm Codoped SnO_2 nanoparticles and their structural, microstructural, optical and photocatalytic properties. *Mater Chem Phys.,* **147:** 563-571.

Fageria, P., Nazir, R., Gangopadhyay, S., Barshilia, H.C., Pande, S., (2015). Graphitic-carbon nitride support for the synthesis of shape-dependent ZnO and their application in visible light photocatalysts. *RSC Adv.,* **5**: 80397–80409.

Fang, J., Shi, F. C., Bu, J., Ding, J. J., Xu, S. T., Bao, J., Ma, Y. S., Jiang, Z. Q., Zhang, W. P., Gao, C., Huang, W. X., (2010). One-step synthesis of bifunctional TiO_2 catalysts and their photocatalytic activity. *J. Phys. Chem. C.,* **114**: 7940-7948.

Farzaneh Saadati, Narjes Keramati & Mohsen Mehdipour Ghazi, (2016). Influence of parameters on the photocatalytic degradation of tetracycline in wastewater: A review. *Critical Reviews in Environmental Science and Technology,* **5**: 1-26.

Fujishima, A., Honda, K. (1972). Electrochemical photolysis of water at a semiconductor electrode. *Nature,* **238**: 37-38.

Gamal Hasan, HamdiAli Mohammed, Mohammed Althamthami, Abdelhamid Khele f, Salah Eddine Laouini, Souhaila Meneceur, (2023). Synergistic effect of novel biosynthesis $SnO_2@Fe_3O_4$ nanocomposite: A comprehensive study of its photocatalytic of Dyes & antibiotics, antibacterial, and antimutagenic activities. *Journal of Photochemistry and Photobiology A: Chemistry*, **443**: 114874.

Gohari, S. M., Yangjeh, A. H., (2016). Fabrication of novel magnetically separable visible-light-driven photocatalysts through photosensitization of Fe_3O_4/ZnO with $CuWO_4$. *J.Indust.Eng.Chem.* **44**:174-184.

Gomez, P. J., Dominguez, S., Bringas, E., Rivero, M.J., Ortiz, I., Dionysiou, D.D., (2017). Review and perspectives on the use of magnetic nanophotocatalysts (MNPCs) in water treatment. *Chem. Eng. J.*, **310**: 407–427.

Gu, M., Kushima, A., Shao, Y., Zhang, J.G., Liu, J., Browning, N.D., Li, J., Wang, C., (2013). Probing the Failure Mechanism of SnO_2 Nanowires for Sodium-Ion Batteries. *Nano Letters*, **13(11)**: 5203–5211.

Han, Y. T., Wu, X., Ma, Y. L., Gong, L. H., Qu, F. Y., Fan, H. J., (2011). Porous SnO_2 Nanowire Bundles for Photocatalyst and Li Ion Battery Applications. *Cryst Eng Com.*, **13**: 3506-3510.

Haque, E., Jun, J. K., & Jhung, S. H., (2011). Adsorptive removal of methyl orange and methylene blue from aqueous solution with a metal-organic framework material, iron terephthalate (MOF-235). *Journal of Hazardous Materials*, **185(1)**: 507–511.

Haritha, E., Roopan, S.M., Madhavi, G., Elango, G., Al-Dhabi, N.A., Arasu, M.V., (2016). Green chemical approach towards the synthesis of SnO_2 NPs in argument with photocatalytic degradation of diazo dye and its kinetic studies. *J Photoch Photobio B*, **162**: 441-447

Hasnat, M.A., Siddiquey, I.A., Nuruddin, A., (2005). Comparative photocatalytic studies of degradation of a cationic and an anionic dye. *Dyes Pigments.* **66**: 185–196.

Hays, J., Punnoose, A., Baldner, R., Engelhard, M.H., Peloquin, J., Reddy, K., (2005). Relationship between the structural and magnetic properties of Co-doped SnO_2 nanoparticles. *Phys Rev B*, **72**: 075203.

He, Y., Zhang, L., Fan, M., Wang, X., Walbridge, M.L., Nong, Q., Wu, Y., Zhao, L., (2015). Z-scheme SnO_{2-x}/g-C_3N_4 composite as an efficient photocatalyst for dye degradation and photocatalytic CO_2 reduction. *Sol. Energy Mater. Solid Cells*, **137**: 175–184.

Hirami, Y., Hunge, Y.M., Suzuki, N., Rodríguez-González, V., Kondo, T., Yuasa, M., Fujishima, A., Teshima, K., Terashima, C., (2023). Enhanced degradation of ibuprofen using a combined treatment of plasma and Fenton reactions. *J Colloid Interface Sci.*, **642**: 829–836.

Ho-Pan Lin, Chiing-Chang Chen, Wenlian William Lee, Ya-Yun Lai, Jau-Yuan Chen, Ya-Qian Chen, Jing-Ya Fu, (2016). Synthesis of a $SrFeO_{3-x}/gC_3N_4$ heterojunction with improved visible-light photocatalytic activities in chloramphenicol and crystal violet degradation. *RSC Advances,* **6**: 2323-2336.

Hou, L.R., Yuan, C.Z., Peng, Y., (2007). Synthesis and photocatalytic property of SnO_2/TiO_2 nanotubes composites. *J Hazard Mater,* **139**: 310-315.

Huang, Jia, Gang Nie, Yaobin Ding, (2020). Metal-Free Enhanced Photocatalytic Activation of Dioxygen by g-C_3N_4 Doped with Abundant Oxygen-Containing Functional Groups for Selective N-Deethylation of Rhodamine B. *Catalysts*, **10**: 1-16.

Hunge, Y.M., Yadav, A.A., Kang, S.W., Lim, S.J., Kim, H., (2023). Visible light activated MoS_2/ZnO composites for photocatalytic degradation of ciprofoxacin antibiotic and hydrogen production. *J Photochem Photobiol A: Chem.,* **434**:114250.

Hung-Lin Chen, Fu-Yu Liu, Xinyu Xiao, Jing Hu, Bo Gao, Dechun Zou, Chiing Chang Chen, (2021). Visible-light-driven photocatalysis of carbon dioxide and organic pollutants by $MFeO_2$ (M = Li, Na, or K). *Journal of Colloid and Interface Science*, **601**: 758-772.

Huo, Y. N., Zhang, X. Y., Jin, Y., Zhu, J., Li, H. X., (2008). Highly active $La_2O_3/Ti_{1-x}B_xO_2$ visible light photocatalysts prepared under su-percritical conditions. *Appl. Catal. B.* **83**: 78-84.

Ikehata, K., Naghashkar, N.J., Gamal El-Din, M., (2006). Ozonation and advanced oxidation treatment of emerging organic pollutants in water and wastewater.

Ozone Sci. Eng., **28**: 353–414.

Jana, S., Pramanik, S., Show, B., Mondal, A., Mukhopadhyay, S., (2022). A new strategy to fabricate SnS-SnO_2 heterostructure with excellent photoresponse and charge transport properties: Efficient photocatalyst for fast photoreduction of Cr (VI). *Mater. Sci. Engin. B* **275**: 115520.

Javad Didari, Abbas Sadeghzadeh-Attar, (2021). Ni-N codoped SnO_2/Fe_2O_3 nanocomposite as advanced bifunctional photocatalyst for simultaneous photocatalytic redox conversion of Cr (VI) and As (III). *Journal of the Taiwan Institute of Chemical Engineers*, **119**: 232-244.

Jia Huang, Gang Nie, Yaobin Ding, (2020). Metal-Free Enhanced Photocatalytic Activation of Dioxygen by g-C_3N_4 Doped with Abundant Oxygen-Containing Functional Groups for Selective N-Deethylation of Rhodamine B. *Catalysts*, **10**: 1-16.

Jing, S., Cao, M., Ren, L., Hu, C., (2011). Fe_3O_4/Graphene Nanocomposites with Improved Lithium Storage and Magnetism Properties. *J.Phys.Chem.C.***115**: 14469−14477.

Jordan, A., Scholz, R., Wust, P., Fähling, H., Felix, R., (1999). Magnetic fluid hyperthermia (MFH): Cancer treatment with AC magnetic field induced excitation of biocompatible superparamagnetic nanoparticles. *J Magn Magn Mater.*, **201**: 413-419.

Josephson, L., Tsung, C.H., Moore, A., Weissleder, R., (1999). High-Efficiency Intracellular Magnetic Labeling with Novel Superparamagnetic-Tat Peptide Conjugates. *Bioconjugate Chem.*, **10**: 186-196.

Kamat, P V., (2012). TiO_2 nanostructures: Recent physical chemistry advances. *Journal of Physical Chemistry C*, **22**: 11849–11851.

Kamat, P.V., (2007). Meeting the Clean Energy Demand: Nanostructure Architectures for Solar Energy Conversion. *J. Phys. Chem. C*, **111**: 2834–2860.

Kashif, N., Ouyang, F., (2009). Parameters effect on heterogeneous photocatalysed degradation of phenol in aqueous dispersion of TiO_2. *J Environ Sci.,* **21**: 527-533.

Keerthana, S.P., Yuvakkumar, R., Ravi, G., Manimegalai, M., MehboobaliPannipara, A.G., Al-Sehemi, R.A., Gopal, M.M., Hanafah DhayalanVelauthapillai, (2021). Investigation on (Zn) doping and anionic surfactant (SDS) efect on SnO_2 nanostructures for enhanced photocatalytic RhB dye degradation. *Environ Res.* **199**:111312.

Khataee, A., Zarei, M., (2011). Photocatalysis of a dye solution using immobilized ZnO nanoparticles combined with photoelectrochemical process. *Desalination*, **273**: 453-460.

Kim Nguyen Van, Ha Tran Huu, Viet Nga Nguyen Thi, Thanh Lieu Le Thi, Duy Huong Truong, ThanhTam Truong, NgocNhiem Dao, Vien Vo, DaiLam Tran, Y asser Vasseghian, (2022). Facile construction of S-scheme SnO_2/g-C_3N_4 photocatalyst for improved photoactivity. *Chemosphere*, **289**: 133120.

Kim, D.H., Lee, G.W., Kim, Y.C., (2012). Interaction of zinc interstitial with oxygen vacancy in zinc oxide: An origin of n-type doping. *Solid State Commun.,* **152**: 1711-1714

Kim, Y.S., Kim, Y.H., (2003). Application of ferro-cobalt magnetic fluid for oil sealing. *J Magn. Magn. Mater,* **267**:105-110.

Kooshki, H., Sobhani-nasab, A., Eghbali-arani, M., Ahmadi, F., Ameri, V., Rahimi-nasrabadi, M., (2018). Eco-friendly synthesis of $PbTiO_3$ nanoparticles and $PbTiO_3$/carbon quantum dots binary nano-hybrids for enhanced photocatalytic performance under visible light. *Sep. Purif. Technol.,* **211:** 873–881.

Kovács, K., He, S., Mile, V., Csay, T., Takács, E., Wojnárovits, L., (2015). Ionizing radiation induced degradation of diuron in dilute aqueous solution. *Chem Cent. J.,* **9**: 104-115.

Kumar, M., Bhatt, V., Abhyankar, A.C., Kim, J.D., Kumar, A., Patil, S.H., Yun, J.H., (2018). New insights towards strikingly improved room temperature ethanol sensing properties of p-type Ce doped SnO_2 sensors. *Sci. Rep.,* **8**: 8079.

Lal Lianmawii, Mohondas Singh, N., (2023). Luminescence and photocatalytic degradation of indigo carmine in the presence of Sm^{3+}doped ZnS nanoparticles. *Scientific Reports*, **13**: 22450.

Li, F., Li, X., Hou, M., Cheah, K., Choy, W., (2005). Enhanced photocatalytic activity of Ce^{3+}–TiO_2 for 2- mercaptobenzothiazole degradation in aqueous suspension for odour control. *Appl Catal A-Gen.,* **285**: 181-189.

Li, L.L., Zhang, W.M., Yuan, Q., Li, Z.X., Fang, C.J., Sun, L.D., Wan, L.J., Yan, C.H., (2008). Room temperature ionic liquids assisted green synthesis of nanocrystalline porous SnO_2 and their gas sensor behaviors. *Cryst. Growth Des.,* **8**: 4165–4172.

Li, Q., Xuan, Y.M., Wang, J., (2005). Experimental investigations on transport properties of magnetic fluids. *Exp Therm Fluid Sci.,* **30**:109-116.

Li, X., Huang, X., Liu, D., Wang, X., Song, S., Zhou, L., Zhang, H., (2011). Synthesis of 3D Hierarchical Fe_3O_4/Graphene Composites with High Lithium Storage Capacity and for Controlled Drug Delivery. *J. Phys. Chem. C.* **115**: 21567−21573.

Li, Y., Sasaki, T., Shimizu, Y., Koshizaki, N., (2008). Hexagonal-closed-packed, Heirarchical amorphous TiO_2 nancolumn arrays: Transferability, enhanced photocatalytic activity, and superamphiphilicity without UV Irradiation. *J. Am. Chem. Soc.* **130**: 14755-14762.

Liew, M.C., Ahmad, I., Lee, L.M., (2012). Corrosion Behavior of Sn-3.0Ag-0.5Cu Lead-Free Solder in Potassium Hydroxide Electrolyte. *Metallurgical and Materials Trans. A*, **43**: 3742–3747.

Lili, L., Liming, M., Xuechen, D., (2006). Solvothermal synthesis and characterization of Sb-doped SnO_2 nanoparticles used as transparent conductive films. *Materials Research Bulletin,* **41(3)**: 541–546.

Liu, C., Tang, X., Mo, C., Qiang, Z., (2008). Characterization and activity of visible-light-driven TiO_2 photocatalyst codoped with nitrogen and cerium. *J Solid State Chem.,* **181**: 913-919.

Liuqing Yang, Jianfeng Huang, Li Shi, Liyun Cao, Wei Zhou, Kun Chang, Men Xianguang, Guigao Liu, Yanni Jie, Jinhua Ye, (2017). Efficient hydrogen isolation over Sb doped SnO_2 photocatalyst sensitized by Eosin Y under visible light irradiation. *Nano Energy*, **36**: 331-340.

Madkour, M., Abdel-Monem, Y.K., Sagheer, F., (2016). Controlled Synthesis of NiO and Co_3O_4 Nanoparticles from Different Coordinated Precursors: Impact of Precursor's Geometry on the Nanoparticles Characteristics. *Ind. Eng. Chem. Res.,* **55 (50)**: 12733–12741.

Maeda, K., Thomas, A., Takanabe, K., Xin, G., Carlsson, J. M., Domen, K., Antonietti, M. A. (2009). Metal-Free Polymeric Photocatalyst for Hydrogen Production from Water under Visible Light. *Nat. Mater.,* **8**: 76−80.

McMichael, R.D., Shull, R.D., Swartzendruber, L.J., Bennett, L.H., Watson, R.E., (1992). Magnetocaloric effect in superparamagnets. *J Magn Magn Mate.,* **111**: 29-33.

Mei Liu, Wei Shaojie, Wei Chen, Li Gao, Li Xiying, Mao Liqun, Dang Haifeng, (2019). Construction of direct Z-scheme g-C_3N_4/TiO_2 nanorod composites for promoting photocatalytic activity. *J. Chin. Chem. Soc.,* **67**:1-7.

Mei, H., Shoujun, Z., Siyu, L., Yubin, S., Tanglue, F., Songyuan, T., Junjun, L., Bai, Y., (2018). Recent progress on the photocatalysis of carbon dots: Classification, mechanism and applications. *Nanotod.,* **651**:1-18.

Mete, E., Uner, D., Gülseren, O., Ellialtıoğlu, Ş., (2009). Pt-incorporated anatase TiO_2

(001) surface for solar cell applications: First-principles density functional theory calculations. *Phys Rev B,* **79**: 125418.

Mills A., Wang J., (1999). Photobleaching of methylene blue sensitised by TiO_2: an ambiguous system? J. Photochemistry Photobiology A: Chemistry 127: 123–134.

Mistry, B.V., Avasthi, D.K., Joshi, U.S., (2016). Tuning of optical and electrical properties of wide band gap Fe:SnO_2/Li:NiO p–n junctions using 80 MeV oxygen ion beam. *Applied Physics A,* **122**: 1024.

Mohamed Soltan, Mohamed Elsamadony, Ahmed Tawfik, (2017). Biological hydrogen promotion via integrated fermentation of complex agro-industrial wastes. *Applied Energy,* **185(1)**: 929-938.

Mohammad Javad Fakharian-Qomi and Abbas Sadeghzadeh-Attar, (2020). Template Based Synthesis of Plasmonic Ag-modified TiO_2/SnO_2 Nanotubes with Enhanced Photostability for Efficient Visible-Light Photocatalytic H_2 Evolution and RhB Degradation. *Chemistry Select,* **5**: 6001–6010.

Mohammed Ismael, (2019). Ying Wu, A mini-review on the synthesis, structural modification of g-C_3N_4-based materials, and their applications for solar energy conversion and environmental remediation. *Sustainable Energy & Fuels,* **3 (11)**: 2907-2925.

Mohammed Ismael, (2020). A review on graphitic carbon nitride (g-C_3N_4) based nanocomposites: Synthesis, Categories, and their application in photocatalysis. *Journal of Alloys and Compounds,* **846**: 156446.

Mohammed Ismael, (2021). Ferrites as solar photocatalytic materials and their activities in solar energy conversion and environmental protection: A review. *Solar energy materials and solar cells,* **219**: 110786.

Mohammed Ismael, Ying Wu, (2019). Facile synthesis method for fabrication of $LaFeO_3$/g-C_3N_4 nanocomposite as efficient visible-light-driven photocatalyst for photodegradation of RhB and 4-CP. *New J. Chem.,* **43**: 13783-13793.

Mohammed Ismael, (2022). Engy Elhaddad, Michael Wark, Construction of SnO_2/g-C_3N_4 composite photocatalyst with enhanced interfacial charge separation and high efficiency for hydrogen production and Rhodamine B degradation. *Colloids and Surfaces A: Physicochemical and Engineering Aspects*, **638**: 128288.

Mohammed Ismael, (2022). Photo-Fenton reaction enhanced visible-light activity of p- Photo-Fenton reaction enhanced visible-light activity of p-$CuFe_2O_4$/n-g-C_3N_4 heterojunction composites synthesized by a simple ultrasonic-assisted route for organic pollutants degradation. *Materials Research Bulletin*, **151**: 111803.

Mohammed Ismael, (2023). One-step ultrasonic-assisted synthesis of Ni-doped g-C_3N_4 photocatalyst for enhanced photocatalytic hydrogen evolution. *Inorganic Chemistry Communications*, **151**: 110607.

Mohammed Ismael, Michael Wark, (2022). Photocatalytic activity of $CoFe_2O_4$/g-C_3N_4 nanocomposite toward degradation of different organic pollutants and their inactivity toward hydrogen production: The role of the conduction band position. *FlatChem*., **32**: 100337.

Mukherjee S., Sushma V., Patra S., Barui A. K., Bhadra M. P., Sreedhar B., Patra C. R., (2012). Green chemistry approach for the synthesis and stabilization of biocompatible gold nanoparticles and their potential applications in cancer therapy. *Nanotechnology*, **23**: 455-460.

Nethravathia, P.C., Shruthia, G.S., Sureshan, D., Udayabhanua, Nagabhuhanab H., Sharmac, S.C. (2015). Garcinia xanthochymeus mediated green synthesis of ZnO nanoparticles: photoluminescence, photocatalytic and antioxidant activity studies. Ceramic International. **41**: 8680-8687.

Nurul Amal Nadhirah Mohamad, Nur Afiqah Arham, Junaidah Jai, Abdul Hadi, (2014). Plant Extract as Reducing Agent in Synthesis of Metallic Nanoparticles: A Review. *Advanced Materials Research*, **832**: 350-355.

Ogasawara, H., A. Kotani, R. Potze, G.A. Sawatzky, B.T. Thole, (1991).

Praseodymium 3d and 4d-core photoemission spectra of Pr_2O_3. *Phys. Rev. B* **44**: 5465–5469.

Ong, W.J., Tan, L.L., Chai, S.P., Yong, S.T., and. Mohamed, A. R., (2014). Facet-dependent photocatalytic properties of TiO_2-based composites for energy conversion and environmental remediation. *Chem Sus Chem*., **7**: 690–719.

Ouyang S., Zhang H., Li D., Yu T., Ye J., Zou Z. (2006). Electronic structure and photocatalytic characterisation of a novel photocatalyst $AgAlO_2$. *J. Phys. Chem.B,* **110**: 11677-11682.

Pan C., Xu J., Wang Y., Li D., Zhu Y., (2012). Dramatic Activity of $C_3N_4/BiPO_4$ Photocatalyst with Core/Shell Structure Formed by Self- Assembly. *Adv. Funct. Mater.,* **22**: 1518−1524.

Piguet, C., Buenzli, J.C.G., Bernardinelli, G., Hopfgartner, G., Williams, A.F., (1993). Self-assembly and photophysical properties of lanthanide dinuclear triple-helical complexes. *J Am Chem Soc.,* **115**: 8197- 8206.

Poulin, S., Franca, R., Moreau-Be´langer, L., Sacher, E., (2010). Confirmation of X-ray photoelectron spectroscopy peak attributions of nanoparticulate iron oxides, using symmetric peak component line shapes. *J. Phys. Chem. C,* **114**:10711–10718.

Pouretedal, H.R., Norozi, A., Keshavarz, M.H., Semnani, A., (2009). Nanoparticles of zinc sulfide doped with manganese, nickel and copper as nanophotocatalyst in the degradation of organic dyes. *J. Hazard. Mater,* **162**: 674–681.

Prakash, K., Senthil Kumar, P., Pandiaraj, S., Saravanakumar, K., Karuthapandian, S., (2016). Controllable synthesis of SnO_2 photocatalyst with superior photocatalytic activity for the degradation of methylene blue dye solution. *J Exp Nanosci.* **11**: 1138–1155.

Prashant V. K., (2007), Meeting the Clean Energy Demand: Nanostructure Architectures for Solar Energy Conversion. *J. Phys. Chem. C,* **111**: 2834−2860.

Premjit Singh N, Ramananda Singh N., Rangeela Devi Y., Brojendro Singh Shagolsem, David Singh Th., Rajmuhon Singh N., Mohondas Singh N., (2020). Effects of annealing temperature on structural and luminescence properties of $CdMoO_4$:Dy^{3+} phosphor synthesized at room temperature by co-precipitation method. *Journal of Solid-State Sciences,* **102**: 106172.

Qi, Q., Zhang, T., Liu, L., Zheng, X.J., Lu, G.Y., (2009). Improved NH_3, C_2H_5OH, and CH_3COCH_3 sensing properties of SnO_2 nanofibers by adding block copolymer P123. *Sensor and Actuator B. Chem.*, **141**: 174–178.

Ragupathy.S, Velu Manikandan, Sandhanasamy Devanesan, Mukhtar Ahmed, Rama moorthy. M., Priyadharsan, (2022). A. Enhanced sun light driven photocatalytic activity of Co doped SnO_2 loaded corn cob activated carbon for methylene blue dye degradation. *Chemosphere*, **295**: 133848.

Raj, K., Moskowitz, R., (2002). A review of damping applications of ferrofluids. *Transactions on Magnetics*, **16**:358-363.

Rakibuddin, M., Ananthakrishnan, R., (2016). A novel Ag deposited nanocoordination polymer derived porous SnO_2/NiO heteronanostructure for the enhanced photocatalytic reduction of Cr (VI) under visible light. *New J Chem*., **40**: 3385-3394.

Ramananda Singh Naorem, Premjit Singh Naorem, Brojendro Singh Shagolsem, Nongmaithem Herojit Singh, Jogat Gogoi, Mohondas Singh N. (2022). Effect of annealing temperatures on the structural and photoluminescence properties of Tb^{3+} ions doped $BiPO_4$ nanophosphors. Material Technology. *Advanced Performance Materials,* **37**: 2289-2299.

Rekha Rajput B., Shweta Jamble, N., Rohidas Kale, B., (2022). A review on TiO_2/SnO_2 heterostructures as a photocatalyst for the degradation of dyes and organic pollutants. *Journal of Environmental Management,* **307**: 114533.

Ren L., Huang S., Fan W., Liu T., (2011). One-Step Preparation of Hierarchical

Superparamagnetic Iron Oxide/Graphene Composites Via Hydrothermal Method. *Appl. Surf. Sci.* **258**: 1132−1138.

Reszczyńska, J., Grzyb, T., Sobczak, J.W., Lisowski, W., Gazda, M., Ohtani, B., Zaleska, A., (2014). Lanthanide co-doped TiO_2: the effect of metal type and amount on surface properties and photocatalytic activity. *Appl Surf Sci.,* **307**: 333-345.

Samaneh, D., Ahmad, J. J, Mahdi, F. K, Ali, E., Roshanak, R.K., (2019). Visible-light-driven photocatalytic degradation of Metalaxyl by reduced graphene oxide/Fe_3O_4/ZnO ternary nanohybrid: Influential factors, mechanism and toxicity bioassay. *Journal of Photochemistry & Photobiology A: Chemistry*, **375**: 280-292.

Sarkar, A., Ghosh, A.B., Saha, N., Srivastava, D.N., Paul, P., Adhikary, B., (2016). Enhanced photocatalytic performance of morphologically tuned Bi_2S_3 NPs in the degradation of organic pollutants under visible light irradiation. *Journal of Colloid and Interface Science,* **483**: 49-59.

Sedighi, F., Esmaeili, M., Ali, Z., Nasab, S., Behpour, M., (2018). Synthesis and characterization of $CuWO_4$ nanoparticle and $CuWO_4$/NiO nanocomposite using co-precipitation method; application in photodegradation of organic dye in water. *J. Mater. Sci.,* **29 (16)**: 13737–13745.

Shaalan, N.M., Hamad, D., Abdel-Latief, A.Y., Abdel-Rahim, M.A., (2016), preparation of quantum size of tin oxide: structural and physical characterization. *Progress in Natural Science: Materials International,* **26**: 145-151.

Shen, L., Laibinis, P.E., Hatton, T.A., (1999). Bilayer surfactant stabilized magnetic fluids: Synthesis and interactions at interfaces. *Langmuir*, **15**:447-453.

Sheng Zhou, Ying Liu, Jianmei Li, Yajun Wang, Guiyuan Jiang, Zhen Zhao, Daxi W ang, Aijun Duan, Jian Liu, Yuechang Wei, (2014). Facile in situ synthesis of graphitic carbon nitride (g-C_3N_4)-N-TiO_2 heterojunction as an efficient photocatalyst for the selective photoreduction of CO_2 to CO. *Environmental*

Applied Catalysis B, **158-159**: 20-29.

Shi, S., Gao, D., Qiang, Xu., Yang, Z., Xue, D., (2014). Singly-charged oxygen vacancy-induced ferromagnetism in mechanically milled SnO_2 powders. *RSC Adv.* **4**: 45467.

Shojaei, A.F., Shams-Nateri, A., Ghomashpasand, M., (2015). Comparative study of photocatalytic activities of magnetically separable $WO_3/TiO_2/Fe_3O_4$ nanocomposites and TiO_2, WO_3/TiO_2 and TiO_2/Fe_3O_4 under visible light irradiation. *Microstruct.,* **88**: 211–224.

Singh, D., Verma, S., Gautam, R.K., Krishna, V., (2015). Copper adsorption onto synthesized nitrilotriacetic acid functionalized Fe_3O_4 nanoparticles: kinetic, equilibrium and thermodynamic studies. *J. Environ. Chem.Eng.*, **3**: 2161–2171.

Singh, K. P., Mohan, D., Sinha, S., Tondon, G. S., Gosh, D., (2003). Color Removal from Wastewater Using Low-Cost Activated Carbon Derived from Agricultural Waste Material. Industrial & Engineering Chemistry Research. **42(9)**: 1965–1976.

Singh, L., Luwang, M.N., Srivastava, S., (2014). Luminescence and photocatalytic studies of Sm^{3+} ion doped SnO_2 nanoparticles. *New J Chem.*, **38**: 115-121.

Sobhani-nasab, A., Behpour, M., Rahimi-nasrabadi, Ahmadi, F., Pourmasoud, S., Sedighi, F., (2019). Preparation, characterization and investigation of sonophotocatalytic activity of thulium titanate/polyaniline nanocomposites in degradation of dyes. *Ultrason. Sonochem.*, **50**: 46–58.

Sobhani-Nasab, A., Pourmasoud, S., Ahmadi, F., Wysokowski, M., Jesionowski, H., Ehrlich, M., Rahimi-Nasrabadi, (2019). Synthesis and characterization of $MnWO_4/TmVO_4$ ternary nano-hybrids by an ultrasonic method for enhanced photocatalytic activity in the degradation of organic dyes. *Mater. Lett.*, **238**: 159–162.

Soto-Robles C.A., Luque P.A., Gómez-Gutiérrez C.M., Nava O., Vilchis Nestor A.R., Lugo-Medina E., Ranjithkumar R., Castro-Beltrán A., (2019). Study on the

effect of the concentration of Hibiscus sabdariffa extract on the green synthesis of ZnO nanoparticles, Results in Physics, **15**: 1-25.

Sreeja D.P.S., Neethu S.K. and Sabu K.K. (2021), Phytochemical profiling and antioxidant activities of different parts of Artocarpus heterophyllus Lam. (Moraceae): A review on current status of knowledge. *Future Journal of Pharmaceutical Science*, **30**: 1-7.

Suthakaran, S., Dhanapandian, S., Krishnakumar, N., Ponpandian, N., (2019). Hydrothermal synthesis of SnO_2 nanoparticles and its photocatalytic degradation of methyl violet and electrochemical performance. *Materials Research Express,* **6(8)**: 0850i3.

Tada, H., Mitsui, T., Kiyonaga, T., Akita, T., Tanaka, K., (2006). All-solid-state Z-scheme in CdS–Au–TiO_2 three-component nanojunction system. *Nat. Mater* **5**: 782-786.

Tang J., Zou Z., Ye J., (2004). Efficient photocatalytic decomposition of organic contaminants over $CaBi_2O_4$ under visible-light irradiation. *Angew Chem., Int. Ed.* **43**: 4463-4466.

Tang, J., Zou, Z., Ye, J., (2004). Efficient photocatalytic decomposition of organic contaminants over $CaBi_2O_4$ under visible-light irradiation, *Angew Chem., Int. Ed.,* **43:** 4463-4466.

Tanur Sinha Md, Ahmaruzzaman PP, Adhikari RB., (2017). Green and environmentally sustainable fabrication of Ag-SnO_2 nanocomposite and its multifunctional efficacy as photocatalyst and antibacterial and antioxidant agent. *ACS Sustain. Chem Eng*., **5**: 4645–4655.

Tao Tao, Lijun He, Jin Li, Yanhua Zhang, (2015). A new way for synthesizing SnO_2 nanosheets. *Materials Letters*, **138**: 45-47.

Tao, K., Dou, H.J., Sun, K., (2008). Interfacial coprecipitation to prepare magnetite nanoparticles: Concentration and temperature dependence. *Colloids Surf.,*

320:115-122.

Tao, X., Chen, X., Xia, Y., Huang, H., Gan, Y., Wu, R., (2013). Highly mesoporous carbon foams synthesized by a facile, cost-effective and template-free Pechini method for advanced lithium_sulfur batteries. *J Mater Chem A.*, **1**: 3295–301.

Tojo, S., Tachikawa, T., Fujitsuka, M., Majima, T., (2008). Iodine-doped TiO_2 photocatalysts: correlation between band structure and mechanism. *J Phys Chem C,* **112**: 14948-14954.

Trellu, C., Mousset, E., Pechaud, Y., Huguenot, D., Van Hullebusch, E.D., Esposito, G., Oturan, M.A., (2016). Removal of hydrophobic organic pollutants from soil washing/flushing solutions: A critical review. *Journal of hazardous materials,* **306**: 149-174.

Tu, Y.F., Huang, S.Y., Sang, J.P., Zou, X.W., (2009). Synthesis and photocatalytic properties of Sn-doped TiO_2 nanotube arrays. *J Alloy Compd.*, **482**: 382-387.

Vinodgopal, K., Kamat, P.V., (1995). Enhanced rates of photocatalytic degradation of an azo dye using SnO_2/TiO_2 coupled semiconductor thin films. *Environ sci technol.*, **29**: 841-845.

Vivek Agrahari, MohanChandra Mathpal, Mahendra Kumar, Arvind Agarwal, (2015). Investigations of optoelectronic properties in DMS SnO_2 nanoparticles. *Journal of Alloys and Compounds*, **622**: 48-53.

Wang Yi-Chuen, Lee Ai-Hsuan, Chen Chiing-Chang, (2018). Perovskite-like photocatalyst, $PbBiO_2Br$/PbO/g-C_3N_4: Synthesis, characterization, and visible-light-driven photocatalytic activity. *Journal of the Taiwan Institute of Chemical Engineers,* **93**: 315-328.

Wang, L.Y., Luo, J., Fan, Q., Suzuki, M., Suzuki, I.S., Engelhard, M.H., Lin, Y., Kim, N., Wang, J.Q., Zhong, C., (2005). Monodispersed Core−Shell Fe_3O_4@Au Nanoparticles. *J. Phys. Chem. B* **109**: 21593.

Wang, W., Wang, J., Wang, Z., Wei, X., Liu, L., Ren, Q., Gao, W., Liang Y., Shi, H., (2014). p–n junction CuO/$BiVO_4$ heterogeneous nanostructures: synthesis and highly junction CuO/$BiVO_4$ heterogeneous nanostructures: synthesis and highly efficient visible-light photocatalytic performance. *Dalton Trans*. **43**: 6735–6743.

Wang, W.W., Yao, J.L., (2010). Synthesis of magnetically separable Sn doped magnetite/silica core–shell structure and photocatalytic property. *Mater. Res. Bull.*, **45**: 710–716.

Wang, X., Blechert, S., Antonietti, M., (2012), Polymeric Graphitic Carbon Nitride for Heterogeneous Photocatalysis. *ACS Catal.* **2**: 1596−1606.

Wang, Y., Shi, R., Lin, J., Zhu, Y., (2011). Enhancement of Photocurrent and Photocatalytic Activity of ZnO Hybridized with Graphite-like C_3N_4. *Energy Environ. Sci.* **4**: 2922−2929.

Wang, Z., Du, Y., Zhang, F., Zheng, Z., Zhang, X., Feng, Q., Wang, C., (2013). Photocatalytic degradation of pendimethalin over Cu_2O/SnO_2/graphene and SnO_2/graphene nanocomposite photocatalysts under visible light irradiation. *Mater. Chem. Phys.*, **140**: 373–381.

Wangwei Ren, Jingkai Yang, Jiaxin Zhang, Wei Li, Chaoyang Sun, Hongli Zhao, Yi ntang Wen, Ou Sha, Bo Liang, (2022). Recent progress in SnO_2/g-C_3N_4 heterojunction photocatalysts: Synthesis, modification, and application. *Journal of Alloys and Compounds*, **906**: 164372

Wei L., Shifu C., Wei Z., Sujuan Z., (2009). Titanium dioxide mediated photocatalytic degradation of methamidophos in aqueous phase. *J. Hazard. Mater.* **164**: 154–160.

Wei L., Shifu, C., Wei, Z., Sujuan, Z., (2009). Titanium dioxide mediated photocatalytic degradation of methamidophos in aqueous phase. *J. Hazard. Mater.*, **164**:154–160.

Wei W., Quanguo H., Changzhong J., (2008). Magnetic Iron Oxide Nanoparticles:

Synthesis and Surface Functionalization Strategies. *Nanoscale Res. Lett.,* **3**:397–415.

Wen, Z., Wang, G., Lu W., Wang, Q., Zhang, Q., Li, J., (2007). Enhanced Photocatalytic Properties of Mesoporous SnO_2 Induced by Low Concentration ZnO Doping. *Crystal Growth & Design*, **7**: 1722-1725.

Xiangyu Chen, Deqing Chu, Limin Wang, Wenhui Hu, Huifang Yang, Jingjing Sun, Shaopeng Zhu, Guowei Wang, Jian Tao, Songsong Zhang, (2017). One-step synthesis of novel hierarchical flower-like SnO_2 nanostructures with enhanced photocatalytic activity. *Journal of Alloys and Compounds*, **729**: 710-715.

Xie J., Chen K., Lee H. Y., Xu C., Hsu A. R., Peng, S., Chen X., Sun S., (2008). Ultrasmall c(RGDyK)-Coated Fe_3O_4 Nanoparticles and Their Specific Targeting to Integrin rv3-Rich Tumor Cells. *J. Am. Chem. Soc.* **130**: 7542−7543.

Xinping L, Fuqiang H, Jingcheng X, Wendeng W, Fangfang X. (2008). Heterojunction semiconductor $SnO_2/SrNb_2O_6$ with an enhanced photocatalytic activity: The significance of chemically bonded interface. *Acta Materialia,* **56**: 2699-2705.

Xiong, C., Balkus, K.J., (2007). Mesoporous molecular sieve derived TiO_2 nanofibers doped with SnO_2. *J Phys Chem C***, 111**: 10359-10367.

Xu Chunping , Prasaanth Ravi Anusuyadevi, Cyril Aymonier, Rafael Luque, Samuel Marre, Nanostructured materials for photocatalysis. *Chem. Soc. Rev.*, **48**: 3868-3902.

Xu, P., Zeng, G. M., Huang, D. L., Feng, C. L., Shuang, H., Zhao, M. H., Lai, C., Zhen, W., Huang, C., Xie, G. X., Liu, Z. F., (2012). Use of Iron Oxide Nanomaterials in Wastewater Treatment: A Review. *Sci. Total Environ.,* **424**: 1−10.

Xu, J., Li, Y., Huang, H., Zhu, Y., Wang, Z., Xie, Z., Wang, X., Chen, D., Shen, G., (2011). Synthesis, characterizations and improved gas-sensing performance of SnO_2 nanospike arrays. *J. Mater. Chem.* **21**: 19086–19092.

Xu, J., X. Han, H. Liu, Y. Hu, (2006). Synthesis and optical properties of silver nanoparticles stabilized by gemini surfactant. *Colloids and Surfaces A: Physicochemical and Engineering Aspects,* **273**: 179-183.

Yadav, A.A., Hunge, Y.M., Kang, S.W., Fujishima, A, Terashima, C., (2023). Enhanced photocatalytic degradation activity using the V_2O_5/RGO composite. *J Nanomater.*, **13**: 338.

Yan, Y., Liu, X.L., Fan, W.Q., Lv, P., Shi, W.D., (2012). $InVO_4$ microspheres: preparation, characterization and visible-light-driven photocatalytic activities. *Chemical Engineering Journal,* **200–202**: 310–316.

Yang, X., Zhang, X., Ma, Y., Huang, Y. Wang, Y., Chen, Y. (2009). Superparamagnetic Graphene Oxide−Fe_3O_4 Nanoparticles Hybrid for Controlled Targeted Drug Carriers. *J. Mater. Chem.,* **19**: 2710−2714.

Yang, Z., Lv, L., Dai, Y., Xv, Z., Qian, D., (2010). Synthesis of ZnO–SnO_2 composite oxides by CTAB-assisted co-precipitation and photocatalytic properties. *Appl Surf Sci.,* **256**: 2898-2902.

Yasser K. Abdel-Monem, (2016). Efficient nanophotocatalyt of hydrothermally synthesized Anatase TiO_2 nanoparticles from its analogue metal coordinated precursor. *J. Mater. Sci.*, **27**: 5723–5728.

Yu, C. L., Cai, D. J., Yu, J. C., Chen, X. R., Zhou, Y., Yang, K., (2010). Sol-gel derived S, I-Codoped mesoporous TiO_2 photocatalyst with high visible-light photocatalytic activity. *J. Phys. Chem. Solids.* **71**: 1337-1343.

Yu-Yun Lin, Kuo-Yu Hung, Fu-Yu Liu, Yong-Ming Dai, Jia-Hao Lin, Chiing-Chang Chen, (2022). Photocatalysts of quaternary composite, bismuth oxyfluoride/bismuth oxyiodide/graphitic carbon nitride: Synthesis, characterization, and photocatalytic activity. *Molecular Catalysis,* **528**: 112463.

Zeng-Hui Diao, Jin-Jun Liu, Yong-Xia Hu, Ling-Jun Kong, Dan Jiang, Xiang-Rong Xu, (2017). Comparative study of Rhodamine B degradation by the

systems pyrite/H_2O_2 and pyrite/persulfate: Reactivity, stability, products and mechanism. *Separation and Purification Technology*, **184**: 374-383.

Zhang, G., Xie, C., Zhang, S., Zhang, S., Xiong, Y., (2014). Defect chemistry of the metal cation defects in the p-and n-doped SnO_2 nanocrystalline films. *J Phys Chem C*, **118**: 18097-18109.

Zhang, J., Shi, F. J., Chen, D. F., Gao, J. M., Huang, Z. X., Ding, X. X., Tang, C. C., (2008). Self-assembled 3-D architectures of BiOBr as a visible light-driven photocatalyst. *Chem. Mater.*, **20**: 2937-2941.

Zhang, P., Li, X., Zhao, Q., Liu, S., (2011). Synthesis and optical property of one-dimensional spinel $ZnMn_2O_4$ nanorods. *Nanoscale Research Letters*, **6**: 323.

Zhang, Y., Mori, T., Ye, J., (2012). Polymeric Carbon Nitrides: Semiconducting Properties and Emerging Applications in Photocatalysis and Photoelectrochemical Energy Conversion. *Sci. Adv. Mater.*, **4**: 282−291.

Zhao, S., Chen, J., Liu, Y., Jiang, Y., Jiang, C., Yin, Z., Xiao, Y., Cao, S., (2019). Silver nanoparticles confined in shell-in-shell hollow TiO_2 manifesting efficiently photocatalytic activity and stability. *Chem. Engin. J.*, **367:** 249-259.

Zhijie Xie, Yiping Feng, Fengliang Wang, Danni Chen, Qianxin Zhang, Yongqin Ze ng, Wenying Lv, Guoguang Liu, (2018). Construction of carbon dots modified MoO_3/g-C_3N_4 Z-scheme photocatalyst with enhanced visible-light photocatalytic activity for the degradation of tetracycline. *Applied Catalysis B: Environmental*, **229**: 96-104.

Zhou, X., Jin, B., Chen, R., Feng, P., Fang, Y, (2013). Synthesis of Porous Fe_3O_4/g-C_3N_4 Nanospheres as Highly Efficient and Recyclable Photocatalysts. *Mater. Res. Bull.*, **48**: 1447−1452.

Zhu, Y.F., Zhao, W.R., Chen, H.R., Shi, J.L., (2007). A Simple One-Pot Self-Assembly Route to Nanoporous and Monodispersed Fe_3O_4 Particles with Oriented Attachment Structure and Magnetic Property. *J. Phys. Chem. C*, **111**:

5281.

Zou, Z., Ye, J., Sayama, K., Arakawa, H. (2001). Direct splitting of water under visible light irradiation with an oxide semiconductor photocatalyst. *Nature*, **414**: 625–627.

BIO-DATA

1. NAME : Brojendro Singh Shagolsem

2. DATE OF BIRTH : 12th December 1983

3. FATHER'S NAME **:** Manglem Singh Shagolsem

4. PERMANENT ADDRESS **:** Athokpam Awang Leikai, P.O, P.S-Thoubal, District-Thoubal, State-Manipur (India), PIN-795138

5. EMAIL ADDRESS **:** brojensagolsem@gmail.com

6. EDUCATIONAL QUALIFICATIONS **:**

Examination passed	**Year of Passing**	**Board/ University**	**Class/ Division**	**% of Marks**	**Subjects**
All India Secondary School Examination	1999	Central Board of Secondary Education	I	71.4%	Eng., Hindi, Maths, Science, Social Science
All India Senior School Certificate Examination	2001	Central Board of Secondary Education	I	73.6%	Eng., Maths., Physics, Chemistry, Biology
B. Sc.(H) Chemistry	2006	University of Delhi	II	53.03%	Chemistry, Physics, Maths.,
M.Sc. Agrochemicals and Pest Management	2009	University of Delhi	I	62.75	Agrochemicals

List of Publications

A. Publication from thesis

1. **Brojendro Singh Shagolsem**, Nongmaithem Mohondas Singh (2024). Green synthesis and magnetically separable $Fe_3O_4/SnO_2/g\text{-}C_3N_4$ ternary nanocomposite for degradation of Rhodamine B. inorganic Chemistry Communications. 160, 111877.

   https://doi.org/10.1016/j.inoche.2023.111877. (IF 4.4)
2. **Brojendro Singh Shagolsem**, N. Mohondas Singh (2024). Ternary photocatalyst of $Fe_3O_4/Ag\text{-}SnO_2$ with *Parkia speciosa* extract improves visible-light-driven photocatalytic degradation of dye. Inorganic Chemistry Communication. 162: 112245.

   https://doi.org/10.1016/j.inoche.2024.112245. (IF 4.4)

B. Publication from other areas

1. Kshetrimayum Suresh Singh, Suman Nayak, Esther Lalnunmawii, Mayanglambam Bidyalakshmi Devi, Brojendro Singh Shagolsem, Sushanto Gouda (2024). Pyrolytic oil from Muli bamboo (Melocanna baccifera, Roxb.): Biological potential and possible functional attributes. Journal of Analytical and Applied Pyrolysis. 180:106528.

   https://doi.org/10.1016/j.jaap.2024.106528 (IF 5.7)
2. Ramananda Singh Naorem, Naorem Premjit Singh, **Brojendro Singh Shagolsem**, Nongmaithem Herojit Singh, Jogat Gogoi, Nongmaithem Mohondas Singh (2022). Effect of annealing temperatures on the structural and photoluminescence properties of Tb^{3+} ions doped $BiPO_4$ nanophosphors. Materials Technology, Advanced Performance Materials, 37: 2289-2299.

   https://doi.org/10.1080/10667857.2022.2029289. (IF 2.9)
3. N. Premjit Singh, N. Ramananda Singh, Y. Rangeela Devi, **Brojendro Singh Shagolsem**, Th. David Singh, N. Rajmuhon Singh, N. Mohondas Singh (2020). Effects of annealing temperature on structural and luminescence properties of $CdMoO_4:Dy3^+$ phosphor synthesized at room temperature by co-precipitation method. Solid State Sciences, 102: 106172.

   https://doi.org/10.1016/j.solidstatesciences.2020.106172. (IF 3.4)
4. Kh. Devala Devi, **S. Brojendro Singh**, N. Samarjit Singh, Chingakham B.S, Ksh. Punyarani and H. Sunitibala Devi (2015). Evaluation of genetic relationships and chemical assay of *Kaempferia galanga* L. cultivars found in Manipur, North-East India. International Journal of Recent Scientific Research. 6(6): 4366-4373.

ISSN: 0976-3031 (IF pending)

5. Dikash Singh Thingbaijam, Devala Devi Khumallambam, Punyarani Kshetrimayum, Henary Singh Chongtham, **Brojendro Singh Shagolsem**, Brajakishor S. Chingakham, Sunitibala Devi Huidrom (2012). Silver Nitrate and Different Culture Vessels Influence High equency Microrhizome *In Vitro* and Enhanced Growth of Turmeric Plantlet During *Ex Vitro* Acclimatization. Notulae Scientia Biologicae. 4(4): 67-78.
   ISSN 2067-3205 (IF pending)

6. Thingbaijam Dikash Singh, Khumallambam Devala Devi, **Brojendro Singh Shagolsem**, Chingakham Brajakishor Singh and Huidrom Sunitibala Devi (2013). Assessment of genetic stability in traditional ginger cultivated in Manipur: North-East India base on molecular and chemical markers. Analytical Letters.46:2941-2953.
   https://10.1080/00032719.2013.814059 (IF 1.9)

7. **S. Brojendro Singh**, W. Radhapiyari Devi, Marina A, W. Indira Devi, N. Swapana, Chingakham B. Singh (2013). Ethnobotany, phytochemistry and pharmacology of *Ageratum conyzoides* Linn (Asteraceae). Journal of Medicinal Plant Research. 7(8): 371-385.
   10.5897/JMPR12.897 (Scopus)

8. Wangkheirakpam Radhapiyari Devi, **S Brojendro Singh**, Chingakham B Singh (2013). Antioxidant and anti-dermatophytic properties leaf and stem bark of *Xylosma longifolium* clos. BMC-Complementary and Alternative Medicine. 13:155-173.
   https://10.1186/1472-6882-13-155 (Scopus)

9. Reena Laikangbam, M. Damayanti Devi, **S. Brojendro Singh**, C.B. Singh (2013). Evaluation of antioxidant potentials and quantification of phenolic compounds present in different parts of *Roselle.* Journal of Ethnobiology and Traditional Medicine.119: 417-423
   ISJN: 6642-3194

10. C.B. Singh, Kh. Nongalleima, **S. Brojendro singh,** Swapana Ningombam, N. Lokendrajit and L.W. Singh (2012). Biological and Chemical properties of *Zingiber zerumbet* Smith-a review; Phytochemistry review, 11:113-125.
    https://10.1007/s11101-011-9222-4. (IF 7.9)

11. N. Swapana, **S. Brojendro Singh**, Th. Jotinkumar, Ch. Bidyalaxmi devi, M. Sumarjit Singh and C.B Singh (2012). Total phenolic, Total flavonoid contents and Antioxidant activity of a few indigenous fruits grown in Manipur. The Bio scan. 7(1):73-76, 2012.

C. Conference/Seminar

1. Presented “Visible light-driven photocatalytic degradation of dye, enhanced by using a ternary photocatalyst composed of Fe_3O_4/Ag-SnO_2: A green synthesis. At the International Conference on recent advances in Mathematical, Physical and Chemical Sciences (ICRAMPC-2024) organizes by school of physical Sciences, Mizoram University, Aizawl, India, during 21-23rd February, 2024.
2. Presented “Magnetically Recyclable ternary nanocomposite synthesized with Lemon extract: Photocatalytic study of dye decomposition” at International Conference on recent advances in energy materials and its application (ICRAEMA-23) 30th-31st May 2023, organized by the the Department of Physics, Pachhunga University College, Mizoram University, Aizawl, Mizoram, India.
3. Presented “Green synthesis of reusable visible-active heterogenous photocatalyst for water remediation” at International Conference on metallomics, Biodiversity and human health: Recent Advances and synthesis, held at Manipur University during 03-04 March,2023 organized by Department of Life Sciences (Zoology), Manipur University, Canchipur, Imphal, Manipur, India
4. Presented “Green synthesis and magnetically separable ternary nanocomposite for degradation of Rhodamine B” at the Physical Sciences discipline technical session in the 4th Mizoram Science Congress held at Aijal Club, Aizawl during 24025 November,2022 organized by MISTICS in collaboration with MAS, MSS, STAM, GSM, MMS, BIOCONE and MITS.

PARTICULARS OF THE CANDIDATE

NAME OF THE CANDIDATE	:	Brojendro Singh Shagolsem
DEGREE	:	Doctor of Philosophy (Ph.D.)
DEPARTMENT	:	Chemistry
TITLE OF THESIS	:	Magnetically Separable Nanocomposites With Enhanced Photocatalytic Activities For Some Selected Dyes and Pesticides Degradations.
DATE OF ADMISSION	:	05th November, 2020

APPROVAL OF RESEARCH PROPOSAL:

1. **DRC**	:	19th April, 2021
2. **BOS**	:	03rd May, 2021
3. **SCHOOL BOARD**	:	17th May, 2021
4. **MZU REGN. NO**	:	2001043
5. **Ph.D. REGN. NO.& DATE**	:	MZU/Ph.D./1527 of 05.11.2020
6. **EXTENSION**	:	NIL

Head

Department of Chemistry

ABSTRACT

MAGNETICALLY SEPARABLE NANOCOMPOSITES WITH ENHANCED PHOTOCATALYTIC ACTIVITIES FOR SOME SELECTED DYES AND PESTICIDES DEGRADATIONS

AN ABSTRACT SUBMITTED IN PARTIAL FULFILLMENT OF THE REQUIREMENTS FOR THE DEGREE OF DOCTOR OF PHILOSOPHY

BROJENDRO SINGH SHAGOLSEM

MZU REGISTRATION NUMBER: 2001043

Ph.D. REGISTRATION NUMBER: MZU/Ph.D./1527 of 05.11.2020

DEPARTMENT OF CHEMISTRY

SCHOOL OF PHYSICAL SCIENCES

MAY, 2024

ABSTRACT

MAGNETICALLY SEPARABLE NANOCOMPOSITES WITH ENHANCED PHOTOCATALYTIC ACTIVITIES FOR SOME SELECTED DYES AND PESTICIDES DEGRADATIONS

AN ABSTRACT SUBMITTED IN PARTIAL FULFILLMENT OF THE REQUIREMENTS FOR THE DEGREE OF DOCTOR OF PHILOSOPHY

BROJENDRO SINGH SHAGOLSEM

MZU REGISTRATION NUMBER: 2001043

Ph.D. REGISTRATION NUMBER: MZU/Ph.D./1527 of 05.11.2020

DEPARTMENT OF CHEMISTRY

SCHOOL OF PHYSICAL SCIENCES

MAY, 2024

MAGNETICALLY SEPARABLE NANOCOMPOSITES WITH ENHANCED PHOTOCATALYTIC ACTIVITIES FOR SOME SELECTED DYES AND PESTICIDES DEGRADATIONS

BY

BROJENDRO SINGH SHAGOLSEM

Department of Chemistry

Under the supervision of

Prof. N. MOHONDAS SINGH

Submitted

In partial fulfillment of the requirement of the Degree of Doctor of Philosophy in Chemistry of Mizoram University, Aizawl.

ABSTRACT

Point-source pollution of water bodies with organic pollutants from industrial waste and human-made pollution were threatening ecosystems worldwide. Many researchers described several ways to remove wastewater pollutants and prevent marine life death, disease propagation, and ecological degradation requires wastewater dye toxicity removal, which can be done photocatalytically. Wastewater cleanup was better with advanced oxidation methods, and several approaches were documented. Semiconductor photocatalysts have been more popular in the recent decade as a technique to clean up hazardous waste and energy loss utilizing solar power. These photocatalysts were affordable, non-toxic, recyclable, and offer multi-step electron transfer. Recent efforts to develop semiconductor materials with specific sizes, forms, optical, electrical, and catalytic capabilities for energy procurement, biosystems, and conservation have garnered interest. SnO_2 was considered the prevailing n-type semiconductor due to its possession of a large and linear bandgap of 3.6 eV. The distinctive characteristics of this substance were its chemical and thermal stability, high binding energy, transparency, and capacity for storing a significant amount of oxygen. Rhodamine B (RhB), methylene blue (MB), 2,4-Dichlorophenol (2,4-DCP) and Trichloroacetic acid (TCAA), an organic dye and pesticides, have been used in several industries such as paper manufacturing textile production, pharmaceutical, pesticides industries and farmers. The reason for less using of SnO_2 was due to reduce absorption of visible light in sunlight which can be attributed to its wider bandgap. The observed phenomenon leads to a decrease in overall efficiency. Electron-hole pairs were generated within semiconductor nanoparticles (NPs) when exposed to visible or ultraviolet (UV) radiation. The rapid recombination of electron-hole pairs inhibited photocatalytic performance increased. SnO_2 was a promising semiconductor material for photovoltaics, but a high recombination rate and poor photoexcited electron-hole sets limited its photocatalytic efficiency. Metal oxides (SnO_2), semiconductors, can maintain their versatility morphology, compound formation, and particle size dispersion through making heterojunction or doping or co-doping with g-C_3N_4, Ag, Praseodymium or yttrium ion. Research to improve SnO_2 physicochemical properties was significant for several reasons. Doping and semiconductor pairing moved SnO_2

absorption into the visible range. The only easy and useful technique to lower the bandgap was to dope, which attracts and enhances resources and increases visible light photocatalytic activity.

Chapter 1: This chapter provides a comprehensive overview of metal oxides and their photoluminescent properties, including those doped with transition or lanthanide chemicals. A comprehensive list of various methods for creating doping or heterojunction using SnO_2 was provided, and detailed explanations were provided. The discussion also included the spectroscopic properties and applications of SnO_2 doped with other semiconductors, transition elements, and rare earth metals. The text briefly highlighted many processes that contribute to the photodegradation of organic pollutants in aqueous solutions. The impact of contaminant concentration, pH levels, and surface effects will also be considered. The literature reviews and study scope were documented. A review was conducted on the research conducted in the past few decades about developing SnO_2 doped with other semiconductors.

Chapter 2: Characterization of the synthesized materials is a crucial step in determining the properties of the materials using the necessary instruments. This chapter comprehensively discussed the many instrumentation techniques employed in our research, including XRD, FT-IR, SEM, TEM, EDAX, EPR, TOC, BET surface area analysis, Photoluminescence, and VSM. Materials undergo characterization to determine their inherent qualities. The characteristics of a substance are influenced by its morphology and size, which can be studied using TEM or SEM imaging techniques. Similarly, the property, which is determined by the crystallinity of the materials, may be observed using XRD examination.

Chapter 3: A novel environmentally-friendly method for synthesising Fe_3O_4, SnO_2, and their ternary nanocomposite, $Fe_3O_4/SnO_2/g\text{-}C_3N_4$, has been developed. This method employed plant extracts derived from lemon (*Citrus x lemon*) fruits, which were abundant in Mizoram, India. The nanomaterials were synthesised using a hydrothermal method and characterised using UV-Visible, FT-IR, XRD, SEM, TEM, and XPS techniques. The XRD measurement verified the phase purity of the nanocomposite (FSG2). The study looked at how well magnetically separable FSG2

ternary photocatalyst materials broke down rhodamine B (RhB), methylene blue (MB), 2,4-Dichlorophenol (2,4-DCP) and Trichloroacetic acid (TCAA) when exposed to visible light from a 50-watt Philips LED bulb. Measurements were taken every 30 min. A magnet placed outside the aqueous suspension separated the magnetically active ternary photocatalyst, facilitating easy and efficient recycling.

Fe_3O_4/Ag doped g-C_3N_4 was synthesised hydrothermally using plant extract (*Atocarpus heterophyllus* L), resulting in a homogeneous distribution of Ag nanoparticles on g-C_3N_4 sheets. The plant extract worked as a reducing or capping agent, which made it possible to precisely control the spread of Ag at weight percentages of 1, 3, 5, 7, and 9 wt.% on g-C_3N_4. Under LED light, the study examined the effectiveness of Fe_3O_4/Ag doped g-C_3N_4 (FAG3) in photocatalysis. Specifically, it focused on the degradation of rhodamine B (RhB), methylene blue (MB), 2,4-dichlorophenol (2,4-DCP), and trichloroacetic acid (TCAA). Remarkably, the photocatalytic effectiveness of Fe_3O_4/Ag (5 wt.%)-doped g-C_3N_4 (FAG3) was significantly higher than that of Fe_3O_4/g-C_3N_4, resulting in improved elimination of dyes and pesticides. The efficiency of FAG3 was enhanced through surface plasmon resonance, while the presence of photogenerated holes and radicals further improved its breakdown. Using an outside magnet made recycling easier by separating the ternary photocatalyst from the water-based suspension.

SnO_2 is a widely employed and economical photocatalyst in diverse industries, such as industrial polishes, glass and ceramic coatings, construction materials, and gas sensor systems. However, the fast recombination of electrons and holes constrains the process of light emission. To address this problem, a groundbreaking investigation was carried out, utilising an inexpensive and harmless plant extract (Citrus x lemon) precursor containing phytochemicals as a capping agent. Fe_3O_4/Ag_x-Sn_yO_2 nanocomposites were synthesised using different ratios of Ag and $SnCl_2$. The samples were then analysed using FTIR, UV-visible, XRD, SEM, TEM, XPS, and BET surface techniques. The combination of Fe_3O_4/Ag_x-Sn_yO_2 (x:y=1:1, 1:3, 3:1) is a more effective photocatalyst than Fe_3O_4 or SnO_2 individually. The efficiency of the nanocomposite photodecomposition was tested by decomposing dyes and pesticides,

using a 50W LED light. Exposure to LED light enhanced the photocatalytic activity of the Fe_3O_4/Ag_x-Sn_yO_2 (FAS3) (x:y=3:1) nanocomposite. The results demonstrated that the excited charge electrons originating from SnO_2 were capable of transferring to the Ag conductive band, enhancing the charge pair separation process. Enhancing the photocatalytic activity of Fe_3O_4/Ag_x-Sn_yO_2 (FAS3) (x:y=3:1) might result in the more efficient degradation of rhodamine B (RhB), methylene blue (MB), 2,4-dichlorophenol (2,4-DCP), and trichloroacetic acid (TCAA).

This study introduces a meticulous and all-encompassing method for creating Fe_3O_4/Pr^{3+}: SnO_2 (FPS) nanostructures utilising an extract obtained from jackfruit leaves (*Atocarpus heterophyllus* L). This innovative strategy is environmentally conscious and enduring, laying the foundation for a more sustainable future. We performed experiments with varying amounts of praseodymium ions to examine their impact on the structure, purity, size, and efficacy of the Fe_3O_4/Pr^{3+}: SnO_2 photocatalyst. The hydrothermal technique was employed to synthesise and evaluate a visible light-sensitive photocatalyst, utilising a minimal amount of Jackfruit extract. We employed a range of techniques, including UV-visible Spectroscopy, X-ray Diffraction (XRD), Electron Microscope (TEM), Scanning Electron Microscope (SEM), Vibrating Sample Magnetometer (VSM), and others, to analyse and develop this innovative photocatalyst. The results of this study demonstrate the remarkable ability of just 2 ml of Jackfruit extract to produce the Fe_3O_4/(1 at.%)Pr^{3+}: SnO_2 (FPS1) photocatalyst, which has shown outstanding effectiveness in breaking down Rhodamine B (RhB), Methylene blue (MB), 2,4-Dichlorophenol (2,4-DCP), and Trichloroacetic acid (TCAA). This research demonstrates that the material, in its original form, can serve as a unique photocatalyst that is responsive to visible light. The photocatalyst efficiently eradicates and decomposes organic contaminants in water, rendering it a superb substitute for conventional approaches. In addition, it discovered that the material exhibited structural integrity, rendering it a suitable remedy for environmental obstacles. This paper is an invaluable addition to the field of sustainable materials science and novel methodology for developing a photocatalyst minimises the ecological consequences of conventional techniques and offers a superior and more proficient remedy for eradicating organic contaminants in water.

The study suggested a sustainable method for synthesising SnO_2 by mixing $SnCl_2.5H_2O$, NaOH, and an extract derived from stink bean (*Parkia speciosa*). The hydrothermal technique was employed to incorporate varying concentrations of Praseodymium ion (Pr^{3+}) (1, 3, 5, 7, 9, and 11 at.%) and Yttrium ion (Y^{3+}) (1, 3, 5, 7, 9, and 11 at.%) into pre-existing SnO_2 nanoparticles. This resulted in the creation of various types of nanoparticles, such as Pr^{3+}-doped SnO_2 and Y^{3+}-doped SnO_2. A new nanocomposite, termed FPYS, was synthesised by mixing Fe_3O_4 and Pr^{3+},Y^{3+}: SnO_2 nanocomposite. The resulting material exhibits magnetic characteristics. Later, the hydrothermal synthesis method was used to create nanocomposites of FPYS. The use of various methods such as Field-emission scanning electron microscopy (FESEM), high-resolution transmission electron microscopy (HRTEM), Brunauer-Emmett-Teller (BET) analysis, ultraviolet-visible (UV-vis) spectroscopy, energy-dispersive X-ray spectroscopy (EDS), X-ray diffraction (XRD), and X-ray photoelectron spectroscopy (XPS) was employed in the examination of the nanocomposites. The efficacy of photodecomposition of the nanocomposite, which was synthesised, was investigated using certain dyes and pesticides under 50W LED light. When exposed to LED light, the FPYS3 (5 at.%) nanocomposite exhibited heightened photocatalytic activity, indicating that the excited charge electrons could migrate to the dopant conductive band, resulting in accelerated charge pair separation. Adding Pr^{3+} and Y^{3+} ions to SnO_2 improved the photocatalytic degradation of dyes and insecticides.

Chapter 4: This chapter concludes the experiment by summarising its findings and offering a last thought on its relevance and consequences. $Fe_3O_4/SnO_2/g\text{-}C_3N_4$ (FSG2), one of the ternary nanocomposites synthesised in this study, exhibited the most effective response in degrading dyes and pesticides. The repeated transfer of charges at the $SnO_2/g\text{-}C_3N_4$ heterojunction is responsible for this. The degradation constant for the LED-MB-Ternary nanocomposite solution is higher than that for the LED-RhB-Ternary nanocomposite solution. This is because the chemical structures of the two molecules are very different. One noteworthy finding is the strong positive relationship between the rate of mineralisation and the time it takes for a response. Our study revealed that TCAA requires a more extended period to mineralize fully. The

data shows that the ternary nanocomposite method was more effective than TCAA in the mineralization of 2,4-DCP.